Copyright Notice

IIUM ENGINEERING JOURNAL

AIMS & SCOPE OF IIUMENGINEERING JOURNAL

The **IIUM Engineering Journal**, published biannually (January and July), is a carefully refereed international publication of International Islamic University Malaysia (IIUM). Contributions of high technical merit within the span of engineering disciplines; covering the main areas of engineering: Electrical and Computer Engineering; Mechanical and Manufacturing Engineering; Automation and Mechatronics Engineering; Material and Chemical Engineering; Environmental and Civil Engineering; Biotechnology and Bioengineering; Engineering Mathematics and Physics; and Computer Science and Information Technology are considered for publication in this journal. Contributions from other areas of Engineering and Applied Science are also welcomed. The IIUM Engineering Journal publishes contributions under *Regular papers and Invited review papers*. It also welcomes contributions that address solutions to the specific challenges of the developing world, and address science and technology issues from an Islamic and multidisciplinary perspective.

REFEREES' NETWORK

All papers submitted to IIUM Engineering Journal will be subjected to a rigorous reviewing process through a worldwide network of specialized and competent referees. Each accepted paper should have at least two positive referees' assessments.

SUBMISSION OF A MANUSCRIPT

A manuscript should be submitted online to the IIUM-Engineering Journal website at http://journals.iium.edu.my/ejournal. Further correspondence on the status of the paper could be done through the journal website.

INTERNATIONAL ADVISORY COMMITTEE

Table of Contents

MATERIALS AND MANUFACTURING ENGINEERING

MECHANICAL AND AEROSPACE ENGINEERING

EFFECT OF FEED FLOWRATES ON THE PHYSICAL PROPERTIES AND ANTIOXIDANT OF MAHKOTA DEWA (*PHALERIA MACROCARPA*) ENCAPSULATED POWDER

MUHAMMAD NORZAMAN KATHIMAN[1], **SITI KHOLIJAH ABDUL MUDALIP**[1,2*] **AND JOLIUS GIMBUN**[1,2]

[1]*Department of Chemical Engineering, College of Engineering, Universiti Malaysia Pahang, 26300 Gambang, Pahang, Malaysia.*
[2]*Centre of Excellence for Advanced Research in Fluid Flow, Universiti Malaysia Pahang, 26300 Gambang, Pahang, Malaysia.*

[*]*Corresponding author: kholijah@ump.edu.my*

ABSTRACT: This paper presents an experimental study on the encapsulation of Mahkota Dewa extracts by maltodextrin using spray drying. The bioactive compound from dried Mahkota Dewa was obtained using a subcritical water extraction process prior to a spray drying process. The effect of feed flow rate (485 to 2115 ml/h) was investigated using one-factor-at-a-time (OFAT). It was observed that the mean particle size increase varied from 3.55 to 8.38 µm when the feed flow rate increased from 485 to 2115 ml/h. Moisture content increased 4.88 to 6.83% as the feed flow rate increased from 485 to 2115 ml/h, whereas the antioxidant activity increased slightly from 90.48 to 91.65%. The findings from this study showed that decrease in feed flow rate reduces antioxidant activity, moisture content, and particle size.

ABSTRAK: Kertas kerja ini adalah berkenaan kajian eksperimen melalui proses pengkapsulan ekstrak buah Mahkota Dewa dengan menggunakan maltodekstrin melalui teknik pengeringan semburan. Sebatian bioaktif dari buah Mahkota Dewa kering diperoleh melalui teknik pengekstrakan air subkritikal sebelum proses pengeringan semburan. Kesan kadar aliran masuk (485 hingga 2115 ml/jam) dikaji menggunakan konsep satu-faktor-pada-satu-masa (OFAT). Dapatan kajian mendapati bahawa purata saiz zarah meningkat dari 3.55 kepada 8.38 µm ketika kadar aliran masuk meningkat dari 485 sehingga 2115 ml/jam. Kandungan kelembapan meningkat dari 4.88 kepada 6.83% dengan kenaikan kadar aliran masuk dari 485 hingga 2115 ml/jam, sedangkan aktiviti antioksida meningkat sedikit dari 90.48 hingga 91.65%. Dapatan kajian menunjukkan bahawa penurunan kadar aliran masuk berkurang melalui aktiviti antioksida, kandungan kelembapan dan saiz zarah.

KEYWORDS: *Mahkota Dewa; spray drying; antioxidant; maltodextrin*

1. INTRODUCTION

Mahkota Dewa (*Phaleria Macrocarpa (Scheff.) Boerl)*, which is a member of the *Thymelaeaceae* family, is an important herbal species originating from Papua New Guinea Island (Irian Jaya), Indonesia [1]. The plant is quite popular among South East Asian peoples and is traditionally used in local folk medicine as complementary alternative medicine for several diseases such as cancer, hypertension, and diabetes mellitus. The major parts of the plant namely the stem, leaves, egg shell of the seeds, and fruits are mostly enriched in

bioactive compounds such as alkaloids, flavanoids, mangiferin, polyphenols, and saponins [2,3]. In particular, Mahkota Dewa fruit has been related to antioxidant activity and hence, the use of this fruit can be suggested as a strategy to control hyperglycemia problems in diabetic patients. Several studies also have been performed to understand and prove other biological properties related to Mahkota Dewa fruit, such as its anti-carcinogenic, anti-hypertensive, anti-tumour, anti-viral, anti-bacterial, anti-fungal, and anti-inflammatory properties [1]. Previous researchers reported the extraction of bioactive compounds from Mahkota Dewa fruits and leaves using conventional and nonconventional extraction techniques such as maceration [4], microwave [5], subcritical water [6,7], and supercritical carbon dioxide [8]. This is because obtaining the targeted bioactive compounds naturally present in plants depends on the extraction techniques employed.

Other works also reported that the conversion of the liquid extracts to powdered form product is preferred in industry for several reasons. For example, the product in powdered form is easier to handle and has been reported to show better stability, longer shelf-life and more convenience for oral consumption [9]. Polyphenols are an example of the bioactive compounds extracted from the plant parts that are very susceptible to an oxidizing environment. Spray drying is an established method used to convert the liquid extracts to powdered form product and well known in food industry due to its flexibility, low cost and large scale applicability [10]. However, the operation of spray drying that requires high operating temperature, up to 215 °C, may cause a thermal degradation issue to the extracts and poor quality of the powdered product produced [9]. One such method to overcome the issue is encapsulation of the extracts using a suitable carrier agent or polymer. In this situation, the carrier agent acts as a coating wall and provides a physical barrier between the extracts and the external environment. Maltodextrin is frequently employed as a carrier agent in the spray drying of food products. It is a low-cost polysaccharide with a neutral scent and flavour that can diminish powder hygroscopicity if larger doses of the agent are used [11]. According to Raja et al. [12], maltodextrin with dextrose equivalent (DE) of 10 to 20 is appropriate for use as a carrier agent.

Previous studies have described the operating conditions and carrier agents used during spray drying for plants such as *Moringa stenopetala* [13] and saffron [14]. A review on the encapsulation technology application in other plants or food products was also reported by Ray et al. [15]. To our knowledge, no work reported the conversion of Mahkota Dewa extracts to powdered form. Based on this consideration, this study was performed to investigate the effect of different feed flow rates during the spray drying process on the physical properties and antioxidant activity of Mahkota Dewa spray-dried extract. The maltodextrin DE10 was utilised as a carrier agent. The powdered forms of the products obtained were all assessed in terms of antioxidant activity, moisture content, particle size distribution, and physical appearance.

2. MATERIALS AND METHOD

2.1 Materials and Chemicals

The commercial dried Mahkota Dewa fruits were purchased from Ethno Resources Sdn. Bhd, Selangor, Malaysia. The samples were ground to an average size of 520 µm using RETSCH GmbH dry grinder (Germany). The deionized water used for the subcritical extraction process was prepared using Milli-Q, Ultrapure Water Purification System (Massachusetts, USA). The food grade maltodextrin DE10, obtained from San Soon Seng Food Industries Sdn Bhd, Selangor, Malaysia, was used as the carrier agent for the spray drying process. The methanol (99.9 wt% purity) and 1,1-diphenyl-2-picrylhydrazyl

(DPPH), purchased from Merck Sdn. Bhd. (Selangor, Malaysia), were used in the analysis. All compounds were used without any further purification process.

2.2 Extraction of Mahkota Dewa

The Mahkota Dewa was extracted using a subcritical water extraction method described in previous work [7]. About 60 g of ground dried Mahkota Dewa were weighed and mixed with one liter of deionized water in a beaker. The mixture was stirred and placed in a laboratory pressure reactor system (Buchiglasuster Kiloclave, Switzerland) at 106 °C for 5 h to perform the extraction. After that, the vessel was cooled down to room temperature using cooling water. The cooling water was supplied by a Stuart recirculating cooler RE300RC (Staffordshire, UK). The collected extract was filtered to remove the residual solids using Whatman filter paper and kept at -4 °C in a refrigerator until further used in the spray drying process.

2.3 Encapsulation using Spray Drying

Maltodextrin DE10 was dispersed directly into the extract solution and stirred at 1500 rpm using a magnetic stirrer to prepare 20% w/v of spray drying stock solution. The solution was continually stirred and pumped into a laboratory spray-dryer (Lab Plant SD06A, UK) using a peristaltic pump. The inlet air temperature, dry air velocity, and liquid flow rate were set to 200 °C, 3.9 m/s, and 2115 ml/h, respectively. The spray dried powder was collected in a chamber glass bottle, sealed, and kept in the refrigerator at -4 °C until used for analysis. The same procedures were carried out with liquid flow rates of 485, 900, 1305, and 1665 ml/h. The inlet air temperature and dry air velocity were set at 200 °C and 3.9 m/s, respectively. The experiments were carried out in triplicate.

2.4 Characterization Methods

2.4.1 Moisture Content

The moisture content of the sample was measured using an A&D MS-70 moisture analyser. The sample was weighed and placed on the moisture analyser pan at a weight of around one gram. Once the reading became steady, the moisture content shown in percentage value was recorded.

2.4.2 Antioxidant Activity

The antioxidant activities were determined using Tecan Infinite M200 Pro (Switzerland) microplate reader with Magellan software at a wavelength of 517 nm. One milligram of spray dried powder was dissolved in 10 ml of deionized water to make a sample solution. Methanol was used to make a DPPH radical solution at a concentration of one mg/ml. Both solutions were combined and incubated in the dark for 20 min before measuring its absorbance. The DPPH in methanol and ascorbic acid were used as a standard and blank, respectively. The percentage of inhibition was calculated by using Eq. (1):

$$Inhibition\ activity, \% = \left[1 - \left(\frac{A_1}{A_0}\right)\right] \times 100 \tag{1}$$

where A_1 is the absorbance of the sample and A_0 is the absorbance of the control [7].

2.4.3 Particle Size Distributions

A laser diffraction particle size analyser (Malvern 2000 Mastersizer, Malvern Instruments Co., Worcestershire, UK) was used to analyse the particle size distributions. The analyzer was equipped with a sample dispersion unit to ensure that particles were distributed to the measuring region during the analysis. The particle size distribution was

recorded in volume weighted mean.

2.4.4 Morphology

The morphological images were captured using a field emission scanning electron microscope (TM3030 plus, Hitachi High-Technologies Corporation, Japan) at 1e3 kV with a magnification of 1000x. The samples were put on a sample stump made of a double-sided adhesive carbon tape. A Sputter Coater (Quorum Technologies Q300TD, Ltd., United Kingdom) was used to sputter gold onto the samples.

3. RESULTS AND DISCUSSION

3.1 Moisture Content

Moisture content is an important property that determines the flowability, stickiness, and storage stability of microencapsulated powder. It was reported that the powder produced by spray-drying with moisture contents less than 5% is considered safe from microbiological activity and can be stored for long period [16]. The influence of different feed flow rates on moisture content of the spray dried powder is shown in Fig. 1.
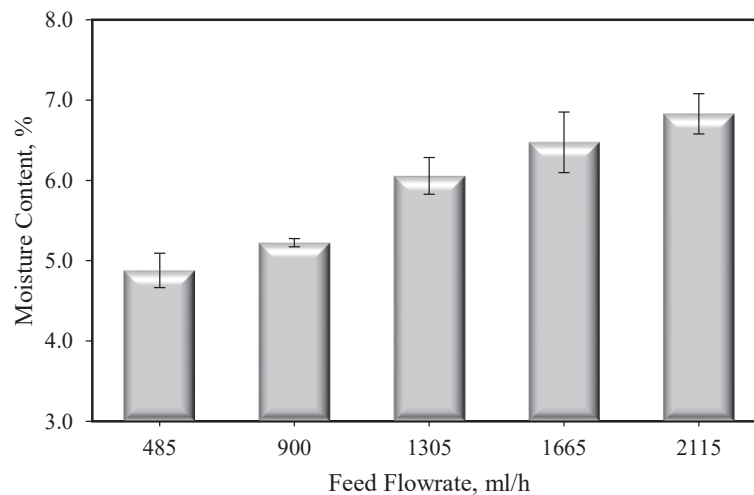
Fig. 1: Moisture content of spray dried powder at different feed flow rates with 0.224 average standard deviation.

As can be seen, the moisture content increased with the increased of feed flow rates pumped into the spray dryer. The lowest moisture content of 4.88 % was achieved at a feed flow rate of 485 ml/h, whereas the highest moisture content of 6.83 % was achieved at a feed flow rate of 2115 ml/h. This result is expected since higher feed flow rates may reduce the contact time between feed samples and drying air. Besides that, the droplets with larger surface area, which were produced at higher feed flow rates, reduce the heat and mass transfer efficiency, hence reducing the water removal during the spray drying process [17]. The result obtained shows similar trends with those reported by Chegini and Ghobadian [18] who studied the effect of feed flow rates on moisture content and bulk density of orange juice powder. Hong and Choi [19] also reported that the powder moisture content increased with the increased of sample pumping rate and inlet air temperature. Braga et al. [20] reported that a feed flow rate of 300 – 900 ml/h used for spray drying of pineapple mint juice showed significant effect on the powder moisture content, where powder with lower

moisture content was obtained when the lower feed flow rate was used. Additionally, other work reported that dripping inside the spray drying chamber was observed at high feed flow rates [21]. However, the phenomenon was not observed for the range of feed flow rates used in this work.

3.2 Antioxidant Activity

Rezende and co-workers reported that the presence of phenolic compounds contribute to the high antioxidant activities in plant extract [22]. Mahkota Dewa fruit extract has been reported to provide beneficial bioactivity results such as antioxidant effects due to the present of mangiferin, saponin, alkaloid, and polyphenols [10,12]. Figure 2 shows the antioxidant activity in spray dried powder at different feed flow rates. A slight increment of the antioxidant activity was observed when the feed flow rate increased. The highest feed flow rate (2115 ml/h) produced spray dried powder with higher antioxidant activity (91.65%). This is probably caused by an inefficient heat transfer that occurs between the feed solution and hot air inside the spray drying chamber at higher feed flow rate. Phisut [23] stated that the inefficient heat transfer inside the main chamber at high feed flow rates may produce powdered product with low yield but high antioxidant activity.
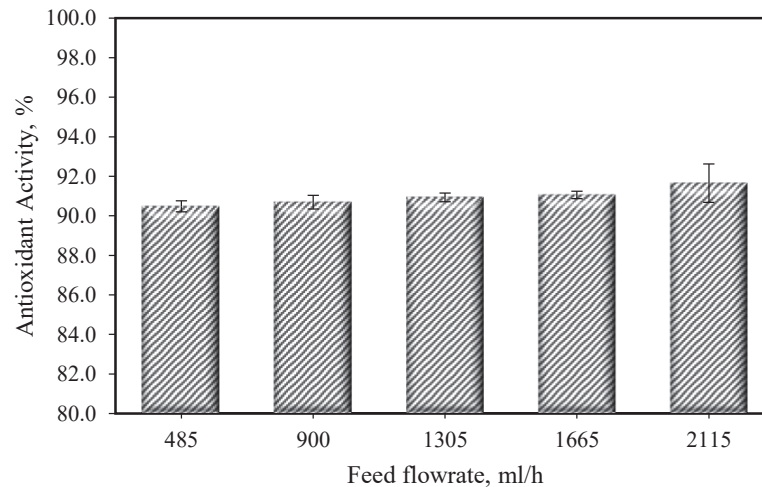
Fig. 2: Antioxidant activity of spray dried powder at different feed flow rates with 0.40 average standard deviation.

3.3 Particle Size Distribution

Figure 3 illustrates the particle size distribution (PSD) of powdered Mahkota Dewa obtained at different feed flow rates. As can be seen, the PSD of the spray dried powder produced are in bimodal shape. The range of PSD for feed flow rates of 485 and 900 ml/h is smaller, which is in between 0.2 to 85 μm. Whereas, for higher feed flow rates, the range of PSD produced is bigger, between 0.9 to 670 μm. The mean diameter and volume weighted mean of spray dried powders produced at different feed flow rates is summarized in Table 1. As shown in the table, the mean diameter of the spray dried power produced is larger at higher feed flow rates. This finding could be related to the high moisture content characteristic of the powdered product produced at high feed flow rates. This is because the powdered product with higher moisture content tends to stick together, thus causing larger particles to form, as shown in Fig. 3. Besides that, bigger droplets obtained at higher feed

flow rates may contribute to the findings. Studies by Phisut [23] and Chegini and Ghobadian [18] also reported that larger PSD was produced at higher feed flow rates.
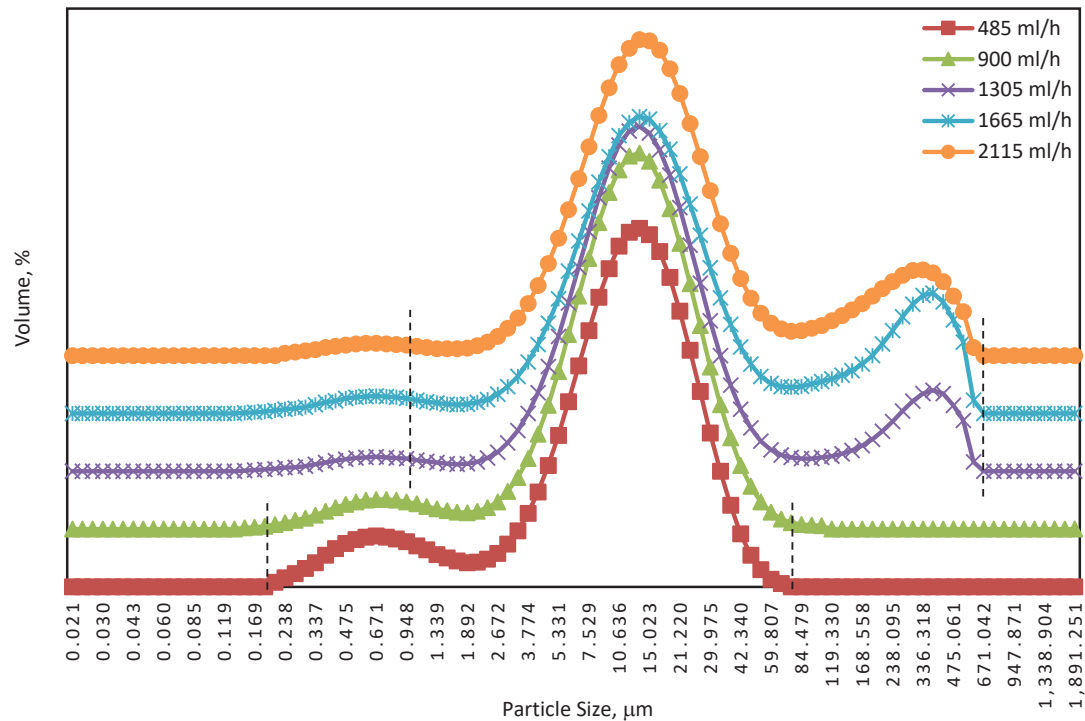
Fig. 3: Particle size distributions of spray dried powder at different feed flow rates.

Table 1: Mean diameter and volume weighted mean of spray dried powders produced at different feed flow rates

Feed flow rate (ml/h)	Mean diameter (µm)	Volume weighted mean D [4,3] (µm)
485	3.549	13.157
900	4.670	14.400
1305	7.169	53.484
1665	7.014	74.706
2115	8.376	60.585

3.4 Morphology

The micrograph images of Mahkota Dewa powder were taken using SEM and shown in Fig. 4. The micrograph images were taken for powdered product obtained with and without maltodextrin DE10 as carrier agent. For experiments with carrier agents, micrograph images were taken for powdered samples obtained using feed flow rates of 485 ml/h and 2115 ml/h. As can be seen in Fig. 4 (a), the particles obtained without maltodextrin are in spherical and irregular forms. No pores were observed on the external surfaces of the powdered product produced but most of it shows shrinking effect. According to Ding et al. [24], the shrinking effect on the particles' surfaces is probably caused by rapid water evaporation during the drying process. Moreover, the shriveled surface, which is a usual characteristic for organic materials produced using spray drying with various sizes, was also observed. As can be seen in Fig. 4 (a), a sample's surface is in the shriveled state and does

not attach to other particles. However, the shriveled particles, especially in Fig. 4 (b), were attaching to one another. This is probably related to the moisture content in the particles. Even though some of the particles were shrunk and had a shriveled surface, other particles had a smooth surface.

(a)   (b)

(c)
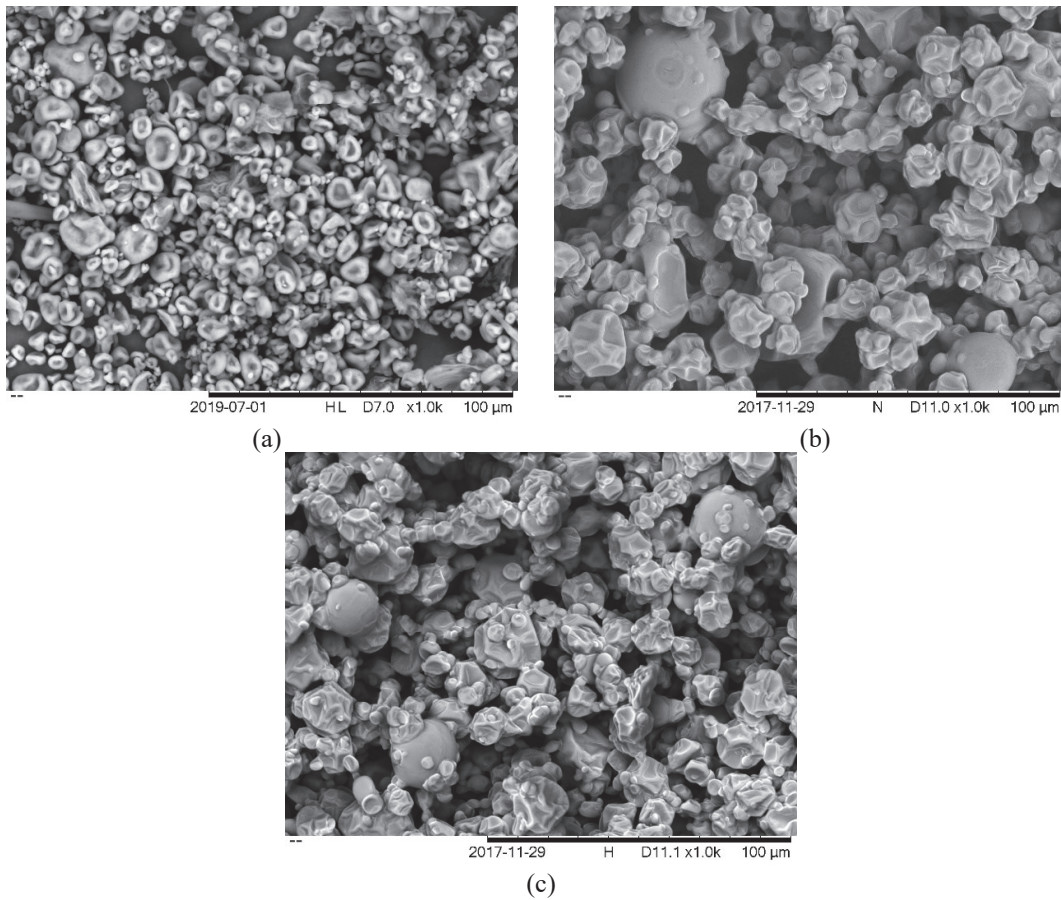
Fig. 4: SEM micrographs of powdered samples obtained at (a) without maltodextrin DE 10 and feed flow rate of 2115 ml/h, (b) with maltodextrin DE 10 and feed flow rate of 2115 ml/h, and (c) with maltodextrin DE 10 and feed flow rate of 485 ml/h. The inlet dry air temperature and air flow rate were fixed at 200 °C and 3.5 m/s, respectively.

Meanwhile in Fig. 4 (c), some of the particles had shriveled surfaces, while others had smooth surfaces. The bulk of the particles had shriveled and constricted surfaces when the inlet air temperature was low. The number of particles with smooth surfaces rose as the drying temperatures increased. This is due to the differences in drying rates, or higher temperatures, which resulted in faster water evaporation and the formation of a smooth and hard outer layer. Nijdam and Langrish [25] demonstrated the formation of more rigid particles when high temperature was used in the spray drying of milk. According to their findings, vacuole shapes form inside a molecule not long after an outer layer appears, and it expands once the molecule temperature exceeds the local ambient boiling point and the vapor pressure inside the vacuole exceeds the local ambient pressure. When the drying temperature is high enough, moisture evaporates quickly and the outer layer becomes dry and hard, preventing the hollow molecule from flattening as it moves towards colder, dryer areas. However, the outer layer remains fluid and supple for longer when the drying temperature is lower, allowing the empty molecule to flatten and wither as it cools [25].

4. CONCLUSION

The effect of different feed flow rates on Mahkota Dewa extracts encapsulated with maltodextrin using a spray drying technique has been studied. The results show that higher feed flow rates produced powdered product with higher moisture content, antioxidant activity and PSD. However, since the powdered product with low moisture content is desirable, the low feed flow rate of 485 ml/h is recommended in this work. Besides, the antioxidant activity produced at 485 ml/h is quite high, which is more than 90%.

ACKNOWLEDGEMENT

REFERENCES

[1]   Altaf R, Asmawi MZ, Dewa AA, Sadikun A, Umar MI. (2013) Phytochemistry and medicinal properties of *Phaleria macrocarpa* (Scheff.) Boerl. extracts. Pharmacognosy Review, 7(13): 73-80. DOI: 10.4103/0973-7847.112853

[2]   Trilaksana N, Riwanto I, Tjandrawinata RR, Winarto R. (2017) Inhibition of Mahkota Dewa (*Phaleria macrocarpa*) bioactive fraction on proliferation of human retinoblastoma tumor cells Y-79 through suppression of mRNA level of cyclin E. Asian Pacific Journal of Tropical Biomedicine, 7(4): 280-287. https://doi.org/10.1016/j.apjtb.2017.01.001

[3]   Ramdani ED, Marlupi UD, Sinambela J, Tjandrawinata RR. (2017) Isolation and identification of compounds from *Phaleria macrocarpa* (Scheff.) Boerl fruit extract. Asian Pacific Journal of Tropical Biomedicine, 7(4): 300-305. DOI : 10.1016/j.apjtb.2016.12.018

[4]   Fariza N, Luqman Chuah A, Pin KY, Dayang Radiah AB. (2014) Optimisation of extraction of *Phaleria macrocarpa* leaves. Medicinal & Aromatic Plants 3(1): 1000149. DOI: 10.4172/2167-0412.1000149

[5]   Alara OR, Abdul Mudalip SK, Abdurahman NH, Mahmoud MS, Obanijesu EO-O. (2019) Data on parametric influence of microwave-assisted extraction on the recovery yield, total phenolic content and antioxidant activity of *Phaleria macrocarpa* fruit peel extract. Chemical Data Collections, 24: 100277. https://doi.org/10.1016/j.cdc.2019.100277

[6]   Kim W-J, Veriansyah B, Lee Y-W, Kim J-H, Kim J-D. (2010) Extraction of mangiferin from Mahkota Dewa (*Phaleria macrocarpa*) using subcritical water. Journal of Industrial and Engineering Chemistry, 16(3): 425-430. doi:10.1016/j.jiec.2009.08.008

[7]   Hashim NA, Abdul Mudalip SK, Harun N, Man RC, Sulaiman SZ, Arshad ZIM, Shaarani SM, Azmir J. (2019) Mahkota Dewa subcritical water extraction process: Experimental and molecular dynamics simulation study. Chemical Engineering & Technology, 42(9): 1747-1756. https://doi.org/10.1002/ceat.201800638

[8]   Azmir J, Zaidul ISM, Sharif KM, Uddin MS, Jahurul MHA, Jinap S, Hajeb P, Mohamed A. (2014) Supercritical carbon dioxide extraction of highly unsaturated oil from *Phaleria macrocarpa* seed. Food Research International, 65: 394-400. https://doi.org/10.1016/j.foodres.2014.06.049

[9]   Gallo L, Ramírez-Rigo MV, Piña J, Bucalá V. (2015) A comparative study of spray-dried medicinal plant aqueous extracts: Drying performance and product quality. Chemical Engineering Research and Design, 104 681-694. https://doi.org/10.1016/j.cherd.2015.10.009

[10]   Fang ZX, Bhandari B. (2011) Effect of spray drying and storage on the stability of bayberry polyphenols. Food Chemistry, 129(3): 1139-1147. https://doi.org/10.1016/j.foodchem.2011.05.093

[11]   Goula AM, Adamopoulos KG. (2010) Effect of maltodextrin addition during spray drying of tomato pulp in dehumidified air: II. Powder properties. Innovative Food Science & Emerging Technologies, 11(2): 342-351. https://doi.org/10.1080/07373930802046377.

[12] Raja KCM, Sankarikutty B, Sreekumar M, Jayalekshmy A, Narayanan CS. (1989) Material characterization studies of maltodextrin samples for the use of wall material. Starch - Stärke, 41(8): 298-303. https://doi.org/10.1002/star.19890410805

[13] Dadi DW, Emire SA, Hagos AD, Eun J-B. (2020) Effects of spray drying process parameters on the physical properties and digestibility of the microencapsulated product from *Moringa stenopetala* leaves extract. Cogent Food & Agriculture, 5(1): 1690316. https://doi.org/10.1080/23311932.2019.1690316

[14] Garavand F, Rahaee S, Vahedikia N, Jafari SM. (2019) Different techniques for extraction and micro/nanoencapsulation of saffron bioactive ingredients. Trends in Food Science & Technology, 89: 26-44. https://doi.org/10.1016/j.tifs.2019.05.005

[15] Ray S, Raychaudhuri U, Chakraborty R. (2016) An overview of encapsulation of active compounds used in food products by drying technology. Food Bioscience, 13: 76-83. http://dx.doi.org/10.1016/j.fbio.2015.12.009

[16] Tontul I, Topuz A. (2017) Spray-drying of fruit and vegetable juices: Effect of drying conditions on the product yield and physical properties. Trends in Food Science & Technology, 63: 91-102. https://doi.org/10.1016/j.tifs.2017.03.009

[17] Can Karaca A, Guzel O, Ak MM. (2016) Effects of processing conditions and formulation on spray drying of sour cherry juice concentrate. Journal of the Science of Food and Agriculture, 96(2): 449-455. https://doi.org/10.1002/jsfa.7110

[18] Chegini GR, Ghobadian B. (2005) Effect of spray-drying conditions on physical properties of orange juice powder, Drying Technology, 23(3): 657-668. DOI: 10.1081/DRT-200054161

[19] Hong J-H, Choi Y-H. (2007) Physico-chemical properties of protein-bound polysaccharide from *Agaricus blazei* Murill prepared by ultrafiltration and spray drying process. International Journal of Food Science & Technology, 42(1): 1-8. https://doi.org/10.1111/j.1365-2621.2005.01116.x

[20] Braga V, Guidi LR, de Santana RC, Zotarelli MF. (2020) Production and characterization of pineapple-mint juice by spray drying. Powder Technology, 375: 409-419. https://doi.org/10.1016/j.powtec.2020.08.012

[21] Tonon RV, Brabet C, Hubinger MD. (2008) Influence of process conditions on the physicochemical properties of açai (*Euterpe oleraceae* Mart.) powder produced by spray drying, Journal of Food Engineering, 88(3): 411-418. https://doi.org/10.1016/j.jfoodeng.2008.02.029

[22] Rezende YRRS, Nogueira JP, Narain N. (2018) Microencapsulation of extracts of bioactive compounds obtained from acerola (*Malpighia emarginata* DC) pulp and residue by spray and freeze drying: Chemical, morphological and chemometric characterization. Food Chemistry, 254: 281-291. https://doi.org/10.1016/j.foodchem.2018.02.026

[23] Phisut N. (2012) Spray drying technique of fruit juice powder: Some factors influencing the properties of product. International Food Research Journal, 19: 1297-1306.

[24] Ding J, Xu Z, Qi B, Cui S, Wang T, Jiang L, Zhang Y, Sui X. (2019) Fabrication and characterization of soybean oil bodies encapsulated in maltodextrin and chitosan-EGCG conjugates: An in vitro digestibility study. Food Hydrocolloids, 94: 519-527. https://doi.org/10.1016/j.foodhyd.2019.04.001

[25] Nijdam JJ, Langrish TAG. (2006) The effect of surface composition on the functional properties of milk powders. Journal of Food Engineering, 77(4): 919-925. https://doi.org/10.1016/j.jfoodeng.2005.08.020

POTENTIAL OF LOW CARBON NANOTUBES DOSAGE ON CHROMIUM REMOVAL FROM WATER

**Nassereldeen Ahmed Kabbashi[1*], Firdaus Abd-Wahab[1],
Warqaa Muhammed Bahaaddin[2], Lubna Muhamed Musa[3],
Abdurahman Nour Hamid[4], and Isam Yasseen Qudsieh[5]**

*[1]Department of Chemical Engineering & Sustainability, Kulliyyah of Engineering,
International Islamic University Malaysia, Jalan Gombak, 53100 Kuala Lumpur, Malaysia.
[2]Department of Environmental Science, Duhok Polytechnic University, Iraq.
[3]Department of horticultural sciences, Faculty of Agriculture, Gezira University, Sudan
[4]Faculty of Chemical & Natural Resources Engineering,
Universiti Malaysia Pahang, Malaysia.
[5]Chemical Engineering Department, College of Engineering, Jazan University,
P.O.Box 706, Jazan 45142, Saudi Arabia.*

[*]Corresponding author: nasreldin@iium.edu.my

ABSTRACT: This paper involves a method of eliminating hexavalent chromium (Cr (VI)) from the synthetic water via a low dosage of carbon nanotubes (CNT). The ability of CNT to remove Cr(VI) from synthetic water through the adsorption process was studied in batch experimentation. The findings revealed up to 100% elimination of Cr(VI) in the 0.07 mg/L Cr(VI) concentration. These excessive elimination proficiencies were credited to the powerful adsorption of chromium ions to the physical properties of the CNT. A pattern layout was created in these experimental runs in order to locate the ideal situation of the Cr(VI) deletion from synthetic water. To accomplish the purposes of the experiment, there were 4 independent variables influencing several points, namely the CNT dosage, the pH of the water, the agitation speed, and the contact time. The StatGraphics Centurion XV software has been used to create the adsorption equivalence and to discover the major impacts to the elimination of Cr(VI). The results show that the adsorption capability of the carbon nanotubes was considerably reliant on the pH of the Cr(VI) solution, supported by the CNT dosage, the contact time, and the agitation speed. The expected optimization, using the adsorption equation, shows that a 1 mg CNT dosage with a pH=2, 120 minutes contact time, and moderate agitation rate at 150 rpm is the most optimal.

ABSTRAK: Kajian ini melibatkan kaedah bagi menyingkirkan kromium (VI) dari air sintetik menggunakan karbon tiub nano berdos rendah. Eksperimen kelompok dilakukan bagi menentukan keupayaaan karbon tiub nano menyingkirkan Cr(VI) dari air sintetik melalui proses penjerapan. Dapatan kajian menunjukkan Cr(VI) telah disingkirkan sebanyak 100% dari kepekatan 0.07 mg/L Cr(VI). Kecekapan penyingkiran ini adalah disebabkan penjerapan ion-ion kromium yang kuat terhadap sifat fizikal nano tiub karbon tersebut. Rekabentuk eksperimen telah dibina bagi menentukan peringkat optima penyingkiran Cr(VI) dari air sintetik. Bagi mencapai matlamat kajian, empat faktor yang terdiri daripada dos nano tiub karbon, pH air, kelajuan goncangan dan masa sentuhan diukur. Perisian StatGraphics Centurion XV telah digunakan bagi mendapatkan nilai setara proses penjerapan dan kesan utama yang menyebabkan tersingkirnya Cr(VI). Dapatan kajian menunjukkan keupayaan penjerapan oleh nano tiub karbon sangat bergantung kepada pH larutan Cr(VI), disusuli dengan dos nano tiub karbon masa sentuhan dan kelajuan goncangan. Penjerapan optimum Cr(VI) dapat dicapai pada tahap

1 mg dos nano tiub karbon, larutan pada pH 2, masa sentuhan selama 120 minit dengan kelajuan goncangan sebanyak 150 rpm.

KEYWORDS: *STatGraphics; low CNT dosage; polluted water; chromium*

1. INTRODUCTION

Carbon nanotubes (CNTs) are new technology. They consist of cylinder-shaped carbon fragments and have various schemes that make them hypothetically beneficial in a wide range of functions in medicines, engineering, biotechnology, and other areas of materials science [1]. They demonstrate extraordinary strength and exceptional electrical properties. The characteristics of nanotubes are defined by their thickness and chiral angle, both of which depend on *n* and *m* [2]. The thickness, d_t, is simply the length of the chiral vector divided by 4, and it has been found that

$$d_t = (Ö_3/p)\, a_{c\text{-}c}\, (m^2 + mn + n^2)^{1/2}, \tag{1}$$

where $a_{c\text{-}c}$ is the space among neighboring carbon atoms in the flat sheet. In turn, the chiral angle is given by

$$\tan^{-1}(Ö_3 n/(2m + n)) \tag{2}$$

The existence of heavy metals in the environment is of prime concern because of their harmfulness to many life forms. Various manufacturing practices produce aqueous wastes that contain heavy metal toxins. Since the bulk of heavy metals do not break down into nontoxic end products, their concentrations must be decreased to appropriate amounts before the release of industrial effluents [3]. Without extraction, the presence of these heavy metals could create threats to public health and disturb the visual quality of potable water. According to the World Health Organization (WHO), the metals of highest immediate alarm are chromium, aluminum, iron, manganese, nickel, cobalt, zinc, copper, mercury, cadmium, and lead. Conventional methods for elimination of metals from industrial effluents involve solvent extraction, chemical precipitation, electrolytic extraction, dialysis, reverse osmosis, cementation, ion exchange, membrane filtration, adsorption and co-precipitation [4,5]. Traditional chemical and physical treatment of low concentration, large volume wastes can be likely very costly [6]. Consumptive processes, such as chemical precipitation, entail large capital and operating costs. Awareness has therefore centered on non-consumptive techniques that involve ion-exchange and other sorption processes. The concept of using low-cost carbons and agricultural products and by-products for the removal of toxic metals from water has been examined by number of sources [7]. Findings to evaluate the capability of scrap rubber to adsorb dissolved metal ions from water found it to be a reasonably effective adsorbent [8].

Chromium removal in water treatment is a big challenge since the maximum limit concentration allowed in drinking water is only 0.1 ppm. Chromium can be found in many oxidation forms; Cr(VI) being the most toxic and soluble, and Cr(III) being the least toxic form of chromium [9]. Conventionally, heavy metals are removed by techniques that produce hazardous chemical wastes and require post-treatment [10]. Therefore, a wider interest has been shown in finding alternative methods to remove Cr species from water to ensure sustainable and consumable water supply. In this premise, low carbon nanotube dosage will be used to remove chromium from water. The elimination of chromium from wastewater can be valuable in environmental research as the carbon nanotubes have comparatively low growth temperature, high yields, and high purities that can be attained and low cost [11]. In another study by El-Shafey [12], he reported that chromium sorption

was highly dependent on the initial pH value with reduction taking place in solutions with pH up to 7, showing sorption maxima in the pH range of 1.8–2.8 for the concentration range of 100–500 mg/L with an increase in the equilibrium pH. Carbon dioxide evolved from the sorption media was determined.

2. METHODS FOR REMOVAL OF Cr(VI)

A number of treatment techniques for the elimination of metal ions from water have been described here, with emphasis on ion exchange, reduction, electrochemical precipitation, electrodialysis, solvent extraction, evaporation, chemical precipitation, reverse osmosis and adsorption [13,14].The physical and chemical properties of Cr(VI) are displayed in Table 1. The Cr(VI) concentration must be eliminated as it comes with deleterious effects to human health and is described as carcinogenic [15]. Table 2 indicates numerous possible health impacts from human exposure to Cr(VI).

Table 1: Physical and chemical properties of Cr(VI)

Parameter	Properties
Physical State	liquid
Appearance	orange
Odor	none reported
pH	~7
Vapor Pressure	14 mm Hg @20 ºC
Vapor Density	0.7
Evaporation Rate	>1 (ether=1)
Viscosity	Not available
Boiling Point	212 °F
Freezing/Melting Point	32 °F
Decomposition Temperature	Not available
Solubility	Soluble in water
Specific Gravity/Density	1.0
Molecular Formula	Solution
Molecular Weight	Not available

(Source: Atieh, 2010)

Table 2: Impact of Cr(VI) to human health

Type of Exposure	Effect
Ingestion	May affect kidneys and cause harm. May cause serious gastrointestinal tract irritation with nausea, vomiting, and possible burns.
Eye	Produces eye irritation and likely burns.
Skin	May affect skin sensitization, an allergic reaction, which becomes obvious upon re-exposure to this material. Contact may cause irritation and likely burns. Lengthy skin contact may produce injury, especially if the skin is abraded.
Chronic	Long-time contact or repeated skin contact may affect sensitization dermatitis and likely destruction and/or ulceration. May cause respiratory tract cancer. May cause liver and kidney damage. Chronic inhalation may cause nasal septum ulceration and perforation.
Inhalation	May cause liver and kidney damage. May cause ulceration and perforation of the nasal septum if inhaled in excessive amounts. Causes respiratory tract irritation with likely burns.

(Source: Nomanbhay, 2005)

2.1 Formulation of the Chromium Stock Solution

The stock solution of 1000mg/L of Cr (VI) ions was prepared using 2.829g $K_2Cr_2O_7$ salt or solids. New dilutions were applied for each study of the Cr (VI) elimination which is 0.07mg/l, CNT dosage is from 0.1 to 1 mg, contact time is shown in Table 2 as well as agitation speed. The pH of the solutions was modified using 0.1M HCl and 0.1M NaOH and buffer was employed for keeping the pH of the solutions matching to the pH needed [2].

2.2 The Adsorption Findings

The adsorption capability of carbon nanotubes was established by the matrix design by setting the Cr(VI) concentrations (0.07 mg/L) of 50 mL Cr solution in 100 mL shake flasks, with several carbon nanotubes dosage (1 mg and 0.1 mg). The combination was stirred in a rotary shaker at different speeds (200 rpm, 150 rpm, 100 rpm and 50 rpm) supported by filtration making use of a syringe filter. The filtrate comprising the remaining concentration of Cr(VI) was verified spectrophotometrically at 540 nm after complexation with 1,5 diphenylcarbazide [16]. For the purpose of rate of metal adsorption by carbon nanotubes, the supernatant was studied for remaining Cr(VI) after the contact period of 10, 20, 30, 40, 60, 120 and 1440 minutes. The impact of pH on Cr adsorption by carbon nanotubes was revealed at pH values of 2, 4, and 6. The impact of various dosages of carbon nanotubes were 0.1, 1 mg at 0.07 mg/L Cr(VI) carbon nanotubes was selected. All the variable quantity is shown in Table 3 below whereas Fig. 1 confirms the overall summary of the Cr(VI) elimination using carbon nanotubes.

Table 3: Experimental system layout

No.	Independent Variables	No. of Levels	Description
1	Cr(VI) concentration (mg/L)	1	0.07
2	pH	3	6, 4, 2
3	CNT Dosage (mg)	4	1, 0.1
4	Contact Time (min)	7	10, 20, 30, 40, 60, 120, 1440
5	Agitation Speed (rpm)	4	50, 100, 150, 200

3. OUTCOMES AND ANALYSIS

3.1 Consequences of Variables on the Cr (VI) Elimination

The results obtained showed that the chromium exhibits different types of pH-dependent equilibria in aqueous solution, Cr(VI) is a highly toxic compound causing severe human health effects. For smaller pH (pH=2) values, $Cr_3O_{10}^-$ and $Cr_4O_{13}^{2-}$ varieties are created. The best possible original pH for the adsorption of hexavalent chromium onto carbon nanotubes was detected at pH=2. This implies the creation of more polymerized chromium oxide varieties with reduced pH.

Nearly 100% of Cr(VI) ions were adsorbed from a solution of 0.07 mg/L [Cr(VI)], at pH=2, while the adsorption was reduced by the alteration of the pH from 2 to 4 and 6 (as in Fig. 1). The results showed that alcoholic groups are converted to carboxylic groups while reducing Cr(VI) to Cr(IV). The adsorption of metal ions varies on solution pH, which affects electrostatic attachment of ions to related metal groups.
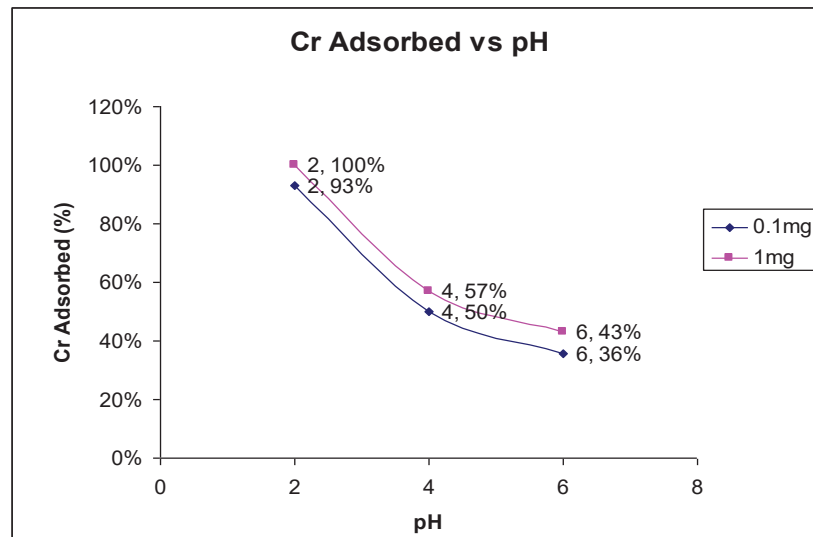
Fig. 1: Impact of pH on the adsorption of Cr(VI) at 0.07 mg/L Cr(VI) concentration.

3.2 Impact of Carbon Nanotubes Amount on Chromium Application

The concentration of both the metal ions and the carbon nanotubes is a substantial component to be studied for efficient adsorption. The amount of adsorption is a function of the original intensity of ions. The carbon nanotubes were different from 10 mg, 5 mg, 1 mg and 0.1 mg and caused interaction with the Cr(VI) solutions of 0.07 mg/L intensities. The concentration of the carbon nanotubes in the 50 mL solution is 2 mg/L for 0.1mg and 20 mg/L for 1 mg CNT. For 1 mg CNT, the elimination of chromium is successful and accomplished 100% elimination with pH=2, agitation speed of 150 rpm and 120 minutes, as displayed in Fig. 2.
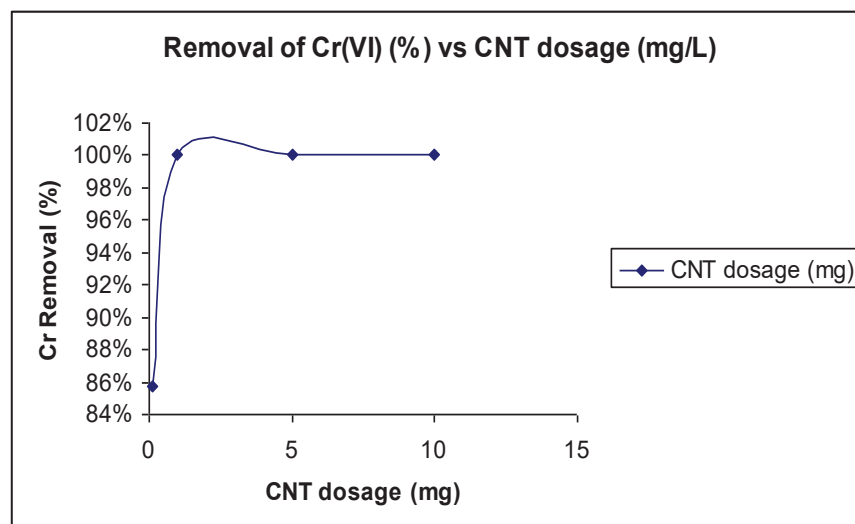
Fig. 2: Impact of CNT amount on Cr(VI) adsorption from solutions at
0.07 mg/L Cr(VI).

3.3 Impact of Agitation Speed

The result of the agitation of the adsorption system in Cr adsorption was observed at 200 rpm, 150 rpm, 100 rpm and 50 rpm of agitation. All agitation speeds were discovered to have positive impact to the adsorption process, as shown in Fig. 3.

Agitation enables appropriate interaction among the metal ions in solution and the CNT binding sites and, by this means, supports efficient moving of chromium ions to the carbon nanotubes sites. At 100 rpm and 50 rpm, the adsorption speeds observed were discovered to be marginally smaller than that of 200 rpm and 150 rpm. These findings reveal that the interaction between solids and liquid is more efficient at 200 rpm and 150 rpm but a medium speed at 150 rpm is the safest. This remark, as in Fig. 3, concurs with the earlier described biosorptive elimination of Cr(VI) by the husk of Bengal gram *(Cicer arientinum)* [17].
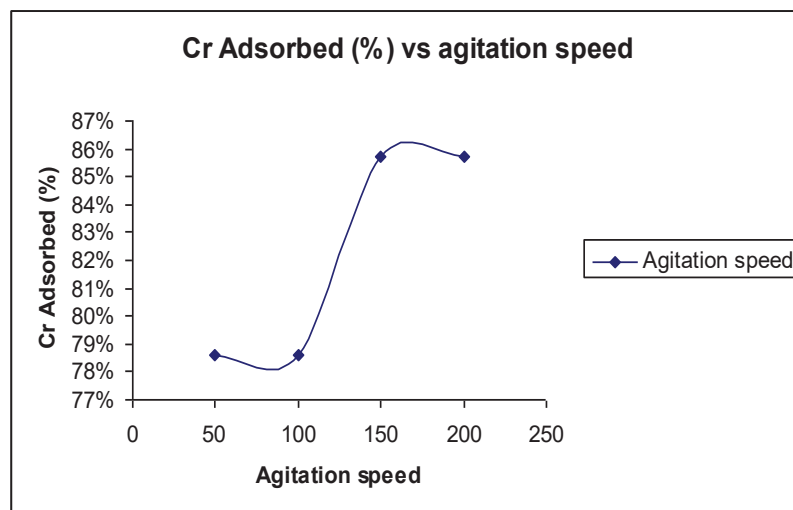
Fig. 3: Impact of agitation speed (rpm) on Cr(VI) adsorption, Cr(VI) concentration=0.1 mg/L.

3.4 Impact of Contact Time

A deviation of contact times was studied to explore its impact on the elimination of Cr (VI). Figure 4 indicates that the reduction ratio improved with rising contact time. At 120 minutes of contact time, the elimination efficacy was almost 100%. This might be clarified by the rise of contact time causing a continuing reduction of Cr (VI) until it achieved its stability. This outcome is coherent with the findings of Gupta et al. [18], and Junyapoon. [19] and Binqiao Ren et al. [20].

3.5 Modelling of Data using StatGraphic Centurion XV Software

The Pareto chart below (Fig. 5) indicates each of the expected consequences in declining order of significance. The amount of each bar is proportionate to the standardized result, which is the expected outcome divided by its standard error. This is comparable to computing a t-statistic for each impact. The perpendicular line can be manipulated to decide which impacts are statistically significant. Any bars which expand away from the line relate to impacts which are statistically significant at the 95.0% trust level. Therefore, 5 consequences are significant. The largest effect is the pH, supported by time, dosage, speed and correlation among speed and pH.
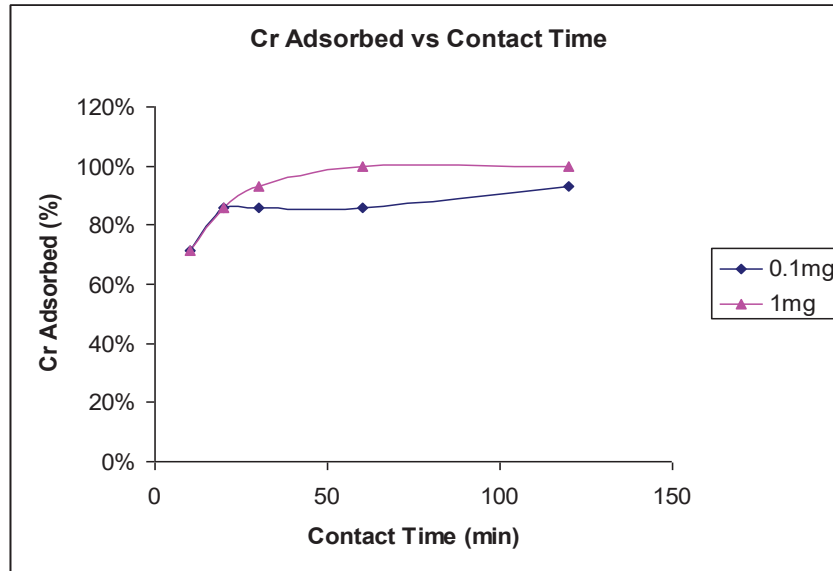
Fig. 4: Impact of contact time on the adsorption of Cr(VI) with [Cr(VI)] = 0.07 mg/L.

The R-squared statistic suggests that the model as equipped supports 51.8007% of the flexibility in percentage elimination. The adjusted R-squared statistic, which is more appropriate for assessing models with diverse numbers of independent variables, is 49.6985%. The standard error of the assessment reveals the standard deviation of the residuals to be 22.8074. The mean absolute error (MAE) of 17.5874 is the average value of the remainders. The Durbin-Watson (DW) statistic tests the residuals to ascertain if there is any significant correlation established on the order in which they appear in the data file. Since the P-value is greater than 5.0%, there is no hint of serial autocorrelation in the residuals at the 5.0% significance level.
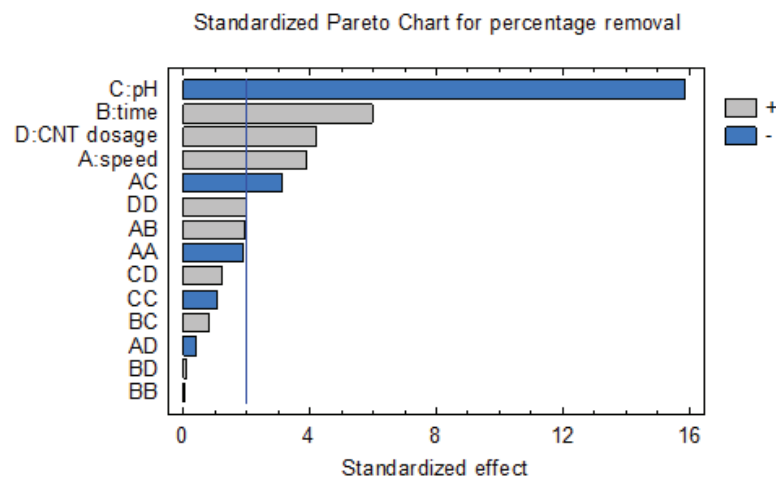
Fig. 5: Pareto chart analysis.

The edges in Fig. 6 signify the expected change in percentage elimination of Cr (VI) as each factor is shifted from its low level to its high level, with all additional factors kept constant at a value halfway between their lows and their highs. Note that all the factors with

16

significant main impacts have a better effect on the response which is the percentage elimination. From the Pareto chart above, the *adsorption equation model* can be created as shown below:

$$CrAdsorbed(\%) = 85.80 - 12.06 * pH + 0.14 * Speed + 0.013 * Time$$
$$- 0.0135 * Speed * pH + 1.89 * CNTDosage$$

Note that the underlying model uses the form of a multiple linear regression model. Each maintained main impact is incorporated in the model by itself, while the two-factor interface is represented by a cross product of *speed* and *pH*. The equation was outlined as illustrated in Fig. 6.
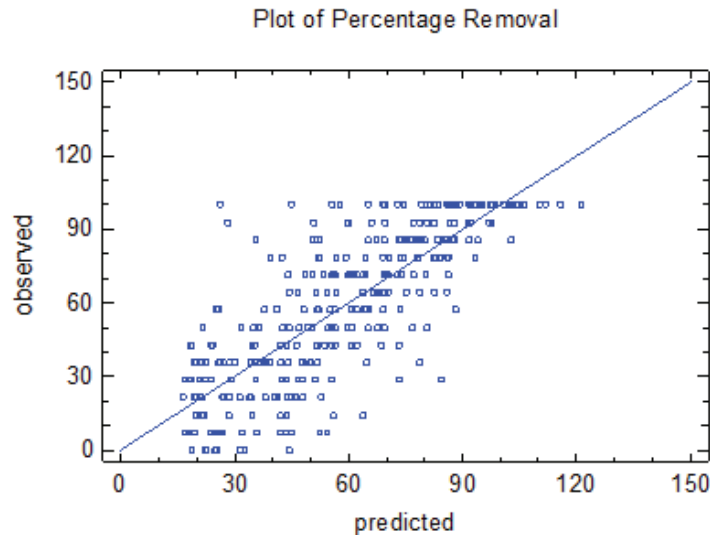
Fig. 6: Multiple linear regression results.

R-squared = 64.1761 percent

R-squared (adjusted for d.f.) = 63.6333 percent

Standard Error of Est. = 18.7668

Mean absolute error = 14.2147

Durbin-Watson statistic = 0.950296 (P=0.0000)

4. CONCLUSION

The observations of the adsorption study on the capability of carbon nanotubes to eliminate Cr(VI) reveals its possibility of usage to separate heavy metals from low concentration water. With 99.99% carbon nanotubes concentration, incredible properties, and structure, the elimination of Cr(VI) was good and could accomplish up to 100% elimination. Hence, the application of the carbon nanotubes to eliminate Cr(VI) has been analysed in this experiment with four factors contributing namely the CNT dosage, the pH of the water, the agitation speed, and the contact time for the Cr(VI) to be adsorbed with the carbon nanotubes.

The experimental design that has been applied is the pattern design or the multilevel factorial. This experiment deals with one level of Cr(VI) concentration, four levels of CNT

dosage, three levels of pH, seven levels of contact time and four levels of agitation speed. There were 336 experimental runs that were done with 2 replicates, the optimum conditions for Cr removal were reached by 1 mg CNT dosage, pH=2, 120 minutes of contact time, and a moderate agitation rate of 150 rpm.

REFERENCES

[1]   Iijima S. (1991) Helical microtubules of graphitic carbon. Nature, 354: 56-58.

[2]   Atieh MA, Bakather OY, Tawabini BS, Bukhari AA, Khaled M, Alharthi M, Fettouhi M, Abuilaiwi FA. (2010) Removal of chromium (III) from water by using modified and nonmodified carbon nanotubes. J. Nanomater. https://doi.org/10.1155/2010/232378.

[3]   El-Sheikh AH. (2008) Effect of oxidation of activated carbon on its enrichment efficiency of metal ions: Comparison with oxidized and non-oxidized multi-walled carbon nanotubes. Talanta, 75: 127-134. https://doi.org/10.1016/j.talanta.2007.10.039.

[4]   Mishra S, Bharagava RN. (2016) Toxic and genotoxic effects of hexavalent chromium in environment and its bioremediation strategies. J. Environ. Sci. Heal. - Part C Environ. Carcinog. Ecotoxicol. Rev., 34: 1-32. https://doi.org/10.1080/10590501.2015.1096883.

[5]   Baig M, Mehmood B, Matin A. (2004) Removal of chromium from industrial effluents by sand filtration. Electron J Env. Agric Food Chem., 2.

[6]   Lee CK, Low KS, Kek KL. (1995) Removal of chromium from aqueous solution. Bioresour. Technol., 54: 183-189. https://doi.org/10.1016/0960-8524(95)00130-1.

[7]   Mitra S, Sarkar A, Sen. S (2017) Removal of chromium from industrial effluents using nanotechnology: A review. Nanotechnol. Environ. Eng., 2. https://doi.org/10.1007/s41204-017-0022-y.

[8]   Baral SS, Das SN, Rath P. (2006) Hexavalent chromium removal from aqueous solution by adsorption on treated sawdust. Biochem. Eng. J., 31: 216-222. https://doi.org/10.1016/j.bej.2006.08.003.

[9]   Hummers WS, Offeman RE. (1958) Preparation of Graphitic Oxide. J. Am. Chem. Soc., 80: 1339.

[10]   Wang K, *et al*. (2015) One-pot preparation of cross-linked amphiphilic fluorescent polymer based on aggregation induced emission dyes. Colloids Surfaces B Biointerfaces., 126: 273-279. https://doi.org/10.1016/j.colsurfb.2014.12.025.

[11]   Dakiky M, Khamis M, Manassra A, Mer'eb M. (2002) Selective adsorption of Cr(VI) in industrial adsorbents. Adv. Environ. Res., 6: 533-540.

[12]   El-Shafey EI. (2005) Behaviour of reduction-sorption of chromium (VI) from an aqueous solution on a modified sorbent from rice husk. Water. Air. Soil Pollut., 163: 81-102. https://doi.org/10.1007/s11270-005-8136-4.

[13]   William PJ. (1985) Industrial Wastewater Treatment Technology, 2nd Ed, Butterworth-Heinemann, London.

[14]   Demirbas E, Kobya M, Senturk E, Ozkan T. (2004) Adsorption kinetics for the removal of chromium (VI) from aqueous solutions on the activated carbons prepared from agricultural wastes. Water SA, 30: 533-539. https://doi.org/10.4314/wsa.v30i4.5106.

[15]   Nomanbhay SM, Palanisamy K. (2005) Removal of heavy metal from industrial wastewater using chitosan coated oil palm shell charcoal. Electron. J. Biotechnol., 8: 43-53. https://doi.org/10.2225/vol8-issue1-fulltext-7.

[16]   Eaton A, Ramirez LM, Haghani A. (2001) The Erin Brockovich Factor-Analysis of Total and Hexavalent Chromium in Drinking Waters, AWWA Water Qual. Technol. Conf. Nashville, TN.

[17]   Ahalya N, Kanamadi RD, Ramachandra TV. (2005) Biosorption of chromium (VI) from aqueous solutions by the husk of Bengal gram (*Cicer arientinum*). Electron. J. Biotechnol., 8: 258-264. https://doi.org/10.2225/vol8-issue3-fulltext-10.

[18]   Gupta VK, Shrivastava AK, Jain. N (2001) Biosorption of chromium(VI) from aqueous solutions by green algae *Spirogyra* species. Water Res., 35: 4079-4085. https://doi.org/10.1016/S0043-1354(01)00138-5.

[19] S. Junyapoon, &S. Weerapong. (2006) Removal of hexavalent chromium from aqueous solutions by scrap iron filings. Kmitl Sci. Tech. J., 6: 1-12.

[20] Ren B, Zhang Q, Zhang X, Zhao L, Li H. (2018) Biosorption of Cr(vi) from aqueous solution using dormant spores of *Aspergillus niger*. RSC Adv., 8: 38157-38165. https://doi.org/10.1039/c8ra07084a.

PHYSICOCHEMICAL AND FUNCTIONAL PROPERTIES OF COMPOSITE FLOURS BASED ON MOCAF AND TEMPEH FLOUR FOR MAKING COOKIES

DITA KRISTANTI* **AND WORO SETIABOMA**

[1]*Research Center for Food Technology and Processing,*
National Research and Innovation Agency, Yogyakarta, 55861, Indonesia.
[2]*Research Center for Appropriate Technology,*
National Research and Innovation Agency, Subang, 41213, Indonesia.

Corresponding author: dita.kristanti@gmail.com

ABSTRACT: Gluten and casein free cookie products are increasingly in demand by consumers. Gluten and casein free cookies were made using mocaf as a substitute for gluten-free flour and tempeh flour as a casein-free protein source. The characteristics of a good cookie composite flour made from mocaf and tempeh flour need to be known. The purpose of this study was to determine the physicochemical and functional properties of a cookie composite flour based on mocaf and tempeh flour. The composite flour was mixed by dry mixing. The composite flour formulations were: C0 (100% wheat flour); C1 (100% mocaf); C2 (75% mocaf and 25% tempeh flour); C3 (50% mocaf and 50% tempeh flour); C4 (25% mocaf and 75% tempeh flour) and C5 (100% tempeh flour). The results showed that addition of tempeh flour increased the ash, protein, fat, minerals, a* value, b* value, and water absorption capacity. The addition of tempeh flour was proven to reduce moisture content, carbohydrates, lightness, and whiteness index value. The cookie composite flour made from 75% mocaf and 25% tempeh flour had a gelatinization profile similar to 100% wheat flour, so this formula was recommended as a cookie composite flour.

ABSTRAK: Produk kuki bebas gluten dan kasein semakin meningkat dalam permintaan pengguna. Kuki bebas gluten dan kasein dibuat menggunakan mocaf sebagai pengganti tepung bebas gluten dan tepung tempe sebagai sumber protein bebas kasein. Ciri-ciri tepung komposit biskut yang baik diperbuat daripada tepung mocaf dan tempeh perlu diketahui. Tujuan kajian ini adalah untuk menentukan sifat fizikokimia dan fungsian bagi tepung komposit biskut berasaskan tepung mocaf dan tempeh. Tepung komposit telah dicampur dengan adunan kering. Formulasi tepung komposit ialah C0 (100% tepung gandum); C1 (100% mocaf); C2 (75% mocaf dan 25% tepung tempeh); C3 (50% mocaf dan 50% tepung tempeh); C4 (25% mocaf dan 75% tepung tempeh) dan C5 (100% tepung tempeh). Hasil kajian menunjukkan penambahan tepung tempeh meningkatkan kadar abu, protein, lemak, mineral, nilai a*, nilai b*, dan kapasiti penyerapan air. Penambahan tepung tempeh terbukti dapat mengurangkan kandungan lembapan, karbohidrat, ringan, dan nilai indeks keputihan. Tepung komposit biskut yang diperbuat daripada 75% mocaf dan 25% tepung tempe mempunyai profil gelatinisasi yang serupa dengan 100% tepung gandum, jadi formula ini disyorkan sebagai tepung komposit biskut.

KEYWORDS: *casein free; composite flour; cookies; gluten free; mocaf; tempeh flour*

1. INTRODUCTION

Cookies are a type of biscuit that are relatively crunchy and have a dense texture. The ingredients that are often used to make cookies are wheat flour and soft sugar, starch, skim milk, egg yolks, shortening, and emulsifier. Most cookies produced and consumed in Indonesia use wheat flour as a main ingredient. The demand for wheat flour in Indonesia is relatively high for the food industry. This is a serious problem since wheat flour cannot be produced in Indonesia, so it needs to be imported.

In general, low protein wheat flour (8-9%) is a raw material for cookies that has advantages of gluten and gliadin protein contents compared to other flours. The gluten protein plays a role in providing rigidity while gliadin protein provides sticky properties. The expansion of dough volume is not required in the process of making cookies so it is possible to use gluten-free flours and thus make cookies from local commodity flours. Local commodity flour can be used as an alternative source to replace wheat flour as an effort to strengthen food security in Indonesia.

Modified cassava flour (mocaf) is a fermented flour from cassava. The use of mocaf flour as a partial or whole substitute in baked products has been widely carried out. The sensory evaluation of baked products made from mocaf was more acceptable than baked products made from wheat flour [1]. However, the low protein content of mocaf caused the protein of baked products from mocaf to be lower than baked products made from wheat flour [1]. Kristanti et al. [2] reported that mocaf contained 11.54% moisture content, 1.12% ash, 0.55% protein, 4.81% fat, and 81.96% carbohydrate.

Tempeh is a vegetable protein source in food that is made from fermented soybeans. Enzyme hydrolysis occurs during fermentation, which causes improvements in texture, flavor, and aroma. According to Reyes-Bastidas et al. [3], fermentation affected the reduction of anti-nutrients and increase in nutritional value in tempeh through enzyme hydrolysis. The addition of tempeh flour caused an increase in protein in cookies [1] and instant baby porridge [2]. Omosebi and Otunola [4] reported that the proximate composition of the tempeh flour consists of 44.27-44.85% protein, 0.38-0.42% crude fiber, 16.45-17.12% fat, 5.60-5.72% ash, 2.50-3.00% moisture content, and 33.52-32.57% carbohydrate.

Mocaf and tempeh flour were used for cookie composite flour production in this study. Cookies made from mocaf flour and tempeh are gluten- and casein-free. Autism is a disorder in which the body cannot digest gluten and casein proteins, this occurs because the body does not produce the dipeptidylpeptidase IV enzyme. Therefore, cookies made from mocaf and tempeh flour are expected to be used as alternative foods for autism sufferers.

Composite flour is made from two or more flours to get the desired material characteristics for a product. Research on the characteristics of composite flour with a mixture of mocaf and tempeh flour or soybean flour in noodles [5] and biscuits [6] have been carried out. The combination of flour in cookie composite flour will affect the dough and final product characteristics. Chandra et al. [7] reported that the physicochemical properties of a dough were determined by an interaction between the composition, structure, and molecular changes of the combined components. The purpose of this study was to determine the physicochemical (proximate, mineral, and color) and functional properties (swelling power, solubility, water and oil absorption capacity, emulsion activity and stability, and gelatinization profile) of composite flour based on mocaf and tempeh flour for cookie products.

2. METHODOLOGY

2.1 Material

Modified cassava flour (mocaf) was obtained from "Tanjung Siang" Small and Medium Enterprises (SME) in Subang, Indonesia. Tempeh was obtained from SME of *Koperasi Tahu Tempe Indonesia (Kopti)* in Subang. The tapioca was bought from a local market in Subang.

2.2 Tempeh Flour Process

Fresh tempeh was sliced with a thickness of 10-20 mm. Tempeh slices were steamed at a temperature of 85 °C for 10 minutes to deactivate the enzymes and fungi in the tempeh. The steamed tempeh slices were drained then dried at 50 °C for ± 5 hours. The dried tempeh slices were ground and sieved using a 40 mesh sieve [1]. The nutritional content of tempeh flour that was used in this study was 10.78% moisture content, 1.10% ash, 45.25% protein, 35.18% fat, and 7.63% carbohydrate [2].

2.3 Cookie Composite Flour Process

The process of cookie composite flour was carried out by weighing mocaf, tempeh flour, and tapioca according to the compositions shown in Table 1. These composite flour formulas had been used to make cookies in previous studies [1]. The tapioca in this formula was used to produce cookies with a sturdy structure. All the ingredients were mixed by dry mixing using a mixer (Philips HR 1559, China) and then stored in plastic for analysis.

Table 1: The composition of cookie composite flour formula

Formula	Wheat Flour (g)	Mocaf (g)	Tempeh Flour (g)	Tapioca (g)
C0	100	-	-	5
C1	-	100	-	5
C2	-	75	25	5
C3	-	50	50	5
C4	-	25	75	5
C5	-	-	100	5

where C0 (100% wheat flour), C1 (100% mocaf), C2 (75% mocaf and 25% tempeh flour), C3 (50% mocaf and 50% tempeh flour), C4 (25% mocaf and 75% tempeh flour), C5 (100% tempeh flour).

2.4 Physicochemical Properties Analysis

Proximate analysis, including moisture and ash contents, were analyzed by gravimetric method [8]; protein was obtained by Dumas method using DuMAster Buchi D-480, Switzerland; fat was determined using the Soxhlet method, and carbohydrate was calculated by the difference method [8]. The mineral content of calcium (Ca), iron (Fe), zinc (Zn), and magnesium (Mg) were analyzed using flame atomic absorption spectrometry (AAS) GBC type 933AA.

The color properties (L*, a*, b* values) of cookie composite flour were measured using the NH310 Chromameter using the CIE method. The degree of whiteness (whiteness index) was calculated using equation (1).

$$\text{whiteness index} = 100 - \sqrt{((100 - L)\,x\,2) + (b\,x2) + (c\,x\,2)} \qquad (1)$$

2.5 Functional Properties Analysis

The functional properties include swelling power, solubility, water absorption capacity (WAC), oil absorption capacity (OAC), emulsion activity, emulsion stability, and gelatinization profile. Each sample (200 mg) was added to 10 ml of distilled water then homogenized using a vortex mixer VM-300 (Gemmy Industrial Corp., Taiwan). The homogenous sample was heated at a temperature of 95 °C for 30 minutes in a water bath (GSL, D-30938 Burgwedel, type 1086, Germany). The samples were centrifuged (Thermo Scientific type SL 40R centrifuge) at 3000 rpm for 15 minutes to separate the gel and supernatant. The gel was weighed to determine the swelling power, while the supernatant was placed in a constant beaker glass then dried using an oven at a temperature of 105 °C until constant weight to determine the solubility. Swelling power and solubility were calculated using Eqs (2) and (3).

$$\text{swelling power} \left(\frac{g}{g}\right) = \frac{(W2 - W3)}{W1} \tag{2}$$

$$\text{solubility (\%)} = \frac{W4}{W1} x\ 100\% \tag{3}$$

where W1 = sample weight (g), W2 = gel + centrifuged tube weight (g), W3 = sample + centrifuged tube weight (g), W4 = dry supernatant weight (g).

Water and oil absorption capacity analysis were referred to in Chandra et al. [7] with a modification. Each sample (1 g) was added to 10 ml of distilled water or soybean oil then homogenized using a VM-300 vortex mixer. The homogenous sample was allowed to stand at room temperature (30±2 °C) for 30 minutes. The samples were centrifuged (SL 40R centrifuge) at 3000 rpm for 15 minutes to separate the precipitate and supernatant. The supernatant was decanted, while the precipitate and the centrifuge tube were weighed. The water and oil absorption capacity were calculated using Eq. (4).

$$\text{water or oil absorption capacity (\%)} = \frac{W2}{W1} x\ 100\% \tag{4}$$

where W1 = sample weight (g), W2 = natant weight

Emulsion capacity and stability analysis were referred to in Chandra et al. [7] with a modification. Each sample (500 mg) was added with 5 ml of distilled water and 5 ml of soybean oil then homogenized with a vortex mixer. The samples were centrifuged at 3000 rpm for 15 minutes. Emulsion capacity was expressed as a percent ratio between the height of emulsion layer and mixture solution. After measurement, the emulsion was heated at 80 °C for 30 minutes in a water bath. The samples were then cooled at room temperature for 15 minutes and centrifuged at 3000 rpm for 15 minutes. Emulsion stability was expressed as a percent ratio between the height of the emulsion layer mixture solution after the heating process.

Gelatinization profile was analyzed using a Perten Instruments Rapid Visco Analyser (RVA), Tec Master (Sweden) with the STD1 method. The operating conditions of the RVA were a standard sample weight (3.5 g); standard water weight (25 g), and base water content (14%). The weighed sample and distilled water were heated and maintained at 50 °C for 1 minute, the temperature then increased to 95 °C in 4 minutes and maintained at 95 °C for 3 minutes. Furthermore, the temperature cooled again to 50 °C in 4 minutes and maintained at 50 °C for 2 minutes. The rotational speed in the initial time (10 seconds) was 960 rpm, then reduced and maintained at 160 rpm throughout the test. The temperature at peak viscosity was expressed as gelatinization temperature (P temp), the

highest viscosity was expressed as peak viscosity (PV), the final viscosity after being maintained at 95 °C was expressed as hot paste viscosity (HPV), breakdown viscosity (BD) was expressed as the result reduction of PV with HPV, the final viscosity after being maintained at 50 °C was expressed as cold paste viscosity (CPV), the setback viscosity (SB) was expressed as the result of the reduction of CPV with HPV, the stability ratio (SR) was expressed as HPV divided by PV, and the ratio setback (SBR) was expressed as CPV divided by HPV [9].

2.6 Statistic Analysis

The data were analyzed using the IBM SPSS Statistics 20 program. The data was analyzed with one-way analysis of variance (ANOVA) followed by Duncan's test at a significance level of $p < 0.05$. All data were shown as mean with standard deviation.

3. RESULTS AND DISCUSSION

The chemical properties of the cookie composite flour are shown in Table 2. The increase in addition of tempeh flour significantly ($\alpha < 0.05$) decreased moisture content and carbohydrate, however increased the ash, protein, and fat of the cookies composite flour. These results supported the previous research in that an addition of tempeh flour caused a decrease in moisture content and carbohydrate and an increase in protein and fat of cookies made from tempeh flour and mocaf [1]. A study by Yulianti et al. [5] showed that the percentage increase of tempeh flour had the effect of increasing protein but had no effect on moisture content, ash, or fat of pasta composite flour. The protein and fat of these cookie composite flours were contributed by the tempeh flour. Tempeh flour contained 45.25%db protein and 35.18% fat [2]. Omosebi and Otunola [4] reported that protein and fat content of the tempeh flour were 44.27-44.85% and 16.45-17.12%, respectively.

Table 2: The chemical composition of cookie composite flour

Samples	Chemical composition (%db)				
	Moisture	**Ash**	**Protein**	**Fat**	**Carbohydrate**
C0	13.87±0.11[a]	0.59±0.02[f]	12.95±0.07[e]	1.45±0.02[e]	71.15±0.17[b]
C1	10.11±0.05[b]	1.14±0.04[e]	1.87±0.05[f]	0.72±0.02[f]	86.14±0.09[a]
C2	8.94±0.18[c]	1.24±0.06[d]	13.98±0.43[d]	7.20±0.03[d]	68.75±0.54[c]
C3	7.63±0.15[d]	1.40±0.01[c]	25.69±0.46[c]	13.38±0.12[c]	52.08±0.47[d]
C4	6.56±0.09[e]	1.79±0.08[b]	37.22±0.09[b]	19.47±0.11[b]	35.01±0.06[e]
C5	5.45±0.10[f]	2.60±0.11[a]	48.09±0.11[a]	25.59±0.12[a]	18.29±0.20[f]

Values are expressed as mean ± standard deviation. The means in the same raw with different letters were significantly different at p < 0.05. The treatments code were C0 (100% wheat flour), C1 (100% mocaf), C2 (75% mocaf and 25% tempeh flour), C3 (50% mocaf and 50% tempeh flour), C4 (25% mocaf and 75% tempeh flour), C5 (100% tempeh flour).

The zinc (Zn), calcium (Ca), and magnesium (Mg) content of cookies composite flour were significantly ($\alpha < 0.05$) increased in line with the increase in percent addition of tempeh flour (Figure. 1). These results supported the research results of Kristanti et al. [1], where the mineral content (Fe, Zn, Ca and Mg) of tempeh mocaf cookies increased with the enhancement of percent tempeh flour. The mineral contents of tempeh flour were quite high, especially iron at 0.011-0.014%, calcium at 0.19-0.21%, and zinc at 0.0046-0.0050% [4].

Fig. 1: The mineral concentration of cookies composite flour.
The treatments code were C0 (100% wheat flour), C1 (100% mocaf), C2 (75% mocaf and 25% tempeh flour), C3 (50% mocaf and 50% tempeh flour), C4 (25% mocaf and 75% tempeh flour), C5 (100% tempeh flour).

The lightness (L* value) and whiteness index of cookies composite flour were significantly ($\alpha <0.05$) decreased with the addition of tempeh flour (Table 3). The decrease in the value of L* and whiteness index showed that the color of cookie composite flour tended to be darker. However, the a* and b* values were significantly ($\alpha <0.05$) increased with the addition of tempeh flour. The a* and b* values showed in a range between 0-60, this indicated that the color of cookie composite flour tended to be reddish or yellowish. The color properties of cookie composite flour were influenced by the color of the tempeh flour. The C5 cookie composite flour (100% tempeh flour) had a lowest L* value and whiteness index, and had highest a* and b* values.

Table 3: The color properties of cookie composite flour.

Samples	Chemical composition			
	L*	a*	b*	Whiteness Index
C0	68.18±0.86^a	1.22±0.03^f	9.04±0.11^e	57.92±0.77^a
C1	65.10±0.97^b	1.34±0.02^e	7.54±0.11^f	56.22±0.84^b
C2	63.53±0.64^c	2.75±0.02^d	10.53±0.11^d	50.25±0.55^c
C3	60.01±0.23^d	3.46±0.04^c	12.48±0.14^c	44.07±0.05^d
C4	56.51±0.42^e	4.40±0.12^b	14.48±0.27^b	37.64±0.04^e
C5	52.38±0.23^f	6.15±0.09^a	15.99±0.10^a	30.24±0.18^f

Values are expressed as mean ± standard deviation. The means in the same raw with different letters were significantly different at $p < 0.05$. The treatment codes were C0 (100% wheat flour), C1 (100% mocaf), C2 (75% mocaf and 25% tempeh flour), C3 (50% mocaf and 50% tempeh flour), C4 (25% mocaf and 75% tempeh flour), C5 (100% tempeh flour).

The results of this study supported previous research, where the value of L* and whiteness index decreased, while the values of a* and b* increased along with the increase

in the percentage of tempeh flour in cookies [1]. Yulianti et al. [5] reported that an increase in the percentage of tempeh flour had an effect on decreasing the whiteness value of pasta composite although it was not significantly different. The addition of soy flour was shown to reduce the L* value in the bakery composite flour [6,9].

The water and oil absorption capacity of cookie composite flour from mocaf and tempeh flour (C1, C2, C3, C4, and C5) were significantly (α <0.05) higher than wheat flour (C0). The increase in an addition of tempeh flour significantly (α <0.05) increased WAC, but had no effect on OAC (Figure. 2). The tempeh used in the tempeh flour process was made from soybeans. The results of Julianti et al. [10] studies showed that wheat flour had a lower WAC and OAC than composite flour from sweet potato, maize, soybean and xanthan gum. The increase of soybean concentration did not been affect the WAC and OAC of bakery composite flour [9,10]. The WAC and OAC of tempeh flour were 2.61-2.77 g/g and 0.96-0.98 g/g [4].

Fig. 2: The water and oil absorption capacity of cookie composite flour.
The treatment codes are C0 (100% wheat flour), C1 (100% mocaf), C2 (75% mocaf and 25% tempeh flour), C3 (50% mocaf and 50% tempeh flour), C4 (25% mocaf and 75% tempeh flour), C5 (100% tempeh flour).

WAC and OAC are the important parameters for bakery products. WAC was related to the viscosity of an ingredient, important in the development process, and maintaining the consistency of bakery products [11]. Aremu et al. [12] reported that oil had a function of retaining and enhancing taste, and extending the shelf life of bakery products. Protein affects the WAC and OAC of a material, it consists of hydrophilic and hydrophobic groups. The hydrophilic groups can interact with water, while the hydrophobic groups can interact with oil.

Swelling power and solubility of the cookie composite flour can be seen in Fig. 3. Swelling power of C1, C2, and C3 cookie composite flour were significantly (α <0.05) higher than wheat flour (C0). Solubility of C1, C2, C3, C4, and C5 cookies composite flour were significantly (α <0.05) higher than wheat flour (C0). The increase in the addition of tempeh flour was generally significant (α <0.05) in reducing the swelling power of the cookie composite flour. The increase in addition of soybeans caused a decrease in swelling power of composite flour of bakery products [9,10]. High protein

content in cookie composite flour may cause starch granules to adhere to the protein matrix, thereby limiting the interaction between starch and water. It is thought to cause a decrease in swelling power. The decrease in solubility of cookie composite flour was thought to be caused by a destruction of starch granules after the gelatinization process so that they were not strong enough to hold water.
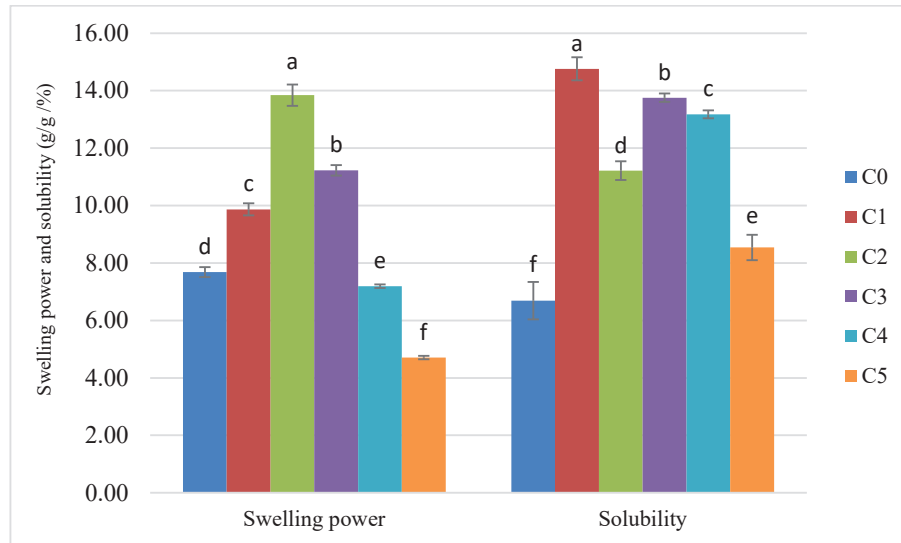
Fig. 3: The swelling power and solubility of cookie composite flour.
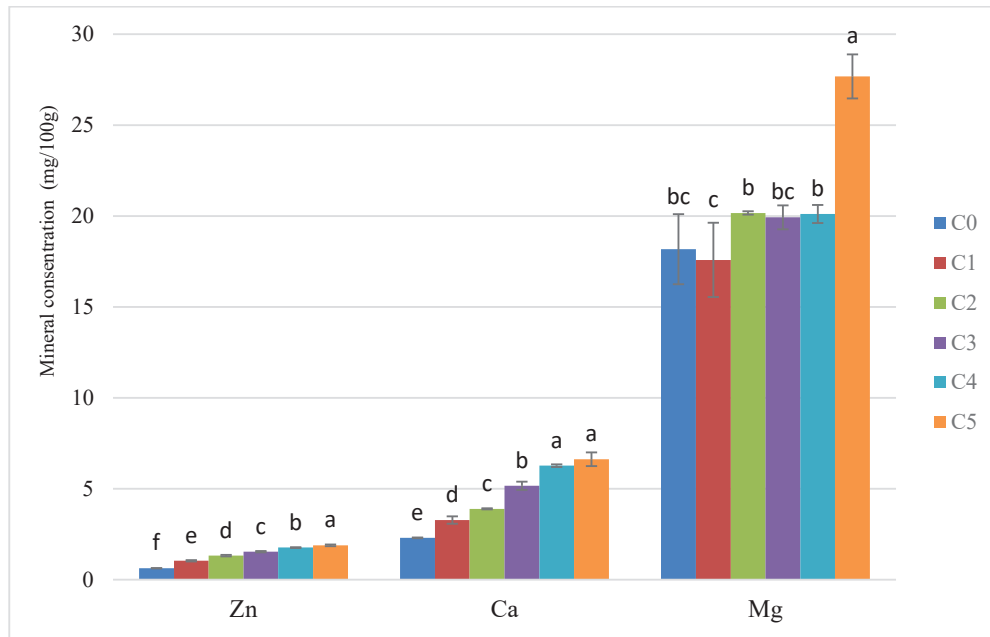The treatment codes are C0 (100% wheat flour), C1 (100% mocaf), C2 (75% mocaf and 25% tempeh flour), C3 (50% mocaf and 50% tempeh flour), C4 (25% mocaf and 75% tempeh flour), C5 (100% tempeh flour).

The results of this study showed that the emulsion activity and stability of cookie composite flour were significantly different ($\alpha<0.05$) between treatments (Figure. 4). The greater the proportion of tempeh flour, the lower the emulsion activity and stability. This was possible because the protein content of cookie composite flour affects the formation of hydrophilic and hydrophobic bonds in the emulsion. The quality and quantity of protein content was not proven to affect the formation of the emulsion. The emulsion formation and stability were determined by protein denaturation and unfolding to form hydrophilic and hydrophobic surfaces [13].

The gelatinization profile of the cookie composite flour is shown in Table 4. The results showed that the gelatinization temperature of C0, C1, C2, and C3 cookie composite flours were not significantly different ($\alpha<0.05$), while C4 and C5 cookie composite flours were not read (error). The increase in the proportion of tempeh flour significantly ($\alpha<0.05$) decreased the PV, HPV, BD, CPV, SB, and SR values, while it also showed a significantly ($\alpha<0.05$) increased SBR value for the cookie composite flour. The results of this study were in line with previous research. A study by Tharise et al. [9] reported that gelatinization temperature of wheat flour was not significantly different with bakery composite flour. The PV, HPV, BD, and CPV values of wheat flour were significantly lower than that of bakery composite flour with added soybean flour [9]. According to Yulianti et al. [5] results studies, the increase in the addition of tempeh flour had an effect of reducing the PV, CPV, and SB values, increasing the gelatinization temperature and BD, but had no effect on the HPV value of the composite flour. The increase in the addition of soybean flour to bakery composite flour had the effect on decreasing the PV, HPV, BD, CPV, and SB values, increasing the SR and SBR values, but had no effect on

the gelatinization temperature [9,10]. Ratnawati et al. [6] reported that an addition of soybean flour increased the SB value and decreased the PV, BD, and HPV values of biscuit composite flour.
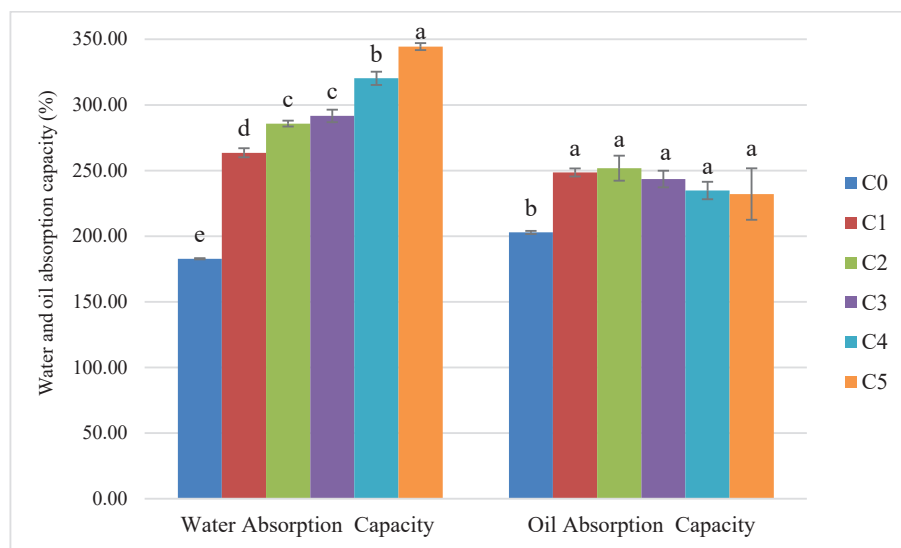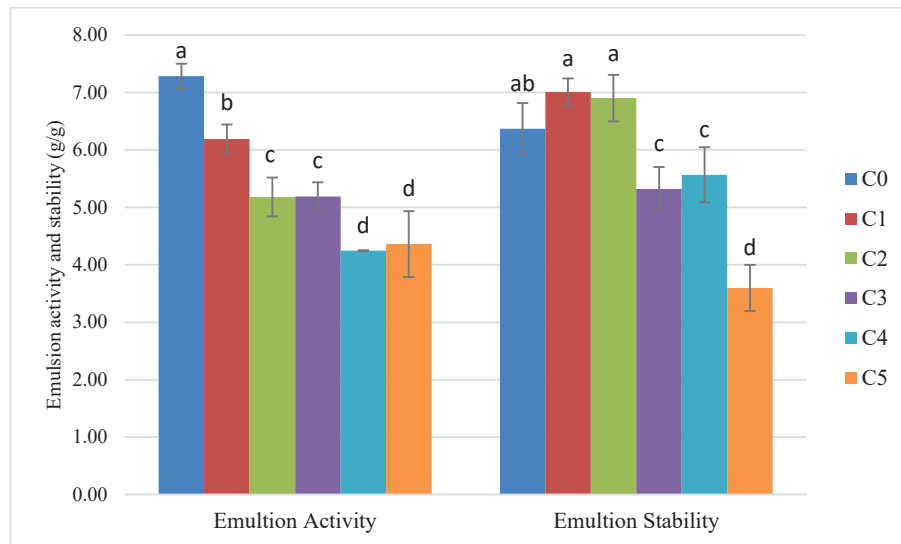

Fig. 4: The emulsion activity and stability of cookie composite flour.
The treatment codes are C0 (100% wheat flour), C1 (100% mocaf), C2 (75% mocaf and 25% tempeh flour), C3 (50% mocaf and 50% tempeh flour), C4 (25% mocaf and 75% tempeh flour), C5 (100% tempeh flour).

Changes in the gelatinization profile, such as a decrease in the value of PV, HPV, BD, CPV, SB, and SR might cause by the high protein and fat content of cookie composite flour (Table 2). High protein content of flour might limit the interaction between starch and water, thereby inhibiting the starch gelatinization process. The swelling process of starch granules was inhibited which might cause a decreasing of viscosity [14]. Fat content in the ingredients had been shown to inhibit the starch gelatinization process. Fat might form a complex bond with amylose, which is hydrophobic, so that it had the effect of inhibiting the binding of water and reducing the viscosity of the material. The amylose and starch content in the composite flour also affected the gelatinization process of starch.

In general, the gelatinization profile of C2 cookies composite flour was similar to that of wheat flour (C0), especially the DB, SB, SR, and SBR values. The decrease in BD and CPV in C2 cookies composite flour indicated the ability to form a gel after the cooking process was followed by cooling and gel resistance to maintain consistency during the stirring process. According to Devi et al. [15] studies, the gelatinization profile wheat flour variety H5 490, which was of a good quality for making cookies, had lower PV, HPV, CPV, and SB values than wheat flour variety HD 2967, which was of a poor quality. The gelatinization profiles of wheat flour varieties H5 490 included PV, HPV, BD, CPV, SB, and the gelatinization temperature were 3050 cP, 2343 cP, 707 cP, 3762 cP, 1419 cP, 80.70 °C, respectively [15]. Based on the Devi et al. [15] study, C2 cookie composite flour had a good gelatinization profile, so this formula was recommended as a cookie composite flour.

Kristanti and Setiaboma

Table 4: The gelatinization profile of cookie composite flour

Samples	Gelatinization profile							
	P temp.	PV	HPV	BD	CPV	SB	SR	SBR
C0	73.13±5.47[a]	3267.67±122.07[b]	3140.00±115.54[b]	747.33±102.84[b]	2451.33±194.88[b]	816.33±98.55[a]	0.98±0.00[b]	0.77±0.04[c]
C1	71.85±0.43[a]	3798.00±26.16[a]	5609.33±26.16[a]	2492.33±44.47[a]	3117.00±27.51[a]	681.00±37.03[b]	1.48±0.01[a]	0.56±0.01[f]
C2	72.75±0.09[a]	2670.00±43.03[c]	2668.00±29.31[c]	798.00±12.00[b]	1870.00±18.19[c]	800.00±27.87[a]	1.00±0.01[b]	0.70±0.00[d]
C3	73.82±0.38[a]	1336.00±7.55[d]	980.67±30.57[d]	118.67±25.15[c]	862.00±9.85[d]	474.00±6.08[c]	0.73±0.02[c]	0.88±0.02[b]
C4	err	330.67±4.51[e]	234.67±4.51[e]	17.00±0.00[d]	217.67±4.51[e]	113.00±0.00[a]	0.71±0.00[c]	0.93±0.00[b]
C5	err	42.67±1.53[f]	26.33±1.53[f]	3.00±0.00[d]	23.33±1.53[f]	19.33±2.31[d]	0.62±0.04[d]	0.89±0.01[a]

Values are expressed as mean ± standard deviation. The means in the same raw with different letters were significantly different at $p < 0.05$. The treatment codes are C0 (100% wheat flour), C1 (100% mocaf), C2 (75% mocaf and 25% tempeh flour), C3 (50% mocaf and 25% tempeh flour), C4 (25% mocaf and 75% tempeh flour), C5 (100% tempeh flour).

4. CONCLUSION

The increase in addition of tempeh flour has been shown to increase the ash, protein, fat, minerals (Zn, Ca, Mg), and water absorption capacity as well as decrease the moisture content, carbohydrates, lightness value, and whiteness index of cookie composite flour. The gelatinization profile of cookie composite flour made from 75% mocaf and 25% tempeh flour was similar to 100% wheat flour, so this formula was recommended as a cookie composite flour. The characteristics of recommended cookie composite flour were moisture content (8.94%), ash (1.24%), protein (13.98%), fat (7.20%), carbohydrates (68.75%), zinc (1.32 mg / 100 g), calcium (3.90 mg / 100 g), magnesium (20.17 mg / 100 g), lightness value (63.53), whiteness index (50.25), swelling power (13.84 g/g), solubility (11.22%), WAC (188.77%), OAC (117.85%), breakdown viscosity (798.00 cP), and setback viscosity (800.00 cP).

ACKNOWLEDGEMENT

REFERENCES

[1] Kristanti D, Setiaboma W, Herminiati A. (2020) Physicochemical and Organoleptic Characteristics of Mocaf Cookies with Tempeh Flour Additions. Biopropal Ind., 11: 1-8.

[2] Kristanti D, Herminiati A, Yuliantika N. (2021) The Physicochemical Properties of Mocaf-Based Baby Instant. J. Ris. Teknol. Ind., 15: 12-22.

[3] Reyes-Bastidas M, Reyes-Fernández E, López-Cervantes J, Milán-Carrillo J, Loarca-Piña G, Reyes-Moreno C. (2010) Physicochemical, Nutritional and Antioxidant Properties of Tempeh Flour from Common Bean (*Phaseolus vulgaris* L.). Food Sci. Technol. Int., pp. 427-434.

[4] Omosebi MO, Otunola ET. (2013) Preliminary studies on tempeh flour produced from three different Rhizopus species. Int. J. Biotechnol. Food Sci., 1: 90-96.

[5] Yulianti LE, Sholichah E, Indrianti N. (2019) Addition of Tempeh Flour as a Protein Source in Mixed Flour (Mocaf, Rice and Corn) for Pasta Product. IOP Conference Series: Earth and Environmental Science, 251(1): 012037.

[6] Ratnawati L, Desnilasari D, Kumalasari R, Surahman DN. 2020 Characterization of modified cassava flour (Mocaf)-based biscuits substituted with soybean flour at varying concentrations and particle sizes. Food Res., 4: 645-651.

[7] Chandra S, Singh S, Kumari D. (2015) Evaluation of functional properties of composite flours and sensorial attributes of composite flour biscuits. J. Food Sci. Technol., 52: 3681–3688.

[8] AOAC (1995) Official Methods of Analysis of The Association of Official Analytical Chemist, 14 ed. Airilington, AOAC Inc.

[9] Tharise N, Elisa J, Nurminah M. (2014) Evaluation of physico-chemical and functional properties of composite flour from cassava, rice, potato, soybean and xanthan gum as alternative of wheat flour. Int. Fiood Res. J., 21: 1641-1649.

[10] Julianti E, Rusmarilin H, Ridwansyah, Yusraini E. (2017) Functional and rheological properties of composite flour from sweet potato, maize, soybean and xanthan gum. J. Saudi Soc. Agric. Sci., 16: 171-177.

[11] Niba LL, Bokanga MM, Jackson FL, Schlimme DS, Li BW. (2001) Physicochemical Properties and Starch Granular Characteristics of Flour from Various Manihot Esculenta (Cassava) Genotypes. Food Chem. Toxicol., 67: 1701-1705.

[12]   Aremu MO, Olaofe O, Akintayo ET. (2007) Functional Properties of Some Nigerian Varieties of Legume Seed Flours and Flour Concentration Effect on Foaming and Gelation Properties. J. Food Technol., 5: 109-115.

[13]   Raikos V, Neacsu M, Russell W, Duthie G. (2016) Comparative study of the functional properties of lupin, green pea, fava bean, hemp, and buckwheat flours as affected by pH. Food Sci. Nutr., 2: 802-810.

[14]   Kaushal P, Kumar V, Sharma HK. (2012) Comparative study of physicochemical, functional, antinutritional and pasting properties of taro (*Colocasia esculenta*), rice (*Oryza sativa*) flour, pigeonpea (*Cajanus cajan*) flour and their blends. LWT - Food Sci. Technol., 48: 59–68.

[15]   Devi A, Sindhu R, Khatkar BS. (2019) Morphological, pasting, and textural characterization of starches and their sub fractions of good and poor cookie making wheat varieties. J. Food Sci. Technol., 56: 846-853.

EVALUATION OF DUCTILITY OF REINFORCED CONCRETE STRUCTURES WITH SHEAR WALLS HAVING DIFFERENT THICKNESSES AND DIFFERENT POSITIONS

RIFAT RESATOGLU*AND SHAHRAM JKHSI

Department of Civil Engineering, Near East University, Nicosia, Northern Cyprus

*Corresponding author: rifat.resatoglu@neu.edu.tr

ABSTRACT: Ductility is one of the main criteria in reinforced concrete (RC) structures. ASCE 7-10 seismic design code recognizes the importance of ductility in earthquake-resistant structures. The structures need to be designed to have sufficient strength and ductility for overall safety against earthquake forces. Both the strength and the ductility are mutually associated to enhance structural seismic safety in this study. Previous studies showed that a shear wall gives different performance based on its position in building structures. This paper presents the position of the shear walls and shear wall thicknesses effects on ductility. A total of 96 two-dimensional (2D) models are analyzed for this work using ETABS software. The non-linear static analysis (pushover) method is used to analyze and design these RC building structures with shear walls. It is concluded that an increase in shear wall thickness causes a decrease in ductility values, and a decrease in ductility value will also occur when the shear wall position changes from edge to middle.

ABSTRAK: Kemuluran adalah salah satu kriteria utama dalam struktur konkrit bertulang (RC). Kod reka bentuk ASCE 7-10 seismik dunia menyedari pentingnya kemuluran dalam struktur tahan gempa. Struktur perlu dibina bagi mencapai ketahanan kekuatan dan kemuluran yang mencukupi bagi keselamatan keseluruhan terhadap kekuatan gempa. Kekuatan dan kemuluran dihubungkan bersama bagi meningkatkan keselamatan tahan gempa dalam kajian ini. Kajian sebelumnya menunjukkan bahawa dinding ricih memberikan prestasi yang berbeza berdasarkan kedudukannya dalam struktur bangunan. Kertas ini menunjukkan kedudukan dinding ricih dan ketebalan dinding ricih kesan pada kemuluran. Sebanyak 96 model dua dimensi (2D) dianalisis dalam kajian ini menggunakan perisian ETABS. Kaedah analisis statik bukan linear (pushover) digunakan bagi menganalisis dan merancang struktur bangunan RC ini dengan dinding ricih. Kesimpulannya peningkatan ketebalan dinding ricih menyebabkan penurunan nilai kemuluran, dan penurunan nilai kemuluran juga akan terjadi ketika posisi dinding ricih berubah dari tepi ke tengah.

KEYWORDS: *ductility; non-linear static analysis; earthquake design; pushover curve; shear wall*

1. INTRODUCTION

According to past earthquakes, several reinforced concrete structures have either failed or sustained different degrees of destruction. Overall, knowing the seismic efficiency of structures has been a question for science communities for a long time [1]. One of the most dangerous natural hazards is an earthquake that causes great losses of life and property damage [2].

Earthquake-resistant structural system design depends on standardized seismic requirements to provide secure quality of life during massive earthquakes [3]. It is essential to build analytical modeling to evaluate the seismic behavior of current systems and to modify structural performance properties such as strength, stiffness, and deflection to better-desired performance specifications [4].

The destruction depends not only on the scale of the earthquake but also on the form of the structural system. Of utmost importance here, the dual system includes structural reinforced concrete frames with shear walls (MRFSW). Dual structural frameworks are generally utilized as structural frameworks offering resistance to gravity and lateral forces [5].

In engineering structures, the concept of the formation of structural systems corresponds with the resistance to lateral forces of building structures. Based upon the variety of stresses that may occur throughout the structural elements due to the implementation of forces, the widely utilized structural systems are divided into various groups [6]. The structural system formation is designed to work against longitudinal forces of gravity and lateral loads affected by wind or earthquake actions. Gravity loads and lateral loads are the primary loads that are exposed to building structures [7].

Shear walls are among the most widely applied systems in buildings to withstand lateral loads. Implementing a shear wall is an effective solution to stiffen structural systems under lateral loads. The primary function of a shear wall is to increase the rigidity and strength of the building for lateral resistance [8]. Shear walls are widely utilized as a longitudinal structural component across modern buildings to withstand the lateral loads caused by winds and earthquakes. If a reinforced concrete shear wall is built to become a ductile element, it already conducts forces significantly better. To increase the ductility of shear walls, the shear wall's general geometric measurements, the form and quantity of reinforcement, and the relation against the other components through the building support should be taken into consideration [9]. The location, number and curtailment of shear walls act an important factor for the soft story structures to displace during an earthquake. To minimize the negative influence of twisting in buildings, shear walls should be perfectly symmetrically positioned through plan [10].

The capacity of members or structural components that show displacement is generally indicated by the required ductility ratios, μ, in earthquake-resistant design. [11]. The ratio of maximum displacement identifies ductility proportion (Δm) to the related displacement at the beginning of yield (Δy) [12].

Pushover analysis is a static non-linear technique that progressively raises the amount of the horizontal loads, preserving a specified distribution sequence throughout the height of the structure. Pushover analysis, considering the maximum load and the peak inelastic deformation, will define a building's performance. Influences of nonlinear static analysis can be modified once a mechanism of collapse has been formed. The primary benefit of pushover analysis is to obtain an over-strength estimation and provide a sense of the system's general ability to sustain inelastic displacement ductility [13]. Nonlinear pushover analysis offers sufficient knowledge regarding the building's durability, deformation capability, the discovery of the yield displacement, and the ultimate displacement, which are all used to compute the building structure's ductility from dividing the maximum displacement by the displacement of the yield [14]. The pushover analysis assesses the structural system's predicted quality by measuring the structural system's strength and deflection. This approach computes the building's base shear capability and the performance stages of each building component against various degrees of earthquake force [15].

2. OBJECTIVE OF THE STUDY

This present work aims to assess the RC structural buildings' ductility using various parameters with different thicknesses and different positions of shear walls. The research study evaluates the seismic assessment and the ductility of the 2D models of dual systems (MRFSW) using the pushover method. Moreover, to evaluate the degree of impact on ductility value, different parameters such as span length, compressive strengths of concrete, number of stories, various thicknesses of the shear wall, and different positions of the shear wall are chosen.

3. LITERATURE REVIEW

The effect of shear walls upon RC building structures' seismic efficiency is presented in this study. An estimate was made to assess losses in building structures, including suitable concrete and reinforced materials and shear walls besides beams and columns. These research findings will help select appropriate materials for structural buildings and shear walls in order to avoid destruction [16].

The impact of shear wall position in seismic resistance is defined [17]. The usage of the shear wall will efficiently decrease the displacement of the structure and story drifting. The shear walls' positioning in the centre of structures evenly provides an excellent performance that decreases the displacement and story-drift. Shinde and Raut [18] studied the varying shear wall thicknesses throughout similar buildings at various levels, preserving the places around similar positions and their impact upon multi-storied buildings' deformation. It is discovered, according to the findings, that the thickness already raises the rigidity, and by increasing the height and thickness, the deformation of shear walls decreases. The suitability of pushover analysis has been discussed for seismic evaluation of mid-rise to high-rise shear wall building structures and showed that pushover analysis understates the inner story drifts, especially those located on the top floors of building structures, and magnifies inelastic maximum roof displacement [19].

Carrillo et al. [20] studied ductility for earthquake design of RC walls for low-rise houses. The study contrasts and explains RC walls' ductility value generally utilized in one-floor and two-floor houses. Ductility capabilities in this research will be utilized to estimate the power modification and displacement amplification factors. The purpose of ductility throughout structural buildings is to guarantee that they have a specific amount of energy dispersion and deformation to prevent brittle destruction throughout the event of an earthquake [21].

Considering the reaction of a structural framework to seismic behavior may be managed by limiting lateral displacements, the ductile approach should be designed [22]. The major energy absorbing component utilized by the current design technique to produce a ductile performance throughout a seismic loading cycle was plastic hinges. As per seismic design rules in current building codes, structures shall withstand minor to severe earthquakes without harm, at most without major damage or collapse [23]. Throughout a large seism, the structure should get a low-cost resistance. Plastic energy might be employed during the design by ground shaking a structure for efficiency assessment. The appropriate amount of ductility is crucial for RC structure collapse prevention [24].

Venkatesh et al. [25] investigated the structural performance of RC moment-resisting frames with and without shear walls at various places to withstand seismic loads, as used in modern building techniques. In the condition of shear walls, the outcomes show higher resistance to horizontal loads. The impact of shear walls on the vulnerability of structures is

demonstrated in [26]. Shear walls were examined for a G+8 story structure with and without shear walls. Once compared to the models without the shear wall, the shear wall model showed a significant decline in horizontal displacement. Because the structure's stiffness had increased, the displacement of the story had decreased.

4. METHODOLOGY

4.1 Introduction

The analyzed RC dual system (MRFSW) is designed in accordance with ASCE 7-10 seismic design code. Shear walls can minimize the lateral displacement of the building structures during the impact of earthquakes. The implementation of shear walls is a functionally effective solution for stiffening structures.

The pushover analysis method is used to verify the yield displacement, maximum displacement, maximum base shear, and ductility ratio for 96 models with several thicknesses and positions of shear walls including various parameters such as span length, number of stories and compressive strengths of concrete. The location of the models is assumed to be in Washington DC, United States of America.

4.2 Material Properties and Details of Models

The material properties and details of the models are given below in Table 1 and Table 2, respectively.

Table 1: Material properties of models

Material	Value
Compressive strength($f'c$)	250, 300 kgf/cm^2
Fy of reinforcement steel	420 N/mm^2.
Steel modulus of elasticity	200,000 N/mm^2
Concrete modulus of elasticity	23500 and 25743 N/mm^2
Unit weight of concrete	24 kN/m^3
Live load	2 kN/m^2
Super dead load	1.5 kN/m^2
Masonry load	14 kN/m
Shear modulus, G	99847.2, 109377 kgf/cm^2

Table 2: Details of 2D models

Parameters	Value
Number of stories (S)	Low (4), mid (8), and high-rise building (12)
Number of spans(N)	5 spans
Height of stories(h)	Typical story height (3.2m) and ground floor height (4m)
Span length(L)	5m, 5.5m, 6m, and 7m.
Positions of the shear wall.	Middle and edge
Thicknesses of shear wall	250mm and 300mm
Location of buildings	Washington DC, USA
Column section size for 4,8 and 12 stories	400mm*400mm, 400mm*650mm, and 400mm*800mm
Beam section sizes for 4,8 and 12 stories	350mm*400mm, 350mm*450mm, and 400mm*500mm

| (a) edge | (b) middle |
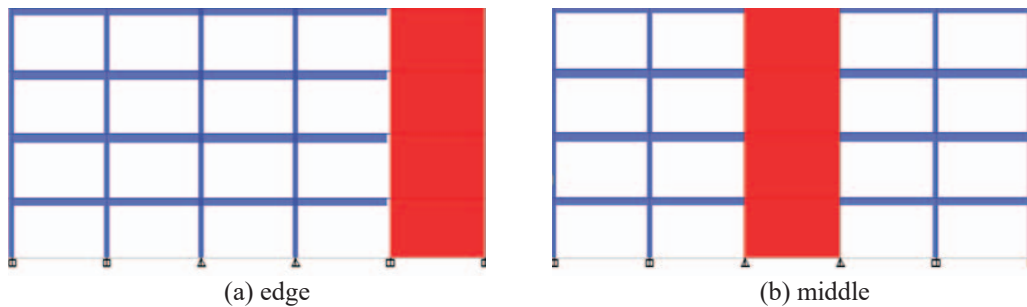
Fig. 1: Different positions of the shear wall.

4.3 Seismic Analysis Methods

Every structure must be designed in a way to resist lateral forces including earthquakes [27]. In order to determine the performance and the maximum response of the structures, instead of the use of complicated nonlinear dynamic analysis, a nonlinear static analysis was employed, which is a simpler and quicker method for the estimation of the structural response.
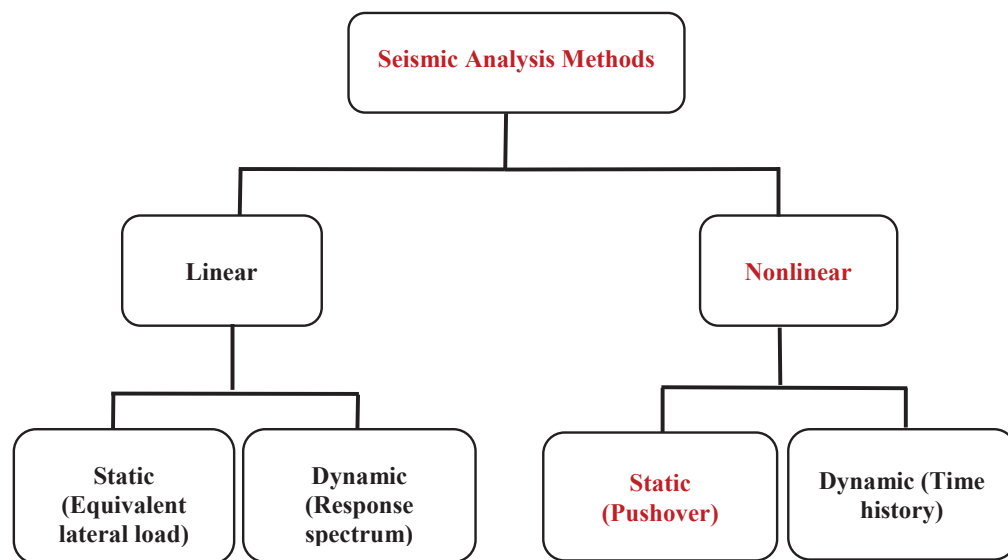
Fig. 2: Seismic analysis methods.

4.4 Bilinear Curve of Pushover Curve

The request for a straightforward approach to estimate the non-linear analysis of a structure against earthquake loading is widely recognized as the pushover study. Pushover Curves illustrate the structure's nonlinear nature and a base shear deformed curve against the construction's lateral floor displacement. This method is dependent upon the principles of FEMA356, assuming equal regions underneath the primary curve and bilinear curves. A bilinear pushover curve has been constructed for every design building method and reflects various earthquake designs and building efficiency stages. So, each curve has been defined via 2 points: yields of capability and ultimate capacity. The maximal capacity was achieved after the general structural framework was developed as a total approach. A 15 percent reduction in strength occurred by failing specific components to reach the deformation

36

capability. Consequently, the strength referring to the optimum capacity does not always correlate with the actual highest power reported through the study. Furthermore, the yield capability is not the building's power while the member's initial yield occurs.
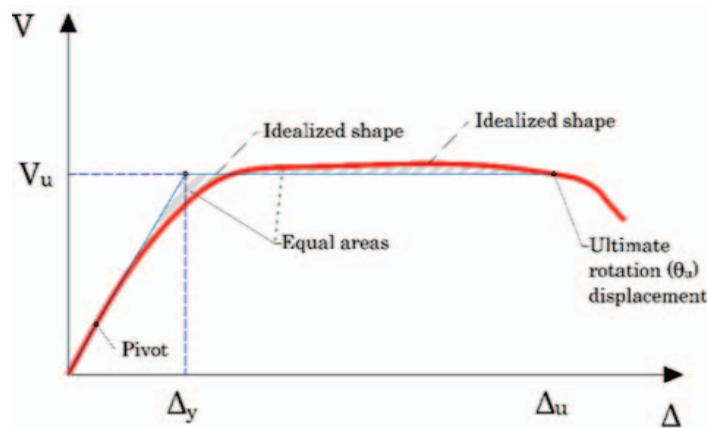
Fig. 3: The bilinear curve of pushover curve [11].

4.5 Sample of the Bilinear Curve of Capacity Curve

The ratio between the maximum displacement and linear displacement in a bilinear capacity curve is defined as the ductility factor. In order to estimate a bilinear curve from the capacity curve, the area under both curves must be identical. To determine the global yield point, the capacity curve is usually simplified as a bilinear curve that has the same area with respect to the axis of spectral displacement, which is referred to as the equal energy rule. The main intent for this procedure is to find the area under the pushover curve, which corresponds to the dissipated energy during earthquake, and it should be equal to the area under the bilinear curve. That area calculation is carried out using AutoCAD, which is a commercial computer-aided design and drafting software application. These areas above the capacity curve and below the bilinear curve are shown in Fig. 4.
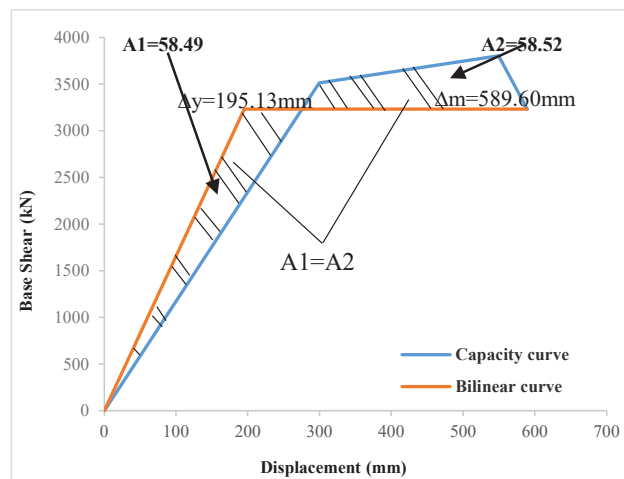
Fig. 4: Bilinear relationship of base shear versus roof displacement.

Thus, the pushover curve is exported from ETABS to Microsoft Excel and is then transferred to AutoCAD. In this stage, a horizontal line is drawn from 85% of the pushover

curve's maximum base shear. This line intersects the pushover curve and is passes it. Another line is drawn from the coordinate centre and intersects with the drawn horizontal line. After that, the areas below the pushover curve and above the pushover curves are compared with each other, and the position of the second drawn line is changed until both areas are the almost equal.

5.   RESULTS AND DISCUSSIONS

5.1 Results

The results of yield displacement, maximum displacement, maximum base shear that were obtained from the pushover curve, and the ductility ratio calculated by dividing Δ_m over Δ_y, as shown in equation (1), are summarized in Table 3, Table 4, and Table 5 with compressive strength ($f'c$), $300\ kgf/cm^2$ for low-rise, mid-rise, and high-rise buildings, respectively.

The equation for finding ductility ratio:

$$\mu = \frac{\Delta_m}{\Delta_y} \tag{1}$$

Table 3: Results of pushover analysis and ductility values for low-rise (4-story) buildings

No. of models	Span length(m)	Thickness of shear wall (mm)	Position of shear wall	Δ_y (mm)	Δ_m (mm)	μ
1	5	250	Edge	128.30	296.81	2.31
2	5.5	250	Edge	123.23	305.63	2.48
3	6	250	Edge	118.11	319.15	2.70
4	7	250	Edge	106.12	340.23	3.20
5	5	250	Middle	77.61	149.74	1.92
6	5.5	250	Middle	70.42	158.83	2.25
7	6	250	Middle	64.64	163.29	2.53
8	7	250	Middle	54.81	172.37	3.14
9	5	300	Edge	51.01	112.78	2.21
10	5.5	300	Edge	50.21	120.85	2.40
11	6	300	Edge	49.32	129.44	2.62
12	7	300	Edge	47.12	148.23	3.14
13	5	300	Middle	76.24	136.62	1.79
14	5.5	300	Middle	69.12	145.29	2.10
15	6	300	Middle	63.15	152.47	2.41
16	7	300	Middle	55.90	169.22	3.02

5.2 The Effect of Span Length on Ductility Values

Ductility values of various span lengths are shown in Tables 3, 4, and 5, and a comparison of ductility values with different span lengths is shown in Fig. 5. This figure shows an increase in ductility value by 6%, 10%, and 31% caused by increasing the span length with 10%, 20%, and 40%, respectively. On the other hand, once span length increases, a reduction in yield displacement and an increase in maximum displacement can occur.

The parameters used in this section are the shear wall position, which is located in the middle, and the number of stories, i.e., 4-story.

Table 4: Results of pushover analysis and ductility values for mid-rise (8-story) buildings

No. of models	Span length(m)	Thickness of shear wall (mm)	Position of shear wall	Δ_y (mm)	Δ_m (mm)	μ
1	5	250	Edge	102.07	306.39	3.00
2	5.5	250	Edge	101.25	326.63	3.22
3	6	250	Edge	100.01	340.13	3.40
4	7	250	Edge	85.06	361.68	4.25
5	5	250	Middle	142.05	380.48	2.67
6	5.5	250	Middle	140.19	394.31	2.81
7	6	250	Middle	129.13	407.55	3.15
8	7	250	Middle	112.2	430.00	3.83
9	5	300	Edge	105.49	296.34	2.80
10	5.5	300	Edge	100.30	318.20	3.17
11	6	300	Edge	102.60	332.62	3.24
12	7	300	Edge	89.65	355.00	3.95
13	5	300	Middle	169.44	366.70	2.16
14	5.5	300	Middle	158.41	384.28	2.42
15	6	300	Middle	153.10	399.69	2.61
16	7	300	Middle	134.01	423.80	3.16

Table 5: Results of pushover analysis and ductility values for high-rise (12-story) buildings

No. of models	Span length(m)	Thickness of shear wall (mm)	Positions of shear wall	Δ_y (mm)	Δ_m (mm)	μ
1	5	250	Edge	103.12	521.45	5.05
2	5.5	250	Edge	104.92	545.32	5.19
3	6	250	Edge	106.32	566.45	5.32
4	7	250	Edge	110.87	615.16	5.47
5	5	250	Middle	159.51	639.68	4.01
6	5.5	250	Middle	150.20	663.20	4.41
7	6	250	Middle	152.01	684.15	4.50
8	7	250	Middle	143.25	719.45	5.02
9	5	300	Edge	87.02	399.28	3.95
10	5.5	300	Edge	106.59	426.88	4.00
11	6	300	Edge	100.04	443.96	4.43
12	7	300	Edge	93.12	466.56	5.01
13	5	300	Middle	195.13	589.60	3.02
14	5.5	300	Middle	190.12	605.43	3.18
15	6	300	Middle	185.05	659.45	3.56
16	7	300	Middle	168.64	692.04	4.00
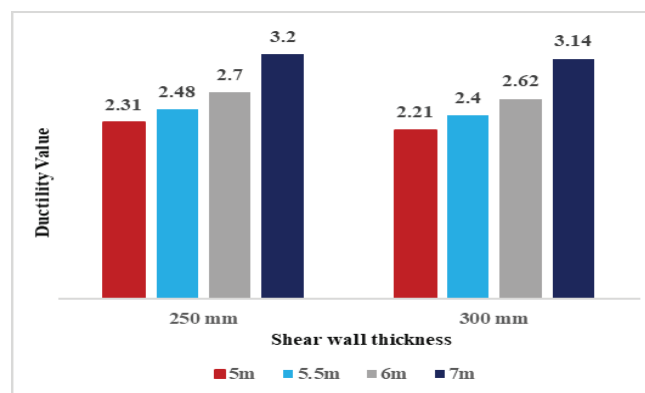
Fig. 5: The Comparison between the ductility values for different span lengths in a 4-story building.

5.3 The Effect of Number of Stories on Ductility Values

In this section, the effect of the number of stories on ductility values is defined. Ductility values of various numbers of stories are shown in Tables 3, 4, and 5. The ductility value is increased by 33% by increasing the number of stories from 4 to 8 and by 71% from 4 to 12. This can be seen in Fig. 6. The increment in the number of stories leads to increased yield displacement and ultimate displacement, which is how ductility value rises.

Parameters used in this section are: shear wall thickness = 300 mm, and shear wall position = middle.
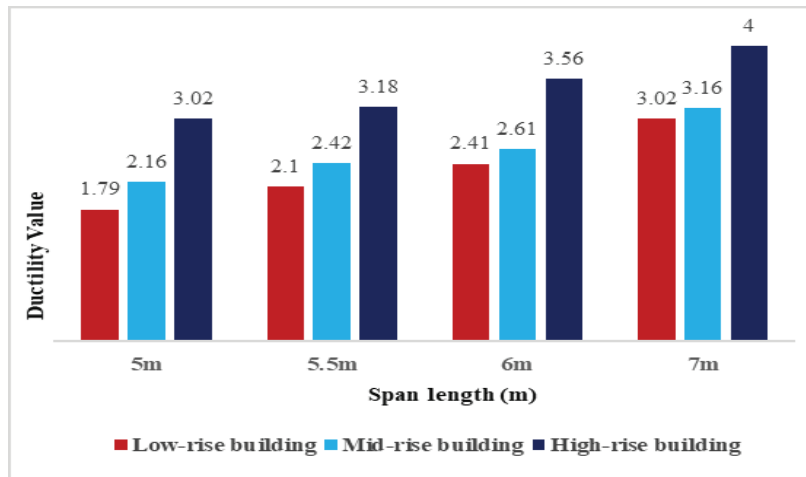
Fig. 6: Comparison of the values of ductility of different number of stories.

5.4 The Effect of Different Thicknesses and Positions of the Shear Wall on Ductility Values and Capacity (Pushover Curve)

The impact of different shear wall thicknesses and positions on ductility ratio is described in this section. Table 3, 4 and 5 illustrate ductility rates with variations in different shear wall thicknesses and positions, respectively. As seen in Fig. 7, as shear wall thickness increases from 250 mm to 300 mm, a decrease in ductility values will occur by 15%. Increasing shear wall thicknesses from 250 mm to 300 mm caused an increment in yield displacement (Δ_y) and a decrease in maximum displacement (Δ_m) will occur that resulted in a reduction in ductility values. Moreover, as shown in Fig. 8, increasing shear wall thickness causes an increase in maximum base shear.

As shown in Fig. 9, when shear wall position changes from edge to middle, it causes a decrease in ductility value of 20 % and causes an increase in both yield displacement (Δ_y), and ultimate displacement (Δ_m). As shown in Fig. 10, a change in shear wall position from edge to middle induces an increase in maximum base shear.
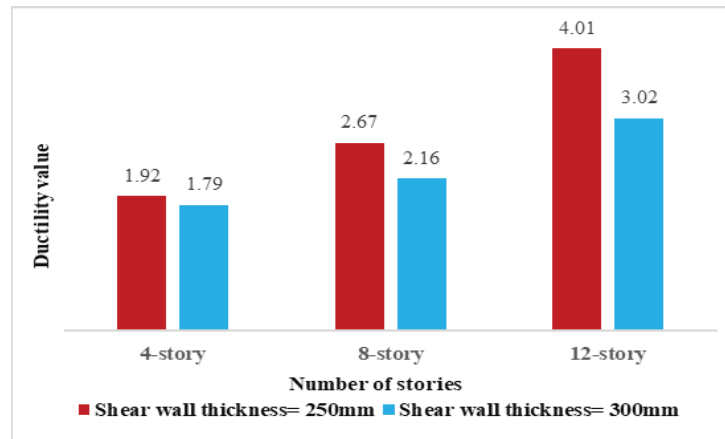
Fig. 7: Comparison between the values of ductility for different thicknesses of shear wall.
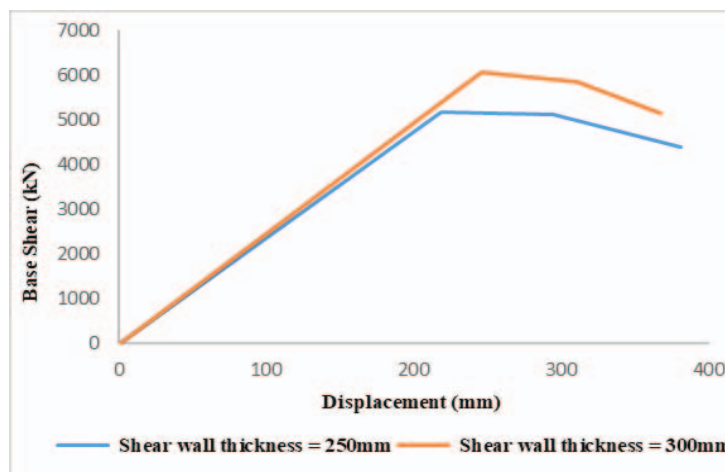
Fig. 8: The impact of the different thicknesses of the shear wall on the capacity (pushover) curve.
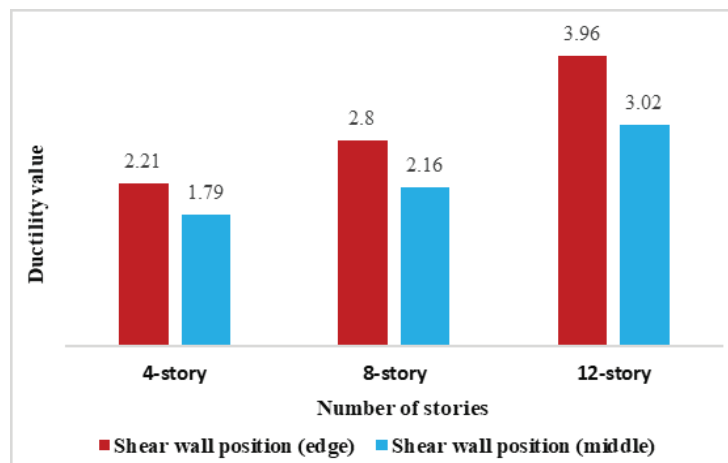
Fig. 9: Comparison of the ductility values of different positions of shear wall.
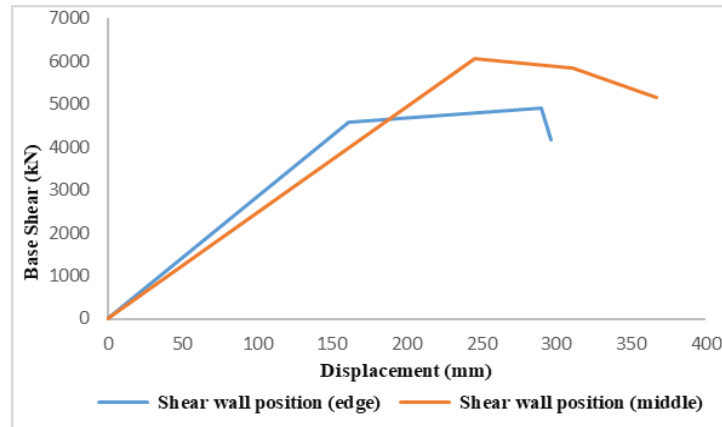
Fig. 10: The impact of the different positions of the shear wall on the capacity (pushover) curve.

6. CONCLUSIONS

In this paper, the two-dimensional dual system (MRFSW) has been studied. The models are designed with different thicknesses and shear wall positions to evaluate the ductility, maximum displacement, yield displacement, and maximum base shear. The summarized outcomes of this study are as follows:

- Increasing span length causes an increase in ductility value in low, mid, and high-rise buildings. It has also been observed that by increasing the span length, there will be an increase in the yield displacement and maximum displacement.
- By increasing the span length, it has been observed that the maximum base shear force decreases in all building models.
- Increasing the number of stories causes an increase in ductility value because the stiffness of the building will decrease by adding more floors.
- When the shear wall thickness was increased from 250 mm to 300 mm, it was observed that there was a decrease in ductility values.
- It has been observed that increasing shear wall thickness causes an increase in maximum base shear force.
- The ductility rate is noticed to decrease by increasing the shear wall thickness.
- When the shear wall position changes from edge to middle, it causes a reduction in ductility value.
- By changing the shear wall position from the edge to the middle, an increase in both the yield displacement and the ultimate displacement has been found.
- Changing the shear wall position from edge to middle causes an increase in maximum base shear force for all story buildings.

REFERENCES

[1] Chou CC, Tsai WJ, Chung PT. (2016) Development and validation tests of a dual-core self-centering sandwiched buckling-restrained brace (SC-SBRB) for seismic resistance. ScienceDirect, 121(15): 30-41.
[2] Yön B, Sayın E, Onat O. (2017) Earthquake and structural damages. Earthquakes-Tectonics, Hazard and Risk Mitigation, 21(3): 319-339.

[3] Furtado A, Rodrigues H, Arêde A, Varum H, Grubišić M, Šipoš TK. (2018) Prediction of the earthquake response of a three-story infilled RC structure. Engineering Structures, 171: 214-235.

[4] Ravikumara HS, Kulkarni SR, KS BNA. (2015) Study of plastic hinge formation in R.C frames with non-linear static analysis. An International Journal of Research in Engineering and Technology, 4(9): 179-182.

[5] Zerbin M, Aprile A, Spacone E. (2020) New formulation of ductility reduction factor of RC frame-wall dual systems for design under earthquake loadings. Soil Dynamics and Earthquake Engineering, 138: 106279.

[6] Rana EN, Rana S. (2014) Structural Forms Systems for Tall Building Structures. SSRG International Journal of Civil Engineering, 1(4): 33-35.

[7] Esmaili O, Epackachi S, Samadzad M, Mirghaderi SR. (2008) Study of structural RC shear wall system in a 56-story RC tall building. The 14th world conference earthquake engineering.

[8] Madhu S. (2018) Optimum location of shear walls in a R.C building. International Journal of Scientific & Engineering Research, 9(7): 2229-5518.

[9] LovaRaju K, Balaji DK. (2015) Effective location of shear walls on the performance of building frame subjected to earthquake load. International Advanced Research Journal in Science, Engineering and Technology, 2(1): 123-129.

[10] Rokanuzzaman M, Farjana K, Anik D, Reza S. (2017) Effective location of shear walls on the performance of building frame subjected to lateral loading. International Journal of Advances in Mechanical and Civil Engineering, 4(6): 23-31.

[11] Vielma-Perez JC, Mulder MM. (2018) Improved procedure for determining the ductility of buildings under seismic loads. Revista Internacional de Métodos Numéricos para cálculo y diseño en Ingeniería, 34(1): 61-66.

[12] Mehta BB, Vasani PC. (2014) Ductility requirements for buildings. Applied Mechanics Department, 216: 113-122.

[13] Khoshnoudian F, Mestri S, Abedinik F. (2011) Proposal of lateral load pattern for pushover analysis of RC buildings. Computational Methods in Civil Engineering, 2(2): 169-183.

[14] Wang Z, Martinez-Vazquez P, Zhao B. (2020). Pushover analysis of structures subjected to combined actions of earthquake and wind. Engineering structures, 221: 111034.

[15] Kadid A, Boumrkik A. (2008) Pushover analysis of RC frame structure. Asian Journal of Civil Engineering, 9(1): 75-83.

[16] Ozkul T, Kurtbeyoglu A, Borekci M, Zengin B, Kocak A. (2019) Effect of shear wall on seismic performance of RC frame buildings. Engineering Failure Analysis, 100: 60-75.

[17] Tarigan J, Manggala J, Sitorus T. (2018) The effect of shear wall location in resisting earthquake. MS&E, 309(1): 012077.

[18] Shinde SB, Raut NB. (2016) Effect of Change in Thicknesses and Height in Shear Wall on Deflection of Multistoried Buildings. International Journal of Civil Engineering and Technology, 7(6): 587-591.

[19] Huang K, Kuang JS. (2010) On the Applicability of Pushover Analysis for Seismic Evaluation of Medium- and High-rise Buildings. The Structural Design of Tall and Special Buildings, 19: 573-588.

[20] Carrillo J, González G, Rubiano A. (2014) Displacement ductility for seismic design of RC walls for low-rise housing. Latin American Journal of Solids and Structures, 11(4): 725-737.

[21] Xu, Y. Y., Lin, Z. R., & Zhang, T. (2016). Design features and significance of the ductile reinforced concrete frame structure. In Design, Manufacturing and Mechatronics: Proceedings of the 2015 International Conference on Design, Manufacturing and Mechatronics, 183-189.

[22] Sococol I, Mihai P, Olteanu-Donțov I. (2019) Ductility–Concept for Improving the Seismic Response for Structural Reinforced Concrete Frame Systems. Buletinul Institutului Politehnic din lasi. Sectia Constructii, Arhitectura, 65(1): 17-30.

[23] Mantawy H. (2015) Ductility of RC Frame Buildings Subjected to the Recent New Zealand Earthquakes. 5(1): 1–8.

[24] Skhakov R. (2003) Seismic energy dissipation and ductility of RC elements section. In Fifth National Conference on Earthquake Engineering, 21(4): 22-32

[25] Venkatesh SV, Bai HS, Navanitha C. (2009) Performance of RC Frame with and without Shear Wall Subjected to Earthquake Load. In Proceedings of Civil Engineering Conference-Innovation without limits, 18(1): 19-21.

[26] Bongilwar R, Harne VR, Chopade A. (2018) Significance of Shear Wall in Multi-Storey Structure with Seismic Analysis. In IOP Conference Series: Materials Science and Engineering, 330(1): 12-17.

[27] Rathod SD, Bhokare SS, Dhiwar PS, Shinde RN. (2017) Comparative Pushover Analysis of RCC, Steel and Composite High Rise Building Frame (G+11) Using ETABS. Journal of Information, Knowledge, and Research in Civil Engineering, 4(2): 88-94.

NEW APPROACH TO PREDICT FECAL COLIFORM REMOVAL FOR STORMWATER BIOFILTER APPLICATIONS

SAI HIN LAI[1*], CHUN HOOI BU[1], REN JIE CHIN[2*], XIANG TING GOH[3] AND FANG YENN TEO[4]

[1]Department of Civil Engineering, Faculty of Engineering, Universiti Malaya, 50603 Kuala Lumpur, Malaysia.
[2]Department of Civil Engineering, Lee Kong Chian Faculty of Engineering and Science, Universiti Tunku Abdul Rahman, 43000 Kajang, Malaysia.
[3]Department of Parasitology, Faculty of Medicine, Universiti Malaya, 50603 Kuala Lumpur, Malaysia.
[4]Department of Civil Engineering, Faculty of Engineering, University of Nottingham (Malaysia Campus), 43500 Semenyih, Malaysia.

[*]Corresponding author: laish@um.edu.my; chinrj@utar.edu.my

ABSTRACT: Fecal coliform removal using stormwater biofilters is an important aspect of stormwater management. A model that can provide an accurate prediction of fecal coliform removal is essential. Therefore, feedforward backpropagation neural network (FBNN) and adaptive neuro-fuzzy inference system (ANFIS) models were developed using a range of input features, namely grass type, the thickness of biofilter, and initial concentration of E. coli, while the estimated final concentration of *E. coli* was the output variable. The ANFIS model shows a better overall performance than the FBNN model, as it has a higher R^2-value of 0.9874, lower MAE and RMSE values of 3.854 and 6.004 respectively, and a smaller average percentage error of 14.2%. Hence, the proposed ANFIS model can be served as an advanced alternative to replace the need for laboratory work.

ABSTRAK: Penyingkiran kolifom tinja menggunakan turas biologi (bioturas) air hujan merupakan aspek penting dalam pengurusan air hujan. Model yang dapat menunjukkan anggaran tepat tentang penyingkiran kolifom tinja adalah penting. Oleh itu, model rangkaian suapan neural perambatan belakang (FBNN) dan sistem adaptasi inferen neuro-fuzi (ANFIS) telah dibentukkan menggunakan pelbagai ciri input, iaitu jenis rumput, ketebalan bioturas dan kepekatan awal E. coli, manakala anggaran kepekatan akhir bagi *E. coli* merupakan hasil pembolehubah. Model ANFIS menunjukkan peningkatan keseluruhan yang lebih baik berbanding model FBNN, kerana ia mempunyai nilai R^2 yang lebih tinggi iaitu 0.9874, nilai MAE dan RMSE yang lebih rendah iaitu sebanyak 3.854 dan 6.004 masing-masing, dan ralat peratusan purata yang lebih kecil sebanyak 14.2%. Oleh itu, model ANFIS yang dicadangkan boleh dijadikan alternatif awal bagi menggantikan keperluan kerja makmal.

1. INTRODUCTION

Biofiltration systems such as swale and bio-detention systems are increasingly popular low-energy treatment technologies for improved stormwater management, e.g. increase of

infiltration, reduction of peak flow, improvement of water quality and increase of surrounding aesthetic value. Stormwater biofilters can be defined as vegetated vertical infiltration systems that can achieve runoff volumes and contaminant load reductions for urban environments [1]. They have shown promising yet variable removal of fecal microorganisms [2-4]. Fecal coliform bacteria are a group of bacteria that are passed through the fecal excrement of humans, livestock, and wildlife and they are the indicator bacteria. The most common member of fecal coliform bacteria is *Escherichia coli*.

Vegetation and filter media depth may affect the capability of stormwater biofilters in removing fecal coliform. In the past two decades, researchers from around the world have experimented with biofilters using different design elements to investigate the biofiltration system in removing fecal coliform [5-10]. These studies reported that vegetation type or filter media depth caused variable bacteria removal performance. A previous study in Australia reported that biofilters planted with native grasses (*Paspalum conjugatum* and *Buchloe dactyloides*) and shrubs (*Melaleuca incana*, *Leptospermum continentale*) showed improved *E. coli* removal, possibly due to reduced infiltration rates in vegetated biofilter systems. In addition, the leaf or seed extracts of *L. continentale* demonstrated potential antibacterial activity against *E. coli* [7]. With regards to filter media depth, it was reported that *E. coli* concentration decreased with increasing filter media depth [7]. Nevertheless, there is no data available for the influence of native vegetation and filter media depth on microbial removal by stormwater biofilters in Malaysia. Therefore, in this study, the effect of biofilter designs (i.e., vegetation type, media thicknesses), as well as the inflow concentration in fecal coliform removal, are investigated to fill the gap of knowledge.

Artificial intelligence (AI) appears as a popular tool in providing the solution to complex non-linear problems and its application on issues relevant to environmental and hydrological researches has been widely seen, i.e. application of artificial neural networks (ANN), fuzzy logic and adaptive neuro-fuzzy systems (ANFIS) for the solution of water/ wastewater and air pollution-related environmental problems [11], integration of ANN and genetic algorithms (GA) for water quality modelling [12], implementation of machine learning classification to detect simulated increases of de facto reuse and urban stormwater surges in surface water [13], performance prediction of stormwater biofilters in heavy metal removal and risk mitigation using multilinear regressions (MLR), neural network (NN), and random forest (RF) [14], etc. Therefore, this study aims to introduce the use of feedforward backpropagation neural network (FBNN) and adaptive neuro-fuzzy inference system (ANFIS) to predict the final concentration of fecal coliform for different conditions of stormwater biofilters. The proposed model can serve as an advanced method to replace the need for laboratory work. This study is innovative as it adds value to the current development of AI applications in improving stormwater management systems.

2. MATERIALS AND METHODS

2.1 Experimental Works

In this study, four native plants, namely Cow grass (*Axonopus compressus*), Pearl grass (*Axonopus compressus,* dwarf), Philippine grass (*Zoysia matrella*), and Japanese grass (*Microstegiumvimineum*) were selected. The biofilter columns were set up as shown in Fig. 1.
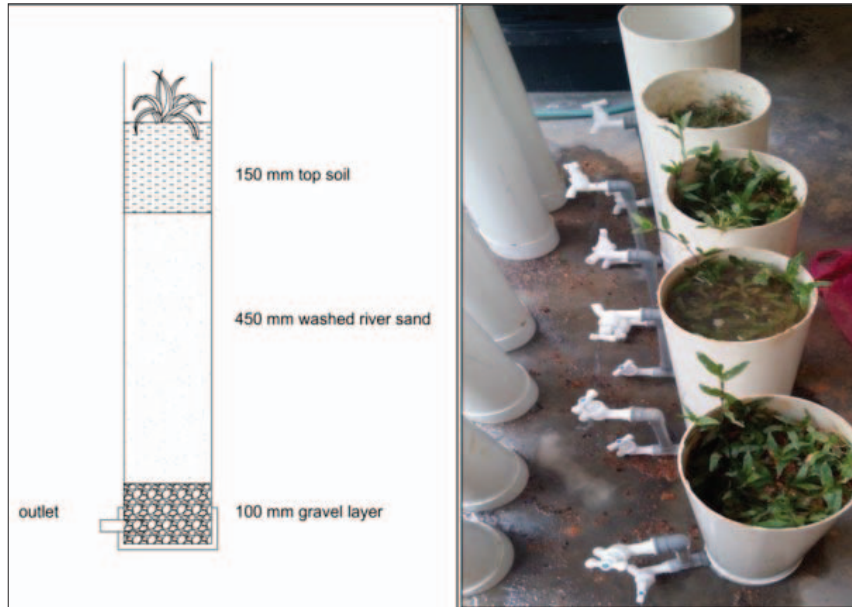
Fig. 1: The setup of biofilter columns used in this study.

The main constituent that forms the filter media was washed river sand. Four different depths were fixed in the sand columns, which are 150 mm, 250 mm, 350 mm and 450 mm. With respect to each depth, the recorded average hydraulic conductivity was 60.2, 47.1, 35.4 and 25.4 mm/hr, respectively. The values fell within the ranges recommended by Urban Stormwater Management Manual of Malaysia (MSMA) [15].

One month before conducting the experiments, the biofilter columns were planted with native vegetation for the plants to mature. An amount of 80 L of water was collected from a local pond to act as stormwater in the experiments.

Four liters of water were poured into every biofilter column and the filtered water was collected. The analysis was carried out for the number of remaining indicator bacteria. A vacuum pump was then used to further filter the collected water sample through sterile nitrocellulose membrane filters. The membrane filters had characteristics of 0.45 μm pore size and 47 mm diameter. The membrane was transferred to a sterile petri dish with an absorbent pad (Millipore, Bedford, MA, USA) containing lauryl sulfate membrane medium (Oxoid, Hampshire, UK) agar plates. The plate was sealed with parafilm and incubated at 30 °C for 4 hours to resuscitate the growth of bacteria before further incubation at 44.5 °C for 14 hours. Fecal coliform that formed yellow colonies were counted and expressed as colony-forming units (CFU) per 100 mL (CFU/100 mL).

The water samples collected before and after the filtration were termed inflow and outflow concentration respectively. The removal efficiency of the biofilter columns can be obtained using Eq. (1).

$$\log removal = \ log_{10} \frac{Influent\ pathogen\ concentration}{Effluent\ pathogen\ concentration} \tag{1}$$

2.2 Architecture of the Feedforward Backpropagation Neural Network (FBNN) Model

Data used in this study can be retrieved from the authors' previous work [10]. Feedforward backpropagation neural network (FBNN), as shown in Fig. 2, has been

commonly used in different fields of applications, particularly in developing non-linear mathematical/prediction models [16-17].
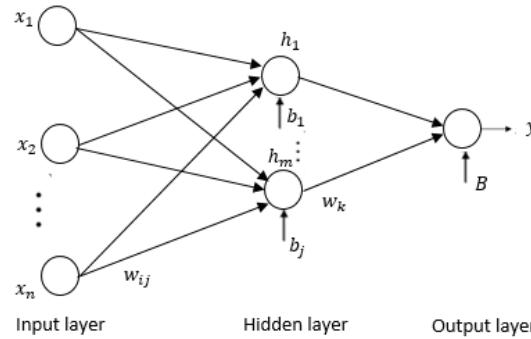
Fig. 2. The general architecture of the FBNN model.

The net values at each hidden neuron (with first pattern inputs and random weight and bias) are presented as [16]:

$$netvalue_j = \sum_{i=1}^{n} w_{ij}x_j + b_j \tag{2}$$

where $netvalue_j$ is net input to node i in hidden or output layer, x_j are the inputs to node i (or output of the previous layer), w_{ij} are the weights representing the power of the relationship between the ith node and jth node, n is the number of nodes and b_j is the bias related to node j.

The transfer function is required to activate the neurons. In this research study, the sigmoid function is chosen as the activation function.

$$h_j = \frac{1}{1+e^{-netvalue_j}} \tag{3}$$

where h_j is the output node of j and is an element of the inputs to the nodes in the next layer.

The net values at the output layer and output neuron values are calculated by Eqs. (4) and (5) respectively.

$$netvalue = \sum_{k=1}^{m} w_k h_k + B \tag{4}$$

$$output\ neuron\ values = \frac{1}{1+e^{-netvalue}} \tag{5}$$

where B is the bias.

In this study, the inputs for the FBNN model were grass type, the thickness of the biofilter, and the initial concentration of *E. coli*. The expected resulting output of the model is the final concentration of *E. coli*. The architecture of the feedforward backpropagation neural network (FBNN) for the final *E. coli* concentration prediction is shown in Fig. 3.

In addition, data sorting is one of the crucial procedures in developing any FBNN model. This is to ensure the smoothness of the overall process and to obtain a model with a respectively high level of accuracy. A proper size of training-testing data is required so that the model can learn enough possible input-output patterns [18-19]. There is no fixed guideline while setting the training to testing ratio. However, it was normally suggested to set the training dataset within the range of 60% to 80% while the remaining 20% to 40% becomes the testing dataset [20-21]. Since this study is considered as very first attempt to introduce the application of artificial intelligence in predicting the final concentration of

fecal coliform with respect to different conditions of stormwater biofilters, the upper limit of 80% is selected so that the developed model will be provided with the most possible input-output patterns.
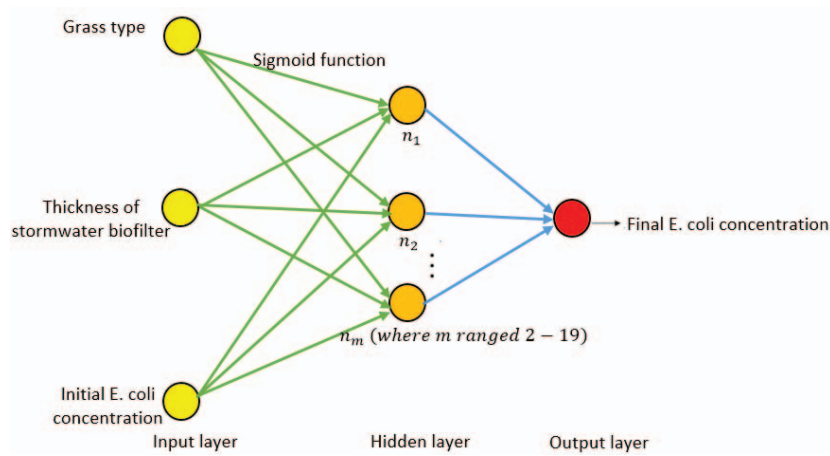
Fig. 3: The architecture of the FBNN model.

The number of hidden layers and the transfer function were set as one and a sigmoid function, respectively [21]. This is mainly due to its performance achievement in the prediction and forecasting model. Meanwhile, the training algorithm is selected as Levenberg-Marquardt (trainlm), since it is suited for function fitting (nonlinear regression) problems [22-24].

While designing the architecture of the FBNN, the determination of the number of hidden neurons is one of the main challenging tasks. This is due to the sensitivity of the networks to the number of hidden neurons. Underfitting problems may appear if there are too few neurons while overfitting issues may arise if there are too many neurons. Therefore, it is important to choose a proper number of neurons [25]. For this study, the hidden neurons were set within the ranges of 2 to 19.

2.3 Architecture of Adaptive Neuro-Fuzzy Inference System (ANFIS) Model

The integration of different techniques to form a hybrid AI model becomes the main trend of the development of AI applications. Adaptive neuro-fuzzy inference system (ANFIS) is a technique that integrates both neural networks and fuzzy logic principles within a single framework. This may strengthen the ability of the model to reach a higher level of accuracy [26-28]. A basic ANFIS architecture is presented in Fig. 4 [29-31].
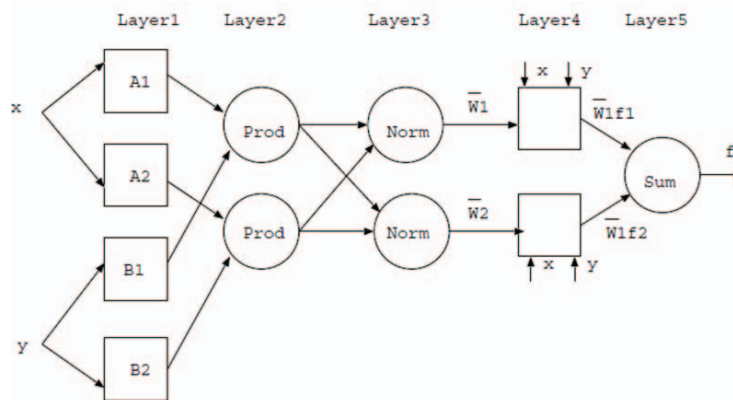
Fig. 4: The general architecture of ANFIS.

Two rules were used in the method of "If-Then" for Takagi-Sugeno fuzzy model, as shown in the following:

$$\text{Rule 1: If x is } A_1 \text{ and y is } B_1, \text{ then } f_1 = p_1 x + q_1 y + r_1 \tag{6}$$

$$\text{Rule 2: If x is } A_2 \text{ and y is } B_2, \text{ then } f_2 = p_2 x + q_2 y + r_2 \tag{7}$$

where A_1, A_2, B_1 and B_2 are the membership functions for each input x and y (part of the premises), f_1 and f_2 are the outputs within the fuzzy region specified by the fuzzy rule, while p_1, q_1, r_1, p_2, q_2 and r_2 are linear parameters in part- Then (consequent part) of Takagi-Sugeno fuzzy inference model [26].

ANFIS architecture consists of five layers excluding the input layer (layer 0). The description of each layer is shown as follows [26]:

1. Layer 0: It is an input layer that has n nodes, where n is the number of inputs to the system.

2. Layer 1: It is the fuzzification layer. Every node in this layer adapts to a function parameter. The output from each node is a degree of membership value that is given by the input of the membership functions. The typical membership function is shown below:

$$\mu_A(x) = \frac{1}{1+\left|\frac{x-c_i}{a_i}\right|^{2b_i}} \tag{8}$$

where a_i, b_i and c_i are parameters for the function. The parameters in this layer are defined as premise parameters.

3. Layer 2: Every node in this layer is a fixed or nonadaptive node. The output is the product of all the incoming signals. Each node in this layer represents the fire strength for each rule. T-norm operator with general performance, such as the AND, is used to obtain the output:

$$O_{2i} = w_i = \mu_{Ai}(x) * \mu_{Bi}(y), i = 1, 2 \tag{9}$$

4. Layer 3: It is the normalization layer. Each node in this layer is fixed. Each node is a calculation of the ratio between the *i*-th rules firing strength and the sum of all rules' firing strengths. The result is known as the normalized firing strength. The strength of all rules is normalized by:

$$O_{3i} = \bar{w}_i = \frac{w_i}{\sum_i w_i} \tag{10}$$

5. Layer 4: It is a layer of adaptive nodes. Every node in this layer is an adaptive node to output, with a node function defined as:

$$O_{4i} = \bar{w}_i f_i = \bar{w}_i(p_i x + q_i y + r_i) \tag{11}$$

where $\bar{w}_i$ is the normalized firing strength from the third layer and $(p_i x + q_i y + r_i)$ is a parameter in the node. The parameters in this layer are referred to as consequent parameters. It is assumed in Eq. (11) that all the universe of discourse for all input variables can be defined using the selected type of the membership functions, and the final output is computed using the regression parameters for each rule R. The regression parameters are the premise parameters in Eq. (11) which define the shape of the selected type of the membership function for each input variable. Consequently, the training process aims at tuning the premise and consequence parameters to achieve the desired output.

6. Layer 5: It is an output layer whose function is the summation of net outputs of the nodes in the fourth layer using the formula as shown:

$$\sum_i w_i f_i = \frac{\sum_i w_i f_i}{\sum_i w_i} \tag{12}$$

While determining the input and output features as well as sorting data for ANFIS model development, a procedure that is similar to the FBNN model development was followed. The input features were made up of grass type, the thickness of stormwater, and the initial concentration of *E. coli*, while the output feature was the final concentration of *E. coli*, as depicted in Fig. 5. The number of membership function (mf) was set as three. In order to tune the patterns of the ANFIS network, the hybrid optimization method, which is the combination of backpropagation and least square-type approaches, was selected. The models were trained using different input membership functions, i.e. *trimf, trapmf, gbellmf, gaussmf, gauss2mf, pimf,* dsigmf and *psigmf,* and output membership function, i.e. constant and linear membership function.
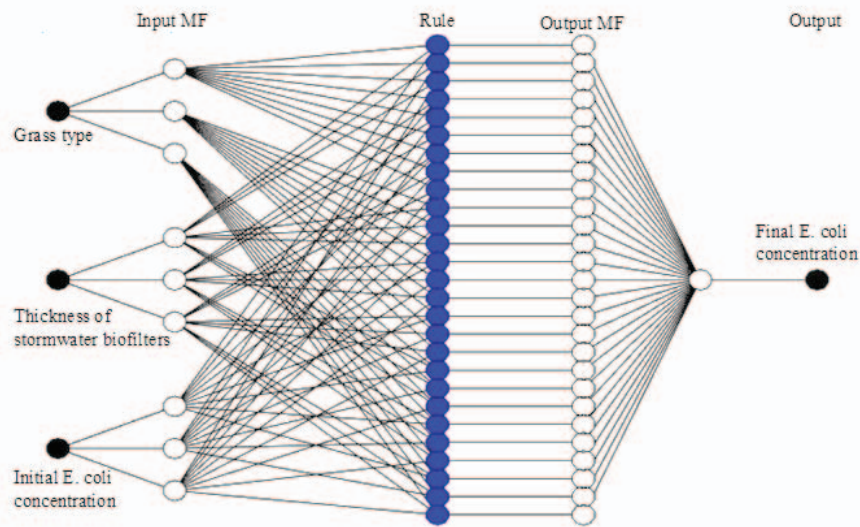
Fig. 5: The architecture of the ANFIS model.

2.4 Model Performance Evaluation

The commonly used analyses for model performance evaluation are coefficient of determination (R^2), mean absolute error (MAE), mean squared error (MSE), root mean squared error (RMSE), and percentage error (% error). These are the relevant important indicators to show the suitability of the developed model in predicting the final concentration of *E. coli*.

$$R^2 = \left(\frac{n \sum x_i y_i - \sum x_i \sum y_i}{\sqrt{n \sum x_i^2 - (\sum x_i)^2} \sqrt{n \sum y_i^2 - (\sum y_i)^2}} \right)^2 \tag{13}$$

$$MAE = \frac{\sum |y_i - x_i|}{n} \tag{14}$$

$$RMSE = \sqrt{\frac{1}{n}\sum(y_i - x_i)^2} \tag{15}$$

$$Percentage\ error = \frac{|True\ value - Predicted\ value|}{True\ value} \times 100\% \tag{16}$$

where n is the number of data pairs, x is the observed variable, y is the predicted variable.

3. RESULTS AND DISCUSSION

3.1 Experimental Works

As shown in Fig. 6, the removal capability of Cow grass on a 450 mm depth river sand column together with 150 mm of topsoil and 100 mm of gravel drainage layer revealed the highest fecal coliform mean log removal (2.4 *log*) compared to other biofilter columns. It agrees with the findings in Barrett et al. [32] and Chandrasena et al. [5] which indicated that vegetated biofilters improved FC removal.

Mean log removal of fecal coliform by four vegetations vs four filter media depths

	150mm	250mm	350mm	450mm
Pearl	0.72	1.21	1.48	2.22
Cow	1.03	1.45	1.74	2.42
Japanese	0.96	1.2	1.38	2.05
Philippines	0.74	1.25	1.43	2.15
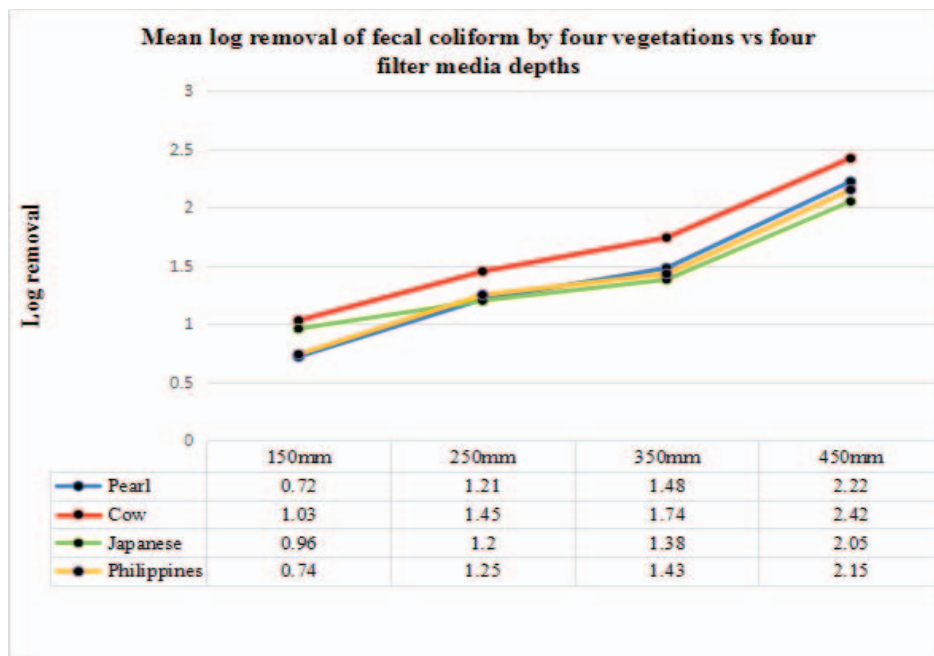
Fig. 6: Mean log removal of fecal coliform of four vegetations vs four filter media.

Planting of grasses, sedges, and shrubs in bioretention systems not only fulfils an esthetic purpose but also improves pathogen removal [33-35]. In the present study, Cow grass was found to be more suitable to use in stormwater biofilters because the survival rate of Cow grass was the highest compared to Pearl, Philippine, and Japanese grass. The bigger root mass of Cow grass improved the removal rates of FC due to its effect on biofilter retention time. It is hardy and able to grow with minimal to no fertilizer. The physical appearance of Pearl grass is similar to Cow grass but it has shorter, rounder, and thicker leaves. Pearl grass needs more water compared to Cow grass to grow and is less hardy. As for Philippine grass, it needs regular trimming about once every 2 weeks. Meanwhile, Japanese grass blades are softer, shorter, and compact. They grow rather slowly, require frequent watering, and in dry soil, they tend to die off.

Apart from vegetation type, the physiochemical nature of filter media in biofilters plays a significant role in microbe removal [36-37]. In this study, the major component that constituted the filter media was washed river sand, offering an effective and low-cost means of treating stormwater. The finding is in-line with the previous studies which reported that sand filters showed satisfying outputs on fecal coliform removal in stormwater treatment [5]. Barrett et al. [32] reported that Austin sand filters achieved high FC (85%) and *E. coli* removal (97.1%) in an experiment to test for biofiltration performance.

In terms of depth, the biofilter with 150 mm media depth exhibited an inconsistent performance in removing fecal coliform. This may be mainly because the preferential flow was more prone to occur in lower media depth due to the intermittent wet-drying cycle. It was found that, in order to achieve > 1 *log* fecal coliform removal, 250 mm should be the minimum media depth required. On the other hand, the mean FC removal at 350 mm depth filter was slightly higher than the 250 mm depth filter but it exceeded 2 *log* for all types of biofilter columns at 450 mm depth filter.

3.2 Models Development

3.2.1 FBNN Models

The proposed FBNN models, which were developed with a range of hidden neurons from 2 to 19, were evaluated using the selected statistical analyses. However, since there were so many developed models, only the selected models were presented in this paper.

Table 1 depicts the performance of all the developed FBNN models from the aspect of R^2, MAE, RMSE and average percentage error (% error). Based on the common theory, a higher R^2-value indicates that the model has a higher ability to explain all the variance within the model. In this case, the highest R^2-value is 0.9285, as shown in model IV.

Table 1: Statistical performance of the selected FBNN models with respect to the different number of neurons

Model	Number of neurons	R^2	MAE	RMSE
I	14	0.8646	6.014	9.926
II	15	0.0650	27.850	65.771
III	16	0.8910	5.107	9.194
IV	17	0.9285	4.204	7.322
V	18	0.9249	4.512	7.423
VI	19	0.0630	57.487	122.191

While evaluating the performance of a FBNN model, a smaller error value is always favorable. This is because the smaller the calculated value, the better the accuracy of the estimated output. From the aspect of MAE and RMSE, model IV achieves the lowest values, displaying a value of 4.204 and 7.322, respectively.

All the above-discussed aspects indicate that model IV is the best-performed model. The appropriateness of model IV to predict the final *E. coli* concentration is further verified using the average percentage error. Percentage error is another common indicator. Fig. 7 contains the average percentage error of the selected FBNN models. Model IV shows the lowest average percentage error (27.5%), indicating that it has the highest level of accuracy among the examined models.
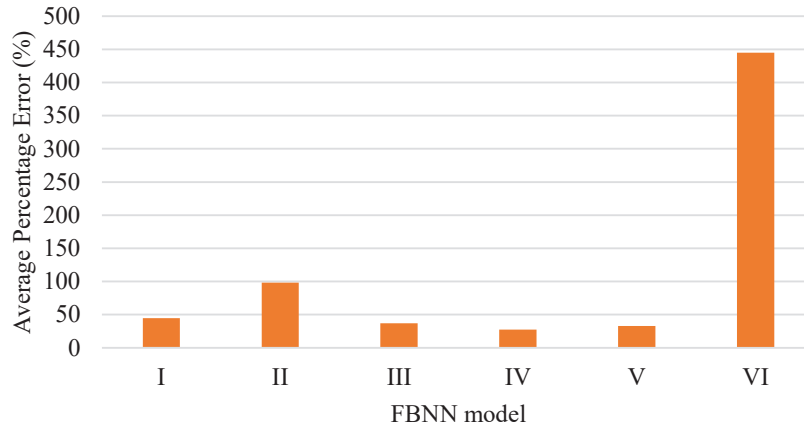
Fig. 7: The average error of the developed FBNN models.

Overall, model IV appears as the most suitable FBNN model to predict the final *E. coli* concentration for the stormwater biofilters application. This is because it has the highest R^2-value (0.9285), the lowest values of MAE (4.204) and RMSE (7.322), and the smallest average percentage error (27.5%).

3.2.2 ANFIS Models

A total number of 16 ANFIS models were developed, and their respective performances are contained in Table 2. In terms of R^2-value, if the value is near 1, indicating that the observed values and the predicted values have a strong linear relationship. In other words, the observed values and predicted values are almost similar if the R^2-value approximates 1. Referring to Table 2, the highest R^2-value is 0.9874.

On the other hand, the models with the output linear membership function (model II, IV, VI, VIII, X, XII, XIV, and XVI), in general, show a better performance than the models with constant output membership function. Therefore, it can be deduced that the output linear membership function is more suitable for the development of the ANFIS model to deal with the stormwater biofilters application. In this case, model IV displays the lowest MAE and RMSE values.

Table 2: Performance in terms of R^2, MAE and RMSE for the developed ANFIS models.

Models	NMFs	MFTI	MFTO	R^2	MAE	RMSE
I	3	trimf	constant	0.7994	11.397	23.885
II	3	trimf	linear	0.9112	7.820	15.866
III	3	trapmf	constant	0.7994	11.397	23.885
IV	3	trapmf	linear	0.9874	3.854	6.004
V	3	gbellmf	constant	0.8231	11.260	22.428
VI	3	gbellmf	linear	0.9217	7.665	14.892
VII	3	gaussmf	constant	0.7909	11.451	24.394
VIII	3	gaussmf	linear	0.9215	7.706	14.908
IX	3	gauss2mf	constant	0.7784	11.471	25.126
X	3	gauss2mf	linear	0.9216	7.626	14.910
XI	3	pimf	constant	0.7714	11.597	25.534
XII	3	pimf	linear	0.9214	7.688	14.927
XIII	3	dsigmf	constant	0.7709	12.328	25.502
XIV	3	dsigmf	linear	0.9215	7.630	14.915
XV	3	psigmf	constant	0.7726	12.253	25.406
XVI	3	psigmf	linear	0.9218	7.629	14.892

From the perspective of average percentage error, model IV has achieved the lowest value if compared with other investigated models, recording at 14.2%, as shown in Fig. 8. In other words, it can achieve an average accuracy of around 86%. In general, no guideline was set for the range of acceptable error in certain engineering applications. However, a smaller error is always preferable. As this is the first attempt to introduce the use of ANFIS in predicting the final *E. coli* concentration for stormwater biofilters application, such an average accuracy is encouraging.
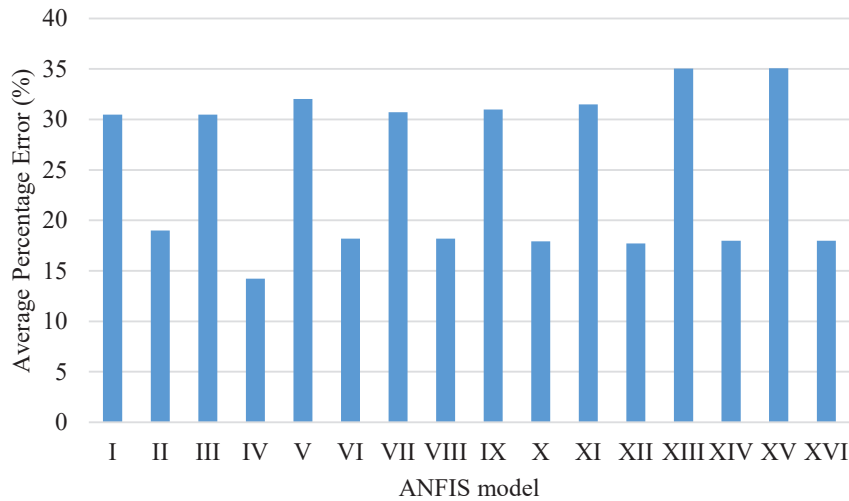
Fig. 8. Average percentage error of the ANFIS model.

In short, model IV is the model with the best performance while evaluating through the series of analytical analyses. It exhibits the highest R^2-value of 0.9874, the lowest MAE and RMSE of 3.854 and 6.004 respectively, and the smallest average percentage error of 14.2%.

3.2.3 AI Models Comparison

This study investigates both FBNN and ANFIS as the advanced methods to predict the final E. coli concentrations. After conducting the performance evaluation through a series of statistical analyses, the best-performed model for each approach was identified. Table 3 shows the comparison of the selected model in terms of R^2, MAE, RMSE and average percentage error.

Table 3: Comparison between the best-performed FBNN and ANFIS model

Model	R^2	MAE	RMSE	Average percentage error
FBNN model IV	0.9285	4.204	7.322	27.5
ANFIS model IV	0.9874	3.854	6.004	14.2

Among all the examined statistical indicators, ANFIS model IV achieved a better performance than that of FBNN model IV. Overall, it shows an improvement from FBNN to ANFIS. The most significant enhancement can be seen from the aspect of the average percentage error. The value has been reduced from 27.5% to 14.2%, showing an improvement of around 50%.

The architecture of the best-performed ANFIS model is therefore described as follows:

- Network inputs: Grass-type, the thickness of biofilters, initial *E. coli* concentration

- Network output: Final *E. coli* concentration
- Number of membership functions: 3
- Input membership function: trapmf
- Output membership function: Linear
- Optimization method: Hybrid

4. CONCLUSIONS

The main purpose of this study was to develop an artificial intelligence (AI) model to serve as an alternative to predict the final E. coli concentration in the application of stormwater biofilters in stormwater management practices. Both feedforward backpropagation neural network (FBNN) and adaptive neuro-fuzzy inference system (ANFIS) models have seen their application in different fields of study, especially while dealing with non-linear regression problems. Both techniques are appropriate for this task because it has the capability to learn the relationships between input-output variables for a complex physical relationship and hence provide an output with a considerably high level of accuracy.

In this study, it is found that a single-layer feedforward backpropagation neural network (FBNN) with 17 hidden neurons to be the most suitable model for the final E. coli concentration prediction. Meanwhile, the ANFIS model with the number of membership function of 3, input trapmf membership function and output linear membership function has shown the best performance among the examined models. The selection of the models was supported by the results of a range of statistical analyses. The selected FBNN model and ANFIS model were then further compared using the same series of statistical analyses to investigate their appropriateness to achieve the main goal of this study.

In conclusion, the ANFIS model appears as the more suitable model for the final E. coli concentration prediction after comparing it with the selected FBNN model. In short, ANFIS is an effective tool to provide a more accurate simulation of the non-linear behavior between the final E. coli concentration and the factors affecting it. With such a model, it allows the user to determine the final E. coli concentration and thereby the removal percentage of the biofilters application by inserting the relevant input parameters into the model. Since this study is seen as the first attempt to implement the artificial intelligence techniques in predicting the final coliform concentration under different stormwater biofilter conditions, two basic techniques (BPNN and ANFIS) were chosen for the model development. To further enhance the model performance in terms of accuracy and effectiveness, the integration of optimization algorithms such as genetic algorithm (GA), ant colony algorithm (ACO), etc. to the proposed model can be performed.

REFERENCES

[1]   Payne EG, Fletcher TD, Cook PL, Deletic A, Hatt BE. (2014) Processes and drivers of nitrogen removal in stormwater biofiltration. Crit. Rev. Environ. Sci. Technol., 44: 796-846.

[2]   Kanda R, Kishimoto N, Hinobayashi J, Hashimoto T, Tanaka S, Murakami Y. (2017) Influence of temperature and COD loading on biological nitrification-denitrification process using a trickling filter: An empirical modeling approach. Int. J. Environ. Res., 11: 71-82.

[3]   Samhan SA, Al-Sa'ed RM, Mahmoud NJ. (2007) Removal of pathogenic microorganisms in pilot-scale UASB-septic tanks and Albireh urban wastewater treatment plant in Palestine. Water Int., 32: 798-809.

[4]   Wang R, Li X, Feng Y, Tariq F, Li K, Wei Y, . . . Chen L. (2019) Removal of formaldehyde from the air with a suspended growth bioreactor. Int. J. Environ. Res., doi:https://doi.org/10.1007/s41742-019-00228-2

[5]   Chandrasena GI, Pham T, Payne EG, Deletic A, McCarthy DT. (2014) *E. coli* removal in laboratory scale stormwater biofilters: Influence of vegetation and submerged zone. J. Hydrol., 519: 814-822

[6]   Li Y, McCarthy DT, Deletic A. (2016) *Escherichia coli* removal in copper-zeolite-integrated stormwater biofilters: Effect of vegetation, operational time, intermittent drying weather. Ecol. Eng., 90: 234-243.

[7]   Chandrasena GI, Shirdashtzadeh M, Li Y, Deletic A, Hathaway, JM, Mccarthy DT. (2017) Retention and survival of E. coli in stormwater biofilters: Role of vegetation, rhizosphere microorganisms and antimicrobial filter media. Ecol. Eng., 102: 166-177.

[8]   Galbraith P, Henry R, McCarthy DT. (2019) Rise of the killer plants: investigating the antimicrobial activity of Australian plants to enhance biofilter-mediated pathogen removal. J. Biol. Eng., 13: 52.

[9]   Hunt WF, Smith JT, Jadlocki SJ, Hathaway JM, Eubanks PR. (2008) Pollutant removal and peak flow mitigation by a bioretention cell in urban Charlotte, N.C. J. Environ. Eng., 134: 403-408.

[10]   Bu CH, Lai SH, Goh XT, Chong WT, Chin RJ. (2021) Influence of filter media depth and vegetation on Faecal Coliform removal by stormwater biofilters. Water Environ. J., 35: 181-189.

[11]   Yetilmezsoy K, Ozkaya B, Cakmakci M. (2011) Artificial intelligence-based prediction models for environmental engineering. Neural Netw. World, 3: 193-218.

[12]   Chau, K-w. (2006) A review on integration of artificial intelligence into water quality modelling. Mar. Pollut. Bull., 52: 726-733.

[13]   Thompson KA, Dickenson ER. (2021) Using machine learning classification to detect simulated increases of de facto reuse and urban stormwater surges in surface water. Water Res., 204: 117556.

[14]   Fang H, Jamali B, Deletic A, Zhang K. (2021) Machine learning approaches for predicting the performance of stormwater biofilters in heavy metal removal and risk mitigation. Water Res., 200: 117273.

[15]   DID Malaysia (2012) Urban stormwater management manual for Malaysia 2nd Edition. Kuala Lumpur, Department of Irrigation and Drainage Malaysia.

[16]   Chin RJ, Lai SH, Shaliza I, Wan Zurina WJ, Ahmed Elshafie AH. (2019) New approach to mimic rheological actual shear rate under wall slip condition. Eng. Comput., 35: 1409-1418.

[17]   Deng B, Chin RJ, Tang Y, Jiang C, Lai SH. (2019) New approach to predict the motion characteristics of single bubbles in still water. Appl. Sci., 9: 3981.

[18]   Alimissis A, Philippopoulos K, Tzanis CG, Deligiorgi D. (2018) Spatial estimation of urban air pollution with the use of artificial neural network models. Atmos. Environ., 191: 205-213.

[19]   Zhang Y, Chen H, Yang B, Fu S, Yu J, Wang Z. (2018) Prediction of phosphate concentrate grade based on artificial neural network modeling. Results Phys., 11: 625-628.

[20]   Akter T, Desai S. (2018) Developing a predictive model for nanoimprint lithography usingartificial neural networks. Mater. Des., 160: 836-848.

[21]   Chin RJ, Lai SH, Shaliza I, Wan Zurina WJ, Elshafie A. (2019) Rheological wall slip velocity prediction model based on artificial neural network. J. Exp. Theor. Artif. Intell., 31: 659-676.

[22]   Pham DT, Sagiroglu S. (2001) Training multilayered perceptrons for pattern recognition: a comparative study of four training algorithms. Int. J. Mach. Tools Manuf., 41: 419-430.

[23]   Demuth H, Beale M. (2014) Neural Network Toolbox for Use with MATLAB User's Guide Version 4. Natick, MA, The MathWorks Inc.

[24]   Sharma B, Venugopalan K. (2014) Comparison of Neural Network Training Functions for Hematoma Classification in Brain CT Images. IOSR J. Comput. Eng., 16: 31-35.

[25]   Alsmadi MK, Omar KB, Noah SA (2009) Back propagation algorithm: The best algorithm among the multi-layer perceptron. Int. J. Comput. Sci. Netw., 9: 378-383.

[26]   Chin RJ, Lai SH, Shaliza I, Wan Zurina WJ, Elshafie A. (2020) ANFIS-based model for predicting actual shear rate associated with wall slip phenomenon. Soft Comput., 24: 9639-9649.

[27]   Ghasemi E, Kalhori H, Bagherpour R. (2016) A new hybrid ANFIS–PSO model for prediction of peak particle velocity due to bench blasting. Eng. Comput., 32: 607-614.

[28]   Korotkikh V, Korotkikh G (2008) On principles in engineering of distributed computing systems. Soft Comput., 12: 201-206.

[29]   Jang JS (1993) Adaptive network-based Fuzzy Inference System. IEEE Trans. Syst. Man Cybern. Syst., 23: 665-685.

[30]   Jang JS, Sun CT. (1997) Neuro-Fuzzy and soft computing: A computing approach to learning and machine intelligence, Englewood Cliffs, New Jersey, Prentice Hall.

[31]   Jang JS, Sun CT, Mizutani E. (1997) A computational approach to learning and machine intelligence. Neuro-Fuzzy and Soft Computing. Upper Saddle River, New Jersey, Prentice-Hall.

[32]   Barrett ME, Limouzin M, Lawler DF. (2013) Effects of media and plant selection on biofiltration performance. J. Environ. Eng., 139: 462-470.

[33]   Read J, Fletcher TD, Wevill T, Deletic A. (2009) Plant traits that enhance pollutant removal from stormwater in biofiltration systems. Int. J. Phytoremediation, 12: 34-53.

[34]   Kim MH, Sung CY, Li MC (2012). Bioretention for stormwater quality improvement in Texas: removal effectiveness of *Escherichia coli*. Sep. Purif. Technol., 84: 120-124.

[35]   Li YL, Deletice A, Alcazar L, Bratieres K, Fletcher TD, McCarthy DT. (2012) Removal of *Clostridium perfringens*, *Escherichia coli* and F-RNA coliphages by stormwater biofilters. Ecol. Eng., 49: 137-145.

[36]   Hermawan AA, Chang JW, Pasbakhsh P, Hart F, Talei A. (2018) Halloysite nanotubes as a fine grained material for heavy metal ions removal in tropical biofiltration systems. Appl. Clay Sci., 160: 106-115.

[37]   Sileshi R, Pitt R, Clark S. (2016) Prediction of flow rates through various stormwater biofilter media mixtures. Proceedings of the World Environmental and Water Resources Congress, West Palm Beach.

GRANULAR SUBBASE IMPROVEMENT WITH RECYCLED CONCRETE AGGREGATES IN TROPICAL AREAS

**DANIELA L. VEGA A.[*], JOSE EDUARDO SALCEDO FONTALVO,
RICHARD JIMENEZ TRIANA, DULCE MARIA PALACIOS DEL BARRE,
CESAR FRESNEDA SALDARRIAGA**

*Department of Civil and Environmental Engineering,
Universidad de La Costa, Barranquilla, Colombia.*

[*]*Corresponding author: dvega7@cuc.edu.co*

ABSTRACT: Use of Recycled Concrete Aggregate (RCA) for Granular Subbase (GSB) in the tropical area is evaluated in this work. Among the materials widely studied as replacements in granular and surface layers is RCA. Its mechanical behavior in granular layers has mainly been evaluated with tests such as California Bearing Ratio (CBR). However, abrasion is also a determining property in the strength of these materials. In this study, the performance of Natural Aggregates (NA) with replacement of RCA was evaluated for use as GSB in a tropical area. Even though several laboratory tests were performed, the focus of the article lies on the performance in the Los Angeles (LA) abrasion test. Two replacement percentages of coarse RCA were considered: 10 and 15 % by weight of aggregates. The RCA and NA were characterized according to different laboratory tests: Granulometry, Absorption, Atterberg Limits test, Plasticity, Specific Gravity, and LA abrasion. In turn, all results were compared with Colombian specifications for a typical GSB in the area. In addition, a simple Life Cycle Assessment (LCA) was included to evaluate the environmental impacts of the base and alternative scenarios. The results show that GSB with 10% RCA present a higher abrasion resistance than the GSB with 15% RCA. Even better results are obtained with 10% RCA than with natural GSB. Specifically, average LA abrasion test losses of 30.86, 29.80 and 32.07% were obtained for NA, 10% RCA and 15% RCA, respectively. The LCA results show an increase of 50% and 75% in energy consumption by comparing the base scenario with 10 and 15% RCA replacement, respectively. This leads to an increase of 40 and 80% in carbon monoxide (CO) emissions for 10 and 15% RCA replacement respectively, and 100% in carbon dioxide (CO_2) emissions for both alternative scenarios.

ABSTRAK: Penggunaan Agregat Konkrit Kitar Semula (RCA) bagi Subtapak Butiran (GSB) bagi kawasan tropika telah dikaji dalam kajian ini. Antara bahan yang banyak dikaji sebagai bahan ganti dalam butiran dan lapisan permukaan adalah RCA. Ciri-ciri mekanikal dalam lapisan butiran telah diuji, terutamanya dengan ujian seperti Nisbah Bearing California (CBR). Walau bagaimanapun, pelelasan juga merupakan ciri penting dalam menentukan ketahanan material. Kajian ini merupakan prestasi Agregasi Semulajadi (NA) dengan ganti RCA yang diuji bagi penggunaan GSB di kawasan tropika. Walaupun pelbagai ujian makmal telah dijalankan, fokus artikel ini terletak pada prestasi ujian pelelasan Los Angeles (LA). Dua gantian bagi peratus RCA kasar telah diambil kira: iaitu pada agregat berat 10% dan 15%. Ciri-ciri RCA dan NA dikategori berdasarkan pelbagai ujian lab yang pelbagai: Granulometri, Penyerapan, ujian Had Atterberg, Keplastikan, Graviti Tertentu dan Pelelasan LA. Kemudian, kesemua dapatan kajian dibandingkan dengan ciri-ciri Kolombia bagi ciri tipikal GSB di kawasan itu. Tambahan, Pentaksiran Kitar Hidup (LCA) yang ringkas dimasukkan bagi menilai impak terhadap alam terhadap

penggunaanya pada pangkal bijirin dan pada senario alternatif. Dapatan kajian menunjukkan GSB yang menggunakan RCA 10% mempunyai rintangan lelasan tertinggi berbanding GSB dengan RCA 15%. Tambahan, dapatan kajian yang lebih baik didapati daripada RCA 10% berbanding GSB semula jadi. Terutama pada purata ujian lelasan LA telah mengalami penyusutan sebanyak 30.86, 29.80 dan 32.07% bagi NA, RCA 10% dan RCA 15%, masing-masing. Dapatan LCA menunjukkan peningkatan sebanyak 50% dan 75% pada penggunaan tenaga dengan perbandingan senario Subtapak Butiran dengan gantian RCA 10% dan 15%, masing-masing. Ini membawa kepada peningkatan sebanyak 40% dan 80% emisi karbon monoksida (CO) bagi gantian RCA 10% dan 15% masing-masing, dan emisi karbon dioksida (CO_2) 100% bagi kedua-dua senario alternatif.

1. INTRODUCTION

In recent years, the use of Recycled Concrete Aggregate (RCA) has been widely recognized worldwide, as it contributes to the preservation of the environment and has several economic and social benefits that make this alternative sustainable. In civil engineering projects, this material has been widely studied as a replacement for natural aggregates in asphalt mixtures [1]–[3], concrete mixtures [4]–[6] and as granular base improvement, just to mention a few [7]–[9].

RCA is a material composed of virgin aggregates covered by a layer of cement mortar [8], these wastes are part of the composition of Construction and Demolition (C&D) waste. Bonded cement mortar is related to different undesirable characteristics of RCA behavior, such as higher absorption, lower durability, and lower mechanical behavior; compared to natural aggregates [3], [10]. However, as a replacement of the Natural Aggregates (NA) in road structures in certain percentages, RCA have shown a relatively good performance [10]. In general, studies show that RCA replacements in pavement structure is an alternative to controlling C&D waste, since it reduces the consumption of natural aggregates and protects the environment [8], [11], [12]. Its use on pavements has been categorized worldwide as a viable, cost-effective, and sustainability-friendly alternative [10], [13].

The stiff and durable structure of the RCAs allows them to be used in the Granular Subbase (GSB) and Granular Base (GB) instead of conventionally used materials [9]. Some studies have been carried out to evaluate and compare the properties of natural granular layers vs. granular layers with RCA replacements. From the results reported in the literature regarding mechanical properties such as the California Bearing Ratio (CBR) and the LA abrasion test, it has been determined that RCAs are comparable to NA [14], highlighting that lower strengths and higher abrasions are observed but they fulfill the standards for GSB. In terms of resilient modulus, it has been established that GB with RCA show higher results than natural aggregates [14]. In addition, they found that RCA had better mechanical properties than NA but had higher permanent deformation. In general, RCAs meet the desired criteria for granular layers, showing satisfactory performance in mechanical behavior [9], [15].

In addition, the environmental effects of the use of RCA in road construction must be considered. It has been established that the use of RCA as a replacement in highway structures reduces greenhouse gas emissions and energy use [10], [14]. The environmental savings that can be achieved with this alternative are mainly related to the production of the materials [14], [16]. A saving of about 16% in CO_2 generation has been established, when comparing the production of NA versus a 70% NA and 30% RCA mix [17].

On the other hand, another important variable in the environmental analysis of the use of RCA in pavement structures is the transportation of the material [14], [18]. Thus, when transportation is not included in the scope of the analysis, large environmental advantages are observed [19], [20]. However, when transportation of materials is considered, it can be concluded that there are savings in energy use only if the recycling facilities are close to the construction sites [10], [21]. In general, it has been established that, under certain replacement percentages and hauling distances, the use of RCA in highway structures is an innovative and ecofriendly solution [10], [14], [17].

The influence of RCA on properties such as CBR, resilient modulus, granulometry and others, has been extensively evaluated in the literature, but few studies have focused on abrasion [14], [22]. This resistance characteristic can be influenced by RCA replacements, so it is studied in detail in this research.

Considering the evidence, the present research has been proposed to evaluate the improvement of a GSB with RCA substitutions. Two percentages of coarse RCA replacement were considered: 10 and 15%. The RCA and GSB were characterized according to different laboratory tests: Granulometry, Absorption, Atterberg Limits test, Plasticity, Specific Gravity, and LA abrasion test. The main comparison of the alternative scenarios versus the natural one was based on the resistance of the samples in the LA abrasion test. In addition, environmental impacts were calculated by a LCA, using the PaLATE 2.0 tool. The analysis was carried out considering a base scenario of the construction of a pavement with a 100% natural GSB, and as alternative scenarios, substitutions of 10% and 15% in the same granular layer were evaluated.

2. METHODOLOGY

For the laboratory tests, samples of the granular materials (natural and recycled) were evaluated individually and then mixed with 10 and 15% replacements of coarse Recycled Concrete Aggregate (RCA). The recycled material was obtained from the demolition of a three-story house, located in the Campo Alegre neighborhood, Barranquilla - Colombia. A portion of a concrete beam was extracted from the area, which was initially subjected to crushing processes in the laboratory. The crushing was carried out using a Bico Brarun jaw crusher (Fig. 1) with a V-Belt Drive system, with a jaws capacity of 2¼ x 3" which allows a reduction of the material from 3/8 to 1/16". To obtain smaller sizes, manual crushing was performed in the laboratory.

Physical and mechanical properties were evaluated on Natural Aggregates (NA) and RCA, as described below. In order to obtain results that can be comparable with other studies, American Society for Testing and Materials (ASTM) standards were used for the development of the tests [23]–[27]. At the same time, these standards are the basis for many standards in different countries such as Colombia. Thus, having them as a basis can guarantee internationally comparable and representative results for the study area.

In addition, all tests performed satisfy Granular Subbase (GSB) Colombian standards [28]. Specifically, the results were compared with the standards for a GSB with 37.5 mm (GSB38) as nominal maximum size.
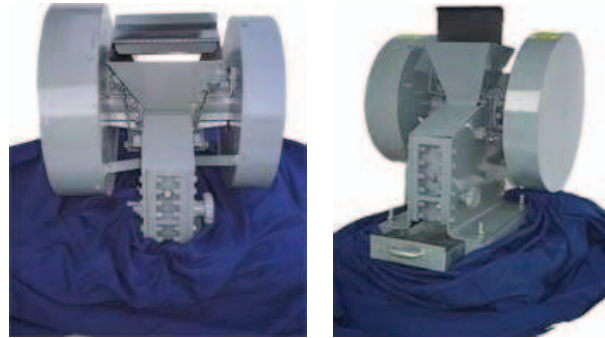
Fig. 1: Laboratory Scale Jaw Crusher used for the crushing of recycled material [29].

Finally, each laboratory test was performed on at least three different samples of the material. It is important to mention that with the number of samples evaluated for each test, a clear trend in the results was observed. The tests carried out and their respective standards are mentioned in Table 1.

Table 1: Test, tested material and standard considered

Test	Tested material	Standard
Granulometry	NA, RCA, 10 and 15% RCA replacements	ASTM D6913 [26]
Density, Relative density and Absorption	RCA	ASTM C127 [24]
Atterberg Limits and Plasticity	NA and RCA 10 and 15% RCA replacements	ASTM D4318 [25]
Specific gravity	RCA	ASTM D854 [23]
LA abrasion	NA, RCA, 10 and 15% RCA replacements	ASTM C131 [27]

3. RESULTS AND DISCUSSION

The section is divided into two parts: The first corresponds to the characterization of the samples of the granular subbase and recycled aggregates and the second part corresponds to the characterization of the Granular Subbase (GSB) mixed with coarse Recycled Concrete Aggregate (RCA) at 10 and 15% with respect to their dry mass.

3.1 Characterization Tests on Natural and Recycled Aggregates

(A) Granulometry Test

The granulometry test was carried out including sieves from 1 1/2" to No. 200. Fig. 2 presents the granulometry curve of the three samples evaluated for (a) Natural Aggregates (NA) and (b) RCA, including the limits established for GSB with 37.5 mm (GSB38) as nominal maximum size [28].

The natural aggregate complies with the granulometry parameter for GSB38 (dashed red and blue lines), showing a curve within the range established by the standard. Considering the crushing method used for the RCA, it was to be expected that its granulometry would not comply with the parameters established for GSB38. Therefore, the RCA should be blended with the necessary sizes so that its particle size complies with the range established by the standard [28] or it can be used as a partial replacement in granular

layers as analyzed in this work. In addition, ₍Fig. 3₎ shows the particle size distribution of one of the RCA samples evaluated.

(a)

(b)
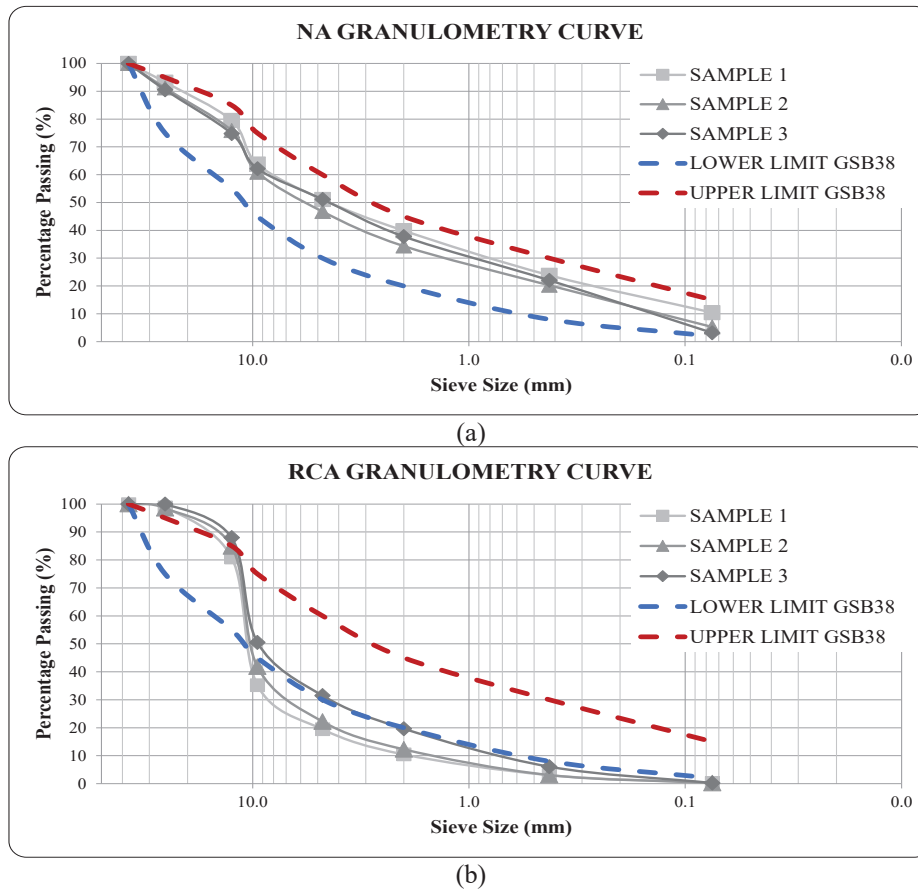
Fig. 2: Granulometry curve of (a) NA and (b) RCA.

Fig. 3: Particle size distribution of one of the RCA samples evaluated.

(B) Density, Relative density and Absorption Test

Considering that absorption is one of the properties that most affects the behavior of the RCA and therefore of the mixtures where they are replaced [10]; density, relative density and absorption tests were carried out on the coarse fraction of the RCA.

Table 2: Density, Relative density, and Absorption results of coarse RCA. A = mass of oven-dry test sample in air; B = mass of saturated-surface-dry test sample in air; C = apparent mass of saturated test sample in water

Specimen	A [g]	B [g]	C [g]	Relative Density (OD) $\dfrac{A}{(B-C)}$	Relative Density (SSD) $\dfrac{B}{(B-C)}$	Apparent Relative Density $\dfrac{A}{(A-C)}$	Absorption [%] $\left[\dfrac{(B-A)}{A}\right]x100$
1	5072	5253	3035	2.29	2.37	2.49	3.57
2	5050	5251	3101	2.35	2.44	2.59	3.98
3	5010	5201	3089	2.37	2.46	2.61	3.81

The oven-dry (OD), saturated-surface-dry (SSD), apparent relative density, and absorption results of the three samples evaluated are shown in Table 2. These agree with those reported in the literature. Where OD is in the range of 2.20 to 2.40, SSD between 2.31 and 2.68, apparent between 2.42 and 2.70, and absorption between 1.43 and 8.05 for the coarse fraction of RCA [14], [22], [30], [31].

(C) Atterberg Limits and Plasticity Test

Atterberg limits and plasticity index tests were performed on three samples of NA and RCA. The results show a non-plastic behavior for the NA and slightly plastic for the RCA. Specifically, the RCA results show a Liquid Limit (LL) of 33.54% and a Plastic Limit (PL) of 2.24% on average, complying with GSB38 standards [28].

(D) Specific Gravity Test

The specific gravity of three samples of fine RCA were evaluated and the results show an average of 2.64. This agrees with the literature which shows a range of 2.14 to 2.65 for this property in fine RCA [14].

(E) LA Abrasion Test

LA abrasion tests were performed on three samples of NA and RCA. The results were compared as a measure of resistance and are shown in Fig. 4. The figure shows the requirements for low (NT1), medium (NT2) and high (NT3) traffic levels for GSB38 [28], and both materials fulfill it. Specifically, the limit for the different transit levels is a loss in abrasion of 50%. An average of 30.86 and 35.72% in abrasion loss were obtained for the NA and RCA, respectively.

The results agree with those reported in the literature. It is stated that the RCA has lower resistance in LA abrasion test than the NA [17], [22] and shows weight loss between 27.3 and 39.0% [14].

3.2 Characterization Tests on GSB with RCA Replacements

Once the materials (natural and recycled) were characterized by the physical and mechanical properties tests described above, the evaluation of the alternative scenarios continued. The mechanical evaluation of the alternatives and their comparison with the base scenario was carried out based mainly on the results of the LA abrasion test. Properties such as granulometry and plasticity were also evaluated and compared according to GSB38 standards [28].
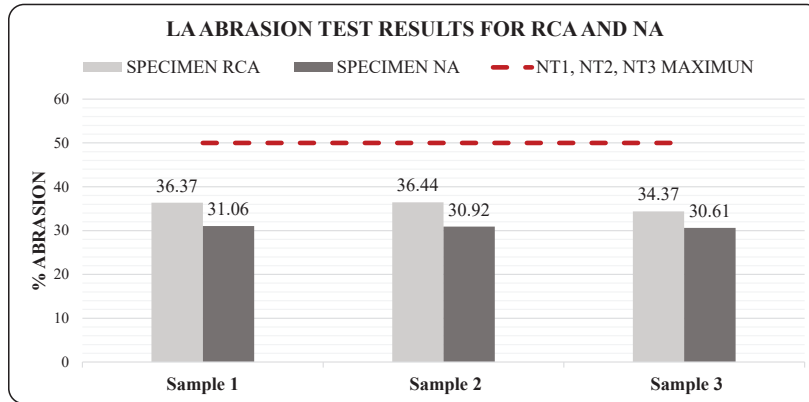
Fig. 4: LA abrasion test results for NA and RCA.

The alternative scenarios correspond to 10 and 15% coarse RCA replacements. It should be noted that these percentages were determined considering the literature [14], [17], [22]. For both replacements, 10 and 15% coarse RCA, three samples were evaluated for the granulometry test.

As shown in Fig. 5, the granulometry curve of both alternatives of RCA replacement comply with GSB38 standards (dashed red and blue lines) [28]. A similarity in the granulometric curves was observed, as the size distributions remained similar, varying mainly in the percentage of RCA substitution.

(a)

(b)
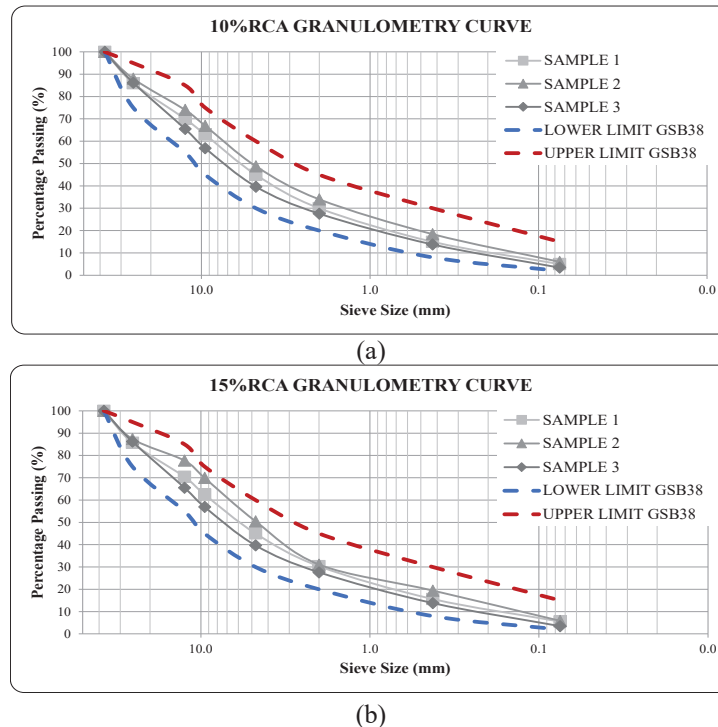
Fig. 5: Granulometry curve of NA with (a) 10% and (b) 15% coarse RCA.

For plasticity, no significant changes were observed due to the influence of the RCA replacements. For both alternatives, slightly plastic behavior is found, with PL of around 2.5% on average. This satisfies the standards for GSB38, established as a maximum of 6% [28].

Comparing the results of the LA abrasion test (Fig. 6), it is observed that the 15% RCA mixes show a weight loss 2.27% higher than the 10% RCA mixes, on average. On average, values of 29.80 and 32.07% in abrasion loss were obtained for 10 and 15% RCA replacement, respectively. In addition, the replacement of 15% RCA decreases the LA abrasion resistance when compared to the natural sample. Whereas, with the 10% RCA replacement, a small increase in this property is observed.
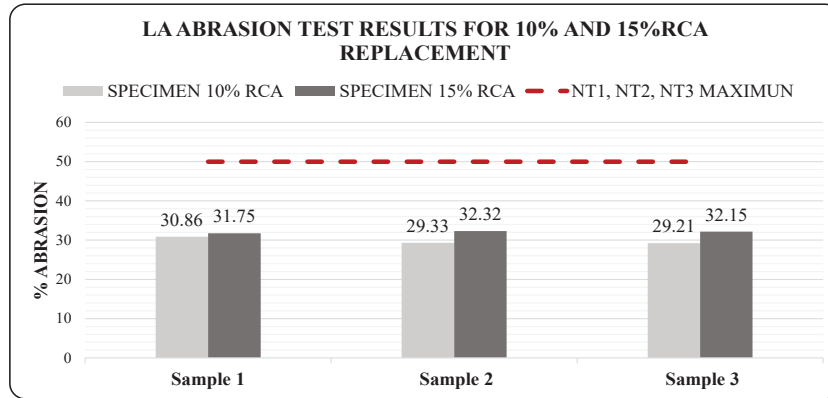
Fig. 6: LA abrasion test results for 10% and 15% RCA replacement.

It is observed in Fig. 6 that the highest value obtained for abrasion with 10% RCA is 30.86% while the lowest value is 29.21%. When analyzing the 15% RCA replacement, it is observed that the highest value is 32.32% compared to the minimum which is 31.75%. These values are very similar in the literature, which are less than 35% [14], [22]. However, both alternatives comply with the requirement for GSB38 [28] established as a maximum of 50% for the different levels of traffic (Low: NT1, Medium: NT2, High: NT3).

Subsequently, Table 3 contains the average percentage results of LA abrasion loss and differences found when comparing the results of the alternative scenarios versus the NA. This indicates that, for replacements higher than 10% RCA, the abrasion resistance of the granular layer decreases. Wider replacement rates should be evaluated to determine an optimal replacement range.

Table 3: Average percentage results of LA abrasion loss and differences
between NA and alternative scenarios

Average results (%)	Difference (%)
NA 30.86	-
10%RCA 29.80	1.06
15%RCA 32.07	-1.21

Finally, Fig. 7 presents the ratio between LA abrasion tests with 10% and 15% RCA replacements with respect to the result obtained for NA (i.e., LA abrasion with replacement with RCA/LA abrasion with NA). Therefore, greater values than 1 represent negative influence; lower than 1 suggests a positive influence, and a value equal to 1 represents null influence.

The results show that with a replacement of 10% RCA, values lower than the reference value (1) are obtained, which are related to a reduction in the abrasion. On the other hand, a replacement with a 15% RCA suggests values higher than 1, demonstrating an increase in abrasion.
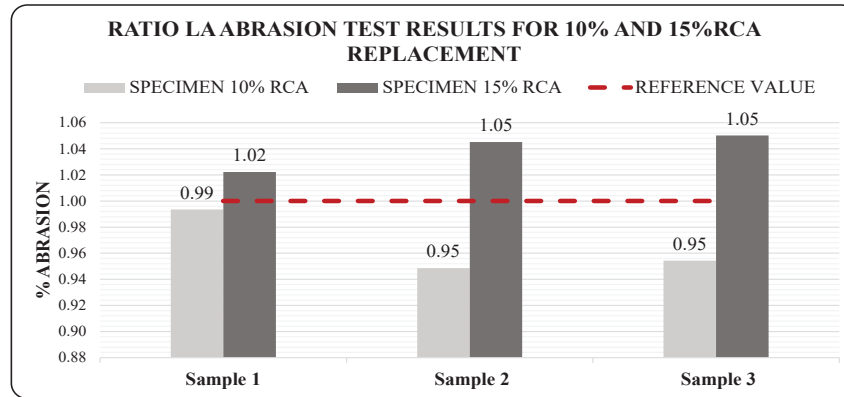
Fig. 7: Ratio LA abrasion test results for 10% and 15% coarse RCA replacement.

Analyzing the values presented in Fig. 7, it is observed that for 10% RCA a maximum ratio of 0.99 and a minimum of 0.95 was obtained, while for 15% RCA the maximum value was 1.05 and the minimum was 1.02. This shows that there is a trend of decreasing abrasion when GSB is replaced with 10% RCA. When analyzed with 15% RCA replacement, an upward trend in abrasion loss is obtained. Consequently, the abrasion values increase when 15% RCA replacement is reached and decreases for 10% RCA. Thus, an optimum value can be found between the percentage of RCA and the maximum decrease of abrasion as evidenced in the literature [14], [22].

3.3 Environmental Results

Environmental impacts were calculated by a life cycle analysis (LCA) using the PaLATE 2.0 tool. It was carried out considering as a base scenario the construction of a pavement with a 100% natural GSB, and as alternative scenarios substitutions of 10% and 15% in the same granular layer were evaluated.

In this study, the functional unit was defined as the construction of the GSB of a typical Colombian road section: 1 km in length and 1 lane of 3.5 m wide. Considering the typical conditions of the area and the regulations [28], the following design characteristics were established: (1) a traffic value of 5×10^6 Equivalent Single Axle Load (ESAL) of 80 kN; (2) CBR of 30%; (3) service life of 10 years; (4) a GSB modulus of 200 MPa. Considering the above, 22 cm was considered as the GSB thickness. Therefore, the construction of 770 m^3 of GSB was evaluated for both the base and alternative scenarios.

The PaLATE 2.0 tool evaluates 12 environmental impacts, considering the stages of Materials Production, Materials Transportations and Processes (Equipment). It is important to highlight that in this study hauling distances were not considered, with the purpose of only considering the replacement of the RCA as a variable. Thus, the environmental impacts are related to Materials Production and Processes (Equipment). In addition, of the 12 impacts, the following impacts were considered: energy (MJ), water consumption (kg), CO_2 (kg), particulate matter with a diameter of 10 microns or less PM_{10} (kg), and CO (kg).

The results presented in Table 4 suggest that the use of RCA as a replacement in GSB implies a significant increase in energy consumption and water consumption. This would

be related to the activities involved in the RCA production process [10], [17]. In turn, this represents an increase in emissions of the different impacts evaluated.

Specifically, the LCA results show an increase of 50% and 75% in energy consumption by comparing the base scenario with 10 and 15% RCA replacement, respectively. This leads to an increase of 40 and 80% in CO emissions for 10 and 15% RCA replacement respectively, and 100% in CO_2 emissions for both alternative scenarios. In terms of PM_{10} emissions, a 50% increase was observed when comparing the base scenario with 15% RCA replacement.

Table 4: Environmental results of base and alternatives scenarios

	Energy [MJ]	Water Consumption [kg]	CO_2 [kg]	PM_{10} [kg]	CO [kg]
100% NA	13669	1	1000	2	5
10%RCA	20504	1	2000	2	7
15%RCA	23922	1	2000	3	9

The environmental results contrast with those reported in the literature. It has been established that the use of RCA tends to represent a saving in emissions of different pollutants. Savings of 16% in CO_2 generation are reported when comparing the production of NA versus a mixture of 70% NA and 30% RCA [17]. In addition, significant savings in CO emissions and energy consumption have also been found when evaluating the use of RCA replacements in pavement structures [13].

However, when high percentages of RCA (45% replacement) are analyzed, increases of 20% in CO_2 generation and 10% in emissions of Particulate Matter with a diameter of 2.5 microns or fewer of $PM_{2.5}$ have been found [10]. Also, increases in impacts such as climate change and eutrophication have been reported by including RCA in concrete [21]. In general, environmental impacts are sensitive to the percentage of replacement and hauling distances of RCA, so the use of RCA does not necessarily imply environmental savings [10], [21]. Thus, the environmental results are a function of the case study conditions and characteristics such as the functional unit evaluated.

4. CONCLUSIONS

The performance of natural aggregates with 10 and 15% replacement of coarse Recycled Concrete Aggregate (RCA) was evaluated for use as Granular Subbase (GSB) in Colombia as a tropical area. Initially, the physical and mechanical characterization of both materials (natural and recycled) was carried out considering Granulometry, Absorption, Atterberg Limits test, Plasticity, Specific Gravity, and Los Angeles LA abrasion test. At least three samples of each material were considered for each test. Noting that with the number of samples evaluated for each test, a clear trend in the results was observed.

Then, results of Natural Aggregates (NA) versus 10 and 15% RCA replacement as alternative scenarios were evaluated and compared. The main comparison was based on the resistance of the samples in the LA abrasion test. This is because abrasion is a determining property in the strength of these materials, however few studies have focused on its influence [14], [22]. Therefore, the objective of the research is to evaluate how aggregate abrasion varies when a significant percentage of RCA is added.

All results were compared with the GSB with 37.5 mm (GSB38) as nominal maximum size standards according to Colombian regulations. This is because GSB38 is the typical GSB in the area. In addition, a simple Life Cycle Assessment (LCA) was included to evaluate the environmental impacts of the base and alternative scenarios. The LCA was conducted considering Materials Production and Processes (Equipment) stages and including 5 environmental impacts: energy (MJ), water consumption (kg), CO_2 (kg), particulate matter with a diameter of 10 microns or less PM_{10} (kg) and CO (kg).

Based on the conditions and results of the study, the following can be concluded:

- The granulometry of the NA complies with GSB38 standards, while the RCA shows a curve outside the range stipulated by the standard [28]. Therefore, the RCA would have to be mixed with other aggregates to achieve an acceptable granulometry curve.

- The densities and absorption of the fine RCA agree with those reported in the literature [14], [22], [30], [31]. With averages of 2.34, 2.42, 2.56 and 3.79% for OD, SSD, apparent, and absorption, respectively.

- The plasticity of the RCA complies with GSB38 standards, showing an average result of 2.24%. For the NA, a Plastic Limit (PL) showing non-plastic behavior was obtained.

- The specific gravity of the fine RCA agrees with the literature [14], showing an average value of 2.64.

- The results of the LA abrasion test comply with the standards for both materials. As expected, a higher loss is observed in the RCA. Specifically, an average weight loss of 30.86% was found for the NA and 35.72% for the RCA.

- When evaluating the 10 and 15% RCA replacements, the granulometry curves complied with GSB38 standards; the plasticity did not show major changes and complies with the requirement for this property in GSB38 too [28].

- The results of the LA abrasion test show that GSB with 15% RCA has higher losses than that with 10% RCA. Specifically, it is observed that the 15% RCA mixes show a weight loss 2.27% higher than the 10% RCA mixes, on average.

- On average, values of 29.80 and 32.07% abrasion loss were obtained for 10 and 15% RCA replacement, respectively.

- The replacement of 15% RCA decreases the LA abrasion resistance compared to the natural sample. Whereas, with 10% RCA substitution, a small increase in this property is observed compared to the natural sample.

- For replacements higher than 10% RCA, the abrasion resistance of the granular layer decreases. Wider replacement rates should be evaluated to determine an optimal replacement range.

- The environmental results show that the use of RCA as a replacement in GSB implies a significant increase in energy consumption and water consumption. In turn, this represents an increase in emissions of the different impacts evaluated. This would be related to the activities involved in the RCA production process [10], [17].

- Specifically, the LCA results show an increase of 50% and 75% in energy consumption by comparing the base scenario with 10 and 15% RCA replacement, respectively. This leads to an increase of 40 and 80% in CO emissions for 10 and 15% RCA replacement respectively, and 100% in CO_2 emissions for both alternative scenarios.

ACKNOWLEDGEMENT

REFERENCES

[1]   Tahmoorian F, Samali B, Yeaman J, Mirzababaei M. (2022) Evaluation of volumetric performance of asphalt mixtures containing recycled construction aggregate (RCA). International Journal of Pavement Engineering, 23(7): 2191-2205. https://doi.org/10.1080/10298436.2020.1849686

[2]   Tahmoorian F, Samali B. (2017) Experimental and correlational study on the utilisation of RCA as an alternative coarse aggregate in asphalt mixtures. Australian Journal of Civil Engineering, 15(2): 80-92.

[3]   Daquan S, Yang T, Guoqiang S, Qi P, Fan Y, Xingyi Z. (2018) Performance evaluation of asphalt mixtures containing recycled concrete aggregates. International Journal of Pavement Engineering, 19(5): 422-428.

[4]   Ogbonna AC. (2018) Laboratory evaluation of the characteristics of continuously reinforced concrete pavement incorporating recycled concrete aggregate. Australian Journal of Civil Engineering, 16(1): 38-45.

[5]   Jindal A, Ransinchung RN-GD, Kumar P. (2017) Study of pavement quality concrete mix incorporating beneficiated recycled concrete aggregates. Road Materials and Pavement Design, 18(5): 1159-1189.

[6]   Cai X, Wu K, Huang W, Yu J, Yu H. (2021) Application of recycled concrete aggregates and crushed bricks on permeable concrete road base. Road Materials and Pavement Design, 22(10): 2181-2196.

[7]   Lopez-Uceda A, Ayuso J, Jiménez JR, Galvín AP, Del Rey I. (2020) Feasibility study of roller compacted concrete with recycled aggregates as base layer for light-traffic roads. Road Materials and Pavement Design, 21(1): 276-288.

[8]   Aghililotf M, Palassi M, Ramezanianpour AM. (2021) Mechanical and durability assessment of unconfined recycled concrete aggregates and natural aggregates used in road constructions. International Journal of Pavement Engineering, 22(12): 1518-1530.

[9]   Toka EB, Olgun M. (2021) Performance of granular road base and sub-base layers containing recycled concrete aggregate in different ratios. International Journal of Pavement Engineering, 1-14. DOI 10.1080/10298436.2021.1916819

[10]   Vega A DL, Santos J, Martinez-Arguelles G. (2022) Life cycle assessment of hot mix asphalt with recycled concrete aggregates for road pavements construction. International Journal of Pavement Engineering, 23(4): 923-936.

[11]   Martinez-Arguelles G, Coll MD, Pumarejo LGF, Cotte EHS, Rondon H, Pacheco CA, ... & Espinoza RGL. (2019) Characterization of recycled concrete aggregate as potential replacement of natural aggregate in asphalt pavement. In IOP Conference Series: Materials Science and Engineering, 471(10): 102045.

[12]   Vega A DL, Gilberto MA, dos Santos JM. (2019) Life cycle assessment of warm mix asphalt with recycled concrete aggregate. In IOP Conference Series: Materials Science and Engineering, 603(5): 052016.

[13]   Devaki H, Shanmugapriya S. (2022) LCA on construction and demolition waste management approaches: A review. Materials Today: Proceedings. https://doi.org/10.1016/j.matpr.2022.03.286

[14]   Aytekin B, Mardani-Aghabaglou A. (2022) Sustainable Materials: A Review of Recycled Concrete Aggregate Utilization as Pavement Material. Transportation Research Record, 2676(3): 468-491.

[15] Kim J. (2022) Influence of quality of recycled aggregates on the mechanical properties of recycled aggregate concretes: An overview. Construction and Building Materials, 328: 127071.

[16] Colangelo F, Forcina A, Farina I, Petrillo A. (2018) Life cycle assessment (LCA) of different kinds of concrete containing waste for sustainable construction. Buildings, 8(5): 70.

[17] Martinez-Arguelles G, Acosta MP, Dugarte M, Fuentes L. (2019) Life cycle assessment of natural and recycled concrete aggregate production for road pavements applications in the Northern Region of Colombia: case study. Transportation Research Record, 2673(5): 397-406.

[18] Kadawo A, Sadagopan M, During O, Bolton K, Nagy A. (2021) Combination of LCA and circularity index for assessment of environmental impact of recycled aggregate concrete. Journal of Sustainable Cement-Based Materials, 1-12. https://doi.org/10.1080/21650373.2021.2004562

[19] Nayana AY, Kavitha S. (2017). Evaluation of CO_2 emissions for green concrete with high volume slag, recycled aggregate, recycled water to build eco environment. Int. J. Civ. Eng. Technol, 8: 703-708.

[20] Kurda R, Silvestre JD, de Brito J. (2018) Life cycle assessment of concrete made with high volume of recycled concrete aggregates and fly ash. Resources, Conservation and Recycling, 139: 407-417.

[21] Yazdanbakhsh A, Bank LC, Baez T, Wernick I. (2018) Comparative LCA of concrete with natural and recycled coarse aggregate in the New York City area. The International Journal of Life Cycle Assessment, 23(6): 1163-1173.

[22] Verian KP, Ashraf W, Cao Y. (2018) Properties of recycled concrete aggregate and their influence in new concrete production. Resources, Conservation and Recycling, 133: 30-49.

[23] BICO Braun International, Manufacturers of mining and geological laboratory test equipment. [www.bicoinc.com].

[24] ASTM (2010). Standard test methods for specific gravity of soil solids by water pycnometer D854.

[25] ASTM (2012). Standard test method for density, relative density (specific gravity), and absorption of coarse aggregate C127.

[26] ASTM (2010). Standard test methods for liquid limit, plastic limit, and plasticity index of soils D4318.

[27] ASTM (2009). Standard test methods for particle-size distribution (gradation) of soils using sieve analysis D6913.

[28] ASTM (2010). Standard Test Method for Resistance to Degradation of Small-Size Coarse Aggregate by Abrasion and Impact in the Los Angeles Machine C131

[29] INVIAS (2013). Capítulo 3-Afirmados, Subbases y Bases Art. 300 Disposiciones generales para la ejecución de afirmados, sub-bases y bases granulares y estabilizadas

[30] Kurda R, de Brito J, Silvestre JD. (2017) Influence of recycled aggregates and high contents of fly ash on concrete fresh properties. Cement and Concrete Composites, 84: 198-213.

[31] Pickel D, Tighe S, West JS. (2017) Assessing benefits of pre-soaked recycled concrete aggregate on variably cured concrete. Construction and Building Materials, 141: 245-252.

SECURE SLICING AND ALLOCATION OF RESOURCES OF 5G NETWORKS IN SOFTWARE-DEFINED NETWORKING / NETWORK FUNCTIONS VIRTUALIZATION

ALI J. RAMADHAN

Department of Computer Techniques Engineering,
College of Technical Engineering,
University of AlKafeel, Najaf 31001, Iraq

Corresponding author: ali.j.r@alkafeel.edu.iq; ali.j.r@ieee.org

ABSTRACT: In 5G communications, higher data rates and lower latency are needed due to the high traffic rate. Though resource wastage is avoided by secure slicing, sliced networks are exploited by DDoS attackers. Thus, in the present paper, traffic-aware setting up is PRESENTED for resource allocation and secure slicing over the virtualization of 5G networks enabled by software-defined network/network functions. In the proposed method (called T-S^{3}RA), to authenticate user devices, Boolean logic is used with key derivation based on passwords. Moreover, the traffic arrangement is based on the 5G access points. To implement secure resource allocation and network slicing, deep learning models are used. Renyi entropy computation is employed to predict the DDoS attackers. Through the experimental results, the effectiveness of the presented approach is proved.

ABSTRAK: Melalui komunikasi 5G, kadar data yang tinggi dan latensi yang rendah amat diperlukan kerana kadar trafik yang tinggi. Walaupun pembaziran sumber dapat dielakkan melalui pemotongan selamat, rangkaian yang dipotong sering dieksploitasi oleh penyerang DDoS. Oleh itu, kajian ini menyediakan persekitaran sedar-trafik bagi peruntukan sumber dan pemotongan selamat ke atas rangkaian 5G secara maya melalui fungsi rangkaian takrif-perisian. Melaui pendekatan yang dicadangkan (iaitu T-S3RA), peranti pengguna disahkan terlebih dahulu menggunakan logik Boolean dengan perolehan kunci berdasarkan kata laluan. Di samping itu, susunan trafik adalah berdasarkan titik akses 5G. Bagi melaksanakan peruntukan sumber yang selamat dan pemotongan rangkaian, model pembelajaran mendalam telah digunakan. Pengiraan Entropi Renyi dibuat bagi meramal penyerang DDoS. Dapatan eksperimen mengesahkan keberkesanan pendekatan yang dicadangkan.

1. INTRODUCTION

Network slicing is a critical issue for 5G networks beneath a single physical infrastructure. Generally, network slicing is defined as selection of slices and appropriate allocation of resources for each user [1-4]. Presently, higher service-satisfaction rates are required by network equipment. For instance, for a 4K ultra HD video streaming application, it is essential to meet more stringent service requirements like high throughput, high reliability, low latency, and higher storage space. Larger throughput and limited delay are

required by this application, thus needing the implementation of resource allocation and network slicing.

Resource allocation and joint network slicing were presented as the main solution for meeting the requirements of users' quality of service (QoS). Using the service type is among the greatest methods to create a slice. Data traffic includes the type of service used for configuring the network slicing. Moreover, a quick and dynamic response should be offered to satisfy the constraints of service level agreement (SLA). Mainly, the present solutions for resource allocation and network slicing are expensive computationally while not supporting the mixed slice requests [5,6].

Appropriate support is provided by a software-defined network (SDN) for resource allocation and network slicing since it includes the functionality of processing the slice requests and performing data traffic arrangement [7]. SDNs have various benefits based on network slicing. Moreover, they currently are extensively researched for numerous applications. These advantages include reliable communication, long-distance, urgent solutions, and communication for optimizing problems [8-10]. For similar cases, a heuristic algorithm is utilized. Computations require a huge deal of time in these algorithms, due to their complexity.

Poor results are obtained by the present resource-allocation and network-slicing methods owing to the massive arrival rate of resource requests, numerous network slice requests, and high data traffic within a network slice [11]. Moreover, concentrated SDN controllers are also influenced since they behave as a single-point failure, unable to control most urgent service requests (ultralow latency). Through a multi-controller SDN environment, these issues are solved. The final decision is made by the controller in the SDN/network function virtualization (NFV)-based slicing to appropriately direct the slices [12-15].

The present study aims to handle the massive heterogeneous services from diverse tools with 5G networks connections [16-22]. Currently, three key services are evolved in 5G namely, ultra-reliable low-latency communication (URLLC), massive machine-type communication (mMTC), and enhanced mobile broadband (eMBB) (Table I).

The QoS and security requirements of networks were increased by integrating SDN/NFV and 5G. Resource allocation and network slicing in a 5G network enabled by SDN/NFV are challenging since the optimum set of resources and proper slice must be defined. Resource allocation and network slicing are implemented in most studies for a few heterogeneous services while considering very restricted metrics. Furthermore, fast resource allocation and network slicing are required owing to various throughputs, mobilities, data rates, and delays in different services. The QoS can be improved by a universal system.

For proper resource allocation and slice selection, a concentrated SDN controller is not practicable since slice privacy and security are not considered and there is higher participation of DDoS attackers. Thus, massive quantities of traffic are sent to a particular slice by these attackers. Nevertheless, the QoS requirement for UE cannot be satisfied by the secure network slicing alone since it is essential to serve the high-priority traffic first, in terms of the type of service.

The slice network is performed by the global controller while allocating optimal resources to achieve diverse service needs from users. The present study mainly includes the following points.

The 5G AP audits each authority in a VAP to insert, eliminate, and adjust the operations. Using a password-based key derivation function 2 (PBKDF2) in terms of Boolean logic is considered along with three input parameters including a physically unclonable function (PUF), secret key, and timestamp. An asymmetric queue model was used to perform traffic scheduling oriented by Bernoulli's theorem. Packet delay, data rate, and packet length were used to schedule the traffic flow. Two high- and low-priority queues were fixed within the 5G AP. Each queue includes asymmetric service rates based on the arrival rate. The international mobile subscriber identity, traffic type, fair SLA, device mobility, and slice capacity are considered in network slicing.

The present work primarily focused on SLA constraints between the service provider and user leading to the fair SLA while slicing the network. First, it tried to calculate the service availability ratio (SAR), throughput ratio (TR), response time ratio (RTR), and service reliability ratio (SRR) accompanied by the fairness or weight for each service. To perform resource allocation, HopFieldNet is used as a quick neural network to find resources for each slice. Through the proposed dynamic-flow offloading outline at the local control plane, overloading at network slices is handled. Using a fast-weighted bipartite graph ($F\omega BG$) was considered in terms of transmission rate, switch service capacity, and loss rate to map multiple flows to the optimal switches enhancing the network reputation. Packet classification through Renyi entropy was run along with the device authentication. The bandwidth usage is estimated here, for the switches. Ultimately, the NS3.26 simulator was used for the experiments to assess the proposed scheme exhibiting highly satisfactory performance compared to the formerly presented schemes based on several metrics like throughput, response time, latency, packet loss ratio, packet transmission ratio, bandwidth consumption, slice acceptance ratio, and slice capacity.

The rest of this paper is organized as follows. Earlier studies on resource allocation and network slicing are provided in Section 2 to recognize the research gap. The main problems explored from the present studies are highlighted in Section 3. The presented traffic-aware scheduling is detailed in Section 4 for resource allocation and secure slicing (T-S³RA) architecture along with its essential algorithms. The proposed architecture is compared in Section 5 with former methods in terms of the experimental results. Finally, our contributions are summarized in Section 6 while outlining future improvements.

2. RELATED WORK

2.1 Secure Network Slicing

Multiple users are allowed to reach a single network followed by authentication through secure slicing. Moreover, users' performances on the slice are assessed by verification of attributes like the strength of passwords and the existence of malware [23]. In the study of Wang et al. [24], mitigation of DoS attacks in an SDN was focused on through switch bandwidth congestion prediction. Specifically, a complete judgment score was determined for each switch representing attack severity. Through trust values, multiple buffer queues the priority can be managed by the manager considering various users' priorities. A weighted round-robin algorithm was used to schedule flow requests from users. The compromises by DoS attackers are estimated. Through authentication of the users, attack prevention is achieved. Thus, attackers are easily eliminated before overloading the controller.

The VIKOR multicriteria decision-making approach was proposed by Porambage et al. [25] for network slicing within a 5G environment to find node significance (topology and

resource attributes) and thus rank the nodes. A candidate physical path is defined among the slice nodes, for maximizing the slice acceptance ratio. However, there is a major drawback in VIKOR namely, the marginal slice acceptance ratio, which should be higher for the high-priority traffic.

Accessing the slice by third-party application services, secure keying is made [26], which ensures consent from the monitored devices as well as security features for the keying outline. Hence, the security feature is demonstrated by establishing 5G services. The key distribution server initially creates the cryptographic keys. The ELGamal Cryptosystem was proposed for a key generation where two sets of keys are generated including private and public keys. The resources are made here for key generation.

2.2 Resource Allocation and Network Slicing

The optimal workload allocation was proposed by Ma et al. [27] for distributed 5G-based SDN/NFV networks. An end-to-end network slicing architecture was designed in this method for supporting several services like URLLC and eMBB. Moreover, through slicing the requests from clients in the integrated environment (edge computing, NFV, and SDN), the network operating cost is decreased. Network slicing was performed by Dawaliby et al. [28] in a large-scale Internet of Things (IoT) environment (long-range extensive area network). In this work, three slices of the network were segregated including the reliability and urgency-aware slice, best-effort slice, and reliability-aware slice. First, one-to-many matching (defined by the number of IoT devices allocated to the virtual slices) was used to implement cooperative slicing. Then, a one-to-one matching game was used to allocate the resources for each slice (inter-slice resource allocation). The higher processing time is used by the coalitional multigame theory resulting in higher computational complexity.

Packet-based data traffic scheduling was suggested to enhance resource assignment and sharing in 5G slice networks [29]. Two operations modes are utilized including dynamic sharing resource (DSR) and static sharing resource (SSR). The allocated capacity weight is determined to assign the resource for each slice and thus the allocated one. The fairness for resource distribution per slice is calculated in the final analysis. A global network controller is needed for operating massive types of slices like popular, sensitive, and heavy slices. The radio resource management (RRM) was investigated by Koutlia et al. [30] for multiple slice management. Using the RRM function here, the radio resources are divided and allocated. Slicing and allocation provisioning were proved by an interaction between the SD-RAN and eNB controller. The QoS requirements for real-time traffic are not met by a single controller while not suiting the complex application setups (Drone Control and AR/VR).

A slice management scheme was proposed by An et al. [31] to assign resources in terms of priority. In this scheme, forwarding high-priority slice requests is performed while transmitting the lower-priority slices and shortest paths to other paths. They used 200 nodes to perform the experiments. Through a grid network topology, the nodes were deployed. The average throughput for slices was more than 6%, 13%, and 7% in the final analysis while minimizing the delays of the slices by 11%–14%. The shortest path is used by the flow (high-priority) forwarding within the data plane although it is not available for all cases. Thus, it is essential to install the corresponding flow in the controller when there is no consistency between flow and a flow table. Hence, a bandwidth scarcity problem is a resultant for users under static resource assignment.

A network slice embedding model was presented by Tang et al. [7] in terms of reliability. The number of slice requests is increased by the model while reducing the failure rate of the network slices simultaneously. A Lyapunov optimization model was used in this

model to allocate resources and ensure queue stability. The network stability and reliability were guaranteed while effectively improving the network throughput. However, obtaining an abundance of network slices is difficult with lower interoperability between the SDN/NFV and 5G network.

Service function chaining is utilized for network slicing [32], in which a set of service function chains is included in each slice to deal with any traffic per slice. Then, the trade-offs between slicing and execution runtime are examined by designing a greedy-based heuristic algorithm. Ultimately, the required bandwidth and delay are obtained through an optimization model. The mobility of network slices is not taken into account, which reduces the QoS and QoE.

A scheme was developed by Alfoudi et al. for network slicing resource management (NSRM) [33] for the allocation of resources for each slice within a network. An LTE network was considered in this work for various slice allocations and fair distribution of bandwidth among slices. Deploying the controller, all the slices are handled by the LTE slice controller for each slice. The radio network resources are assigned through the LTE slice controller by a virtual eNodeB. It is very difficult to dynamically provision the slice requests. For instance, large slice request handling is required by the Industry 4.0 application.

Narmanlioglu et al. conducted service-aware multi-resource allocation for cellular networks defined by software [34]. In this work, joint network allocation was demonstrated along with scheduling the available network resources for determining the network slices. Based on the SLA priorities and constraints, network resources are specifically provided. For each priority, the analytic hierarchy process (AHP) is utilized to calculate the resources (latency, throughput, reliability, and storage). Through experiments, they evaluated the method for vertical subscribers and industries cost-efficiently. The network slice capacity is the main factor to determine the needed resources. Though, AHP is not able to concurrently support multiple traffic flow resource allocation.

The vehicular ad hoc network environment was examined by a dynamic end-to-end slicing method supporting 5G communications [35]. Two kinds of slice services were examined including Video and Web. Resources were assigned for network slices in a single physical network infrastructure. In both the control and data planes, the handling of different services from numerous users is supported through virtualized network functionality customization. However, high throughput is not provided by this end-to-end method for limited latency service types.

Two eMBB and V2X services were examined by Albonda and Pérez-Romero [36]. They used two approaches of heuristic algorithm and reinforcement learning for resource allocation and network slicing for various slices. According to the simulation results, the latency is reduced by 0.18 s (by 0.26 s for a fixed slicing ratio). However, multiple traffic classes are not supported by this approach in each slice. Furthermore, latency can be further reduced by a global controller for each service type.

An optimal and quick response method is presented for resource slicing within heterogeneous cellular networks [37]. The real-time advent of slice requests is captured first by this technique through a semi-Markov decision procedure (deep double dueling) to predict the service resources and time. Through several experiments, the performance of the presented deep dueling method was demonstrated for resource slicing. Several challenges are caused by large and dynamic network slices in the control and data plane. Such challenges are addressed by presenting load balancing amongst multiple network service

chains. Hence, a novel concept was used (point of existence) to solve the scalability problem while accepting only limited slice users [38-40].

3. PROBLEM DEFINITION

Resource allocation and network slicing are run in SDN/NFV-based 5G networks based on the service requests of user devices [41-43]. Massive service requests from the user can be handled through a multiclass queuing and traffic analysis model. Low-complexity traffic predictors are employed utilizing a soft gated recurrent unit (GRU) to allocate the resources through deep neural networks (DNNs). Moreover, a multistage analysis is conducted for three various slices (URLLC, mMTC, and eMBB) to carry out M/M/n/K-based queuing.

These studies have the following limitations: first, they are oriented by the load, thus, non-real-time traffic for scheduling before real-time traffic is caused by the high response time for processing high-priority class packets. Second, based on a first-come-first-serve (FCFS) protocol, particular slices are scheduled thus further increasing the response time leading to poor QoS for received requests. Third, a single point of failure occurs in an SDN, when it is not possible to handle the requests from various users through a single controller. Fourth, the response time is incremented by running both DNN and GRU for more realistic and QoS-constrained traffic. Furthermore, a huge deal of energy and time is used by the DNN. Fifth, a random seek pattern is run by the FCFS since requests are not reordered by the slice for minimizing service delay. Besides, fair level SLA constraints are not used by the queuing theory. Since the service must be provided with an availability of 99.99%, ensuring service timeouts of less than 0.01% and completing the 99.99% of the services are essential within the resources. Additionally, resources are not distributed properly when utilizing FCFS for scheduling.

For embedded services, a dynamic flow migration was proposed under SDN/NFV-aided 5G networks to decrease the dynamic traffic load per slice [44]. To address this issue, a heuristic algorithm was used. This approach has the following drawbacks: (1) Adaptive flow migration is needed owing to the limited performance of the Poisson traffic model. (2) An optimal solution was required by the routing path for flow migration and in former approaches, delay-sensitive traffic cannot be run. (3) The heuristic algorithm is not able to present an optimal solution when arriving at an unexpected flow at the controller. In the present work, the above-mentioned problems are resolved through network slicing, dynamic offloading, resource allocation, security, as well as packet classification.

4. SYSTEM MODEL

To design the presented T-S³RA within an SDN/NFV-permitted 5G network, the mobile device authentication processing abilities were used along with network slicing, traffic scheduling, as well as dynamic offloading, and resource allocation.

4.1 Network Overview

Designing the T-S³RA model for resource allocation and secure network slicing included a global control plane, local control plane, user plane, and data plane. Some entities are contained in the suggested T-S³RA model such as tools ($d_1 \dots d_n$), VAP ($VA_1 \dots VA_n$), 5G APs ($AP_1 \dots AP_n$), controllers (GC), switches ($PS_1 \dots PS_n$ and $VS_1 \dots VS_n$) and some LCs ($LC_1 \dots LC_n$). The secure credentials are submitted in the devices to the 5G AP. Generally, there are limited components at the data and control planes based on the resources. Moreover, it is essential to use these resources for sending and receiving responses from

users as well as for action processing. The VA is removed when not needed. Hence, using the multi controllers resolves the single-controller-failure problem as a result of using both virtual and physical switches. Hence, the overload problem is solved.

In network slicing, more packet losses and delays are induced by massive traffic. Thus, slicing is performed while scheduling the traffic and allocating the resources through deep learning methods. Through dynamic offloading actions, imbalance issues are avoided. Via various credentials, these actions are kept in the data plane while considering the resource wastage problem. Hence, through entropy calculations, DDoS attackers are detected arriving at the switches.
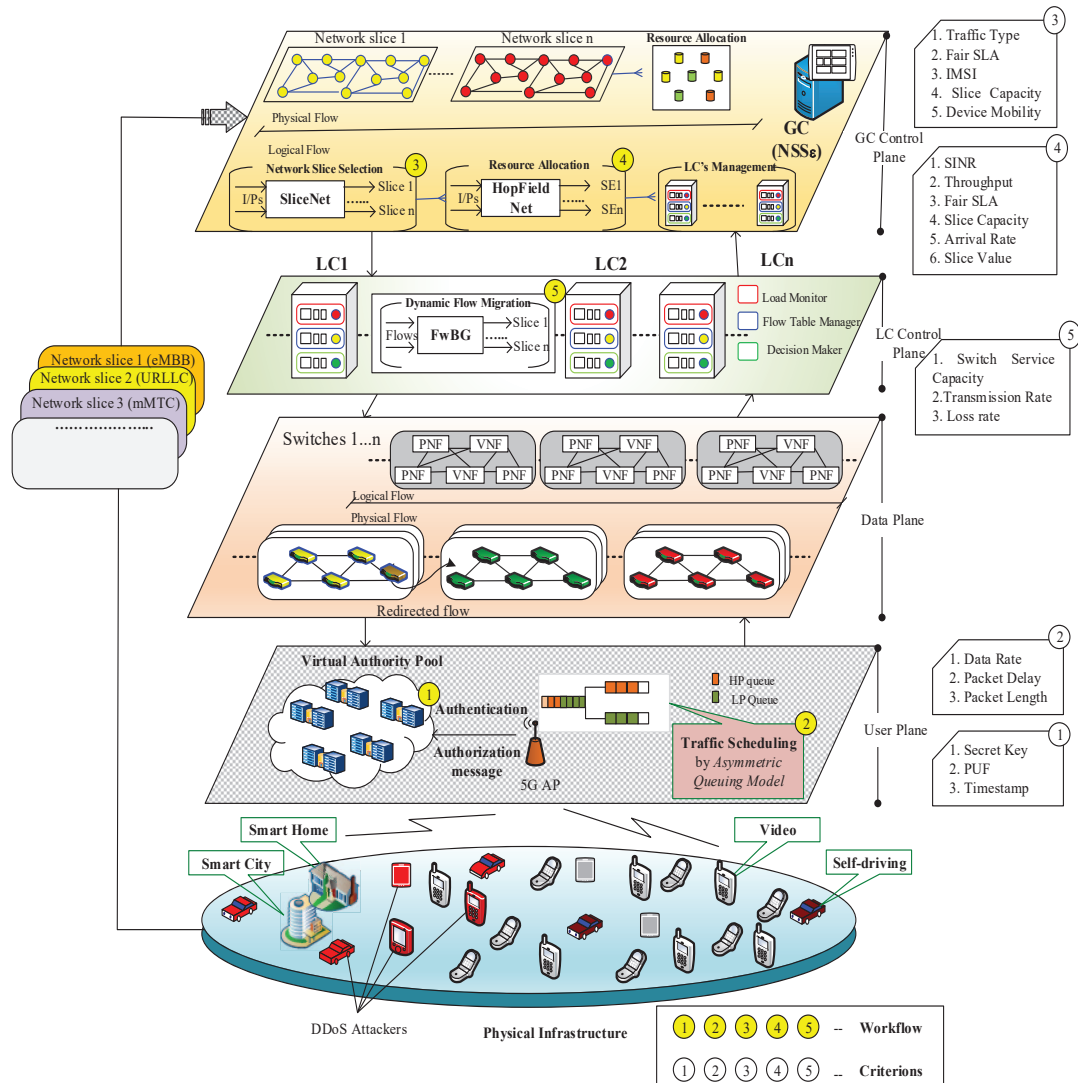
Fig. 1: The system architecture [1].

Figure 1 shows the proposed T-S^{3}RA architecture. The main network entities include: (1) All IoT tools with access to the network through the 5G communications network are known as the tools. Such devices are dynamic in movement and heterogeneous in nature. Higher coverage is required to connect them to the 5G AP. All tools are not approved, and unauthorized user participation is also possible. (2) 5G AP armed with higher communication coverage with a higher data rate, lower latency, and higher throughput. (3)

VAP is a pool comprising some virtual authorities but not a single entity. It is often denoted as a specific entity balancing the authentication process. The 5G AP handles the VA creation and deletion process. (4) Switches that are commonly used in the data plane and function by matching the incoming flow with the flow table thus performing the actions. (5) Controllers that are distributed and deployed within the control plane for resource allocation and network slicing. Multiple controllers are utilized in this work to prevent the problem of a single point of failure.

4.2 Device Authentication

The 5G AP audits each authority with a charge for inserting, deleting, and modifying the operations, in the VAP. The PBKDF2 is utilized for authentication using three input parameters including PUF $I?uf$, secret key ς_r, and Timestamp $\dagger$—. The request is accepted for the three valid parameters if not, it is not recognized and ended. The operations are conducted in the Boolean logic function.

PBKDF2 is a function based on the key made by RSA Labs overwhelming the brute force attacks resultant from weak user passwords. The following parameters are used to derive a PBKDF2: an iteration count, i_ς; a pseudorandom function, PRF; a password, pw_d; a salt, $\mathcal{Z}$; an output-derived secret key, ς_r, and a selected output key length, OK_l.

A ς_r of arbitrary length is driven by PBKDF2. In particular, by the PBKDF2, several possible blocks t_i are generated, required for covering the output secret key length. For PRF iteration, each block, t_i is calculated through the count, i_ς. Any number of iterations can be added for a large secret key length. The inputs are the user password in PBKDF2, pw_d l salt values, $\mathcal{Z}$; iteration count, i_ς; puf; timestamp, $\dagger$, and selected output key length, OK_l. A secret key, ς_r yields the output.

$$\varsigma_r = PBKDF2\,(pw_d, OK_l, \mathcal{Z}, i_\varsigma) \tag{1}$$

where ς_r denotes all security credentials' concatenation. Here, two processes of enrollment and verification handle the PUF-based authentication. In the enrollment, all response and challenge pairs of the device are stored by the VA, which is verified when entering a device into the network. The device ID is received by the verifier to determine the random *Challenges Response Pair*. The equivalent response is calculated for the issued challenge. The verifier examines the validity of the response in the database and the made response, ς_r is made for the valid cases.

Here, the Boolean logic operator is represented as o and stated as

$$o = \overline{(\dagger.puf)}.\overline{(\dagger + puf)}.\varsigma_r \tag{2}$$

4.3 Traffic Scheduling

Through traffic scheduling in the 5G AP, congestion was avoided at the SDN controller. Here, the devices' traffic flows are categorized and arranged through an asymmetric queue model operating in terms of Bernoulli's theorem [45,46]. Using three parameters, traffic flow was scheduled including packet delay $I?_d$, data rate τ_γ, and packet length ρ_l. Thus, the total queuing service rate is:

$$I_{-1} + I_{-2} = 1 \tag{3}$$

A zero-packet loss rate is obtained by focusing on the adaptive queue within the two queues. Therefore, HP's service rate of $\delta = 0.75$ was reached and exceeded, while the queue was still in process.

A discrete-time system was considered in this study to schedule services dynamically arriving for slicing requests. Regarding the type of slots and service, all arriving requests were diverse. A random variable $ɣ(T)$ was defined to represent the queue current state as:

$$ɣ(T) = \begin{cases} 0 & Queue\ is\ idle \\ i & Queue\ is\ busy\ with\ n\ services \\ l+1 & Queue\ is\ vacant \end{cases} \tag{4}$$

4.4 Resource Allocation and Network Slicing

The Network slice selection entities (NSS$^\epsilon$s) were fed in the GC to slice the network via SliceNet, which is a light and faster CNN outperforming WaveNet, traditional CNNs, and ByteNet.

Service Type $ṣ_t$, Fair SLA $ḟ_{SLA}$, Slice Capacity $\mathbb{S}_c$ $IMSI$, and Device mobility $d_\mathfrak{M}$ were all taken into account for slicing the network. This work primarily focused on SLA constraints between the service provider and user leading to $ḟ_{SLA}$ while slicing the network. Followed by the fairness (weight) for each service, RTR, SAR, TR, and SRR were calculated.

Forwarding a service request to the controller is performed through the 5G AP over network slicing for a tool. The presented SliceNet is sated as a mapping from the input layer to the output layer as:

$$y = f(ṣ_t, ḟ_{SLA}, IMSI, \mathbb{S}_c, d_\mathfrak{M} \forall (d_i)), \tag{5}$$

In which d_i represents the tool i. The aforementioned parameters are inserted as inputs into the presented SliceNet where the input encoder, decoder, and I/O mixer, are the key components.

The input is obtained from the devices by a convolutional module in three stages of separable conv, ReLU activation, and the layer normalization. The hidden units are normalized and calculated layer-wise in the normalization. Generally, the conv_module is written as:

$$ConvStep\ (w, x) = LN(SepConv, (w, ReLU(X)), \tag{6}$$

Thus, the conv_module is achieved by stacking 4 convolutional phases:

$$h1(X) = Conv\_Step\ (w_{h1}^{3\times1}, X), \tag{7}$$

$$h2(X) = X + Conv\_Step\ (w_{h2}^{3\times1}, h1(X)), \tag{8}$$

$$h3(X) = Conv\_Step_{\ 1,1}(w_{h2}^{15\times1}, h2(X)), \tag{9}$$

$$h4(X) = X + Conv\_Step_{\ 1,1}(w_{h2}^{15\times1}, h3(X)), \tag{10}$$

$$Conv_{Module}(X) = \begin{cases} Dropout\ (h4(X), 0.5) & Training \\ h4(X) & Otherwise \end{cases} \tag{11}$$

where $h\ (1\ldots n)\ (X)$ represents the number of hidden units, and 0.5 is the learning rate.

The service requirements and input feature vector similarities are calculated based on the service type. Two convolution steps are conducted by the *Softmax* function in this module:

$$attention\ 1(X) = ConvStep_{1,1}(w_{a1}^{5 \times 1} X + Time),$$ (12)

$$attention\ (Sr, Ta) = Attend\ (Sr, Ta, Convstep_{4,1}(w_{a1}^{5 \times 1}, attention\ 1(Ta)))$$ (13)

Ultimately, the three components' structure was detailed including I/O mixer, input encoder, and decoder. The concatenation of all the aforementioned components makes the output embedding as:

$$Mix_i = I/O\ (m)[I_e\ (i), O_e(o)],$$ (14)

$$Outputs = Decoder\ (mix)$$ (15)

Ultimately, $y = (y(1), y(2), \dots y(n))$ is obtained in the output layer, which $y(i) = 0,1$ is determined as the slice selection indicator. Thus, y denotes three kinds of services including eMBB, mMTC, and URLLC with different resource configurations. Hence, each service type is represented $S_j = 1 \dots n$ accompanied by the specified network slice. To run resource allocation, HopFieldNet is used as a quick neural network to find the resource for each slice. Considering $SINR$, $Throughput$, f_{SLA}, S_c, arrival rate A_r, and slice value s_v, the resources were determined for each slice request. Here, the resources are assigned for three various processes including computation, communication, and caching as c_j, c_i and c_k respectively.

HopFieldNet is an artificial neural network (ANN) comprising nodes on a single layer. The input nodes in HopFieldNet are synchronously updated in terms of clock time variations. Here, there are the contributing nodes with the connectivity in terms of the defined weight values. The outcomes from network slices are used by HopFieldNet as input to compute the resources for the three groups of slices as URLLC, mMTC, and eMBB. The performance of input loops intended in this network is based on the capability of enriching knowledge, which is operative to resolve complicated computational problems. Designing HopFieldNet with a single layer of input nodes linked to other nodes as feedback connections, redirection of the output to the input is assisted. Here, there is an equal number of inputs, nodes, and outputs, in this T-S³RA system, and totally R_1, R_2, R_3……,R_N nodes are made by resources.

The received input weight value is strong-minded from the separate slice service necessities stated in terms of the weight values in the connection as well as the node's state. The weighted summation of the nodes U is:

$$U_i = \sum_{j=1}^{N} we_{ij} st_j,$$ (16)

where we_{ij} denotes the connectivity weight between i and j, and st_j 10ft he state 10ft he node j. To control the training in HopFieldNet, the Storkey learning rule is used for minimizing the errors well. The Storkey learning rule is mathematically formulated as:

$$we_{ij}^0 = 0 \quad \forall\ i, j,$$ (17)

$$we_{ij}^k = we_{ij}^{k-1} + \frac{1}{N} I_{-i}^k I_{-j}^k - \frac{1}{N} I_{-i}^k h_{ji}^k - \frac{1}{N} h_{ij}^k I_{-j}^k$$ (18)

The weight estimated between i and j is represented by w_{ij}^{ek} in (17) and (18) only after learning the kth pattern, while ξ^k represents the new knowledge pattern. The local field H_{ij}^k is:

$$H_{ij}^k = \sum_{n=1, n \neq i, j}^{N} we_{in}^{k-1} I_{-n}^{\ k}, \tag{19}$$

Premeditating the HopFieldNet, the resources are categorized in terms of the slice service requirements.

As seen in Fig. 5, for categorizing the available resource blocks from the slices, the HopFieldNet with a single layer is $\{x_1, x_2, ...x_i...x_N\}$ and the equivalent outputs are $\{Y_1, Y_2, Y_3, ...Y_i...Y_N\}$. The inputs are received from all NS defined as $\{R_1, R_2, R_3......,R_N\}$. For each separate NS, the output in HopFieldNet is attained.

The advantage of HopFieldNet is its process for associative memory to store part of the information and allocate the rest of the pattern. Recalling the former patterns, using prior information of the resource amount is enabled for each NS. The resource is classified into 3 states. In the suggested T-S^{3}RA, the states of the nodes are estimated as:

$$St = \begin{pmatrix} s_{t1} & s_{t2} & \cdots & s_{ti} & \cdots & s_{tN} \end{pmatrix} \tag{20}$$

For each node, the states st are formulated in a trained matrix, where the three groups, c_i, c_j and c_k are the possible states for the resource. The node st_i state is defined as:

$$st_i = sign(U_i - THRES_N), \tag{21}$$

in which $THRES_N$ represents the threshold, $sign(x) = 1 \forall X \geq 0$, and $sign(x) = -1 \forall X < 0$. No node is related to itself as in this network and all nodes need to follow $w(e) = w(e)$. Thus, the node connectivity weights are stated as:

$$WE = \begin{pmatrix} 0 & w(e)_{12} & \cdots & w(e)_{1i} & \cdots & w(e)_{1N} \\ w(e)_{21} & 0 & , \cdots & w(e)_{2i} & \cdots & w(e)_{2N} \\ \vdots & \vdots & \ddots & \vdots & \cdots & \vdots \\ w(e)_{i1} & w(e)_{i2} & \cdots & 0 & \cdots & w(e)_{iN} \\ & & & \cdots & \ddots & \vdots \\ w(e)_{N1} & w(e)_{N2} & \cdots & w(e)_{Ni} & \cdots & 0 \end{pmatrix} \tag{22}$$

For each node, the threshold $THRES_i$ is presented based on its service requirements. The threshold for the nodes is presented in matrix format as:

$$THRES_N = \begin{pmatrix} \theta_1 \\ \theta_2 \\ \vdots \\ \theta_i \\ \vdots \\ \theta_N \end{pmatrix} \tag{23}$$

where $\{\theta_1, \theta_2, ...\theta_N\}$ represent the separate threshold values for each node. The threshold can be varied considering the existence of the slice requests in each NS. The threshold is updated when a new slice request is included in the device or user. Using the class of the resources at the NS is recognized followed by finding the resources for the NS. Then, the individual NS payment status is confirmed to exactly predict the use of the load by the NS.

4.5 Dynamic Flow Offloading

A higher traffic volume of slices is resultant from an inadequate bandwidth for switches. Comprised $F\omega BG$ is used in terms of the transmission rate, switch service capacity, and loss rate. By $F\omega BG$, multiple flows are mapped to the optimal switches increasing the network reputation. Furthermore, $F\omega BG$ helps to prevent slice capacity problems.

5.   RESULTS AND DISCUSSION

5.1 Simulation Setup

To evaluate the proposed T-S³RA model, the network simulator tool V.NS3.26 was used, which can incorporate the technologies and network modules needed to simulate a network properly. The network simulator was mounted on a system with a 32-bit dual-core processor, the Ubuntu 14.04 LTS OS, and 2 GB of RAM. Table 1 presents the simulation parameters for designing the testbed.

Figure 2 represents the suggested T-S³RA architecture model simulation results. The proposed system with various planes is explained based on the simulation steps, as shown above.
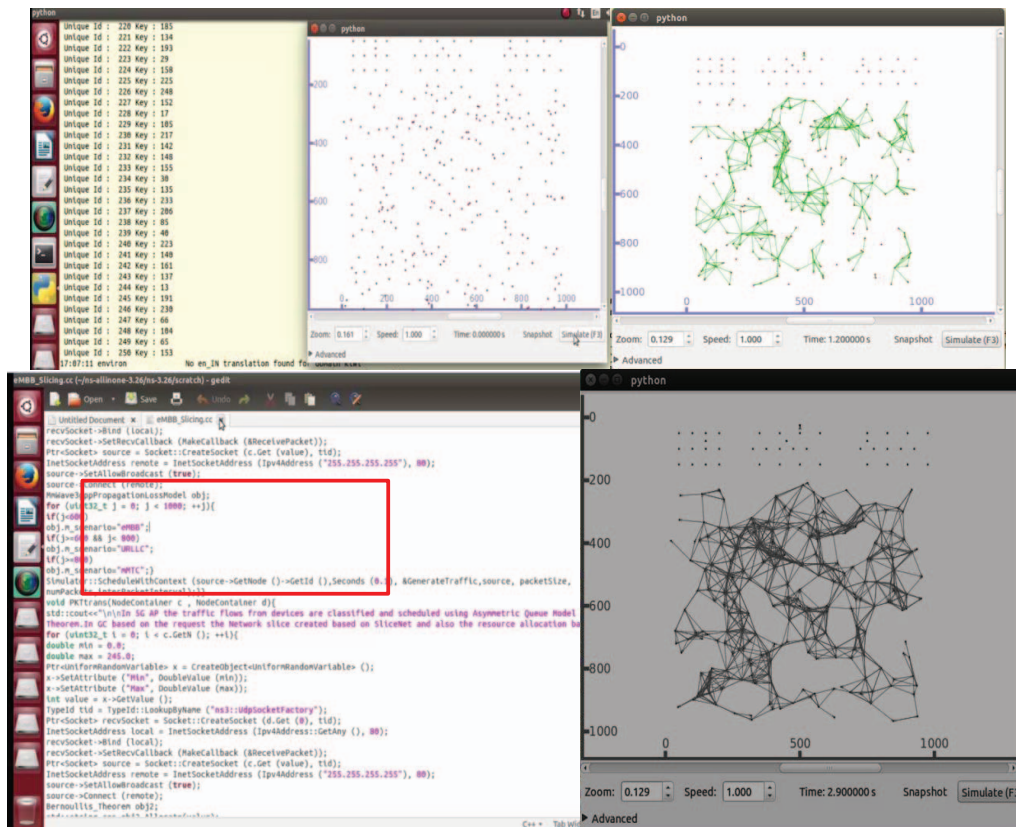
Fig. 2: The Simulation results for key generation, network slicing, and node deployment.

5.2 Comparative Analysis

In this comparative analysis section, the efficiencies of the proposed T-S³RA *are* evaluated based on the methods assessed previously. To compare with the proposed system, some significant metrics are taken into account. To illustrate the performance of former resource allocation and network slicing schemes, the present approaches concentrate on dynamic flow migration (load balancing), resource allocation, or network slicing during network slicing. Thus, the present work focusing on all three procedures accompanied by security helps to avoid resource wastage in the control planes and data. A comparison was made on the performances of T-S³RA for three slices, URLLC, mMTC, and eMBB represented as S1, S2, and S3 respectively.

5.2.1 Effect on Throughput

The throughput performance is demonstrated in Fig. 3 based on the number of slice requests. As seen, the network's throughput possesses greater values in the presented T-S^3RA than the GRU-DNN [42].
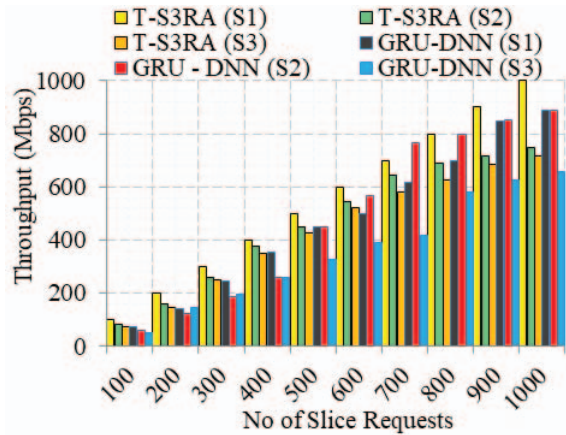
Fig. 3: The throughput against the number of slice requests.

5.2.2 Effect on Latency

Figure 4 shows the comparison of latency performance. A lower latency was obtained by the presented T-S^3RA since it utilizes fast algorithms as well as effective resource allocation and network slicing. More time is required to calculate the hyperparameters and tuning required for the DNN.
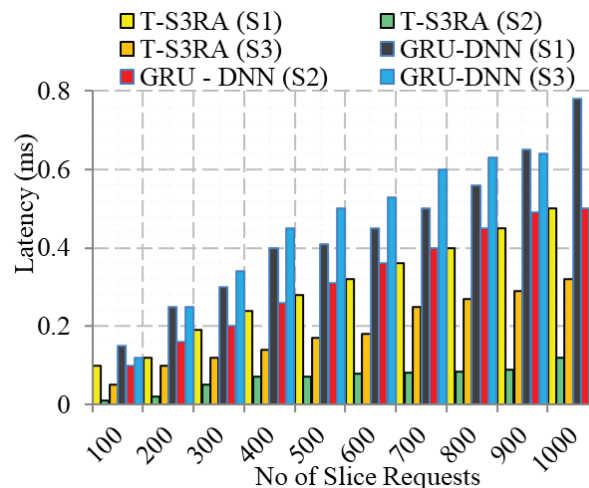
Fig. 4: The latency against the number of slice requests.

5.2.3 Effects on Response Time

According to Fig. 5, the response time performance is improved, by minimizing the latency. The results of the response time comparison are presented in Fig. 5. A considerably small response time was obtained since T-S^3RA is effective and end-to-end secure. An effective algorithm was not used in the present work.
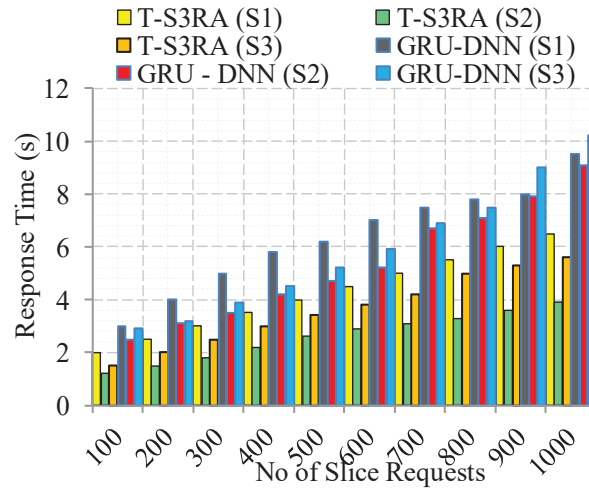
Fig. 5: The response time and the number of slice requests.

5.2.4 Effects on Transmission Ratio

Utilizing the asymmetric queue model, the traffic is arranged at the 5G AP increasing the packet transmission ratio. Moreover, for all slice requests, resources are optimally allocated resulting in a higher packet transmission ratio. The highest packet transmission ratio was obtained for S2 since highly reliable responses are required by these services.

5.2.5 Effects on Packet Loss Ratio

To assess the packet loss performance, the number of devices is considered. According to Fig.11, the packet loss is lower in the considered T-S^{3}RA than in the GRU-DNN.
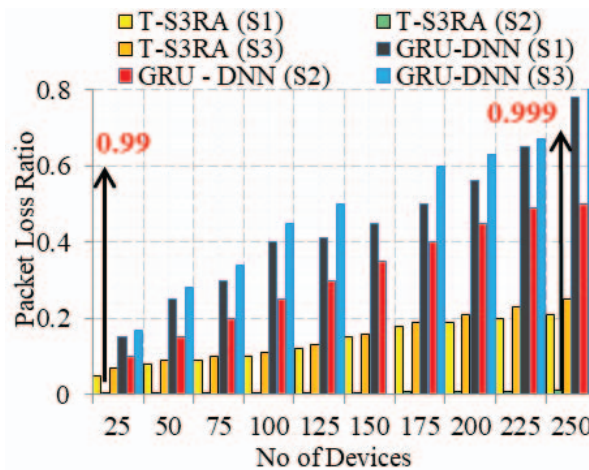
Fig. 6: The packet loss ratio versus the number of devices.

5.2.6 Effects on Slice Capacity

The comparison of the slice capacity vs. the number of devices is presented in Fig. 7. Based on the analysis of slice capacity, high performance is obtained by the proposed T-S^{3}RA.
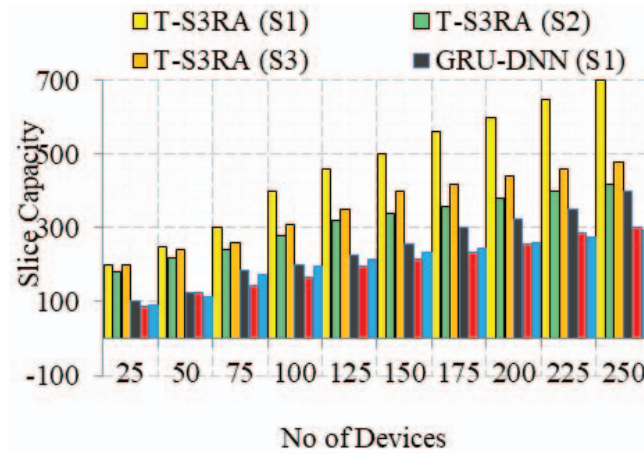
Fig. 7: The slice capacity against the number of devices.

5.2.7 Effects on Bandwidth Consumption

The bandwidth consumptions of the estimated and present outlines are presented in Fig. 8. Traffic offloading along with a multi-controller environment is used by the presented scheme, hence, the lower bandwidth is consumed. However, the higher bandwidth is used for GRU-DNN since there are no single controller problems and massive traffic handling.
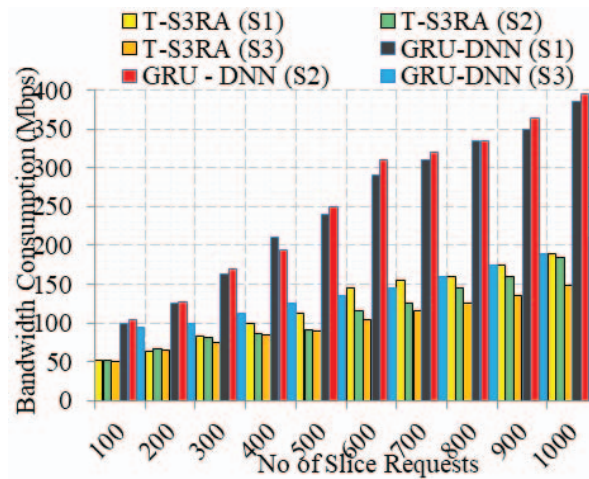
Fig. 8: The bandwidth consumption versus the number of slices.

5.2.8 Effect on Slice Acceptance Ratio

The acceptance ratios of the slice of T-S^{3}RA and GRU-DNN are compared in Fig. 9. Using deep learning-based resource allocation and network slicing can result in a considerably higher slice acceptance ratio. In the former study, the best solution was not obtained using deep learning methods. Therefore, there were poor slice acceptance ratios. Particularly, limited parameters were considered by the problem for slice selection.

Therefore, better efficiency is obtained by the presented T-S^{3}RA compared to the GRU-DNN for all network slices. Moreover, security is ensured by the presented T-S^{3}RA while performing resource allocation and slicing the network.
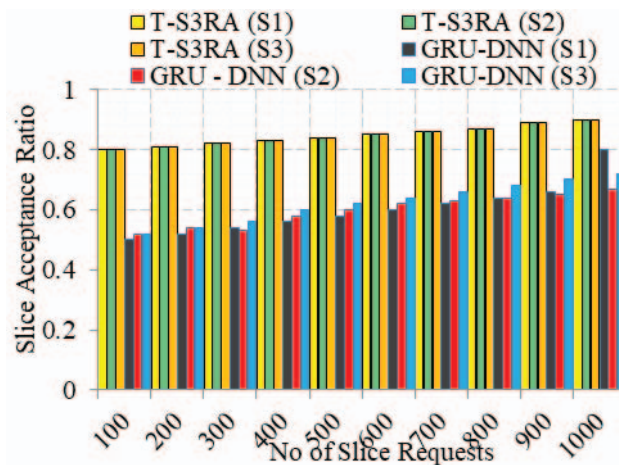
Fig. 9: The slice acceptance ratio against the number of slice requests.

5. CONCLUSION

In the present work, the QoS was enhanced in an SDN/NFV-permitted 5G network in terms of the presented architecture including T-S^{3}RA incorporating the service and SLA necessities for requests arriving from a user or device. There are four planes in the presented architecture including device, local controller, data, and global controller. The users or devices are authenticated through the VA via 5G AP utilizing PBKDF2. For secure communication, the VA is made and authenticated to the 5G AP reducing the communication overhead. Then, the traffic from the 5G AP is categorized into two HP and LP queues. It is held by the asymmetric queue model utilizing Bernoulli's theorem. Then, the HP request is forwarded to the LC for resource allocation and network slicing. SliceNet was proposed in this work for slicing, and resources were assigned utilizing HopFieldNet. Furthermore, to run dynamic flow offloading, $F\omega BG$ was used. To prevent packet dropping and enrich the QoS, the flows were matched with underloaded switches. Furthermore, DDoS attackers were eliminated from the network through packet arrangement utilizing Renyi entropy. Ultimately, the system's performance was assessed in terms of QoS metrics like throughput, latency, response time, packet loss ratio, packet transmission ratio, bandwidth consumption, slice capacity, as well as slice acceptance ratio.

REFERENCES

[1] Ramadhan AJ. (2021) T-S3RA: Traffic-aware scheduling for secure slicing and resource allocation in SDN/NFV Enabled 5G Networks. Int J of Eng Trend and Tech, 69: 215-232. https://doi.org/10.14445/22315381/IJETT-V69I7P229

[2] Barakabitze AA, Ahmad A, Mijumbi R, Hines A. (2020) 5G network slicing using SDN and NFV: A survey of taxonomy, architectures and future challenges. Comput Netw, 167: 106984. https://doi.org/10.1016/j.comnet.2019.106984

[3] Barmpounakis S, Maroulis N, Papadakis M, Tsiatsios G, Soukaras D, Alonistioti N. (2020) Network slicing-enabled RAN management for 5G: Cross layer control based on SDN and SDR. Comput Netw, 166: 106987. https://doi.org/10.1016/j.comnet.2019.106987

[4] Ramadhan AJ. (2020) Smart glasshouse system supported by global system for mobile communications and internet of THINGS: CASE STUDY: TOMATO PLANT. J of Eng Sci and Tech. 15: 3067–3081.

[5]   Borylo P, Tornatore M, Jaglarz P, Shahriar N, Chołda P, Boutaba R (2020) Latency and energy-aware provisioning of network slices in cloud networks. Comput Commun, 157: 1-19. https://doi.org/10.1016/j.comcom.2020.03.050

[6]   Boutigny F, Betgé-Brezetz S, Blanc G, Lavignotte A, Debar H, Jmila H (2020) Solving security constraints for 5G slice embedding: A proof-of-concept. Comput Sec, 89: 101662. https://doi.org/10.1016/j.cose.2019.101662

[7]   Tang L, Zhao G, Wang C, Zhao P, Chen Q (2018) Queue-aware reliable embedding algorithm for 5G network slicing. Comput Netw, 146:138-150. https://doi.org/10.1016/j.comnet.2018.09.014

[8]   Kim Y, Kim S, Lim H (2019) Reinforcement learning based resource management for network slicing. Appl Sci, 9:2361. https://doi.org/10.3390/app9112361

[9]   Raza MR, Natalino C, Öhlen P, Wosinska L, Monti P. (2019) Reinforcement learning for slicing in a 5G flexible RAN. J Lightwave Technol, 37: 5161-5169. https://doi.org/10.1109/JLT.2019.2924345

[10] Sun G, Xiong K, Boateng GO, Liu G, Jiang W. (2020) Resource slicing and customization in RAN with dueling deep Q-Network. J Network Comput Appl, 157: 102573. https://doi.org/10.1016/j.jnca.2020.102573

[11] Ma T, Zhang Y, Wang F, Wang D, Guo D. (2020) Slicing resource allocation for eMBB and URLLC in 5G RAN. Wirel Commun Mob Comput, 2020: 1-11. https://doi.org/10.1155/2020/6290375

[12] Coronado E, Khan SN, Riggio R. (2019) 5G-EmPOWER: A software-defined networking platform for 5G radio access networks. IEEE Trans Netw Serv Manage, IEEE 16: 715-728. https://doi.org/10.1109/TNSM.2019.2908675

[13] Sathi VN, Srinivasan M, Thiruvasagam PK, Murthy SR (January 2020) Novel protocols to mitigate network slice topology learning attacks and protect privacy of users' service access behavior in softwarized 5G networks. IEEE Trans Depend Sec Comput, 1. https://doi.org/10.1109/TDSC.2020.2968885

[14] Thantharate A, Paropkari R, Walunj V, Beard C, Kankariya P. (2020) Secure5G: A deep learning framework towards a secure network slicing in 5G and beyond. Proceedings of the 10th annual computing and communication workshop and Conference (CCWC), 72020:0852

[15] Ni J, Lin X, Shen XS. (2018) Efficient and secure service-oriented authentication supporting network slicing for 5G-enabled IoT. IEEE J Select Areas Commun, 36: 644-657. https://doi.org/10.1109/JSAC.2018.2815418

[16] Afolabi I, Taleb T, Samdanis K, Ksentini A, Flinck H. (2018) Network slicing and softwarization: A survey on principles, enabling technologies, and solutions. IEEE Commun Surv Tutorials, 20: 2429-2453. https://doi.org/10.1109/COMST.2018.2815638

[17] Khan S, Khattak HA, Almogren A, Shah MA, Ud Din I, Alkhalifa I, Guizani M. (2020) 5G vehicular network resource management for improving radio access through machine learning. IEEE Access, 8: 6792-6800. https://doi.org/10.1109/ACCESS.2020.2964697

[18] Ye Q, Zhuang W, Zhang S, Jin AL, Shen X, Li X. (2018) Dynamic radio resource slicing for a two-tier heterogeneous wireless network. IEEE Trans Veh Technol, 67: 9896-9910. https://doi.org/10.1109/TVT.2018.2859740

[19] Le LV, Lin BSP, Tung LP, Sinh D. (2018) SDN/NFV, machine learning, and big data driven network slicing for 5G. Proc IEEE. World Forum (5GWF) 5g: 20-25.

[20] Costanzo S, Fajjari I, Aitsaadi N, Langar R. (2018) Dynamic network slicing for 5G IoT and eMBB services: A new design with prototype and implementation results. Proceedings of the 3rd Cloudification of the Internet of Things (CIoT), 2018: 1-7.

[21] Kammoun A, Tabbane N, Diaz G, Dandoush A, Achir N. (2018) End-to-end efficient heuristic algorithm for 5G network slicing. Proceedings of the 2018 IEEE 32nd international conference on Advanced Information Networking and Applications (AINA), pp 386-392

[22] Trivisonno R, Condoluci M, An X, Mahmoodi T. (2018) mIoT slice for 5G systems: Design and performance evaluation. Sensors (Basel), 18: 635. https://doi.org/10.3390/s18020635

[23] Šeremet I, Čaušević S. (2019) Benefits of using 5G network slicing to implement vehicle-to-everything (V2X) technology. Proceedings of the 2019 IEEE 18th international symposium Infoteh-Jahorina (INFOTEH), pp 1-6

[24] Wang T, Guo Z, Chen H, Liu W. (2018) BWManager: Mitigating denial of service attacks in software-defined networks through bandwidth prediction. IEEE Trans Netw Serv Manage, 15: 1235-1248. https://doi.org/10.1109/TNSM.2018.2873639

[25] Porambage P, Miche Y, Kalliola A, Liyanage M, Ylianttila M. (2019) Secure keying scheme for network slicing in 5G architecture. Proceedings of the 2019 IEEE conference on standards for communications and networking (CSCN), pp. 1-6

[26] Li X, Guo C, Gupta L, Jain R. (2019) Efficient and secure 5G core network slice provisioning based on VIKOR approach. IEEE Access 7: 150517-150529. https://doi.org/10.1109/ACCESS.2019.2947454

[27] Ma L, Wen X, Wang L, Lu Z, Knopp R. (2018) An SDN/NFV based framework for management and deployment of service based 5G core network. China Commun, 15: 86-98. https://doi.org/10.1109/CC.2018.8485472

[28] Dawaliby S, Bradai A, Pousset Y. (2019) Distributed network slicing in large scale IoT based on coalitional multi-game theory. IEEE Trans Netw Serv Manage, 16: 1567-1580. https://doi.org/10.1109/TNSM.2019.2945254

[29] AlQahtani SA. (2020) An efficient resource allocation to improve QoS of 5G slicing networks using general processor sharing-based scheduling algorithm. Int J Commun Syst, 33:e4250. https://doi.org/10.1002/dac.4250

[30] Koutlia K, Ferrús R, Coronado E, Riggio R, Casadevall F, Umbert A, Pérez-Romero J. (2019) Design and experimental validation of a software-defined radio access network testbed with slicing support. Wirel Commun Mob Comput 2019:1-17. https://doi.org/10.1155/2019/2361352

[31] An N, Kim Y, Park J, Kwon DH, Lim H. (2019) Slice management for quality of service differentiation in wireless network slicing. Sensors, 19: 2745. https://doi.org/10.3390/s19122745

[32] Addad RA, Bagaa M, Taleb T, Dutra DLC, Flinck H. (2019) Optimization model for cross-domain network slices in 5G networks. IEEE Trans on Mobile Comput, 19: 1156-1169. https://doi.org/10.1109/TMC.2019.2905599

[33] Alfoudi ASD, Newaz SHS, Otebolaku A, Lee GM, Pereira R. (2019) An efficient resource management mechanism for network slicing in a LTE network. IEEE Access, 7:89441-89457. https://doi.org/10.1109/ACCESS.2019.2926446

[34] Narmanlioglu O, Zeydan E, Arslan SS. (2018) Service-aware multi-resource allocation in software-defined next generation cellular networks. IEEE Access, 6: 20348–20363. https://doi.org/10.1109/ACCESS.2018.2818751

[35] Afaq M, Iqbal J, Ahmed T, Ul Islam I, Khan M, Khan MS. (2020) Towards 5G network slicing for vehicular ad-hoc networks: An end-to-end approach. Comput Commun, 149: 252-258. https://doi.org/10.1016/j.comcom.2019.10.018

[36] Albonda HDR, Pérez-Romero J (2019) An efficient RAN slicing strategy for a heterogeneous network with eMBB and V2X services. IEEE Access, 7: 44771-44782. https://doi.org/10.1109/ACCESS.2019.2908306

[37] Van Huynh N, Hoang DT, Nguyen DN, Dutkiewicz E. (2019) Optimal and fast real-time resource slicing with deep dueling neural networks. IEEE J Sel Areas Commun, 37: 1455-1470.

[38] Aicardi M, Bruschi R, Davoli F, Lago P, Pajo JF. (2018) Decentralized scalable dynamic load balancing among virtual network slice instantiations. Proceedings of IEEE Globecom Workshops (GC Wkshps):1-7.

[39] Zubov D, Kose U, Ramadhan A.J, Kupin A. (2018) Mesh network of eHealth intelligent agents in smart city: A case study on assistive devices for visually impaired people. CEUR W Proce 2255: 65–81.

[40] Chahlaoui F, El-Fenni MR, Dahmouni H. (2019) Performance analysis of load balancing mechanisms in SDN networks. Proceedings of the 2nd International Conference on Networking. Inf Syst Sec:1–8.

[41] Kamath S, Singh S, Kumar MS. (2019) Multiclass queueing network modeling and traffic flow analysis for SDN-enabled mobile core networks with network slicing. IEEE Access, 8: 417-430. https://doi.org/10.1109/ACCESS.2019.2959351

[42] Chergui H, Verikoukis C. (2019) Offline SLA-constrained deep learning for 5G networks reliable and dynamic end-to-end slicing. IEEE J Select Areas Commun, 38: 350-360. https://doi.org/10.1109/JSAC.2019.2959186

[43] AlQahtani SA, Alhomiqani WA. (2020) A multi-stage analysis of network slicing architecture for 5G mobile networks. Telecommun Syst, 73: 205–221. https://doi.org/10.1007/s11235-019-00607-2

[44] Qu K, Zhuang W, Ye Q, Shen X, Li X, Rao J. (2020) Dynamic flow migration for embedded services in SDN/NFV-enabled 5G core networks. IEEE Trans Commun, 68: 2394-2408. https://doi.org/10.1109/TCOMM.2020.2968907

[45] Park K, Li J, Feng SC. (2018) Scheduling policies in flexible Bernoulli lines with dedicated finite buffers. J Manuf Syst, 48: 33-48. https://doi.org/10.1016/j.jmsy.2018.05.013

[46] Md. Zaki FAMMd, Chin TS. (2019) FWFS: Selecting robust features towards reliable and stable traffic classifier in SDN. IEEE Access, 7: 166011-166020. https://doi.org/10.1109/ACCESS.2019.2953565

THE DEVELOPMENT OF WATER POLLUTION DETECTOR USING CONDUCTIVITY AND TURBIDITY PRINCIPLES

Nurulhasanah Amir Hamzah Maju[1], Hasmah Mansor[1*], Teddy Surya Gunawan[1] and Robiah Ahmad[2]

[1]*Department of Electrical and Computer Engineering, International Islamic University Malaysia, PO Box 10, 50728 Kuala Lumpur, Malaysia.*
[2]*Razak Faculty of Technology and Informatic, Universiti Teknologi Malaysia, Jalan Sultan Yahya Petra, 54100 Kuala Lumpur, Malaysia.*

[*]Corresponding author: hasmahm@iium.edu.my

ABSTRACT: Water pollution has caused negative impacts on human health as humans depend solely on water for drinking, cooking, and cleaning. Even more worrying is that the number of polluted rivers seems to increase as time progresses. Due to no real-time monitoring device being implemented, the authorities are unaware of any given river's real-time conditions. Therefore, this research aims to control the water pollution issue by designing and developing a low-cost device that can detect water pollutants and notifies the authorities if abnormalities occur. In this work, various water pollution sources in Malaysia have been identified: biochemical oxygen demand, ammoniacal nitrogen, and suspended solids. The general performance of the proposed device is also evaluated and analyzed. Water quality data is collected by the sensors and is sent to an IoT platform called ThingSpeak through a Wi-Fi module to be visualized and displayed. When the pollution is detected, the website will alert local authorities for their prompt actions. From the experiment conducted, the developed conductivity sensor managed to give readings with 6.84% and 6.35% error compared to the sensor in a benchmark paper and the ready-made sensor, respectively. Besides, the turbidity sensor also managed to give accurate readings according to various types of solution. The success of this research would help to reduce river pollution and provide positive outcomes to the environment.

ABSTRAK: Pencemaran air telah menyebabkan kesan negatif terhadap kesihatan manusia kerana kebergantungan mereka terhadap air untuk minum, memasak dan mencuci. Lebih membimbangkan adalah, jumlah sungai tercemar yang semakin meningkat seiring tahun-tahun yang berlalu. Oleh kerana tiada alat pemantauan masa nyata yang dilaksanakan, pihak berkuasa tidak menyedari keadaan semasa air sungai. Oleh itu, projek ini bertujuan bagi mengawal masalah pencemaran air dengan merancang dan menghasilkan alat kos rendah yang dapat mengesan pencemaran air dan memberitahu pihak berkuasa sekiranya berlaku bacaan yang tidak normal. Melalui kajian ini, pelbagai sumber pencemaran air di Malaysia telah dikenal pasti: permintaan oksigen biokimia, nitrogen amonia dan pepejal terampai. Prestasi umum alat ini juga dinilai dan dianalisis. Kualiti data air dikumpulkan oleh pengimbas dan maklumat dihantar ke platform IoT yang disebut ThingSpeak melalui modul Wi-Fi bagi tujuan tinjauan dan paparan. Apabila pencemaran dikesan, laman web tersebut akan memberi amaran kepada pihak berkuasa tempatan untuk tindakan segera. Melalui eksperimen yang dijalankan, pengimbas kekonduksian yang dihasilkan berjaya memberikan bacaan dengan ralat 6.84% dan 6.35% berbanding pengimbas yang terdapat di kertas penanda aras dan pengimbas siap pakai. Selain itu, pengimbas kekeruhan yang digunakan mampu memberikan bacaan yang tepat mengikut pelbagai jenis larutan. Projek

ini diharap dapat membantu mengurangkan pencemaran sungai dan memberikan impak positif kepada alam sekitar.

1. INTRODUCTION

Due to rapid development and lack of awareness, water quality is compromised as water pollution increases day by day. This research is designed to detect water contaminants in real-time so as to notify the authorities once the pollution occurs. The sensors used to detect the contaminants are a conductivity sensor and a turbidity sensor. This is because these sensors can be used as substitutions to detect suspended solids (SS), ammoniacal nitrogen (NH_3N) and biochemical oxygen demand (BOD). These chemicals impact water bodies as highlighted by the Department of Environment in The Pollution Sources Inventory Report [1].

Water pollution can cause serious health issues to human beings such as typhoid fever and even deadly diseases like cholera [2]. The reason is that the contaminants or toxicants can enter the human's food chain as they eat the fish or animals infected by pollution.

On the other hand, in conjunction with the river pollution issue, the Department of Environment (DOE) conducted a river monitoring program. According to the Environment Quality Report 2017 [3], the percentage of clean rivers in Malaysia had slightly decreased from 47% to 46% in 2017. Unfortunately, the percentage of polluted rivers had somewhat increased from 10% to 11%.

In March 2019, the country had been stunted by the news of toxic dumping in Sungai Kim Kim (Kim Kim river), Pasir Gudang, Johor, Malaysia. The impact of toxic dumping caused breathing difficulties among students in a school near the river [4]. It is believed that early detection of toxins could reduce the aftermath of a dumping incident. This incident has proven the need to have a real-time river pollution detection that can alert the authorities immediately so that prompt actions can be taken to curb the spread of toxicants.

2. METHODOLOGY

This system consists of a self-developed conductivity sensor, SEN0189 turbidity sensor, Arduino UNO, ESP8266 Wi-Fi module and an IoT platform called ThingSpeak. By switching ON the switch, the LED will be turned ON and all of the system components will be activated. The block diagram of the overall system is shown in Fig. 1.
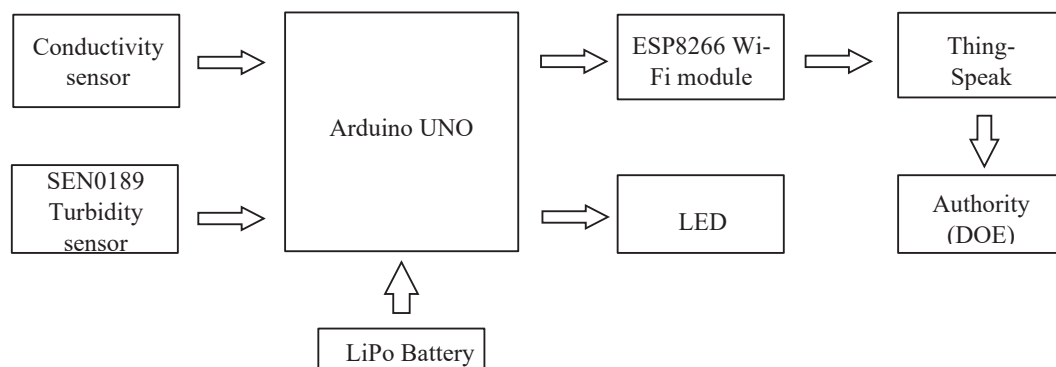
Fig. 1: The system's block diagram.

First, the system started with water quality data collection. The data collected by the conductivity and turbidity sensors are sent to ThingSpeak through the ESP8266 Wi-Fi module for further data aggregation. The Arduino UNO circuit board has been used as the interface between the ESP8266 Wi-Fi module and the sensors. A coding containing a unique API key is programmed into the microcontroller to send data to the IoT platform.

In ThingSpeak, the conductivity and turbidity data are processed, analyzed and visualized. All the necessary calculations and equations regarding the conductivity and turbidity are programmed into the Arduino UNO. Users can simply monitor the water quality through the website as the data are displayed in graphs and a numeric display. In the case of water pollution occurring, an email alert will be automatically sent to the user, which in this case is the Department of Environment (DOE). Considering the outdoor factors, the components are stored in a weatherproofed PVC box to avoid direct contact with the river water. The prototype is shown in Fig. 2. The schematic circuit diagram of this device can be seen in Fig. 3, and the actual system's circuit connection can be seen in Fig. 4.

Fig. 2: The system's prototype.

Fig. 3: The system's schematic circuit diagram.

Fig. 4: The actual circuit's connection.

2.1 The Design of the Conductivity Sensor

Water conductivity is the measure of the amount of electrical current that water can carry in the presence of dissolved solids such as chloride, magnesium, and calcium [5]. Conductivity can be used to detect the presence of the chemicals in the water. However, it is important to note that conductivity cannot identify the type of chemicals, only their presence. The amount of electrical conductivity allowed by DOE according to the National Water Quality Standards (NWQS) is below $6000\mu S/cm$. Rivers with only $1000\mu S/cm$ of conductivity readings are considered as clean rivers.

Water conductivity is commonly expressed in $\mu S/cm$, which is derived from Ohm's law where the voltage is equal to the product of current and resistance.

$$V = IR \tag{1}$$

V = Voltage (V)

I = Current (A)

R = Resistance (Ω)

Conductance is the reciprocal of resistance which can be seen in Eq. (2) The conductance can be measured in Mho (℧) which is the backward spelling for resistance's SI unit, Ohm (Ω). Another unit for conductance is Siemens (S). Both Mho and Siemens can be used interchangeably. In this work, Siemens is used.

$$G = \frac{1}{R} \tag{2}$$

G = Conductance (S)

By substituting the conductance into the Ohm's law equation, the relationship between voltage and conductance is as follows:

$$V = \frac{I}{G} \tag{3}$$

$$G = \frac{I}{V} \tag{4}$$

Next, to acquire the water conductivity value, a cell constant needs to be considered. This is because conductivity is influenced by the distance between the two electrodes and their surface area. The cell constant is defined as the ratio of the distance between the electrodes to their surface area. This is shown in Eq. (5) below.

$$K = \frac{D}{A} (cm^{-1}) \tag{5}$$

K = cell constant

D = distance between the electrodes

A = surface area of the electrodes

Finally, by multiplying the conductance with the cell constant, water conductivity can be obtained, as shown in Eq. (6)

$$\kappa = G \cdot K \ (Siemens/cm) \tag{6}$$

κ=Water conductivity

In this research, the conductivity sensor will collect the water conductivity data and later, the data will be sent to ThingSpeak. Generally, there are three types of conductivity sensors: two-electrode conductivity sensors, four-electrode conductivity sensors, and inductive conductivity sensors. In this work, a two-electrode method is used to design a conductivity sensor. The developed sensor is shown in Fig. 5.

Fig. 4: The developed conductivity sensor.

The sensor is designed using the calibration method by adjusting the distance between the electrodes. The calibration is done so that the results acquired satisfy the standard conductivity reading of tap water which is around $500-800 \ \mu S/cm$ [6]. The sensor is injected with pulse-width modulation (PWM) to mimic an alternating current (AC). This is to avoid the polarization effect. The electrodes used in this sensor are non-insulated copper plate electrodes. The plates are rectangular and have two pill-like shaped holes. The calculated surface area of the copper plates is 12.44 cm². Then, the distance between the copper plate is adjusted to 2 cm, 3 cm, 4 cm and 5 cm. Using the total surface area, the cell constant for each distance can be acquired using Eq. (5). The cell constants correspond to each distance as provided in section 3.1.

2.2 The Concept of Turbidity Sensor

Turbidity is the measure of haziness and cloudiness of water caused by Suspended Solid (SS) and measured in Nephelometric Turbidity Units (NTU). High turbidity can cause an increase in water temperature as the suspended particles absorb heat from the sunlight. The growth of aquatic plants rate is also obstructed as sunlight cannot penetrate through turbid water and this will eventually disturb the photosynthesis process. Following the NQWS, the turbidity level for clean rivers set by the DOE is around 50 NTU and below. According to the Environment Quality Report (EQR), turbidity can be used to indicate the SS [3].

The turbidity sensor in this research employs the orthogonal scattered light detection principle by measuring the light transmitted and scattered rate influenced by Total Suspended Solid (TSS). In this project, the reading obtained from the sensor is processed by the microcontroller, then sent to the cloud for further aggregation process. The SEN0189 turbidity sensor used is provided in Fig. 6.

Fig. 5: SEN0189 turbidity sensor.

This sensor operates at 5 V and a maximum current of 40 mA. By using analog input mode, the turbidity reading gained ranges from 0 to 1023. The Arduino UNO has a 10-bit analog-to-digital converter (ADC) which means it has resolution ranging from 0 to 1023 (2^{10} = 1024). Then, this read value is converted to a voltage using Eq. 7. The value of turbidity in NTU can be obtained from the voltage and turbidity relationship graph provided by DFRobot in Fig. 7. This was done using Eq. 8 obtained from the graph to convert it from voltage to NTU. The graph in Fig. 7 shows that the smaller the output voltage, the higher the turbidity reading.

$$V = read\ value \times \left(\frac{5.0}{1024.0}\right) \tag{7}$$

$$NTU = -1120.4V^2 + 5742.3V - 4352.9 \tag{8}$$
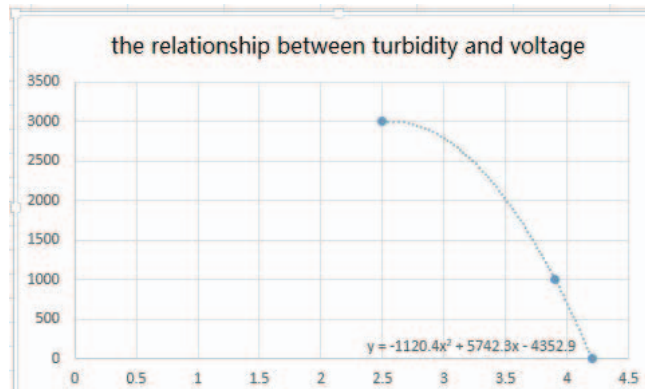
Fig. 6: Turbidity and voltage relationship graph.

2.3 The Component Cost

One of the aims of this research is to develop a water pollution detection system with affordable and minimal costs. Table 1 shows the cost for each item used in this research for the prototype. The total cost for the hardware is RM213.06, which is considered minimal. Other systems on the market could cost up to thousands of ringgits for similar functionality.

Table 1: Itemised prototype (hardware) cost

No.	Item	Quantity	Per Unit Cost (RM)	Total Cost Per Item (RM)
1	Arduino UNO ATmega328P	1	97.60	97.60
2	SEN0189 Turbidity Sensor	1	59.00	59.00
3	ESP8266 Wi-Fi Module	1	14.90	14.90
4	LiPo Battery (7.4 V 900 mAH)	1	20.00	20.00
5	Breadboard	1	2.70	2.70
6	Copper plates	2	2.50	5.00
7	Switch	1	1.50	1.50
8	LED	1	0.05	0.05
9	PVC Box	1	12.31	12.31
Total Cost				**213.06**

3. RESULTS AND DISCUSSION

3.1 Conductivity Sensor

The design of this sensor was done using the calibration method. The distance between the two plates was adjusted accordingly to obtain a conductivity value that satisfies the standard tap water conductivity reading. The standardized conductivity value for tap water is $500 - 800$ µS/cm [6]. The calculated cell constant, readings of current and voltage were recorded in Table 2.

Table 2: Calibration result

Distance [cm]	Current [mA]	Voltage [mV]	Cell constant, K [cm^{-1}]	Conductivity [µS/cm]
2	0.60	280	0.16	344.12
3	0.57	260	0.24	528.57
4	0.53	240	0.32	709.97
5	0.43	186	0.40	928.79

From the result, the 4 cm distance between the electrodes shows a conductivity reading within the range of $500 - 800$ µS/cm. Even though the conductivity reading for a 3 cm distance also falls within the same range, it is safer to choose the 4 cm distance. It can be observed that as the distance increased, the conductivity also increased. However, both voltage and current showed a decrease. This is because the farther the electrodes are from each other, the harder it is for the ions in the solution to travel because of the higher resistance. This results in a lower current flow.

Next, by employing [7] as the benchmark paper, the sensor was tested by dipping it in a 500 ml of water mixed with 2 g of salt. Nine readings were taken, and the results are recorded in Table 3.

Table 3: Conductivity result

No. of readings	Developed sensor [V]	Developed sensor in [7] [V]	Ready-made sensor [V]
1	1.74	1.81	1.90
2	1.75	1.94	1.90
3	1.77	1.87	1.91
4	1.76	1.85	1.91
5	1.80	1.90	1.85
6	1.76	1.90	1.85
7	1.77	1.93	1.89
8	1.77	1.94	1.89
9	1.78	1.94	1.89
Average	**1.77**	**1.90**	**1.89**

From the result obtained, it can be seen that the sensor developed in this research has an almost constant reading, in the range of 1.74 V to 1.80 V. The average voltage difference between the developed sensor in this research and the benchmark paper in only 6.84%. While the average voltage difference between the developed sensor and the ready-made sensor is 6.35%.

3.2 Turbidity Sensor

The turbidity readings were taken by inserting the probe into five different types of solutions: tap, salt, soap, river, and coffee. These solutions were chosen as all of them have different clarity. The river water was collected from the Pusu River near the Female Sports Centre (FSC), International Islamic University Malaysia (IIUM), Gombak campus. The readings were taken three times for each solution to ensure accurate measurements. Table 4 below shows the turbidity result for each solution.

Table 4: Turbidity result

Solution	Reading 1		Reading 2		Reading 3		Average	
	Voltage [V]	Turbidity [NTU]	Voltage [V]	Turbidity [NTU]	Voltage [V]	Turbidity [NTU]	Voltage [V]	Turbidity [NTU]
Tap	4.22	-68.28	4.22	-68.28	4.21	-50.19	4.22	-62.25
Salt	4.29	-346.10	4.30	-365.05	4.29	-346.10	4.29	-352.42
Soap	4.04	565.10	4.03	581.72	4.03	581.72	4.03	576.18
River	2.47	2995.28	2.48	2997.18	2.46	2992.02	2.47	2994.83
Coffee	3.98	755.48	3.99	724.34	3.97	770.96	3.98	750.27

The table shows that tap water has the lowest average turbidity of -62.25 NTU, while river water has the highest average turbidity of 2994.83 NTU. Even though coffee is the darkest solution, it only has an average turbidity of 750.27.

According to the World Health Organization (WHO), tap water is considered safe because the water should have turbidity below 5 NTU to be drinkable [8]. On the contrary, the Pusu River water shows the highest turbidity measurement, and it also exceeds the minimum safe level of turbidity in Malaysia [9], caused by high amount of silt. The high concentration of silt affects the light that penetrates through the liquid. This is because the turbidity sensor works by measuring the amount of light absorbed and scattered by the

suspended solids in the solution. The higher the number of total suspended solids (TSS), the higher the sensor's liquid turbidity.

It can also be observed from Table 4 that the higher the voltage, the lower the turbidity readings. High voltage means that the solution is less hazy because more light penetrates through the solution, resulting in higher voltage.

3.3 ThingSpeak as the IOT Platform

ThingSpeak is an open-source Internet of Things (IoT) platform that allows a user to perform data collection, data aggregation, and receive an email alert. Figure 8 shows the data visualizations of the collected sensors' data. The sampling time set at the coding is 1 second, however, for the reporting purposes, the ThingSpeak platform is 5 minutes. The sampling time and display can be set according to the specifications required by the authority.
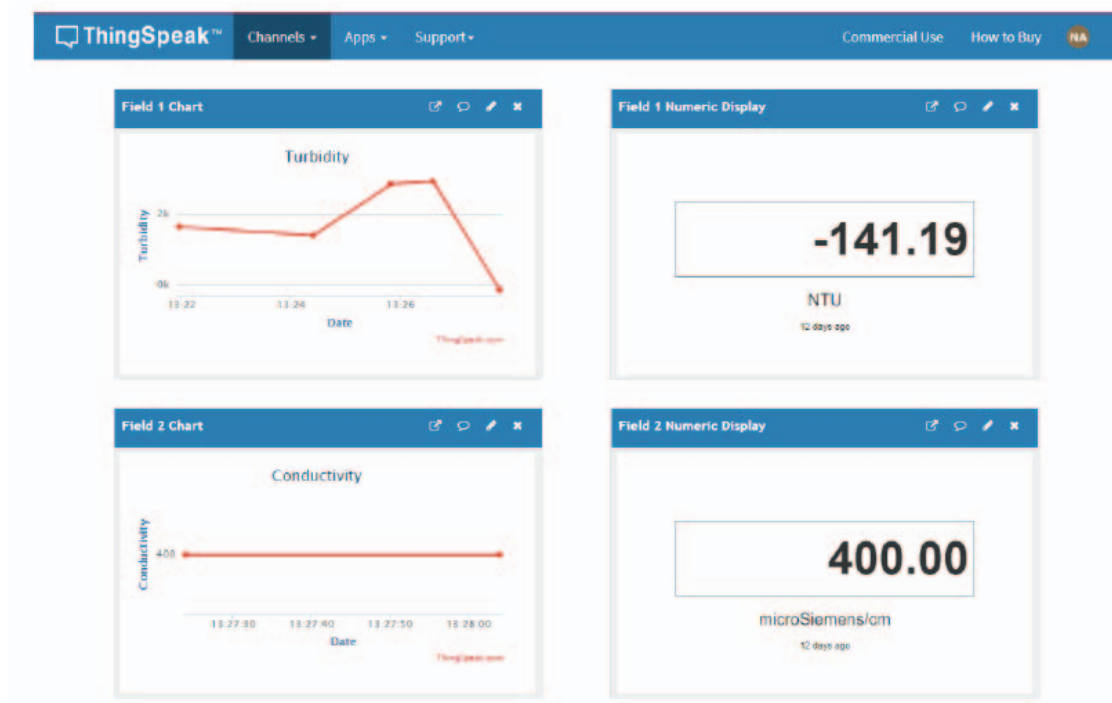
Fig. 8: Water quality measurement data visualization in terms of turbidity (NTU) and conductivity (μS/cm).

4. CONCLUSION

Indeed, water is very valuable to human beings and other living things. However, preserving good water quality has become a big challenge in this modern world. Water pollution cases have increased due to lack of awareness and moral values. Thus, the development of this research aims to help reduce water pollution. In this research, the major contaminants that contribute the most to river water pollution have been identified and studied, namely the BOD, NH_3N, and SS. Moreover, the water pollution detection system has been developed and designed with affordable and minimal costs. Therefore, a low-cost water pollution detection system has been achieved. Next, the water pollution detector device that focuses on detecting major contaminants in Malaysia has been designed. The general performance of the work was evaluated and analyzed. The self-developed

conductivity sensor was able to give readings that have a difference of 6.84% and 6.35% compared to the previous paper and ready-made sensor, respectively. The turbidity sensor was also able to give the correct reading according to a different type of solution. To conclude, the research objectives have been achieved and established.

ACKNOWLEDGEMENT

REFERENCES

[1] Department of Environment (DOE). (2017) Pollution Sources Inventory, in Enviroment Quality Report 2017, pp. 100-105.

[2] Afroz R, Rahman A. (2017) Health impact of river water pollution in Malaysia. Int. J. Adv. Appl. Sci., 4(5): 78-85.

[3] Department of Environment (DOE). (2017) River Water Quality, in Environment Quality Report 2017, pp. 24-60.

[4] 8 critical after inhaling methane in suspected illegal chemical dumping. [Online]. Available: https://www.nst.com.my/news/nation/2019/03/466921/8-critical-after-inhaling-methane-suspected-illegal-chemical-dumping. [Accessed: 26-Jul-2020].

[5] Assad AIG. (2015) Quality of Tap Drinking Water in Kuwait: Physicochemical Characteristics. International Conference on Sustainable Mobility Applications, Renewables and Technology, SMART 2015, pp. 1-4.

[6] Heyda M. (2008) Conductivity Measurement and Theory. [Online]. Available: http://www.mbhes.com/conductivity_measurement.htm. [Accessed: 14-Dec-2020].

[7] Indu K, Choondal JJ. (2016) Modeling, Development & Analysis of Low Cost Device for Water Quality Testing. 2016 IEEE Annual India Conference, INDICON 2016, pp. 1-6.

[8] World Health Organization (WHO). (2017) Water Quality and Health - Review of Turbidity: Information for regulators and water suppliers. Who/Fwc/Wsh/17.01, p. 10.

[9] WEPA, "National Water Quality Standards for Malaysia," WEPA, 2017. [Online]. Available: http://wepa-db.net/en/topic/waterstandard/Malaysia_1_surface.pdf. [Accessed: 13-Mar-2020].

OPTIMAL DISTRIBUTION NETWORK RECONFIGURATION USING MULTI-OBJECTIVE CUCKOO SEARCH ALGORITHM

Azrin Saedi[1], Mohd Shahrin Abu Hanifah[1*], Hilmi Hela Ladin[2] and Siti Hajar Yusoff[1]

[1]*Department of Electrical and Computer Engineering,*
[2]*Departmentt of Mechanical Engineering,*
International Islamic University Malaysia,
Jalan Gombak, 53100 Kuala Lumpur, Malaysia.

[*]*Corresponding author: shahrin@iium.edu.my*

ABSTRACT: In power system electricity delivery, the distribution system has the most electricity loss as the system has the highest R/X ratio and has a radial network at one time. Optimal reconfiguration of the distribution network is needed in order to reduce power losses. However, as it is also involved with multiple objectives and constraint problems such as switching frequency, voltage, and current limits, it is difficult to find the optimal solution. Hence, this paper proposes the Multi-objective Cuckoo Search (MOCS) algorithm to find the optimal reconfiguration of distribution networks by considering minimizing power losses and switch operations. Based on the simulation results on the IEEE-33 bus system, the performance of the MOCS-based scheme has been found to be significantly better than the single-objective algorithm thereby reducing approximately 33% of the power losses.

ABSTRAK Melalui sistem penghantaran jana kuasa elektrik, sistem pengagihan mempunyai pembaziran tenaga elektrik terbesar kerana sistem ini mempunyai nisbah R/X paling tinggi dan mempunyai satu rangkaian radial pada tiap-tiap satu masa. Konfigurasi semula rangkaian pengedaran yang optimum diperlukan bagi mengurangkan pembaziran tenaga. Walaubagaimanapun, oleh kerana ia melibatkan objektif dan kekangan masalah yang pelbagai seperti kadar peralihan, had voltan serta arus, adalah sukar bagi mendapatkan bacaan yang optimum. Oleh itu, kajian ini mencadangkan *Carian Cuckoo Pelbagai Objektif (MOCS)* bagi mencari konfigurasi semula yang optimum bagi sistem pengagihan tenaga dengan mengambil kira pengurangan pembaziran tenaga dan kadar peralihan. Berdasarkan keputusan simulasi pada sistem bas *IEEE-33,* pretasi *MOCS* telah menunjukkan peningkatan yang ketara berbanding algoritma objektif tunggal dan pengurangan sebanyak 33% tenaga.

KEYWORDS: *distribution network reconfiguration (DNR); multi-objective Cuckoo search (MOCS) algorithm; power loss reduction; switch operations; Pareto optimal*

1. INTRODUCTION

An efficient and high-reliability power system is crucial because global electricity demand has increased due to the rising population. Since the primary source of power around the world comes from non-renewable energy sources such as fossil fuels, coal, and natural gas, power loss in electricity delivery can be seen a contributor to global warming

[1]. The distribution system has the most power loss compared with other systems as it has a high R/X ratio. This ratio means the reactance is much higher in the system [2]. System reconfiguration can be manipulated by two methods, power line restructuring and switch opening and closing. The tie switch (normally open) and sectionalizing switch (normally closed) are used to connect and disconnect power to the load entity to reduce the power loss in the distribution network. The procedure of changing the open/closed switch status is called distribution network reconfiguration (DNR). DNR is primarily performed to minimize losses and maximize the load balancing, system reliability, and voltage profile at the network level [3]. To manually change the status of the switches requires much time and cost and consumes energy.

In the literature, two approaches have been used in optimizing this problem, which are using (i) a single-objective approach [4-8] and (ii) a multi-objective approach [9-12]. For the single-objective approach, the author in [4] has focused on minimizing the power/energy losses and network loading index using a hybrid heuristic-genetic algorithm. While authors in [5,6] have compared several heuristic algorithms for minimizing power loss and enhancing voltage profile and applied them with to various scales of the distribution networks. At the same time, [5] has considered the integration of distributed generation (DG) in the network. Other researchers have investigated the optimal placement and sizing of unified power quality conditioners (UPFC) along with DNR for real power loss reduction [7]. However, the common drawback of these approaches is that the values of variables and parameters in each objective function vary depending on the case study and type of the network. Besides, it requires a weight factor in the objective function, which needs to be tuned to get the optimal solution.

On the other hand, multi-objective optimization is a technique when two or more objectives are considered simultaneously to achieve the most desired outcome. This technique is used in many fields like economics, logistics, management, science, and engineering [13]. Unlike single-objective, this approach does not require a weight factor in the objective function. There are trade-offs among the objectives to achieve the outcome as the objectives might conflict with each other [9]. In DNR, research has been conducted using multi-objective approaches such as Multi-objective Evolutionary Algorithm [10] and Non-sorting genetic algorithm [11] for service restoration, and Bayesian learning-based evolutionary algorithm for absorption rate of wind power and voltage stability improvement [12]. However, less work has been reported on minimizing power losses and switching operations simultaneously using single-objective or multi-objective approaches.

Hence, this paper proposes a solution for power loss reduction and switching minimization using the Multi-objective Cuckoo Search (MOCS) algorithm. MOCS is the extended version of the cuckoo search algorithm developed by Yang and Deb [14]. It has been tested against relevant test functions and then successfully applied to numerous problems [15-18]. This study uses MOCS to solve the DNR optimization problem focusing on power loss reduction and switching operations. The optimal model is developed in a MATLAB environment using the IEEE-33 bus test system. Then the result is compared to a single objective cuckoo search algorithm.

2. PROBLEM FORMULATION

In this paper, the DNR problem is formulated as a multi-objective and multi-constrained problem. The various objective functions and constraints considered in this work are explained as follows.

2.1 Objective Functions

The following equations express the objective functions aimed at minimizing the power loss and number of switch operations.

a) Minimization of power losses:

$$\min f_1 = \sum_{i}^{N_{br}} R_i \frac{P_i^2 + Q_i^2}{V_i^2} \tag{1}$$

where N_{br} is the total number of branches, R_i is the branch resistance i, V_i is the voltage at sending end node of ith branch, and P_i and Q_i are the active and reactive power at the sending end node of ith branch.

b) Minimization of switch operations:

$$\min f_2 = \sum_{j}^{N_s} |SWB_j - SWA_j| \tag{2}$$

where N_s is the number of operated switches, SWA_j and SWA_j are the status of jth operated switch in the network before and after reconfiguration.

2.2 Constraints

The followings are the constraints that secure an optimal power flow calculation and preserve the network radial condition [6].

a) **Voltage Limit**

$$V_{i,min} \leq V_i \leq V_{i,max} \tag{3}$$

where $V_{i,min}$ is 0.9 p.u and $V_{i,max}$ is 1.1 p.u which is the voltage limit at end node of ith branch.

b) **Current Limit**

$$I_i \leq I_{i,max} \tag{4}$$

where I_i is the current at ith branch and $I_{i,max}$ is the maximum current at ith branch.

c) **Radial Topology Constraint**

In any network, the number of main loops can be calculated using the following relation:

$$N_{node} - N_{branch} = 1 \tag{5}$$

where the configuration is radial, and the system has no isolated node. The number of nodes in the system is notated as N_{node}.

3. METHODOLOGY

3.1 Multi-objective Cuckoo Search (MOCS) Algorithm

The Cuckoo Search algorithm is based on the aggressive way that cuckoo birds use to sustain the survival of their species. The bird would lay eggs in a host nest, and the survival of the eggs depends on the probability that the host bird discovers the eggs. The host bird would either abandon the nest or throw the eggs if they are discovered. Cuckoo birds develop the way to survive by mimicking the appearance of the host bird egg or the egg

hatched earlier from the host bird egg. The pseudocode and the flowchart of MOCS is shown in Fig. 1 and Fig. 2 respectively.

Initialize objective functions $f_1(\boldsymbol{x}), \ldots, f_K(\boldsymbol{x})\boldsymbol{x} = (x_1, \ldots, x_d)^T$
Generate an initial population of n host nests $\boldsymbol{x}_i$ and each with K eggs
while ($t <$ MaxGeneration) or (stop criterion)
    Get a cuckoo (say i) randomly by Lévy flights
    Evaluate and check if it is Pareto Optimal
    Choose a nest among n (say j) randomly
    Evaluate K solutions of nest j
    if new solutions of nest j dominate those of nest i,
        Replace nest i by the new solution set of nest j
    end
    Abandon a fraction (p_a) of worse nests
    Keep the best solutions (or nest with non-dominated sets)
    Sort and find the current Pareto optimal solutions
end
Postprocess results and visualization

Fig. 1: Multi-objective Cuckoo Search Algorithm Pseudocode [14].
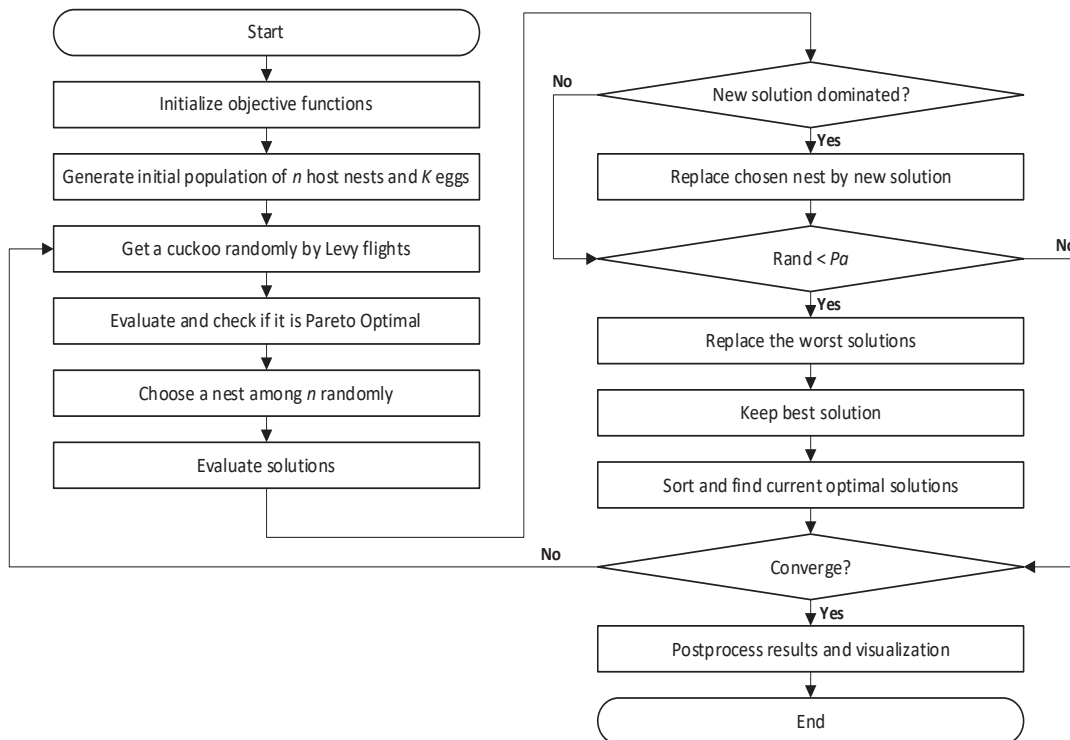
Fig. 2: Multi-objective Cuckoo Search algorithm flowchart.

Cuckoo Search algorithm has three general rules:

1) Each cuckoo bird lays one egg in only one random nest at a time;

2) The best egg would survive for the next generation;

3) The number of available host nests is the same; the probability of laid cuckoo egg to be discovered is between 0 and 1. The host bird would throw away the bird egg or abandon the nest, building a new nest [19].

In the multi-objective Cuckoo Search Algorithm, the first and third general rules are changed:

1) Each cuckoo bird lays K eggs in only one random nest at a time; K refers to the number of objectives.

2) The best egg would survive for the next generation;

3) The number of available host nests is the same. The probability of laid cuckoo K eggs to be discovered is between 0 and 1. The host bird would build a new nest with K eggs in respect of the egg differences. Diversity would happen by random mixing.

3.2 Proposed Algorithm and Pareto Optimal

The algorithm aims to obtain the Pareto Optimal with respect to some switch changes and power loss with the highest voltage stability limit. This algorithm is improved for Pareto Optimal from the MOCS algorithm in [18]. The algorithm steps are:

1. Data of the bus system (e.g. branch, bus and load number) are obtained.
2. Bus voltage and power loss (P_{loss}) are calculated by running the load flow program.
3. Voltage stability limit is calculated by the formula:

   $V_S = \frac{1}{\lambda}$, while λ is the load value.

4. A set of the initially closed switches is defined as $R_i = \left((R_i)_1^1 \quad \cdots \quad (R_i)_{n_e}^1 \right)$.

5. Parameters for the algorithm are set such as nest dimension (n_d), nests number (n), switch opened dimension (n_e), the probability to be discovered, and step size (α), lower limit and upper limit search space, and maximum iteration number (N).

6. Search space $n \times n_d$ is generated randomly. Each row represents a solution, while every element represents power loss for every connection P_c to the load.

$$P_c = \begin{pmatrix} (P_c)_1^1 & \cdots & (P_c)_{n_d}^1 \\ \vdots & \ddots & \vdots \\ (P_c)_1^n & \cdots & (P_c)_{n_d}^n \end{pmatrix}$$

7. Search space $n \times n_e$ is generated. Each row represents a set of switches opened in the distribution network, while every element represents a switch closed for every radial network, $R_c.R_c = \begin{pmatrix} (R_c)_1^1 & \cdots & (R_c)_{n_e}^1 \\ \vdots & \ddots & \vdots \\ (R_c)_1^n & \cdots & (R_c)_{n_e}^n \end{pmatrix}$

8. Then, reactive power $(Q_{loss})'$ would be added to the bus and each P_c row, new power loss $(P_{loss})'$ and bus voltage is calculated.

$$(Q_{loss})' = Q_{load} - P_c$$

9. Then, power loss reduction is calculated as:

   $\Delta_P = P_{loss} - (P_{loss})'$

10. Then, switch change number (j) is calculated as this conditional loop statement:

   for every element $R_i \neq R_c$
   j is incremented by 2

11. The optimal value for minimum power loss (f_1) with the lowest switch change (f_2) is obtained.

12. The bus voltage value is accepted if the bus voltage value is within the range of acceptable value.

13. Levy flight is applied to obtain a new solution.
14. Then, step 6 to 9 is repeated.
15. An unaccepted solution is abandoned, and a new solution is generated
16. Step 12 is repeated.
17. Iteration value is increased if it does not reach the maximum number from step 10.
18. Then, if the voltage stability limit is not the maximum value, the value of λ is increased, and step 3 is repeated. Otherwise, the algorithm is terminated.
19. Then, all surviving solutions of the Cuckoo Search are plotted using the Pareto optimal.

3.3 IEEE-33 Bus Test System

The effectiveness of the MOCS algorithm has been studied on the standard IEEE-33 bus model system [12] in a MATLAB environment using the MATPOWER package [20]. This test model is a power distribution system with 33 busses attached to the load points, and it is connected with 37 switches (sectionalize and tie switches), as shown in Fig. 3. Each load is identified by the number given, and in one mainline, the load number must be in sequence. Any tie switch would connect one point of the load with another point of the load of the different power lines. This tie switch would be closed to accommodate the breakdown of other sectionalizing switches to make sure every load is receiving power. The tie switch and sectionalizing switch can be alternately switched on and off to optimize power loss. This model system can be assumed to have constant base power, S_{base} = 50 MVA, and base voltage, V_{base} = 33 kV. The real power of the load is 3.715 MW, and the reactive power of the load is 2.3 MVAR. Minimum and maximum per-unit voltages are 0.95 p.u and 1.05 p.u, respectively. The initial power losses recorded in the model system is 208.46 kW.
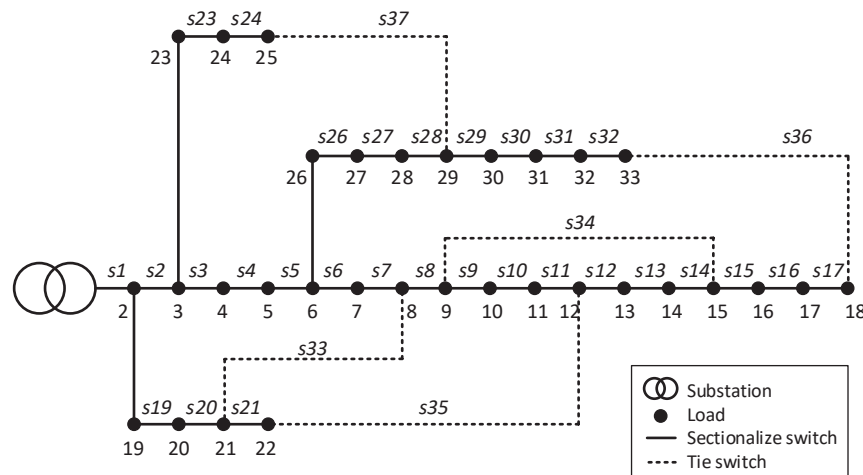
Fig. 3: The initial state of the IEEE-33 bus system [12].

4. RESULTS AND DISCUSSION

In this paper, the MOCS algorithm is used to obtain the optimal DNR for minimizing the power losses and switch operation simultaneously. The result is analyzed using the Pareto optimal front, and the voltage profile for all solutions are presented. Then, it is compared to a single objective approach cuckoo search algorithm. Finally, the performance of MOCS is analyzed using the convergence rate in terms of generalized distance [14] and validated against the multi-objective genetic algorithm (MOGA) [21].

4.1 Pareto Optimal Front

The Pareto front generated by four non-dominated solutions after 50 iterations is presented in Fig. 4. The graph is aligned with Pareto optimal as it shows that the higher number of switch changes, the lower the power loss in the distribution network. The number of operated switches ranges between two and eight, contrary to the broadest possible range between zero and ten. At the same time, the power losses ranged from 138 kW to 156 kW. The detailed result for each Pareto point is tabulated in

Table 1. From the table, all solutions show a significant reduction in power losses after obtaining optimal reconfiguration using MOCS. The lowest power loss is obtained by solution 1, which decreased from 208.46 kW to 138.93 kW, bringing approximately 33% reduction. It requires eight switches to be operated, which are number 7, 9, 14, 32, 33, 34, 35, and 36. On the other hand, the lowest number of operated switches is recorded by solution 4, which only changed switches number 7 and 35. However, the power losses decreased to 155.80 kW, equivalent to a 25% reduction, which is slightly lower.
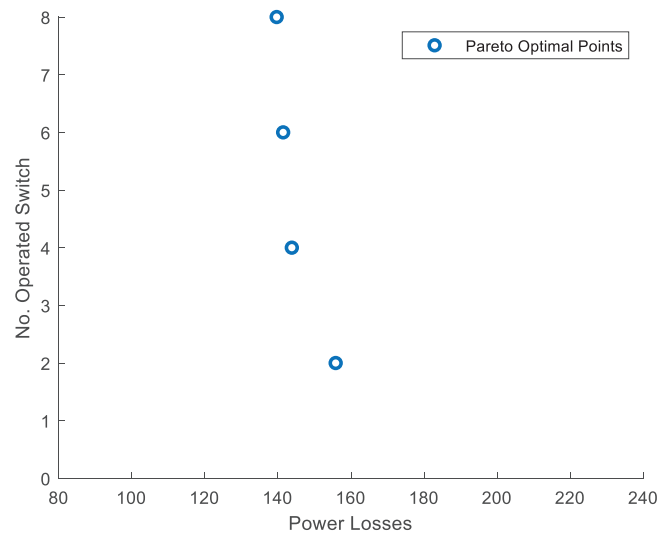
Fig. 4. Pareto Optimal Multi-Objective Cuckoo Search Algorithm.

Table 1: Simulation before and after reconfiguration using MOCS

	Before Reconfiguration	After Reconfiguration			
		Solution 1	**Solution 2**	**Solution 3**	**Solution 4**
Tie Switch	33 34 35 36 37	7 9 14 32 37	7 9 14 36 37	7 11 34 36 37	7 33 34 36 37
Power Loss	208.46 kW	138.93 kW	141.43 kW	143.80 kW	155.80 kW
Power Loss Reduction	-	33.36 %	32.15 %	31.02 %	25.26 %
No. of Operated Switch	-	8	6	4	2
Minimum Voltage	0.911 p.u	0.942 p.u	0.938 p.u	0.938 p.u	0.937 p.u

4.2 Voltage Profile

Fig. 5 presents the voltage profile of IEEE-33 bus system for each solution obtained by MOCS. The graphs show that the voltage profiles are significantly improved after the network is reconfigured across all solutions. Besides, the minimum voltages are also increased by approximately 3% compared to before reconfiguration.

(i) Solution 1	(ii) Solution 2
(iii) Solution 3	(iv) Solution 4
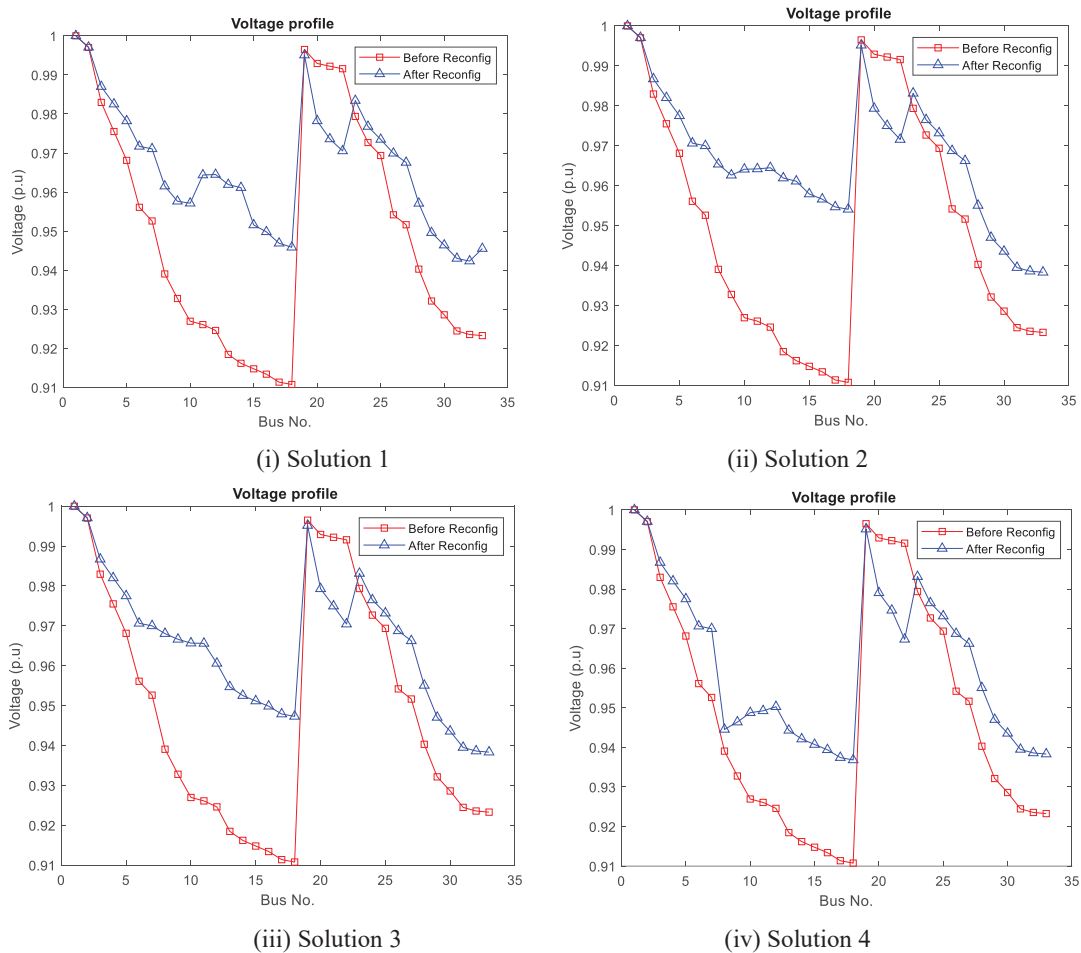
Fig. 5: Voltage profile of the network before and after reconfiguration for each solution.

4.3 Comparison with Single-objective Algorithm

In order to see the effectiveness of the multi-objective technique, the above results are compared with the single-objective approach [22] demonstrated in **Error! Reference source not found.**. It is apparent that the power loss obtained by the single-objective is 157.65 kW which is almost 1% lower power loss reduction compared to the solution 4 recorded by MOCS in

Table 1. Furthermore, in terms of switch operations, both single-objective and multi-objective approaches were at the same level. Overall, MOCS shows better effectiveness compared to the single-objective algorithm. Besides, it provides multiple solutions to be chosen and does not require a weighting factor as a single-objective method.

Table 2: Simulation Result of single objective Cuckoo Search Algorithm

	Before Reconfiguration	**After Reconfiguration**
Tie Switch	33 34 35 36 37	7 34 35 36 37
Power Loss	208.46 kW	157.65 kW
Power Loss Reduction	-	24.38 %
No. of Operated Switch	-	2
Minimum Voltage	0.911 p.u.	0.930 p.u.

4.4 Generational Distance (GD) Measurement

Furthermore, in order to see the proposed MOCS performance, we also tested the same problems using a similar multi-objective technique, which is MOGA [21]. The performance is measured in terms of generational distance (GD)[14]. GD is designed to measure the sum of adjacent distances of solutions sets obtained by different algorithms, especially multi-objective evolutionary algorithms. The comparison of the convergence rates between proposed MOCS and MOGA is plotted in Fig. 6. This figure shows that MOCS converged slightly faster than MOGA even though there were opposite patterns shown at early iterations, which could be neglectable. Nevertheless, overall, MOCS delivers better performance than MOGA.
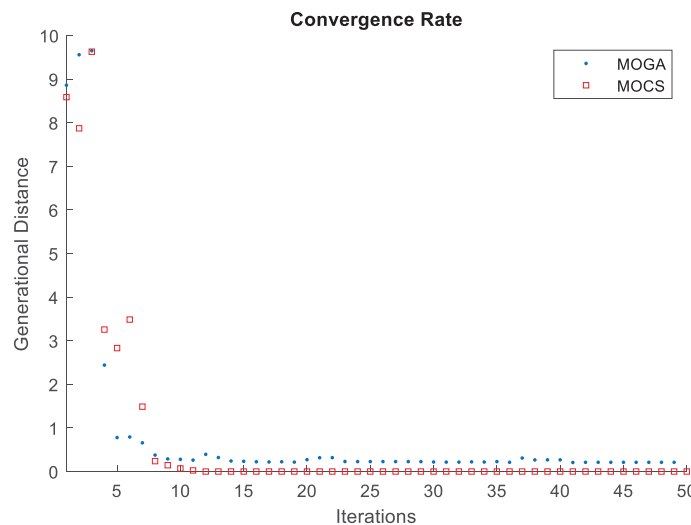
Fig. 6: Convergence comparison between MOCS and MOGA.

5. CONCLUSION

Power losses are critical in electrical power systems due to their impact on system reliability. Thus, distribution network reconfiguration (DNR) is introduced to minimize power losses and switch operations. In this study, a multi-objective Cuckoo Search (MOCS) algorithm for finding the optimal reconfiguration is presented. The simulation result is validated on the standard IEEE-33 bus test system in the MATLAB environment, and MATPOWER package is used for power flow calculation. The results show that MOCS obtained approximately 25% to 33% reduction results of power losses where two to eight switches were operated. Compared to the single-objective approach, MOCS recorded slightly better losses reduction and was on par in terms of switch operations. Besides, the convergence comparison with a similar multi-objective technique, MOGA, indicates the

superiority of MOCS to obtain better optimal reconfiguration. Hence, the objectives of this paper to minimize the power losses and switch operations is achieved.

Furthermore, the obtained Pareto optimal front shows the trade-offs between two objectives in solving the DNR problem. In this case, the system operator can benefit from the results of the MOCS application to decide the priority between power losses and numbers of switch operations based on actual circumstances. As a way forward, this research may be extended to the large-scale networks such as IEEE-69 and IEEE-129 bus system models with the integration of renewable energy sources.

ACKNOWLEDGEMENT

REFERENCES

[1] Surana K, Jordaan SM. (2019) The climate mitigation opportunity behind global power transmission and distribution. Nature Climate Change, 9(9): 660-665. https://doi.org/10.1038/s41558-019-0544-3

[2] Singh B, Chauhan S, Reddy CC. (2017) Power loss minimization in electrical power distribution networks by use of hybrid reconfiguration method. 3rd International Conference on Condition Assessment Techniques in Electrical Systems (CATCON), IEEE. pp. 349-354. https://doi.org/10.1109/CATCON.2017.8280243

[3] Thakar S, Vijay AS, Doolla S. (2019) System reconfiguration in microgrids. Sustainable Energy, Grids and Networks, 17100191. https://doi.org/10.1016/j.segan.2019.100191

[4] Jakus D, Čađenović R, Vasilj J, Sarajčev P. (2020) Optimal Reconfiguration of Distribution Networks Using Hybrid Heuristic-Genetic Algorithm. Energies, 13(7): 1544. https://doi.org/10.3390/en13071544

[5] Nguyen HD, Valeev IM. (2019) Improvement methods for solving the distribution network reconfiguration problem. Energetika, 64(4): 174-185. https://doi.org/10.6001/energetika.v64i4.3892

[6] Landero A, Koziel S, Abdel-Fattah MF. (2019) Distribution network reconfiguration using feasibility-preserving evolutionary optimization. Journal of Modern Power Systems and Clean Energy, 7(3): 589-598. https://doi.org/10.1007/s40565-018-0480-7

[7] Gholami K, Karimi S, Dehnavi E. (2019) Optimal unified power quality conditioner placement and sizing in distribution systems considering network reconfiguration. International Journal of Numerical Modelling: Electronic Networks, Devices and Fields, 32(1): e2467. https://doi.org/10.1002/jnm.2467

[8] Samadaei E, Khosravi A, Sheikholeslami A. (2017) Optimal Allocation of Active Power Filter On real distribution network for improvement of power quality by use of BBO: A case study. IIUM Engineering Journal, 18(1): 85-99. https://doi.org/10.31436/iiumej.v18i1.688

[9] Gunantara N. (2018) A review of multi-objective optimization: Methods and its applications. Ai Q, editor. Cogent Engineering, 5(1): 1502242. https://doi.org/10.1080/23311916.2018.1502242

[10] Sanches DS, London Junior JBA, Delbem ACB. (2014) Multi-Objective Evolutionary Algorithm for single and multiple fault service restoration in large-scale distribution systems. Electric Power Systems Research, 110: 144-153. https://doi.org/10.1016/j.epsr.2014.01.017

[11] Shahrin M, Aoki H. (2016) Application of Multi-Objective Optimization for Service Restoration Problem in Distribution Systems. IEEJ Transactions on Power and Energy, 136(3): 275-283. https://doi.org/10.1541/ieejpes.136.275

[12] Zhong T, Zhang H-T, Li Y, Liu L, Lu R. (2020) Bayesian Learning-Based Multi-Objective Distribution Power Network Reconfiguration. IEEE Transactions on Smart Grid, 12(2): 1174-1184. https://doi.org/10.1109/TSG.2020.3027290

[13] Khan MR, Badran M, Toha SF, Zainal Abidin Z. (2021) Multi-Objective Optimization of Snake Robot in Serpentine Locomotion. IIUM Engineering Journal, 22(2): 364-383. https://doi.org/10.31436/iiumej.v22i2.1691

[14] Yang X-S, Deb S. (2013) Multiobjective cuckoo search for design optimization. Computers & Operations Research, 40(6): 1616-1624. https://doi.org/10.1016/j.cor.2011.09.026

[15] Zainal MI, Yasin ZM, Zakaria Z. (2021) Optimizing Voltage Profile and Loss Minimization using Multi Objective Cuckoo Search Algorithm. 2021 IEEE 11th IEEE Symposium on Computer Applications & Industrial Electronics (ISCAIE), IEEE. pp. 116-122. https://doi.org/10.1109/ISCAIE51753.2021.9431835

[16] Yasin ZM, Aziz NFA, Salim NA, Wahab NA, Rahmat NA. (2018) Optimal Economic Load Dispatch using Multiobjective Cuckoo Search Algorithm. Indonesian J. Electrical Engin. Comp Sci, 12(1): 168. https://doi.org/10.11591/ijeecs.v12.i1.pp168-174

[17] Zhou X, Liu Y, Li B, Li H. (2017) A multiobjective discrete cuckoo search algorithm for community detection in dynamic networks. Soft Computing, 21(22): 6641-6652. https://doi.org/10.1007/s00500-016-2213-z

[18] Rao NT, Sankar MM, Rao SP, Rao BS. (2021) Comparative study of Pareto optimal multi objective cuckoo search algorithm and multi objective particle swarm optimization for power loss minimization incorporating UPFC. Journal of Ambient Intelligence and Humanized Computing, 12(1): 1069-1080. https://doi.org/10.1007/s12652-020-02142-4

[19] Yang X-S, Deb S. (2009) Cuckoo Search via Lévy flights. 2009 World Congress on Nature & Biologically Inspired Computing (NaBIC), IEEE. pp. 210-214. https://doi.org/10.1109/NABIC.2009.5393690

[20] Zimmerman RD, Murillo-Sanchez CE, Thomas RJ. (2011) MATPOWER: Steady-State Operations, Planning, and Analysis Tools for Power Systems Research and Education. IEEE Trans Power Sys, 26(1): 12-19. https://doi.org/10.1109/TPWRS.2010.2051168

[21] Bevilacqua V, Pacelli V, Saladino S. (2011) A Novel Multi Objective Genetic Algorithm for the Portfolio Optimization. Lecture Notes in Computer Science (Including Subseries Lecture Notes in Artificial Intelligence and Lecture Notes in Bioinformatics), pp. 186-193. https://doi.org/10.1007/978-3-642-24728-6_25

[22] Fuad NAA, Azlin AAN, Zahari MFD, Hanifah MSA. (2018) Power Distribution Loss Reduction Using Cuckoo Search. 2018 7th International Conference on Computer and Communication Engineering (ICCCE), IEEE. pp. 333-337. https://doi.org/10.1109/ICCCE.2018.8539252

A NEW HARDWARE ARCHITECTURE FOR HIGH-PERFORMANCE PARALLEL TURBO DECODER

**SUJATHA ELUKURU[1*], SUBHAS CHENNAPALLI[2]
AND GIRIPRASAD MAHENDRA NANJAPPA[2]**

*[1]Department of Electronics and Communications,
Sree Vidyanikethan Engineering College, Andhra Pradesh, India.
[2]Department of Electronics and Communications,
JNTUA College of Engineering, Andhra Pradesh, India.*

[*]Corresponding author: sujathaece88@gmail.com

ABSTRACT: Recent wireless communications demand maximum achievable data rates without intervention. The channel decoder in the physical layer would support such high data rates with a flexible hardware structure. The turbo channel decoder offers flexible hardware architecture and reliable decoding, but the turbo decoder design is complex, and its hardware architecture consumes more power and area in a communication system. Hence, an optimized high-performance turbo decoder architecture with simplified QPP interleaver is needed for supporting various data rates. In this context, this article presented a new hardware architecture with a three-stage pipeline parallel turbo decoding process and each MAP decoder in the proposed parallel turbo decoder with a three-stage micro pipeline process. The proposed structure optimized the circuit complexity and improved the throughput through parallel pipeline decoding process. Also, this article presents a simplified semi-recursive QPP interleaver, which avoids complex 'mod' operations for a high-performance turbo decoder. The performance analysis has been done using Model sim, Xilinx Vivado design suite, and estimated performance analysis was observed on various 28 nm CMOS technology FPGAs and compared with the conventional designs. Analysis of the proposed design showed improvement throughput up to 55.6% and a reduction in the power consumption up to 43% as compared to the recently reported architectures.

ABSTRAK: Komunikasi tanpa wayar terkini menuntut kadar data maksimum yang boleh dicapai tanpa intervensi. Penyahkod saluran dalam lapisan fizikal akan menyokong kadar data yang tinggi dengan struktur perkakasan fleksibel. Penyahkod saluran turbo menawarkan seni bina perkakasan fleksibel dan penyahkodan yang boleh dipercayai. Tetapi, penyahkod turbo merupakan blok yang kompleks, lebih berkuasa dan menggunakan kawasan yang luas dalam sistem komunikasi. Oleh itu, seni bina penyahkod turbo optimum berprestasi tinggi dengan antara lembar QPP yang mudah diperlukan bagi menyokong pelbagai kadar data. Dalam konteks ini, kajian ini merupakan seni bina perkakas baru dengan proses penyahkod turbo selari bersama salur paip tiga peringkat dan setiap penyahkod MAP yang dicadangkan dalam penyahkod turbo selari bersama proses saluran paip mikro tiga peringkat dibentangkan. Struktur yang dicadangkan dapat mengurangkan kerumitan litar dan meningkatkan daya pemprosesan melalui penyahkodan saluran paip selari. Selain itu, kajian ini merupakan antara lembar mudah QPP rekursif, yang dapat mengelakkan operasi 'mod' yang kompleks bagi penyahkod turbo berprestasi tinggi. Analisis prestasi telah dilakukan menggunakan sim Model, reka bentuk suit Xilinx Vivado, dan analisis prestasi anggaran telah diperhatikan pada pelbagai teknologi FPGA CMOS 28 nm dan dibandingkan dengan reka bentuk konvensional. Analisis reka bentuk

yang dicadangkan menunjukkan peningkatan sepanjang 55.6% dan pengurangan penggunaan kuasa sehingga 43% berbanding seni bina laporan terkini.

KEYWORDS: *turbo decoder; MAP decoder; VLSI; interleaver; FPGA*

1. INTRODUCTION

Channel coding techniques are essential for a wireless communication system to achieve a reliable and high-performance transmission between transmitter and receiver, in a noisy channel. State-of-the-art iterative channel codes such as Turbo codes [1], Low-density parity-check codes (LDPC) [2], and Polar codes [3] are often used. Turbo codes offer more flexible architecture for their encoder and decoder than LDPC and polar codes. Also, Turbo codes achieve high diversity, reliable data transmission, and possible large coding gain in fading channels.

The efficient-hardware implementation of Turbo codes, in order to meet real-time constraints, is an active area of research and there is a need for innovation in the VLSI design of high-performance Turbo Decoders in terms of throughput, silicon area, and power-efficiency as well. Hence, the present study is aimed at developing a high-throughput, low area, and low power turbo decoder by modifying the hardware architecture of the decoder, simplifying mathematical computations involved in the decoding and interleaving process, and applying the optimization techniques. Maximum a-posteriori probability (MAP) algorithm introduced by Bahl-Cocke-Jelinek-Raviv (BCJR) [4] for SISO decoders and the simplifications of MAP algorithm called Log-MAP and Max-Log-MAP [5] were studied and Max-log-MAP algorithm is adopted in the design and hardware implementation of the proposed turbo decoder due to its lower complexity than the log-MAP algorithm.

To improve the throughput performance of the turbo decoder, the number of MAP decoders could be increased and all operated in parallel at the cost of degradation in error-correcting performance, especially with higher code rates. Moreover, employing multiple decoders to increase the throughput does not solve the additional challenge of lower latency requirements. The throughput could also be increased by increasing the block size (from 40 to 6144), but this would result in consequent complexities in computational latency, area requirement, and power consumption. The trade-off among the performance parameters could be best compromised by effective hardware design and suitable optimization techniques [6]. Interleaver is an essential part of turbo decoder and is also responsible for BER performance of decoding. The algebraic properties and contention-free property of QPP interleaver [7] guarantee contention-free access to memory and generated addresses.

Also, one of the problems in the implementation of highly parallel decoders is memory contention during decoding, where all the sub-block of MAP decoders simultaneously tries to access the same memory bank on reading or writing the extrinsic information from or into it. To solve this problem, an efficient approach of collision-free parallel interleavers in which data is read or written on the intra-sub block as well as inter-sub block of MAP decoder to achieve low complexity architecture having no additional hardware resources.

Some benchmarked research works on high throughput turbo decoders were discussed here. A high throughput turbo decoder with 8 and 64 parallel radix-2 MAP decoder architecture in 90 nm CMOS technology was proposed [8]. This paper proposed a new ungrouped backward recursion scheme and a new state metric normalization technique to offer retiming and pipelining in architecture for performance improvement. Also, this work adopted a fine-grain clock gating technique to solve the power issue and the throughput achieved is 301 Mbps at 272 mW of power. A highly parallel turbo decoder structure in

2015 was reported [9] to achieve the highest throughput rate of 1.45 Gbps implemented in 90 nm CMOS technology. This work was aimed at improving the decoding efficiency and this improvement was possible by modifying the parallel window MAP decoding algorithm.

A fully parallel turbo decoding [FPTD] algorithm was reported [10] which allows parallel processing to offer higher processing throughput. This novel FPTD algorithm reduced computational complexity by 50% and enhanced its suitability for FPGA implementations. It was concluded that the fully parallel turbo decoder with radix-2 and 6144 parallel MAP decoders resulted in 14.8Gbps but this design utilized 9618 mW of high power at 100 MHz clock frequency. Various VLSI architectures were presented in [11] for the computing blocks of the turbo decoder and made the SISO decoder support Radix- 2/4/8 modes. The design resulted in throughput in the range of 80Mbps to 270 Mbps, reducing power consumption to up to 61% as compared to the other state-of-art designs. A parallel turbo decoder with reverse address generator in interleaver for low latency and high throughput architecture with double buffer technique was proposed in [12] for effective utilization of FPGA resources for broadcasting systems. This work resulted in a throughput performance of 2.12 Gbps at 250 MHz and a latency of 23.2 µsec with 64 parallel map decoders.

A memory-reduced turbo decoder was proposed by a reverse recalculation technique using the Log-MAP algorithm with a focus on power reduction [13]. It was reported that the technique helped to reduce the memory and power consumption as compared to other conventional turbo decoder designs. The Vedic multiplier-based implementation presented in [14] could be preferred in-branch metric calculations in Max-log-MAP algorithms for low latency turbo applications, but the implementation consumes more area. An optimized turbo decoder for performance improvement of turbo decoder, where the parallel computation of state metrics, reusing of memory and single SISO decoder in the hardware implementation was proposed [15]. A low memory turbo decoder with reverse calculation techniques was reported where the trellis diagram was partitioned and the max* operator was simplified [16]. The findings revealed that the architecture achieved a 65% reduction in state metric cache (SMC) capacity with other designs and lower power dissipation. By this motivation, the present study focused on developing a new hardware architecture for parallel turbo decoder to achieve high performance and balanced hardware implementation using optimization techniques.

2. TURBO DECODER DESIGN PERSPECTIVE

The general structure of a turbo decoder consists of two SISO decoders connected through an interleaver and de-interleaver to perform the iterative process of soft bits to provide a-posteriori LLRs after the required number of iterations. The soft-demodulated values of transmitted bits are referred to as a-priori probability values and are fed to constituent SISO decoders as input LLRs, shown in Fig. 1 [17]. Each decoder operates on the systematic and parity bits associated with its constituent encoder and produces soft outputs of the original data bits in the form of a-posteriori probabilities. The extrinsic information is computed using a-posteriori probability values from the SISO decoder, interleaved/non-interleaved a-priori probability values, and interleaved/de-interleaved extrinsic information from another SISO decoder. Such extrinsic information values are shuffled between two SISO decoders and are iteratively processed along with a-priori probability values to produce error-free a-posteriori probabilities of the transmitted bits.
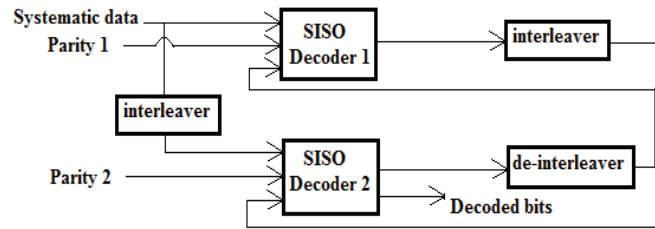
Fig. 1: Block diagram of Iterative Turbo Decoder.

In the iterative process, the MAP algorithm decodes the probabilities for each bit correctly. The complexity of the MAP algorithm has been reduced by operating the algorithm in the log domain variants such as the log-MAP algorithm and max-log-MAP algorithm. In order to realize the high-performance turbo decoder, SISO decoders involved in the turbo decoder should provide high-speed data transmission without significant coding loss. Major tasks of the SISO decoder are computation of branch metrics, state metrics, and LLR computation to extract the final extrinsic information. However, two SISO decoders do not work simultaneously in each half iteration to compute the state metrics. Hence, the present study utilized the turbo decoder with a single SISO decoder for one complete iteration as shown in Fig. 2.
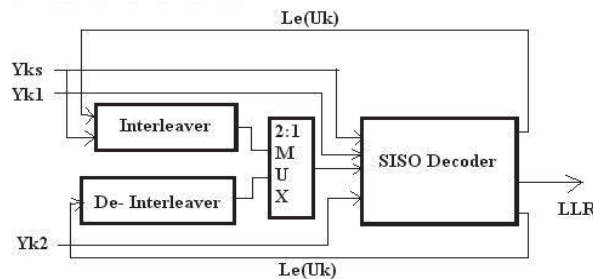

Fig. 2: Block diagram of Turbo Decoder with single SISO Decoder.

The main objective of the present study is to design an efficient parallel turbo decoder that can support higher throughputs using streaming techniques. QPP Interleaver plays a vital role in turbo encoder/decoder error correction. Hardware design of the QPP interleaver involves complex mathematical functions and dependency of previous computations. A semi recursive QPP interleaver is proposed in the present study which simplifies the aforementioned disadvantages of QPP interleaver.

3. QPP INTERLEVER

QPP interleaver is an integral part of the turbo encoder and decoder and it plays a critical role in turbo codes, especially in turbo decoder, for achieving high-speed decoding. For each of the 188 block lengths, a different set of f_1, f_2 parameters were pre-defined in 3GPP LTE [17]. In the recent 3GPP LTE/ LTE-A, QPP interleaver is based on algebraic properties and contention-free properties, providing contention-free memory access for any specified code block size between 40 to 6144. The efficient design of a conflict-free reconfigurable QPP interleaver for turbo encoder and turbo decoder is a pre-eminent task in turbo channel coding scheme. The hardware implementation of QPP interleaver/de-interleaver should support parallel interleaving for the high-performance parallel decoder. This research work proposed the design of reconfigurable semi-recursive QPP interleaver for parallel and direct

computation of address locations of all the bits for turbo decoder by semi recursive computation approach as explained below.

3.1 Semi Recursive QPP Interleaver

The mathematical complexity and dependency of the current address location of the previous address location are solved by the semi-recursive computation method. The address locations of interleaved bits/the sequence of numbers of interleaving $\pi(i)$ of current symbol i in QPP interlever is computed as

$$\pi(i) = (f_1 i + f_2 i^2) \, modK \tag{1}$$

In Eq. 1 [17], parameters $f_1 and\ f_2$ depend on $'K'$ and all the possible variants of block size K and variables $f_1 and\ f_2$, are defined. In hardware implementation of Eq.1, the address computation of current index i, depends on previous computations recursively and this recursive dependency creates high decoding latency and is not preferable for high-performance turbo decoders. The proposed design does not contain mod operation, as mod operator implementation is complex in the hardware design of the QPP interleaver; it is replaced by an Add-Compare-Select (ACS) unit. The ACS unit is composed of only arithmetic operators like addition and subtraction. Replacing the mod operation by the ACS unit is called the modulo normalization technique.

To simplify the complex interleaver computation and to avoid large storage requirements, the proposed semi recursive computation approach for parallel interleaver supports the independent parallel computation of interleaved addresses. The input sequence (Num) is denoted as Metric Weight (MW) and it is represented as MW (1, K+1) in the first column. The subsequent columns are defined as mentioned below.

Case 1: If mod (Num, 2) ≠0, then Num = Num+1 and

MW (2, K+1) = (Num+1)/2;
MW (3, K+1) = MW (2, K+1) - 1;

Case 2: If mod (Num, 2) =0, then Num= Num;
MW (2, K+1) = Num/2;
MW (3, K+1) = Num - MW (2, K+1);

Then, Value (V) is defined as,
V = δ(0) x MW (2, K+1) + δ(1) x MW (3, K+1),
where, δ(0) = f₁ + f₂ and δ(1) = δ(0) + 2f₂ ;

It can be observed from Tables 1 and Table 2, that computation of address locations of 40 bits was done within 5 clock cycles independently. This approach is proposed to minimize the computational complexity and avoid the storage of interleaver tables.

Table 1: Metric weight table in semi recursive order

MW (1, K+1), Num	MW (2, K+1)	MW (3, K+1)	Value (V)	Π(i) = mod (V,40)
0	0	0	0	0
1	1	0	13	13
2	1	1	46	6
3	2	1	59	19
4	2	2	92	12

Table 2: Proposed Parallel Computation of Sub blocks

CLOCK	Sub-block1	Sub-block2	Sub-block3	Sub-block4	Sub-block5	Sub-block6	Sub-block7	Sub-block8
Clock1	0	5	10	15	20	25	30	35
Clock2	1	6	11	16	21	26	31	36
Clock3	2	7	12	17	22	27	32	37
Clock4	3	8	13	18	23	28	33	38
Clock5	4	9	14	19	24	29	34	39

From Tables 1 and 2, it can be observed that the parallel computation of 40 bits has been done with 8 parallel operations. In the first clock cycle, bits 0, 5, 10, 15, 20, 25, 30 and 35 will be computed simultaneously. Similarly in the second, third, fourth, and fifth clock cycles, the parallel computation of the remaining bits is performed in the order shown in Table 2. The proposed method is most suitable for highly parallel turbo decoding architectures. The proposed design and FPGA implementation of a new hardware architecture for a high-performance turbo decoder using streaming techniques is presented below.

4. PARALLEL TURBO DECODER

The parallel decoding approach of turbo decoder with P parallel MAP decoders roughly increases the decoding throughput by a factor of 'P' compared to non-parallel turbo-decoders. Modern parallel hardware architectures can have either spatial or functional parallelization to improve the throughput performance. For a high-performance turbo decoder, this article proposed a new hardware architecture, which is an 8-parallel MAP decoder structure. The proposed architecture is designed in a three-stage pipelined process.

In the first stage, the input LLRs load into the three buffers namely systematic buffer, parity-1 buffer and parity-2 buffer in parallel. Here, the input LLRs could be related to any of 188 block sizes varying from 40 to 6144. In the second stage, the data of eight coded words are processed parallel with the eight BCJR decoders as shown in Fig. 3.

In the second stage, the BCJR decoder is further processed into three micro pipeline stages. Two SISO decoders, named SISO-1 and SISO-2, the first decoder processes the systematic input, parity-1 and a-priori data. Similarly, the second decoder process interleaved systematic input, parity-2, interleaved a-priori data in the micro-pipeline stage is presented below.
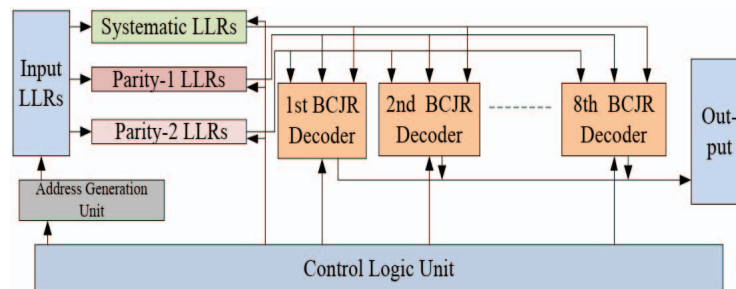

Fig. 3: Block diagram of proposed three-stage pipeline parallel turbo decoder.

In the first micro pipeline stage, all the SISO decoders are processed in parallel with the given two inputs and then extrinsic information is produced as the output of the SISO

decoder. In the second micro-pipeline stage, the produced output information is processed
to interleaved/ de-interleaved block. Finally, in the third micro-pipeline stage, the third input
of de-interleaved a-priori data to SISO decoder blocks to process the extrinsic information.
This three-stage micro pipeline process continues for 8 number of iterations. This process
is depicted in Fig. 4. Then the third pipeline stage of the parallel '8' turbo decoder continues
until maximum convergence is achieved and the output LLRs are processed into the output
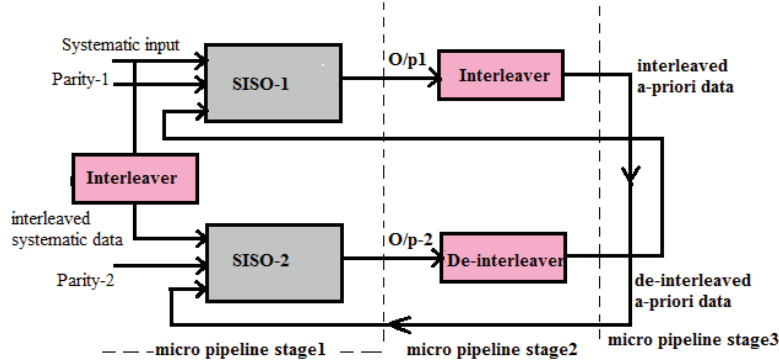buffer.

Fig. 4: Block diagram of three stages micro pipeline Turbo Decoder.

4.1 Simplified Computation of Soft-output

The soft output L can be computed as shown in Eq. 2 [18] from the state metrics and
branch metrics to find maximum value as,

$$L = \max (\alpha_0' + \beta_0 + \gamma_{00}, \alpha_1' + \beta_4 + \gamma_{00}, \alpha_2' + \beta_5 + \gamma_{01}, \alpha_3' + \beta_1 + \gamma_{01},$$
$$\alpha_4' + \beta_2 + \gamma_{01}, \alpha_5' + \beta_6 + \gamma_{01}, \alpha_6' + \beta_7 + \gamma_{00}, \alpha_7' + \beta_3 + \gamma_{00}) -$$
$$\max (\alpha_0' + \beta_4 + \gamma_{11}, \alpha_1' + \beta_0 + \gamma_{11}, \alpha_2' + \beta_1 + \gamma_{10}, \alpha_3' + \beta_5 + \gamma_{10},$$
$$\alpha_4' + \beta_6 + \gamma_{10}, \alpha_5' + \beta_2 + \gamma_{10}, \alpha_6' + \beta_3 + \gamma_{11}, \alpha_7' + \beta_7 + \gamma_{11})$$

$$(2)$$

where, α_0' to α_7' denotes the forward state metrics, β_0 to β_7 denotes backward state metrics
of 8 states and γ_{00} to γ_{11} denotes branch metrics.

Equation 2 is further simplified as Eq. 3 in our proposed simplification for computing
soft output (L) with common γ_{00} to γ_{11},

$$L = \max (\max(s_0, s_1) + \gamma_{00}, \max(s_2, s_3) + \gamma_{01} - \max(t_0, t_1) + \gamma_{11}, \max(t_2, t_3) + \gamma_{10})$$

$$(3)$$

where,

$$s_0 = \max (\alpha_0' + \beta_0, \alpha_1' + \beta_4)$$
$$s_1 = \max (\alpha_6' + \beta_7, \alpha_7' + \beta_3)$$
$$s_2 = \max (\alpha_2' + \beta_5, \alpha_3' + \beta_1)$$
$$s_3 = \max (\alpha_4' + \beta_2, \alpha_5' + \beta_6)$$
$$t_0 = \max (\alpha_0' + \beta_4, \alpha_1' + \beta_0)$$
$$t_1 = \max (\alpha_6' + \beta_3, \alpha_7' + \beta_7)$$

$$t_2 = \max (\alpha_2' + \beta_1, \alpha_3' + \beta_5)$$

$$t_3 = \max (\alpha_4' + \beta_6, \alpha_5' + \beta_2)$$

The extrinsic information/ a-posteriori information $\lambda_{out}(k)$ can be calculated as in Eq. 4 [18], with the aid of L(k), x(k) and y(k) as,

$$\lambda_{out}(k) = \frac{1}{2}L(k) - x(k) - \lambda_{in}(k) \tag{4}$$

where, $L(k)$ denote soft-output, x(k) is the received soft systematic information, $\lambda_{in}(k)$ is a-priori information.

4.2 Performance Analysis

The performance analysis of the channel decoder can be done by decoding delay/latency and the throughput obtained.   But a hardware digital system/circuit performance will be measured in three parameters called power, area, and throughput. This analysis can be done when the proposed architecture is synthesized by hardware design tool like Xilinx ISE/Vivado.

For the proposed design of turbo decoder, the decoding delay is calculated as Eq. 5 and 6 [17] for block sizes less than 264 and from 264 to 6144,

If K< 264,

$$D = (26 + (2f(K,N) + 14)2I) \tag{5}$$

If K≥ 264,

$$D = (26 + (f(K,N) + 46)2I) \tag{6}$$

where, K denote block size, N denote number of decoders and I denote number of iterations and

$$f(K, N) = \begin{cases} \frac{K}{N} & \text{if K is divisible by N} \\ \frac{K}{8} & \text{if K is not divisible by N} \end{cases}$$

Decoding latency (L) is calculated as

$$L = \frac{D}{f_{max}} \ sec \tag{7}$$

The throughput (T) is calculated as

$$T = \frac{[K*f_{max}]}{D} bps \tag{8}$$

where, f_{max} denote the maximum operating frequency, which effects both latency and throughput as in Eq. 7 and 8 [17].

For instance, if the operating frequency of this hardware is about 250 MHz, then the throughput for the block size of 40 bits is 24.38 Mbps and for block size of 6144 bits is 117.7 Mbps.

5. RESULTS AND DISCUSSION

In order to get a higher throughput and lower latency, the most commonly adopted design methodology is to improve the level of parallelism. A new architecture consisting of

an 8-parallel decoder structure has been proposed for the high-performance turbo decoder proposed in the present study. The proposed hardware architecture of the turbo decoder is designed into the three-stage pipeline and three-stage micro-pipeline procedures for high performance. The high-level block diagram is shown in Fig. 5, the simulation waveform and performance analysis of the proposed design are discussed below.

The three-stage pipeline and three-stage micro-pipeline procedure in the proposed parallel turbo decoder is to improve the speed of data processing in the whole structure to improve the throughput and to reduce the latency. The proposed architecture has been designed, simulated in MAT Lab and Modelsim for functionality verification and the simulation waveform is shown in Fig. 6. From the simulation diagram, the throughput latency, or the time taken to produce the first output for the given input, is 1.9 ns.

Fig. 5: High level block diagram of proposed turbo decoder.

Fig. 6: Simulation waveform of proposed parallel turbo decoder.

Then, the RTL schematic shown in Fig. 7 is observed for the proposed architecture in detail for hardware components utilized. Also, the submodules of the proposed parallel decoder, like branch metrics, parallel state metric computations, and LLR computations, are run to find the maximum value of the computed posteriori LLRs to finalize whether the decoded bit belongs to either "0" or "1".
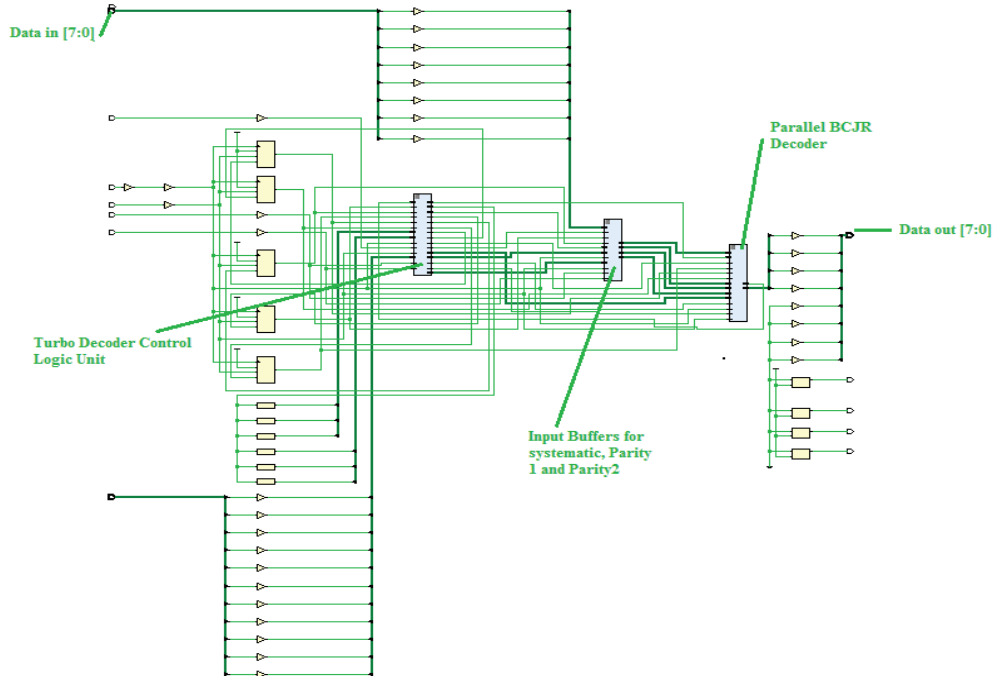

Fig. 7: RTL schematic of proposed parallel turbo decoder using Xilinx VIVADO.

The architecture is implemented over Xilinx Vivado for 28 nm CMOS technology Kintex 7, Vertex-7, and Zynq-7000 Zed FPGA evaluation boards for its performance analysis. The hardware utilization is summarized in Table 3. It can be observed from Table 3 that a much smaller number of logic cells and memory cells are occupied by the proposed design with VLSI optimization techniques than the standard design. As ACS units have been used for metric computation, instead of many arithmetic/logical units, the hardware resource utilization has been reduced. It is evident from the observation that hardware utilization is less at post-implementation than post-synthesis of the design.

Table 3: Hardware resource utilization of parallel turbo decoder

Hardware Resource		Utilization (%) Post-Synthesis	Utilization (%) Post-Implementation	Available
Utilization (%)	FF	809 (0.76%)	809 (0.76%)	106400
	LUT	1072 (2.02%)	1059 (1.99%)	53200
	I/O	38 (19%)	34 (17%)	200
	BRAM	32 (22.86%)	32 (22.86%)	140
	BUFG	1 (3.12%)	1 (3.12%)	32
Power consumption (in Watt)			0.157	

Once the functionality is proven, then the netlist of the design is ready for further processing. Synthesized-netlist has been placed, routed, and checked for timing violations.

The timing report was generated for the proposed design and the critical path delay of 3.04ns and the respective maximum operating clock frequency obtained was 329MHz, as presented in Table 4.

Table 4: Throughput, latency, and power utilization of the proposed turbo decoder

Platform	Critical path delay ns	Max.Clock frequency f_{max} MHz	Block size K	Latency L µs	Throughput T Mbps
Kintex-7 28 nm	3.04	329	40	1.34	32
CMOS	3.04	329	6144	39.67	155

The proposed parallel turbo decoder on Xilinx Kintex-7 FPGA, achieved a throughput of 155 Mbps and 32 Mbps, and the latency of 39.67 µs and 1.34 µs for the block lengths of 6144 and 40, respectively. Furthermore, maximum clock frequency f_{max} of 329 MHz was observed as listed in Table 4. It can be seen from Table 4 that this parallel design achieved 155 Mbps of throughput at maximum flock frequency of 329 MHz and 39.67 µs of latency for block size 6144 on 28 nm CMOS Kintex-7 FPGA.

The proposed parallel architecture with these techniques gives reduction in energy consumption of the proposed architecture compared to the general architecture. The estimated performance analysis of the proposed turbo decoder on various Xilinx FPGA and the comparison of obtained results with other recent turbo decoder designs are shown in Table 5. It is observed that the present work provides a balanced design between performance parameters of speed, area, and power. It is evident from the results that for similar Algorithm, block size, and approximately the same number of interactions, the proposed turbo decoder gives a much better throughput.

Table 5: Comparison of the proposed Turbo decoders with other reported works

Parameter	Z Yan 2016 [19]	Hua. L 2017 [18]	Vadim B 2017 [20]	Rahul 2018 [11]	Farzana 2019 [21]	Farzana 2019 [21]	**Present work**	**Present work**
Target device/ FPGA family	130 nm CMOS	28 nm Vertex-7	Virtex-7 28nm	28 nm Zynq	28 nm Vertex-7	28 nm Vertex-7	**28 nm Vertex-7/Zynq**	Kintex-7
Parallelism/Radix	08-Apr	64	-	8/2	8	-	**8**	**8**
Algorithm	Max-Log MAP	Max-Log MAP	Max-log-MAP	Max-log-MAP	Max-log-MAP	Max-log-MAP	**Max-log-MAP**	**Max-log-MAP**
Block size	6144	6144	6144	6144	6144	6144	**6144**	**6144**
Number of iterations	5.5	8	5	8	8	8	**8**	**8**
Maximum clock rate (MHz)	290	250	270.9	276	86.3	86.3	**252.5**	**329**
Throughput (Mbps)	384.3	2120	5	80	86.3	10.7	**118**	**155**

6. CONCLUSIONS

The present study highlights the concept of a new architecture with a three-stage pipelined parallel turbo decoder and three-stage micro-pipelined MAP decoder. These techniques have specifically improved the throughput and operating clock frequency by

pipelined parallel implementation of the turbo decoder and shortened the critical path delay in the whole design. Algorithmic approximation and architectural optimization like pipelining and parallelizing were used to minimize the critical path and attain a higher throughput. However, the hardware complexity advances linearly as the number of sub-blocks or iterations increases and increased recursions in architecture of the MAP decoder normally limit the throughput of the turbo decoder. The estimated performance has been observed by implementing the proposed parallel turbo decoder at 28 nm CMOS technology Xilinx Kintex7 FPGA and achieved a maximum estimated throughput of 155 Mbps with 8 iterations, which is suitable for 3GPP-LTE-Advanced, as per its specification. The proposed design improved throughput to the tune of 55.6% as compared to other recently reported designs.

From the performance analysis of the proposed turbo decoders and comparison with other recent turbo decoder designs, it is evident that the proposed architecture provides a balanced design among performance parameters, speed, and area. It can be concluded that throughput increases for the optimized turbo decoder and parallel turbo decoder architectures as compared to the standard design. However, the area requirement or power consumption increases proportionately with the throughput.

ACKNOWLEDGEMENT

REFERENCES

[1] Berrou C, Glavieux A, Thitimajshima P. (1993) Near Shannon Limit Error Correcting Coding and Decoding: Turbo-Codes. Proceedings of IEEE International Conference on Communication: pp 1064-1070. doi: 10.1109/ICC.1993.397441

[2] Mackay DJC, Neal RM. (1996) Near Shannon limit performance of low density parity check codes. Electronics Letters, 32(18): 1645-1646. doi: 10.1049/el:19961141

[3] Arıkan E. (2009) Channel polarization: A method for constructing capacity achieving codes for symmetric binary-input memoryless channels. IEEE Transactions on Information Theory, 55(7): 3051-3073. doi: 10.1109/TIT.2009.2021379

[4] Bahl L, Cocke J, Jelinek F, Raviv J. (1974) Optimal decoding of linear codes for minimizing symbol error rate (corresp.). IEEE Transactions on Information Theory, 20(2): 284-287. doi: 10.1109/TIT.1974.1055186

[5] Robertson P, Villebrun E, Hoeher P. (1995) A comparison of optimal and sub-optimal MAP decoding algorithms operating in the log domain. Proceedings of IEEE Intenational Conference on Communications: pp 1009-1013. doi: 10.1109/ICC.1995.524253

[6] Parhi KK. (1999) VLSI Digital Signal Processing Systems: Design and Implementation. Hoboken, NJ: Wiley.

[7] Nimbalker A, Blankenship TK, Classon B, Fuja TE, Costello DJ. (2008) Contention-free interleavers for High Throughput Turbo Decoding. IEEE Transactions on Communications, 56(8): 1258-1267. doi: 10.1109/TCOMM.2008.050502

[8] Shrestha R, Paily R. (2014) High-Throughput Turbo Decoder with Parallel Architecture for LTE Wireless Communication Standards. IEEE Transactions on Circuits and Systems—I: Regular Papers, 61(9): 2699-2710. doi: 10.1109/TCSI.2014.2332266

[9] Jing-shuin L, Ming-Der S, Chung-Yen L, Der-Wei Y. (2015) Efficient Highly Parallel Turbo Decoder for 3GPP LTE-Advanced. International Symposium on VLSI Design Automation and Test (VLSI-DAT): pp 1-4.

[10] Li A, Xiang L, Chen T, Maunder RG, Al-Hashimi BM, Hanzo L. (2016) VLSI Implementation of Fully Parallel LTE Turbo Decoders. IEEE Access, 4: 323-346. doi: 10.1109/ACCESS.2016.2515719

[11] Shrestha R, Sharma A. (2018) VLSI-Architecture of Radix-2/4/8 SISO Decoder for Turbo Decoding at Multiple Data-rates. Proceedings of IFIP/IEEE International Conference on Very Large Sale Integration (VLSI-SoC): pp 131-136. doi: 10.1109/VLSI-SoC.2018.8644753

[12] Luo H, Zhang Y, Li-ke H, Cosmas J. (2017) Low Latency Turbo Decoder implementation for Future Broad Casting Systems. IEEE International Symposium on Broadband Multimedia Systems and Broadcasting: pp 1-4. doi: 10.1109/BMSB.2017.7986227

[13] Shi Y, Zhan M, Zeng J. (2018) FPGA Implementation and Power estimation of a memory reduced LTE-Advanced Turbo decoder. Proceedings of IEEE Conference on IoT, Green Computing and Communications, Cyber, Physical and Social Computing, Smart Data, Block Chain, Computer and Information Technology: pp 607-611. doi:10.1109/Cybermatics_2018.2018.00124

[14] Narayanan A, Murugan S, Bhakthavatchalu R. (2019) Low Latency Max Log MAP based Turbo Decoder. Proceedings of International Conference on Communication and Signal Processing (ICCSP): pp 721-724. doi: 10.1109/ICCSP.2019.8697955

[15] Sujatha E, Subhas C, Giriprasad MN. (2019) Performance improvement of Turbo decoder using VLSI optimization Techniques. IEEE International Conference on Vision, Towards Emerging Trends in Communication and Networking (ViTECoN): pp 84-90. doi: 10.1109/ViTECoN.2019.8899585

[16] Zhan M, Pang Z, Yu K, Wen H. (2021) Reverse Calculation-Based Low Memory Turbo Decoder for Power Constrained Applications. IEEE Transactions on Circuits and Systems I: Regular Papers, 68(6): 2688-2701. doi: 10.1109/TCSI.2021.3068623

[17] Evolved Universal Terrestrial Radio Access (E-UTRA); Multiplexing and Channel Coding. (2008) 3GPP Technical Specification Group Radio Access Network TS 36.212 Rev. 8.3.0 Release 9.

[18] Hua L, Yue Z, Li-ke H, John C. (2017) Low Latency Turbo Decoder implementation for Future Broad Casting Systems. IEEE International Symposium on Broadband Multimedia Systems and Broadcasting, Cagliari, Italy: pp 1-4.

[19] Yan Z, He G, He W, Wang S, Mao Z. (2016) High Performance Parallel Turbo Decoder with Configurable Interleaving Network for LTE application: Integration. The VLSI Journal, 52: 77-90. https://doi.org/10.1016/j.vlsi.2015.05.003

[20] Belov V, Mosin S. (2017) FPGA implementation of LTE turbo decoder using MAX-log MAP algorithm. Sixth Mediterranean Conference on Embedded Computing (MECO): pp 1-4. doi: 10.1109/MECO.2017.7977157

[21] Farzana S, Butt MFU, Agha S, Ng SX, Maunder RG. (2019) Performance Analysis of High Throughput MAP Decoder for Turbo Codes and Self Concatenated Convolutional Codes. IEEE Access, 7: 138079-138093. doi: 10.1109/ACCESS.2019.2942152

FUZZY LOGIC AND PI CONTROLLER FOR PHOTOVOLTAIC PANEL BATTERY CHARGING SYSTEM

Mazbahur Rahman Khan, S. M. A. Motakabber[*]**,
AHM Zahirul Alam and Syed Ahmad Fawwaz Wafa**

*Department of Electrical and Computer Engineering, Faculty of Engineering,
International Islamic University Malaysia,
Jalan Gombak, 53100 Kuala Lumpur, Malaysia.*

[*]*Corresponding author: amotakabber@iium.edu.my*

ABSTRACT: Due to the nonlinear property of the PV panels, there are a few significant restrictions and limitations in the PV solar system. The PV panels always have to depend on environmental conditions such as temperature and solar radiation to generate efficient power. This paper proposed an optimum control system that can handle the uncertainties and nonlinearities of any system by using the Fuzzy Logic Control system (FLC). The proposed system utilized an FLC system for a DC-DC boost converter, tracking the PV panel's maximum power point (MPPT). A PI control system is also used to maintain the continuous power supply for an optimum battery charging system for the DC-DC Buck converter. The goal is to provide constant voltage and appropriate current for charging the battery. It will increase the system efficiency and reduce the losses. It would also increase the battery life cycle and help the battery to charge fast. There are several MPPT methods found in the literature. The FLC can make a precise decision by considering the environmental state of the system. It can get a response to nonlinear environmental conditions instantly. The proposed system yielded an expected accuracy of 92% to 96%, with a system efficiency of 76% to 83%. Besides, it does not require any knowledge about the system since it is a rule-based system. The entire system has been designed in MATLAB/Simulink. The simulation results have been analyzed under 9 environmental states in a 1.0 s period.

ABSTRAK: Berdasarkan struktur tak linear panel PV, terdapat beberapa faktor kekangan yang jelas dan had tertentu dalam sistem solar PV. Panel PV selalunya sering bergantung kepada kondisi persekitaran seperti suhu dan radiasi solar bagi menghasilkan tenaga optimum. Kajian ini mencadangkan sistem kawalan optimum yang dapat mengawal ketidaktentuan dan ketidak linearan apa-apa sistem menggunakan sistem Kawalan Logik Fuzi (FLC). Sistem yang dicadangkan ini menggunakan sistem FLC bagi penukaran penggalak DC-DC, mengesan titik tenaga maksimum panel PV (MPPT). Sistem Kawalan PI turut digunakan bagi menyediakan bekalan tenaga berterusan untuk sistem pengecas bateri optimum melalui penukaran Balik DC-DC. Matlamat adalah bagi menghasilkan voltan berterusan & arus mencukupi bagi mengecas bateri. Ia dapat meningkatkan kecekapan sistem dan mengurangkan pembaziran tenaga. Ia juga dapat meningkatkan kitaran hayat bateri dan membantu bateri mengecas dengan cepat. Terdapat beberapa kaedah MPPT dijumpai dalam kajian terdahulu. FLC dapat menghasilkan keputusan tepat dengan mengambil kira keadaan persekitaran pada sistem tersebut. Ia dapat memberi respon kepada keadaan persekitaran tak linear dengan serta merta. Sistem yang dicadangkan menghasilkan ketepatan yang dijangkakan sebanyak 92% hingga 96%, dengan kecekapan sistem sebanyak 76% hingga 83%. Selain itu, ia tidak memerlukan apa-apa pengetahuan tentang sistem tersebut kerana sistem ini berdasarkan aturan.

Keseluruhan sistem dibangunkan menggunakan MATLAB/Simulink. Dapatan simulasi dikaji menggunakan 9 tahap persekitaran dalam tempoh 1.0 s.

1. INTRODUCTION

In recent decades, the world has been observing tremendous pressure from insufficient available energy resources and several environmental threats such as rising greenhouse gases. According to scientists and environmental researchers, future energy development is dependent on renewable energy since all the non-renewable energy sources like fossil fuels, coal, and natural gases are finite [1,2]. Renewable source Solar cells are also considered one of the possible alternatives to non-renewable energy sources. Considering the advantages of the photovoltaic system, it is gaining popularity day by day. However, the PV panel has some disadvantages, such as low power efficiency (9% - 17%) and high maintenance and installation costs [3, 4]. The power of the PV panels always depends on the environmental condition. The nonlinear change of the environmental condition causes the change in the current and voltage of the PV panel [3,4]. The main challenge is to drive the PV panels at Maximum Power Point (MPP) to make the system more efficient and affordable. The maximum power point tracking (MPPT) is a method or algorithm that extracts the highest power from the PV panel and delivers it to the load [5]. The entire PV system operates on the PV curves, which can be applied under all environmental conditions. It enables the process to provide maximum output power while maintaining maximum efficiency [2]. Many MPPT methods have been designed and applied in literature and journals. Some of the popular MPPT methods are the Constant Voltage (CV) method, the Perturb and Observe (P and O) method [6,7], VSINC method [8] MPPT method by DC-DC Boost converter [5]. This paper has analyzed and proposed an optimum fuzzy logic-based control system to track the MPP from the PV panel. Fuzzy logic is a part of artificial intelligence that can handle the nonlinear properties of any system. It shows better performance compared to the conventional control method. Moreover, it can be implemented on any microcontroller since the fuzzy logic algorithm is simple.

Although PV panel has considered one of the most effective renewable sources, it is unavailable, such nighttime. Due to the limitations of the PV panel and uncertainties of the environmental conditions, a battery storage system is attached for continuing supply to the load when there is no power supply from the PV panel [1]. Furthermore, a suitable charging control system is applied to improve the cost and system efficiency, which would increase the battery lifetime and its efficiency [8]. This paper describes the design of a PI control system as a battery charging controller to ensure that the PV panel will supply the constant current and constant voltage to the Battery under any environmental condition.

A similar study was conducted by Unal Yilmaz and friends in 2018, where they used FLC for MPP tracking and PI controller as a charge controller [4]. Although, the studies did not mention the state of charge (SOC) of the Battery with constant current and voltage supply. The proposed system has used different algorithms for FLC, and the system's efficiency is much higher than that studies. Besides, the proposed system has shown the results of the SOC of the Battery with constant current and constant voltage under variable environmental conditions.

2. CONTROLLER DESCRIPTION

2.1 Fuzzy Logic Controller for MPPT

Many MPPT methods have been designed in literature, such as Perturb and Observe (P&O) method and the Conductance and incremental MPPT method [6,7]. In this project, the fuzzy logic controller (FLC) has been chosen and applied to track the maximum power point from the PV panel over other methods. Figure 1 shows the basic functional block diagram of an FLC. The FLC offers much better performance in handling nonlinearity and uncertainties. The other MPPT method, like the P&O technique, faces disturbance in tracking MPP when the environmental condition changes nonlinearly and rapidly [7]. The FLC is a rule-based system requiring complex mathematical models like root locus and bode plots. Besides, the algorithm is straightforward and can be implemented in a microcontroller [9].
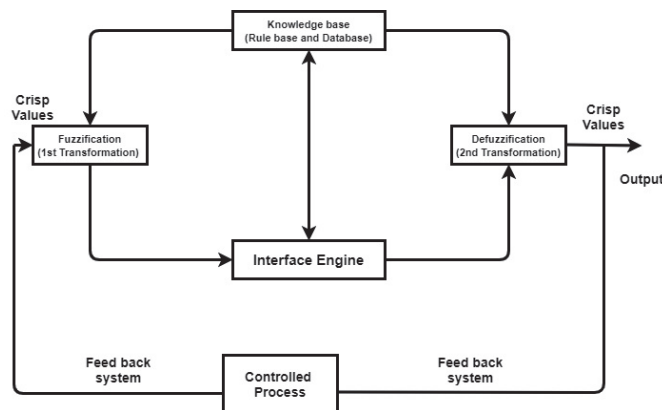

Fig. 1: Block diagram for FLC.

2.2 PI Controller for Constant Voltage Supply

Many research papers prove that the continuous charging and discharging process makes the battery life shorter and can be overcharged and insufficiently charged. Charging a battery up to 70% to 80% is not difficult. The challenging part would be charging the rest 30% to 20% [10]. A fast and efficient charging process requires a continuous power supply. It can be achieved using a specific control system such as fuzzy logic control or PI control strategy [1,3]. Figure 2 shows the basic function of a typical PI controller. This research proposes a PI controller to maintain the appropriate current and constant voltage supply to the Battery since it is simpler and easier to implement than the FLC battery charging method. It also shows precise and satisfactory results [4,8].
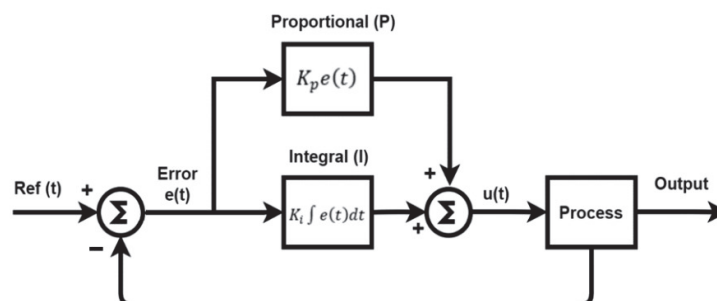

Fig. 2: PI controller block diagram.

The PI has only two constant gains, which are *Kp* and *Ki*. Therefore, by considering the output, *u(t)*, the following equation of the PI controller is derived by [10].

$$u(t) = K_p \, \varepsilon(t) + \frac{1}{\tau} \int_0^t \varepsilon(t)dt \tag{1}$$

3. DESIGN AND IMPLEMENTATION

Figure 3 shows the proposed system block diagram for the PV panel's MPPT and battery charge control. The proposed system consists of a PV panel, a DC-DC boost converter with FLC for maximum power point tracking, and a DC-DC buck converter with a PI controller for the constant current and voltage supply load. A battery has been adopted as an energy storage system - finally, the current and the voltage flow through the FLC from the PV panels. The current and the voltage are used as the input for the FLC. The FLC converts the input and generates the output, the system's duty cycle. The FLC regulates the duty cycle of the PWM (Pulse Width Modulation) scheme, which is applied to switch to the DC-DC converter to control the converter's power.
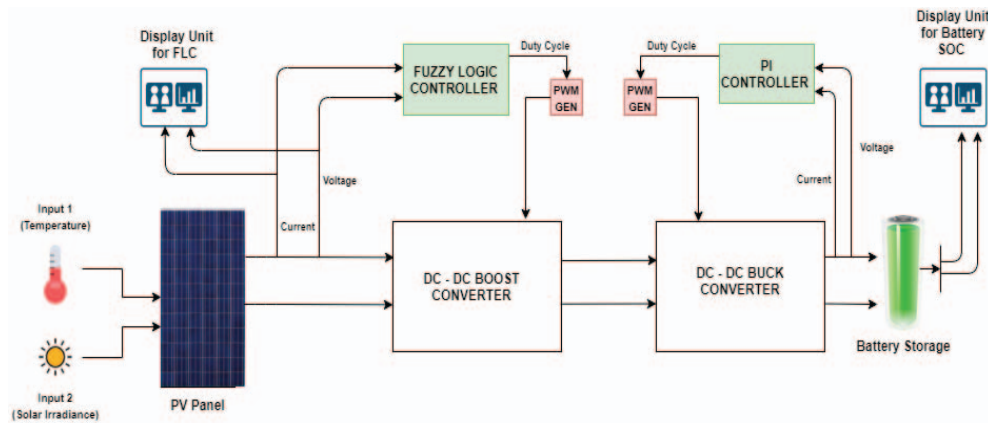

Fig. 3: Proposed system for MPPT and battery charge control of the PV panel.

3.1 Design a Fuzzy Logic Controller

A proposed FLC has been designed based on Fig. 1, and four different logics have been developed using the membership function. Figure 3 shows the main operational steps of the FLC. To get the appropriate output results to track the Solar MPP, each logic of the FLC has to play a different role in the controller.

Step 1: Convert the crisp value into a fuzzy value (Fuzzification). The input (*E*) and Change of Error (*CE*) ranges are selected based on the proposed design. Then, each input (the crisp value) is converted into 5 Fuzziness values. The respected fuzziness values are Negative small (*NS*), Negative big (*NB*), Zero (*ZE*), Positive small (*PS*), and Positive big (*PB*). The input 2 for FLC is the change of PV voltage. The voltage deviation is used to develop the MPPT algorithm for FLC.

Step 2: Selection of membership function. A triangular membership function has been chosen for both inputs and output. The membership function is a graphical illustration to demonstrate the magnitude of input variables. There are five fuzziness values in both input and output, as shown in Fig. 4.

Step 3: Apply the rules. Since each input has 5 fuzzy values, so 5×5 matrix has been applied to generate the output. Therefore, 25 rules have been made to track the MPP of the PV panel. After defining the inputs and the output membership functions, the fuzzy logic rules are made based on Table 1. Where the delta P (ΔPpv) and delta-V (ΔVpv) are the inputs and the reference delta-V (ΔVpv*) is the output of the system.
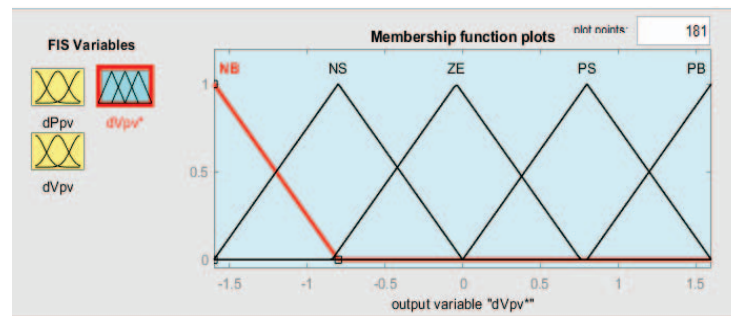
Step 4: Defuzzification: At the final step, the fuzzy values are converted into crisp values to use as an output, a Duty cycle of the system. The FLC uses the rules-based system and generates the output accordingly whenever changes occur on the input side.
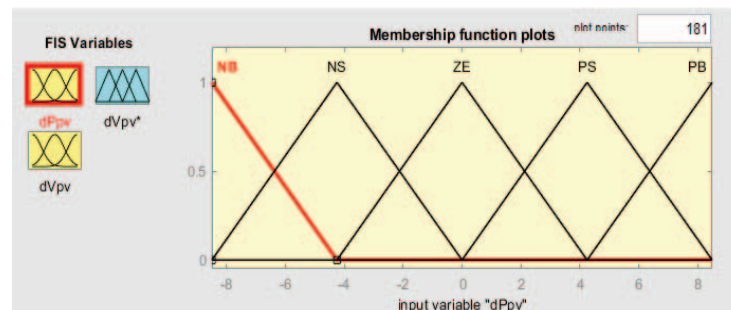
(a)
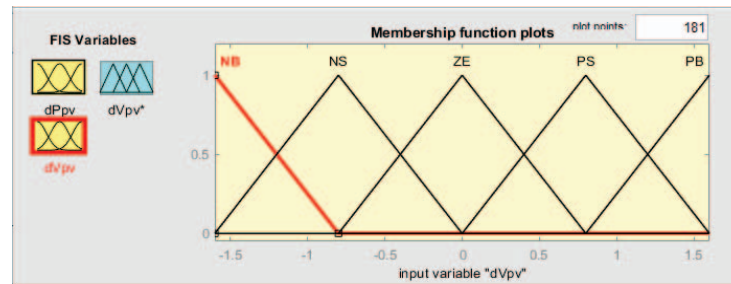
(b)

(c)

Fig. 4: Membership function, (a) input 1, (b) input 2 and (c) output.

Table 1: Rules table of FLC for proposed algorithm

$\Delta V_{pv}*[0/p]$	Vpv [i/p]					
		NB	NS	ZE	PS	PB
$\Delta P_{pv}[i/p]$	NB	PS	PB	NB	NB	NS
	NS	PS	PS	NS	NS	NS
	ZE	ZE	ZE	ZE	ZE	ZE
	PS	NS	NS	PS	PS	PS
	PB	NS	NB	PB	PB	PS

3.2 Design of MPPT Algorithm by Using FLC

The FLC is considered one of the efficient control systems. Giving intellectual and intelligent output under nonlinear conditions makes the FLC unique from other controllers. The basic working strategies of the FLC to achieve the maximum power from the PV panel are, first, the FLC algorithm takes voltage and current from the PV panel as an input to the system. Then it uses to compute the power (P = IV) to find out the controller's inputs. Two inputs of the FLC are considered as the error and the change of error. Finally, the output of the FLC goes through the duty cycle of the PWM to maintain the DC-DC Boost converter [4,7].

$$Error(k) = \frac{P(k) - P(k-1)}{V(k) - V(k-1)} \tag{2}$$

$$Change_{Error(k)} = Error(k) - Error(k-1) \tag{3}$$

Where the $P(k)$ and $V(k)$ are considered as instant power and the voltage of the PV generator, $V(k-1)$ and $P(k-1)$ are the previous current and the previous power, respectively.

TFLC uses the inputs for the MPPT of the PV panel to gain the appropriate outcomes. The following steps should be applied to run the duty cycle of the boost converter. First, the input and the output variables should be specified in the system. Then, the membership function of the system would convert the crisp value into fuzziness and generate the degree of the trueness of the process. Finally, the rule-based system determines the output by observing the input, as illustrated in Fig. 1. The rules are applied to trace the change in power in terms of voltage (dp/dv) that would control by the duty cycle of the PWM to make an appropriate adjustment (increase/decrease) of voltage until the desired maximum power point is achieved [6,9,13]. The entire PV system operates on the P-V characteristic graph under variable conditions. The MPPT algorithm should be designed accordingly to track the maximum power. Figure 5 shows the power versus voltage characteristics of a solar panel and the MPPT algorithm techniques. The power curve Fig. 5 illustrates the maximum power point under the standard condition when the irradiance is 1000 W/m^{2,} and the temperature is 25 ℃. The trained of the curve observed from the curve that, for tracking the MPP from the PV panel, 4 conditions must be as follows.

1. When the P(k) - P(k-1) > 0 and V(k) – V(k-1) > 0, the Voltage should be increased.
2. When the P(k) - P(k-1) > 0 and V(k) – V(k-1) < 0, the Voltage should be decreased.
3. When the P(k) - P(k-1) < 0 and V(k) – V(k-1) > 0, the Voltage should be decreased.
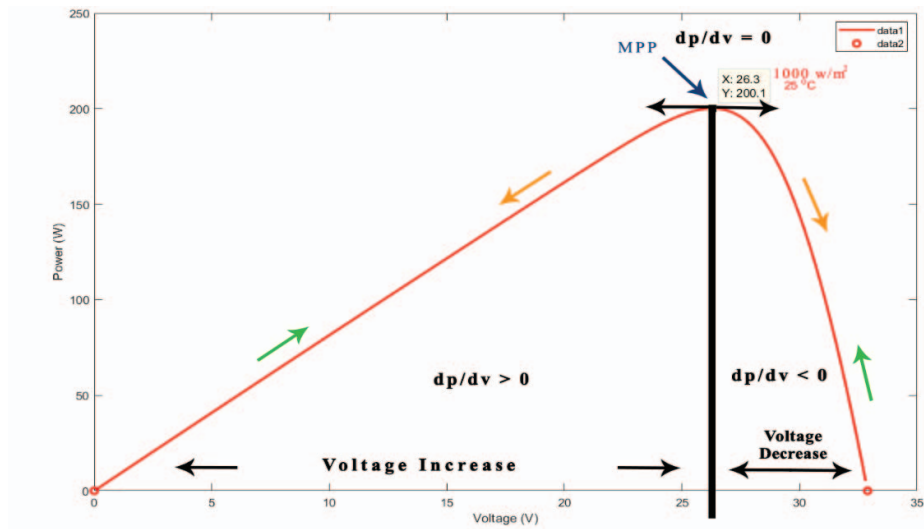4. When the P(k) - P(k-1) < 0 and V(k) – V(k-1) < 0, the Voltage should be increased.

Fig. 5: Power vs voltage characteristic for MPPT algorithm.

The MPPT algorithm has been developed based on Eq. 2 and Eq. 3, and the above conditions. In addition, the MPPT algorithm flow chart has been designed to demonstrate the operations that have taken place inside the system, as shown in Fig. 6.
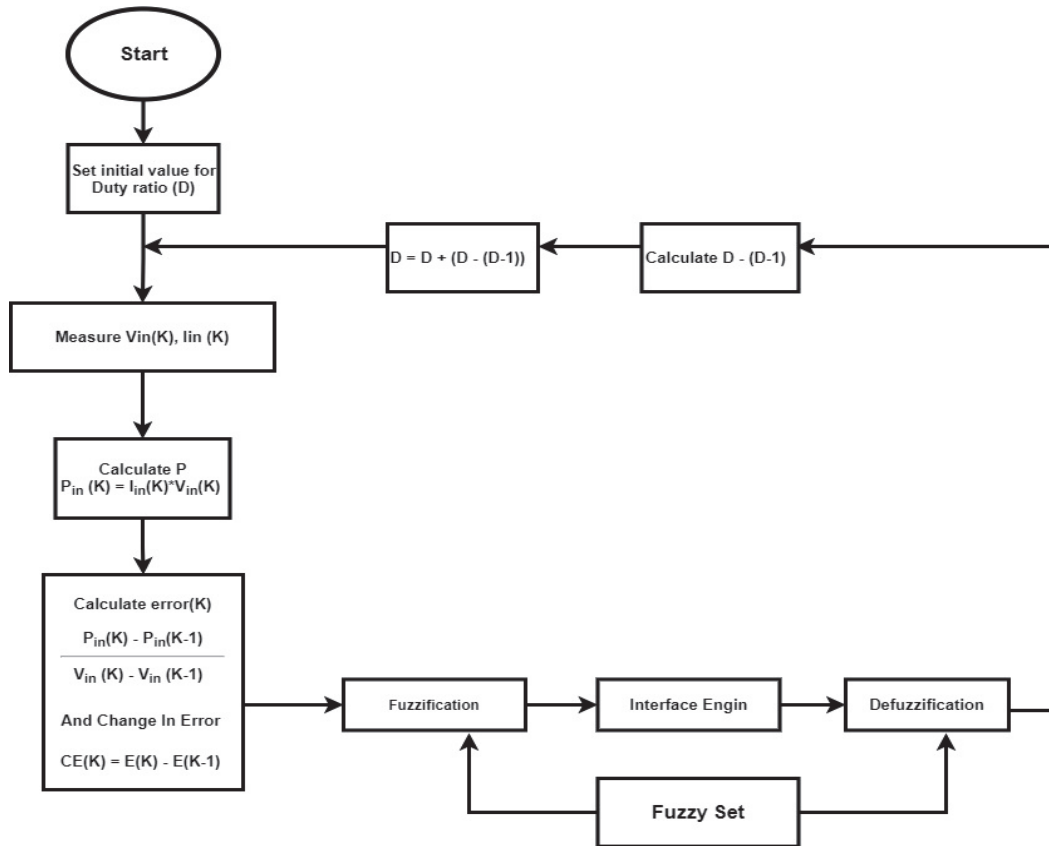

Fig. 6: The operational flow chart of the FLC.

An MPPT algorithm has been developed based on the flow chart, and the system design has been built using the Simulink MATLAB function, as shown in Fig. 7. Table 2 shows the electrical parameters used for the proposed PV panel.
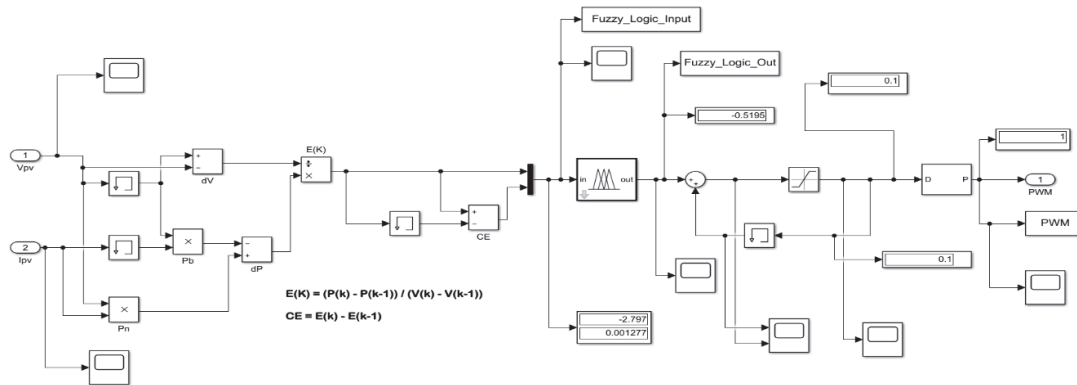

Fig. 7: The MPPT algorithm for the FLC.

Table 2: Electrical characteristic for the proposed PV panel

Parameter	Value
Maximum Power (Pmax)	200 W (+10%/-5%)
Maximum Power Voltage (Vmpp)	26.3 V
Maximum Power Current (Impp)	7.61 A
Open Circuit Voltage (Voc)	32.9 V
Short Circuit Current (Isc)	8.21 A
Temperature Coefficient of Voc	-1.23×10^{-1} V/C
Temperature Coefficient of Isc	3.18×10^{-3} A/C

3.3 Operation of DC-DC Boost Converter

According to the proposed design, a DC-DC Boost converter is used. The efficiency of the maximum power point tracking system depends on the MPPT control algorithm and the MPPT circuit. Usually, the boost converter is connected to the MPPT circuit and the PV panel [7]. It maintains less energy loss when the energy is transferred between two circuits. It also boosts the DC voltage level. In the MPPT algorithm, the FLC is used to switch off the boost converter to control the duty cycle of PWM. The DC-DC boost converter circuit is a switch-based power supply circuit that steps up the system's voltage. It is made of MOSFET, Diode, output capacitor, and an inductor. The MOSFET, the switch of the circuit, played a significant role here since the duty cycle of the PMW generator is connected to MOSFET's gate. It switches ON and OFF the circuits very fast [4].

To find the inductor voltage of the system,

$$V_L = V_{in} - V_{out} \tag{4}$$

To operate the system at the steady-state condition, the current shift on the inductor must be zero during the switching period.

$$\frac{V_{out}}{V_{in}} = \frac{1}{1-D} \tag{5}$$

By using the following equations, the inductor and the capacitor of the boost converter can be found.

$$\Delta I_L = \frac{V_{in\_min} D}{f_s L} \tag{6}$$

where, f_s= switch frequency, L= inductance, D = Duty cycle, V_{in_min}= minimum input voltage. V_{out} = output voltage, V_{in}= input voltage, ΔI_L= estimated inductor ripple current. C = capacitance, I_{out} = output current, ΔV_{out}= estimated output ripple voltage

$$C = \frac{I_{out} \cdot D}{f_s \cdot \Delta V_{out}} \tag{7}$$

3.4 Design and Operation of DC-DC Buck Converter

The Buck converter with the PI control system to achieve the appropriate current and constant voltage has. The goal of using the DC-DC buck converter in the circuit is to step down the voltage and make it appropriate for battery charging. It is also a switch-mode power supply system regulated by a PWM generator like the DC-DC Boost converter. The converter can be used fort he wireless charging system [14]. The DC-DC buck converter circuit reduces the input voltage by stepping up the current. That is another advantage of the buck converter. The PWM generator is connected to the MOSFET's gate to operate the circuit switch. The inductor voltage of the converter can be calculated by the equation [4].

$$V_L = V_{in} - V_{out} \tag{8}$$

$$V_{out} = D \, V_{in} \tag{9}$$

Overall, when the switch is ON, the inductor gets current from the source. When the switch is OFF, the inductor receives current from the capacitor, so the total current becomes more significant than the input source current. The Inductor current of the converter is as follows,

$$\Delta I_L = \frac{V_{out}(V_{out} - V_{in})}{f_s \, L \, V_{in}} \tag{10}$$

The capacitor of the converter [4],

$$\Delta V_{rpl} = \frac{D \, I_L}{8 \, f_s \, C} \tag{11}$$

where, V_{rpl} = ripple voltage.

3.5 PI Controller for Constant Voltage Supply

The PI controller is used in this project as a negative feedback system, as shown in Fig. 8 and Fig. 9. A reference voltage has been set that indicates what the system would do. The PI controller compares these two signals and passes the zero-error signal. PI controller has proportional gain (Kp) that can calculate the present error, and it is helpful to reduce set up time and integral gain (Ki) that can calculate the past error. Furthermore, it is instrumental in lowering the steady-state error [4].

To obtain the constant voltage method, the PI control system is used to control the output voltage of the buck converter. The reference voltage = 26.567 V since this is the fully charged voltage for a 24 V DC lead-acid battery (open-circuit voltage of the battery when

the SOC = 100%). That indicates that when the voltage level reaches that point, the battery stops charging.

Fig. 8: PI controller for constant voltage supply.
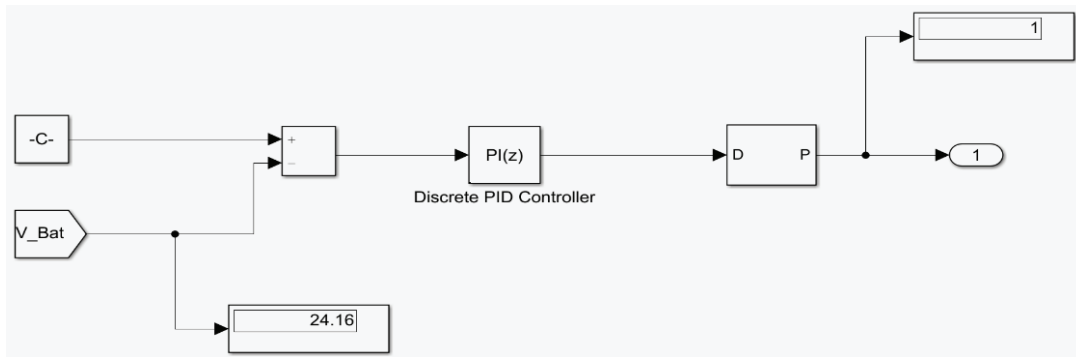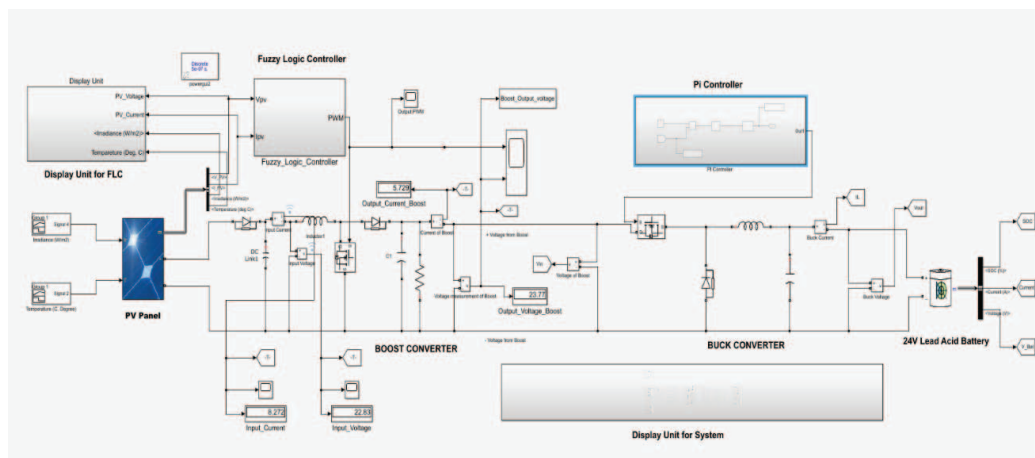

Fig. 9: Simulink model of the proposed system.

4. RESULTS AND ANALYSIS

The proposed design was simulated under nine different states of the environmental condition. The results were compared to determine the accuracy and efficiency of the system, as shown in Fig. 10.
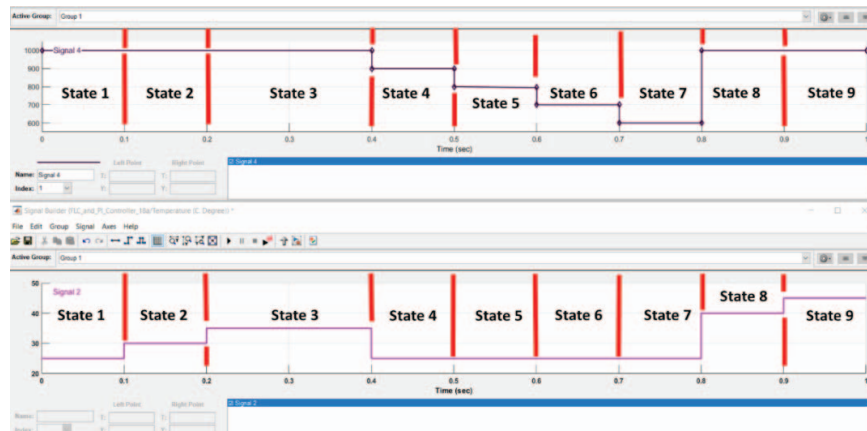
Fig. 10: Inputs of the system.
Irradiance 1000 W/m^2, AM 1.5 spectrum, module temperature 25 ^{o}C.

The MPPT may depend on the characteristic of the PV panel.
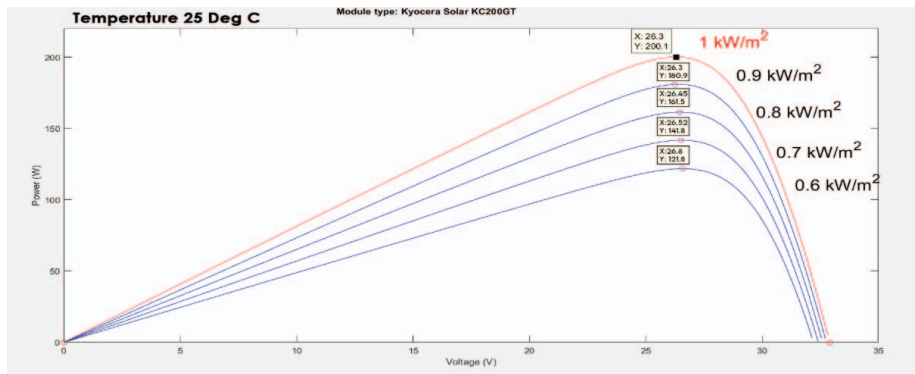
Fig. 11: P-V characteristic curve under variable solar irradiance.
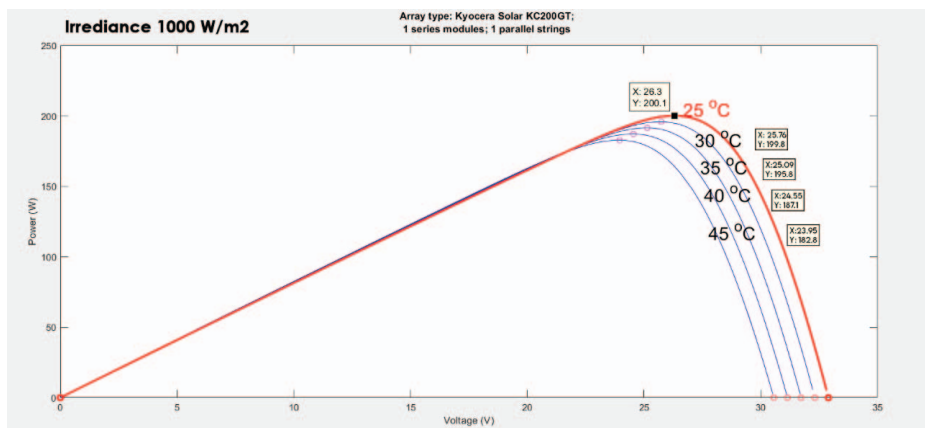
Fig. 12: P-V characteristic curve under variable temperature.

The P-V characteristics curves have been shown in Fig. 11 and Fig. 12 according to nine different states. The simulation results for maximum power point tracking using the FLC algorithm as shown in Fig. 13. The graphs have illustrated the power comparison between PV, DC-DC Boost converter and DC-DC Buck converter circuits. Figures 14, 15 and 16 show the power compensation graphical result of the simulation.
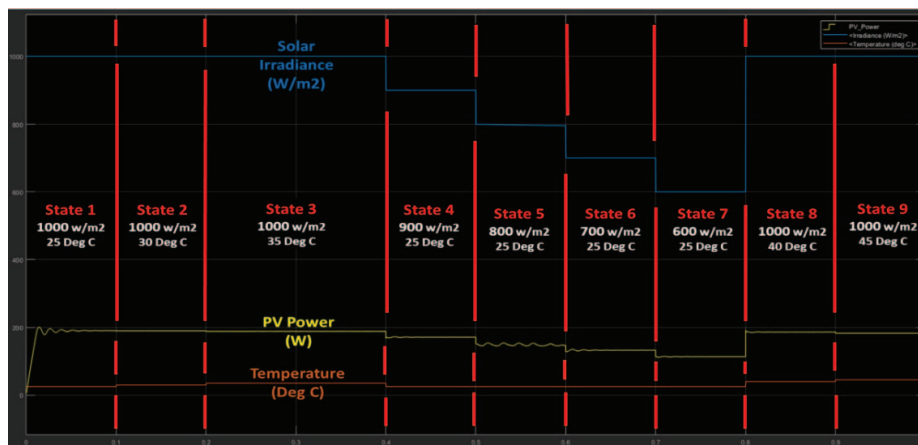
Fig. 13: PV power graph in terms of variable inputs.
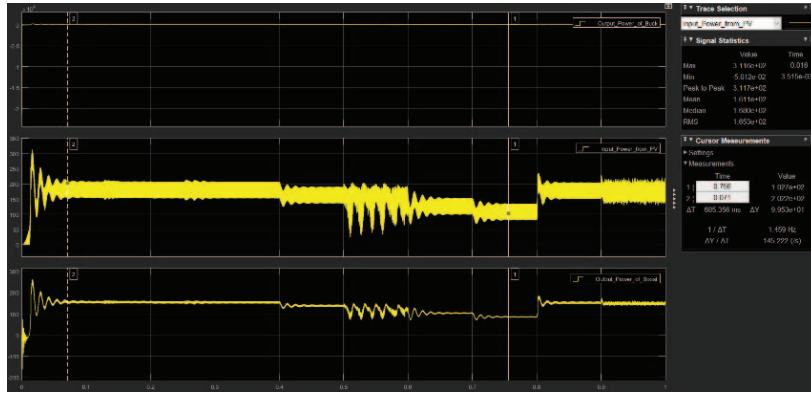
Fig. 14: PV power graph.

Fig. 15: DC-DC Boost power graph.

Fig. 16: DC-DC Buck power graph.

Fig. 17: Voltage comparison graph.

Fig. 18: Current comparison graph.

Figures 17 and 18 show the voltage and current comparison of the systems, respectively. The graphs showed the difference between the input and output voltage of the Boost converter. The yellow line represents the input voltage supplied by the PV panel, and the blue line represents the output voltage, which is used as an input voltage for the DC-DC Buck converter. It is observed that the FLC can track every change in the input signal and produce the output appro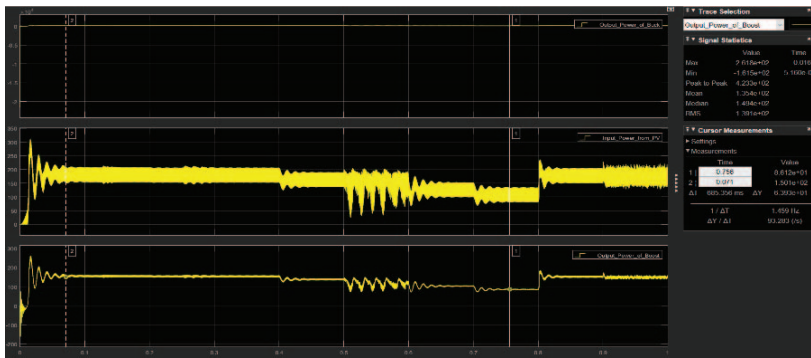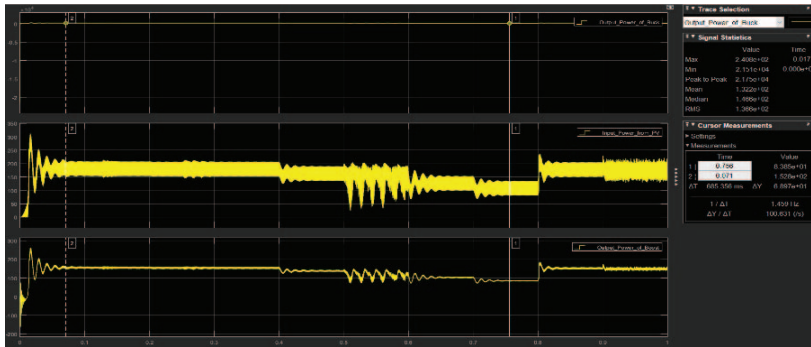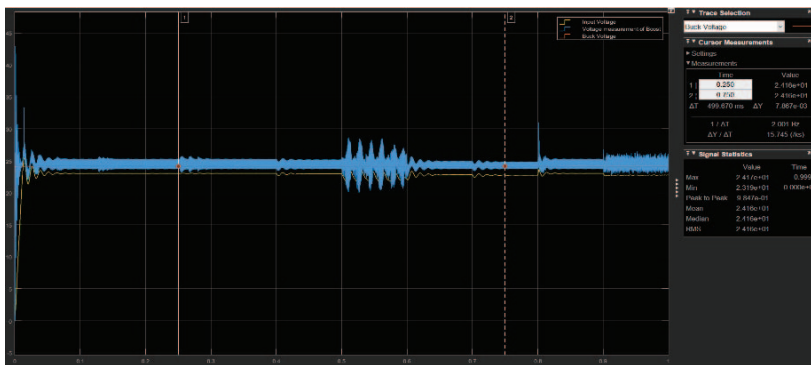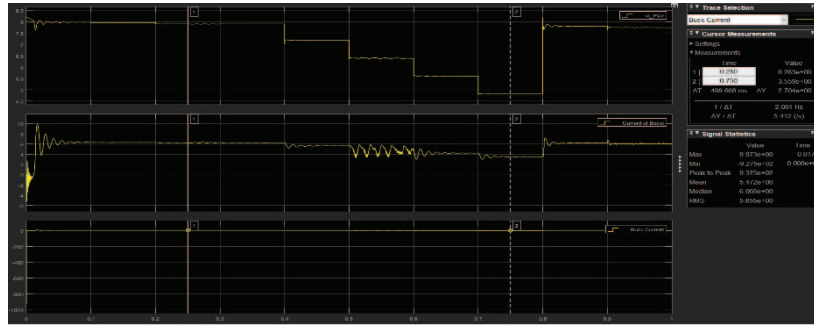priately. The response observation has been done to predict how fast the fuzzy logic controller tracks the MPPT to sudden changes in the input signal. According to the above observation, the FLC takes around 0.004 seconds only to track MPP from the PV panel. Table 3 illustrates the simulation results and the system accuracy and efficiency of the proposed system.

Table 3: The MPPT summary of the results

Environmental State	P(mpp) (W)	P(pv) (W)	Accuracy (%)	P(buck) (W)	Efficiency (%)
State 1: (1000 W/m², 25 °C)	200.1	191.4	95.7	154.4	80.7
State 2: (1000 W/m², 30 °C)	199.3	192.6	96.6	152.5	79.2
State 3: (1000 W/m², 35 °C)	195.0	184.0	94.4	152.1	82.7
State 4: (900 W/m², 25 °C)	180.9	166.6	92.1	136.7	82.1
State 5: (800 W/m², 25 °C)	161.5	148.5	92.0	123.2	83.0
State 6: (700 W/m², 25 °C)	141.8	134.3	94.7	102.2	76.1
State 7: (600 W/m², 25 °C)	121.8	114.8	94.3	84.6	73.6
State 8: (1000 W/m², 40 °C)	187.1	179.8	96.1	154.8	83.0
State 9: (1000 W/m², 45 °C)	182.8	175.9	96.2	150.7	82.6

A constant power supply is essential to charge the Battery efficiently. It would reduce the losses and prolong the battery life. The DC-DC Buck converter with PI controller is used after the DC-DC Boost converter in the circuit to supply the Battery's appropriate current and constant voltage. The simulation results for SOC and constant voltage as shown in Fig. 19.

Figure 20 (a) and (b) show graphical results of how the power and current of a solar panel vary with the variation of environmental parameters, respectively. The graphs shown in Fig. 20(c) are the SOC of the battery in a period of 0.1 s. At time $t = 0.250$ s, SOC = 45.0001% (assume that the Battery was initially charged 45%), and at time $t = 0.750$ s, SOC = 45.0004%. These indicate that the Battery charges linearly despite many changes in the environmental conditions.
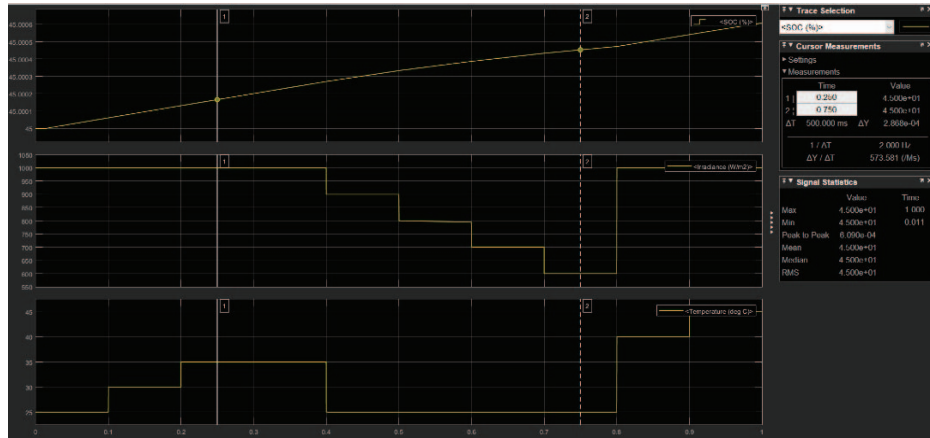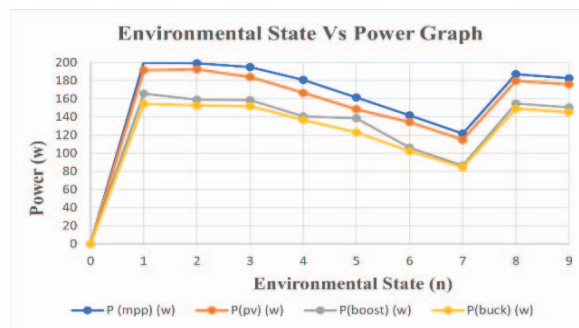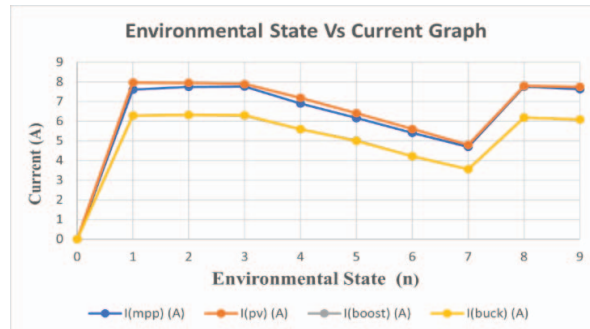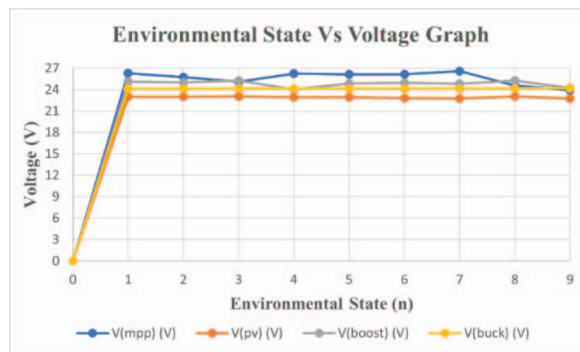
Fig. 19: State of charge (SOC) in terms of different environmental conditions.

(a)

(b)

(c)

Fig. 20: Variation of electrical parameters with environmental state,
(a) power, (b) current, and (c) voltage.

The input and output power, current, and voltage comparison in Fig. 19 have been illustrated under nine variable environmental states. It is observed from Fig. 20(c) that the DC-DC Buck converter voltage is nearly constant and consistent compared to the input voltage (Vpv) from the PV panel and the DC-DC Boost converter voltage (V_{boost}). Since the feedback reference voltage has been set, $V = 26.567$V (fully charged voltage of the Battery) in the PI controller, the output voltage of the buck converter would be settled after reaching that voltage.

Table 4 shows the lead-acid battery's specifications used in the simulation. The Battery's normal operating voltage is 24 V, and the voltage is 26.567 V when it is fully charged, which has been used as a reference voltage for the PI controller.

Table 4: Battery characteristics (from battery datasheet)

Parameter	Value
Voltage Per Unit (V)	24
Maximum Capacity (Ah)	250
Cut-off Voltage (V)	18.3
Internal resistance (Ohms)	0.0010
Operating Temperature Range	-20 to +55 °C
Fully charged Voltage (V)	26.5671

5. CONCLUSION

In this research, the usefulness of the fuzzy logic control system for the PV panel has been discussed and verified. From Table 3 and Fig. 19, it is justified that the proposed fuzzy logic controller effectively handles the nonlinearity and uncertainty of the environmental conditions. This paper also showed a system accuracy of around 92% to 97%. The efficiency with about 73% to 83%, whereas the literature, shows efficiency of around 55% [4,5,7]. According to the literature, charging a battery with a constant voltage and suitable current supply increases the battery life. The proposed system has been used a PI controller to maintain a constant voltage and an appropriate current supply, which can increase the battery life. The Simulink / MATLAB data of the simulation results can be used to conduct the research for hardware implementation by imploring the FLC algorithm in a microcontroller.

REFERENCES

[1]   Aranya SDS, Sathyamoorthi S, Gandhiraj R. (2015) A fuzzy logic-based energy management system for a microgrid. ARPN Journal of Engineering and Applied Sciences, 10(6): 2663-2669.

[2]   Rai N, Rai B. (2018) Control of fuzzy logic-based PV-battery hybrid system for stand-alone DC applications. Journal of Electrical Systems and Information Technology, 5(2): 135-143. https://doi.org/10.1016/j.jesit.2018.02.007

[3]   Greeshma VJ, Sasidharan R. (2016) Battery charging control using fuzzy based controller in a photovoltaic system, International Advanced Research Journal in Science, Engineering and Technology, Sp. Issue of National Conference on Emerging Trends in Engineering and Technology (NCETET'16), 3(3): 114-117. http://iarjset.com/upload/2016/si/NCETET-16/IARJSET-NCETET%2021.pdf

[4]   Yilmaz U, Kircay A, Borekci S. (2018) PV system fuzzy logic MPPT method and PI control as a charge controller. Renewable and Sustainable Energy Reviews, 81: 994-1001. https://doi.org/10.1016/j.rser.2017.08.048

[5]   Abdelhak B, Abdelhalim B, Layachi Z, Sief EB, Amor F. (2018) Fuzzy logic controller to improve photovoltaic water pumping system performance. 6th International Renewable and Sustainable Energy Conference (IRSEC), pp 1-5. DOI: 10.1109/IRSEC.2018.8702841

[6]   Latif T, Hussain SR. (2015) Design of a charge controller based on SEPIC and buck topology using modified Incremental Conductance MPPT. 8th International Conference on Electrical and Computer Engineering: Advancing Technology for a Better Tomorrow, ICECE 2014, 1: 824-827. https://doi.org/10.1109/ICECE.2014.7026999

[7]   Soufi Y, Bechouat M, Kahla S, Bouallegue K. (2014) Maximum power point tracking using fuzzy logic control for photovoltaic system. 3rd International Conference on Renewable Energy Research and Applications, ICRERA 2014, pp 902-906. https://doi.org/10.1109/ICRERA.2014.7016515

[8]   Yau HT, Lin CJ, Liang QC. (2013) PSO based PI controller design for a solar charger system. The Scientific World Journal. https://doi.org/10.1155/2013/815280

[9]   Fannakh M, Ehafyani ML, Zouggar S. (2019) Hardware implementation of the fuzzy logic MPPT in an Arduino card using a Simulink support package for PV application. IET Renewable Power Generation, 13(3): 510-518. https://doi.org/10.1049/iet-rpg.2018.5667

[10] Chabni F, Taleb R, Benbouali A, Amin M. (2016). The application of fuzzy control in water tank level using Arduino. International Journal of Advanced Computer Science and Applications, 7(4): 261-265. https://doi.org/10.14569/ijacsa.2016.070432

[11] Ali OAM, Ali AY, Sumait BS. (2015) Comparison between the effects of different types of membership functions on fuzzy logic controller performance. International Journal of Emerging Engineering Research and Technology, 3(3): 76-83.

[12] Derrouazin A, Aillerie M, Mekkakia-Maaza N, Charles JP. (2017). Multi input-output fuzzy logic smart controller for a residential hybrid solar-wind-storage energy system. Energy Conversion and Management, 148: 238-250. https://doi.org/10.1016/j.enconman.2017.05.046

[13] Noman AM, Addoweesh KE, Mashaly HM. (2012) A fuzzy logic control method for MPPT of PV systems. IECON Proceedings (Industrial Electronics Conference), pp 874-880. https://doi.org/10.1109/IECON.2012.6389174

[14] Motakabber, S. M. A., Alam, AHM Zahirul., Jamal, N. F., Khan, M. R. (2022). Characteristic Study for Wireless Charging System. Asian Journal of Electrical and Electronic Engineering, 2(1), 9–16.

A FUZZY SYSTEM FOR EVALUATING TRUSTWORTHINESS OF USERS IN A SOCIAL NETWORK

MOHAMMAD MAHDI SHAFIEI[1], HOSSEIN SHIRGAHI[2*], HOMAYUN MOTAMENI[1]AND BEHNAM BARZEGAR[3]

[1]*Department of Computer Engineering, Sari Branch, Islamic Azad University, Sari, Iran*
[2]*Department of Computer Engineering, Jouybar Branch, Islamic Azad University, Jouybar, Iran*
[3]*Department of Computer Engineering, Babol Branch, Islamic Azad University, Babol, Iran*

[*]*Corresponding author: h.shirgahi@jouybariau.ac.ir*

ABSTRACT: In recent years, the emergence of various web-based social networks has led to the growth of social network users. These networks have become popular as a medium for disseminating information and communication. Governments and organizations also use social networks as a platform for better services. However, acting in such networks depends on the level of trust that members have with each other. The combination of personality attributes of a person can create a mental impression of the amount of trust that a person has. This amount of trust can affect the person's future interactions. Therefore, trust is an essential and important matter in these networks, especially when someone interacts with someone else on a web-based social network. We discuss this issue in this paper and provide a method for evaluating it. Measuring the accuracy is not easy for the users who are interacting with the social network. Here, the interactions are virtual. In this paper, we have used fuzzy logic to apply ambiguous data and to evaluate trustworthiness by taking into account the various personality attributes of users such as reliability, availability, interest, patience, and adaptability. As we used these attributes as input to the fuzzy system and based on the relevant fuzzy rules, we evaluated the trustworthiness of users in social networks. The proposed fuzzy system is extendable, because in this system, trust can be defined as a set of one or more personality attributes. Epinions social network dataset is also used to simulate and validate the proposed approach. In the proposed method, the MAE value is less than 0.015 and F-Score value more than 0.86. Based on the results, the presented fuzzy system shows an acceptable accuracy for evaluating the trustworthiness of users.

ABSTRAK: Sejak beberapa tahun kebelakangan ini, kemunculan pelbagai rangkaian web sosial telah menyebabkan pertumbuhan pengguna rangkaian sosial. Rangkaian ini telah menjadi popular sebagai medium penularan informasi dan komunikasi. Kerajaan dan organisasi juga menggunakan rangkaian sosial sebagai platfom bagi menyediakan servis perkhidmatan terbaik. Namun, pemakaian rangkaian ini bergantung kepada kepercayaan pengguna antara sesama pengguna. Gabungan ciri-ciri personaliti terhadap seseorang menyebabkan terciptanya persepsi secara mental pada kepercayaan ke atas seseorang. Jumlah kepercayaan ini akan memberi kesan terhadap interaksi yang akan berlaku pada masa depan ke atas individu tersebut. Oleh itu, kepercayaan sangat penting dalam rangkaian ini, terutama apabila seseorang berinteraksi dengan mereka di jaringan sosial web. Isu ini dibincangkan dalam kajian ini dan kaedah evaluasi turut dihuraikan. Mengukur ketepatan pengguna dalam jaringan sosial tidak mudah. Di sini, interaksi berlaku secara maya. Kajian ini menggunakan logik kabur pada data tidak jelas dan bagi mengukur tahap kepercayaan, pelbagai ciri personaliti individu diukur, seperti kebolehpercayaan, kebolehdapatan, minat, kesabaran dan kebolehsesuian. Ciri-ciri tersebut digunakan sebagai input kepada sistem rawak dan berdasarkan peraturan rawak, tahap kebolehpercayaan pengguna diukur dalam rangkaian

sosial. Sistem rawak yang dicadangkan ini boleh dilanjutkan, kerana dalam sistem ini kepercayaan boleh dimaksudkan sebagai satu set atau lebih ciri-ciri personaliti. Anggapan pada set data rangkaian sosial turut digunakan bagi simulasi dan pengesahan kaedah yang dicadangkan. Bagi kaedah yang dicadangkan ini, nilai MAE adalah kurang daripada 0.015 dan nilai skor-F lebih daripada 0.86. Berdasarkan dapatan kajian ini, sistem rawak yang dikaji ini menunjukkan ketepatan yang boleh diterima bagi mengukur tahap kebolehpercayaan pengguna.

1. INTRODUCTION

Trust is a multifaceted concept that can be defined differently according to its application, so it is difficult to determine trust and it is possible to make a mistake. Different domains have brought about different definitions concerning the concept of trust some of which are referred to below. In [1] and [2] psychologists, in their studies, concluded that trust focuses on the mind-set of an individual when he trusts or distrust someone. In [3], trust in computer science generally divides into two parts: 1- User, 2- System. In [4], with respect to a transaction, trust was considered as a relationship between trustor (someone who trusts) and trustee (one who has been trusted). An analysis of [5] for trust in web-based social networks can be found on the basis of the belief that a person has some actions that will bring good results in the future. Based on the definitions given above, this inference stems from different interpretations that may take place with respect to the place and application of the trust. In social networks, one of the topics where trust plays a vital role is the creation and maintenance of relationships, so that one can say that the basis of any relationship is trust.

In web-based social networks, the amount of individual's trust comes from his virtual personality due to his interactions on the web and it can't be compared with daily life as that is face to face. The virtual personality of a person depends on personality attributes that they have viewed virtually. Some of the personality attributes that lead to the trustworthiness of users can be reliability, availability, interest, patience, and adaptability. The point that matters is that these attributes are internal and can be interpreted in a variety of ways, based on a definition that we provide about trust. In this research, we have proposed a method in which the trustworthiness of users can be evaluated depending on one or more personality characteristics. The rest of the paper is organized as follows. In section 2, social networks and related properties are expressed. Section 3 discusses related works about trust in social networks. Section 4 explains the fuzzy system proposed for evaluating trustworthiness. Section 5 describes the evaluation of the proposed the fuzzy system and section 6 discusses the conclusion and future works.

2. SOCIAL NETWORKS AND TRUST MANAGEMENT

Social networks can be specified as a set of nodes and edges that are systematic, so that the nodes describe users, groups, and communities and the edges describe communications. Web-based social networks provide another way to communicate with others, affecting social relationships in the real world. It can be said that many of the relationships created in these networks, despite being virtual, are stronger than real-world relationships [6]. Several definitions of a social network have been proposed in various domains. For example, [7] proposed a graph-based framework with the structure of a decentralized system.

2.1 Social Network Properties

In [8], properties of social networks have been discussed, including the phenomenon of homophily and the small world. Homophily means the readiness of users to cooperate, to establish relationships and to make pledges with others. In [9], homophily is discussed in two types. The first type is status homophily, where users tend to associate with those who have similar social attributes with them, such as race, age, occupation, etc. The second type is value homophily, which is based on values, attitudes, and beliefs. This means that users tend to associate with the users who have similar thinking without considering their situation. The phenomenon of the small world visualizes the world as a "small world", where all users are linked by a small chain. For example, users with similar interests are associated together with web-based social networks.

2.2 The Importance of Trust in Social Networks

The growth of web-based social networks in online communities has become a major source of communication and can be seen from the popularity of social network sites such as Facebook, YouTube, Instagram, and so on [6]. This popularity has been the impetus for the production and growth of many web-based social networks in specific communities. Lots of social networks currently is use are designed to connect and interact with different users in different places [8].

In social networks, the concept of FOAF (Friend of a Friend) has many uses. This concept suggests that someone can interact with a friend of friends and engage in friendship. Given the fact that the trust is the basis of each friendship, trustworthiness may not be true for a friend of friends. For this reason, one of the risks is the security of private data on social networks, according to the concept of FOAF. Such risks have been experienced on social networking sites and are reported in [8, 20].

2.3 Trust Management in Social Network

In [11], trust management systems are classified into three categories: 1) credential and policy-based, 2) reputation based, and 3) social networks based. The main purpose of the first category, which is credential and policy-based, is validating the entity to enable access control. The second category, which is reputation based, builds trustworthy and secure communications by evaluating the reputation and popularity of the entity in the environment. The third category in trust management systems, which is based-on social networks in addition to considering the reputation, use social relationships among peers to establish the trusted relationships.

3. RELATED WORKS

In [1], trust in social networks has been investigated. In [4], an approach was proposed to determine the quantitative content of the shared contents in terms of its trustworthiness. Authors focused on determining trustworthiness of shared content in the health domain as the negative impact of acting on untrustworthy information is high in this domain. In [12], authors provided algorithms for inferring trust among individuals who are not familiar with or interact with each other. Also, a way to extract information and integrate it into applications was investigated. The algorithms proposed for inferring trust depend on the reputation information.

In [13], an algorithm called TidalTrust was proposed to infer trust. The algorithm described in [13] cannot be properly executed to determine the trustworthiness of the Users based on the attributes provided. In [14], a system called PowerTrust was used to calculate peer-to-peer trust. The scalable system had a useful performance but could not be used to build trust in a social network.

In [15], a model for trust evaluation based on gravity was discussed. The proposed method was a two-step process. In the first stage, friendships and strengths were calculated, and in the second stage, the social neighbour was applied to calculate the trust. This model could not evaluate the trustworthiness of the users depending on their personality attributes. Algorithms for calculating behavioural trust were proposed in [16]. The purpose of this paper was to quantify dual trust based on the observed communication pattern. These actions are statistically defined and do not use any semantic information contained in the messages. In [17], social trust was discussed. Two algorithms were presented that access to implicit and explicit social trust. The proposed approach was more robust against manipulation attacks and had its applicability in fields like secure DTN routing. The approach was not directly applicable for evaluating trustworthiness of users in a social network. In [18], a model called STrust was designed to create trusted societies in which members could share their information without worry. The model relied on social capital to derive trust value.

In [19], trust management was discussed as it relates to Internet applications. A notation for specifying trust and recommendation concepts was presented along with a set of tools for specifying, analyzing and monitoring trust relations. In [20], Shirgahi et al. used parameters of social network authority, the value of pages' links authority and semantic authority to assess the trust. In [21], the importance of the trust model was discussed based on user beliefs and credibility. The model is not applicable in the present form to evaluate trustworthiness of users in a Web-based social network. The purpose pursued in [22] was the design of a fuzzy system. This trust model was used in distributed systems, but it could not predict the trust of users in social network. In [23], a genetic algorithm-based approach to inferring trust was introduced. The approach used heterogeneous relations for inferring trust. The algorithm achieved higher accuracy for trust values and was scalable and extensible, but it did not evaluate trustworthiness of users in a social network. The focus of [24] was on graphical representation for modelling trust relationships in multiagent e-commerce environments. The work was not applicable for evaluating trustworthiness of users in a Web-based social network. In [25], a subjective logic to express distrust and to evaluate the trust probability distribution was suggested, but this method could only be used for the binary trust model. In [26], Danesh and Shirgahi provided a way to predict trust in a social network with structural similarities through the neural network. In this method, the web of trust data set was first converted to a structural similarity data set based on the similarity of the trustors and trustees. Then, on the created data set, 70% of the data set was considered as the training data and it was trained based on the multilayer perceptron neural network. Finally, the trained neural network was tested based on the test data.

None of the above-mentioned models could evaluate users' trustworthiness based-on a set of personality attributes. In this research, an approach is adopted in which trustworthiness of users can be evaluated based-on a set of personality attributes. This approach supports an unlimited number of personality attributes that can be defined. In the next section, we will explain the proposed approach.

4. THE PROPOSED APPROACH FOR EVALUATING TRUSTWORTHINESS

A web-based social network can be implemented as a directed graph G (V, E) so that V is a set of nodes that denotes users and E is the set of edges that describe the interactions between these users. The number assigned to each edge from vi to vj (user i to user j), indicates the number of times the user i interacts with the user j. As an example, Fig. 1 illustrates a simple example of this network. This figure consists of a directed graph and the nodes' interactions with each other. The values on each edge represent the total number of interactions performed

by the user with the other users. It should be noted that in this figure, for example I1 is the same as Individual1.
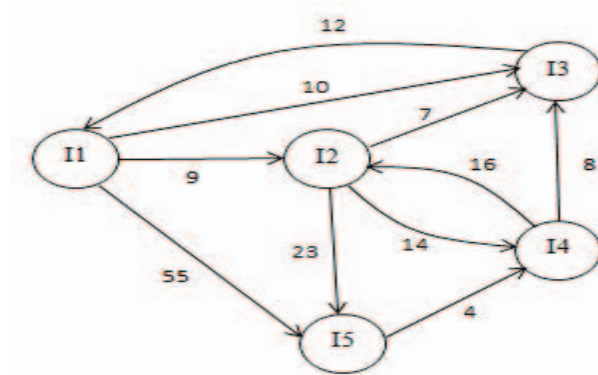

Fig. 1: Web-based social network.

Interactions are different in nature and are based on the rate. The rate of the users interacting corresponds to various attributes. The rating depends on the experience and the feelings received by the users. Rating values are processed using fuzzy logic to evaluate trustworthiness. The two most important criteria of graph that are used to evaluate trustworthiness of users are called In-degree and Out-degree. The In-degree of a node points to the number of the other users interacting with the selected user, and Out-degree of a node points to the number of the users that the selected user interacts with [6]. In other words, it can be said that In-degree node states that the selected user receives information about the other users, and Out-degree node points to the fact that the selected user disseminates information on his personality attributes on the social network to the other users.

Low In-degree and Out-degree nodes denote less interactivity, in other words receiving or disseminating less information; and High In-degree and Out-degree nodes denote more interaction, that is receiving or disseminating more information.

Clearly, it is difficult for a user at Low In-degree to directly determine the trustworthiness of others. The proposed approach requires that each participant (for example, a user) receives ratings of each entity's different attributes with which he is interacting. A rating reflects experiences perceived by each entity about another one based on the attribute selected. Each scale can be used to rate the attributes from -S to +S.

That means, if S=2, then the scale is from -2 to +2. Table 1 shows the rating scale for five personality attributes and their meanings.

In this paper, we chose these five personality attributes based on our own mental perceptions and our studies.

Reliability expresses user ability to do something without failure. Availability indicates that users are always available to interact with and support each other. Interests include factors that make a user attractive. In fact, the more users' interests are similar, the more they can trust each other.

Patience means that a patient user is able to tolerate setbacks, delays, or unexpected challenges without becoming anxious or angry. A patient user has a better mental health. Adaptability is the emotional and current stability of social relationships. An adaptable user can quickly adapt to changes in plans. A user that is adaptable is associated with his various traits and characteristics.

Table 1: Five characteristics and their concepts

Rate	Reliability	Availability	Interest	Patience	Adaptability
-2	Ever unreliable	Ever unavailable	Ever dissimilar interests	Ever impatience	Ever unadaptable
-1	Often unreliable	Often unavailable	Often dissimilar interests	Often impatience	Often unadaptable
0	No comment	No comment	No comment	No comment	No comment
1	Often reliable	Often available	Often similar interests	Often patience	Often adaptable
2	Ever reliable	Ever available	Ever similar interests	Ever patience	Ever adaptable

It is important to note that the proposed method is general and does not depend on the number of attributes. That is, trustworthiness can be considered as a function of characteristics and this is because trust is a mental concept, and it takes different interpretations depending on the conditions and applications. However, to show the usability of the fuzzy system proposed through simulation, 5 attributes have been selected. Trustworthiness is considered as a function of these 5 attributes. Also, the proposed approach has no limitations on the scales used to rate the experiences for simulation.

In general, each rating scale from -S to + S, where S> 0, can be used. An experiences record, in the form of rating various characteristics during different interactions, is maintained by the user about the other user he interacts with. With these experiences, the experience matrix can be formed. Experiences with different parameters in various interactions are stored in the experience matrix.

The experience matrix is used as an input to a fuzzy system to analyse the others' trust. In evaluating the attributes of experience, consider that the user U1 interacts with the user U2 with n interaction. EC_{att} (U1, U2) as a set of experience consisting of n values that represent the feeling experience of the user u1 about the user u2 in n interactions according to attribute defined as follows.

$$EC_{att} (u1, u2) = \{exp_{att},1, exp_{att},2, ..., exp_{att} , n \}$$

As exp_{att}, n is an experience feeling by the user U1 about the user U2 with respect to the $_{att}$ attribute in the nth interaction. EC_{att} values are recorded by each user for all the users they interact with. That way we can define whole expertise perceived through by user U1 for user U2 with respect to the $_{att}$ attribute, as

$$EC_{att} (u1, u2) = mode (EC_{att} (u1, u2))$$

In it, EC_{att} (u1, u2) is the whole experience felt by the user U1 for the user U2 according to the $_{att}$ attribute and the mode (EC_{att} (u1, u2)) is the mode value of the EC_{att} (u1, u2) set.

This Process can be generalized to gain experience of the users about others due to various attributes. Figure 2 is pseudo code that represents a procedure for calculating the experience of the users from the other users. Low values In and Out-degree between U1 and U2 provide less accuracy EC_{att} (U1, U2), while High values provide greater accuracy EC_{att}(U1,U2) Results, while High values provide greater accuracy EC_{att} (U1, U2) Results.

4.1 Generating of Matrix of Experience(EM)

Figure 2 shows the pseudo-code for calculating the experience matrix. For example, Table 2 shows ratings for first user interaction with another user on the five characteristics. By the pseudo-code written in Fig. 2, Table 3 is obtained from Table 2. From Table 3, the matrix of experience is achieved that is shown in Fig. 3. After the matrix of experience is obtained, depending on one or more characteristics, trust can be calculated.

The user can pick the attributes. In fact, the user chooses the specific attributes according to his needs and understanding of trust. The fuzzy system we provided can be used to evaluate trust depending on one or more characteristics. Here, it's important to note that choosing the attributes of trust may vary for each user. This standard of system enables a user to model trust based on his own understanding of what happens in the real world.


```
U₁: first user
Uₙ: nᵗʰ user
X,Y: Temp user variables
k = the number of attributes
X=U₁;
While (X<=Uₙ)
{
            While (Y <=Uₙ)
            {
                    If (X!=Y)
                    {
                    For (att=att₁; att<=attₖ; att++)
                            {
                            Eₐₜₜ(X, Y) = mode (ECₐₜₜ)
                            }
                    }
            J++;
            }
    I++;
    }
```

Fig. 2: Pseudo-code for calculate expertise of the users.

Table 2: Ranking for first user interaction with another user on the five characteristics

Users	Count of interaction	Attributes				
		Reliability	Availability	Interest	Patience	Adaptability
U_2	8	-1,-1,0,1,2,-1,0,1	-2,-2,0,-1,-2,1,0,2	-1,1,0,-1,2,0,1,-1	-1,-2,-1,-2,1,2,-1,0	-2,-1,-1,0,1,-2,-2,-1
U_3	6	2,1,1,2,1,2	1,2,2,1,1,1	1,1,0,2,1,0	-2,-2,1,1,0,-2	2,1,1,0,2,2
U_4	5	1,2,0,2,1	0,1,2,2,2	-2,2,-2,1,0	-1,2,-1,0,1	1,1,1,2,1
U_5	4	-1,-2,-1,-1	-2,-2,-2,-1	-2,-1,-1,-1	-1,-2,-2,-2	-1,-1,-2,-1
U_6	9	1,0,0,1,1,0,1,0,0	0,1,1,1,0,1,0,1,1	1,0,0,1,0,0,1,1,0	1,0,0,-1,-1,0,-1,-1,1	1,1,1,1,0,0,1,0,0

Table 3: User 1's ranking of five characteristics of the other users

Users	Attributes				
	Reliability	Availability	Interest	Patience	Adaptability
U₂	-1	-2	-1	-1	-2
U₃	2	1	1	-2	2
U₄	1	2	-2	-1	1
U₅	-1	-2	-1	-2	-1
U₆	0	1	0	-1	1

$$EM = \begin{bmatrix} -1 & -2 & -1 & -1 & -2 \\ 2 & 1 & 1 & -2 & 2 \\ 1 & 2 & -2 & -1 & 1 \\ -1 & -2 & -1 & -2 & -1 \\ 0 & 1 & 0 & -1 & 1 \end{bmatrix}$$

Fig. 3: Matrix of experience of user U1.

4.2 Fuzzy System for Trust Evaluation of Users

Fuzzy logic has been used to evaluate the trustworthiness based on a rating of 5 personality attributes that have been considered. We use fuzzy logic because there aren't any exact boundaries for separating these interdependent attributes. According to the initial definition, a fuzzy system has three parameters which include inputs, fuzzy inference system and output.

Inputs and outputs are the same as the input and output data we want. The fuzzy inference system uses fuzzy rules to obtain the output. Figure 4 illustrates our fuzzy system. Fuzzy system inputs have five attributes: reliability, availability, interest, patience, and adaptability and the fuzzy system output is trustworthiness. The final values of the ranking of these attributes are obtained by the fuzzy rules that are defined.
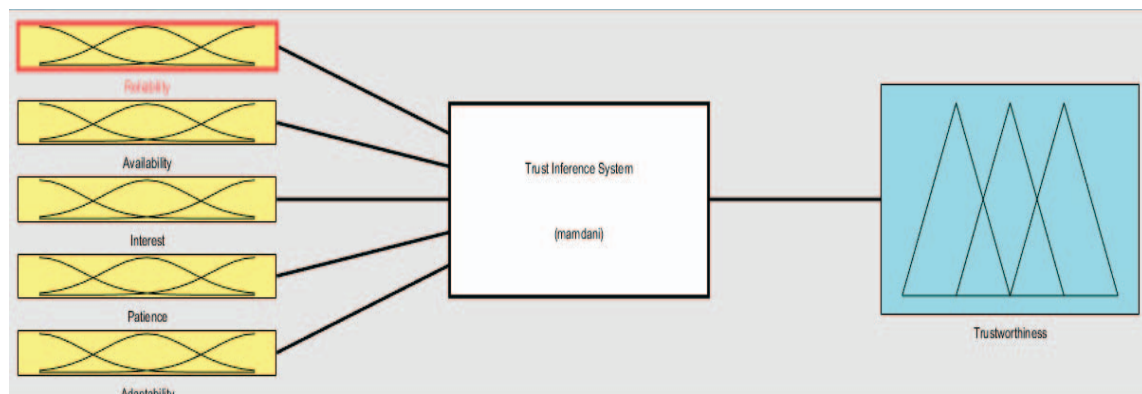
Fig. 4: Overview of fuzzy logic-based trust inference system.

All five attributes that are our fuzzy system inputs have been rated in Table 1. The histogram of the inputs and output variables is shown in Fig. 5. Also, in Fig. 6, the fuzzy sets related to our input and output variables are also shown.

The most important part in fuzzy systems is their rules, they connect the conceptual relation of the input parameters to the output parameters. In this paper these rules are written according to the train datasets. Figure 7 shows an illustration of the rules defined. In general, the 252 fuzzy rules that were used to simulate 5 attributes to gain trustworthiness are included. It is worth noting that any number of attributes can be considered, but as the number of attributes increases, the number of rules can increase exponentially, and as a result, the inference process of the fuzzy system becomes more complicated and the runtime is increased.
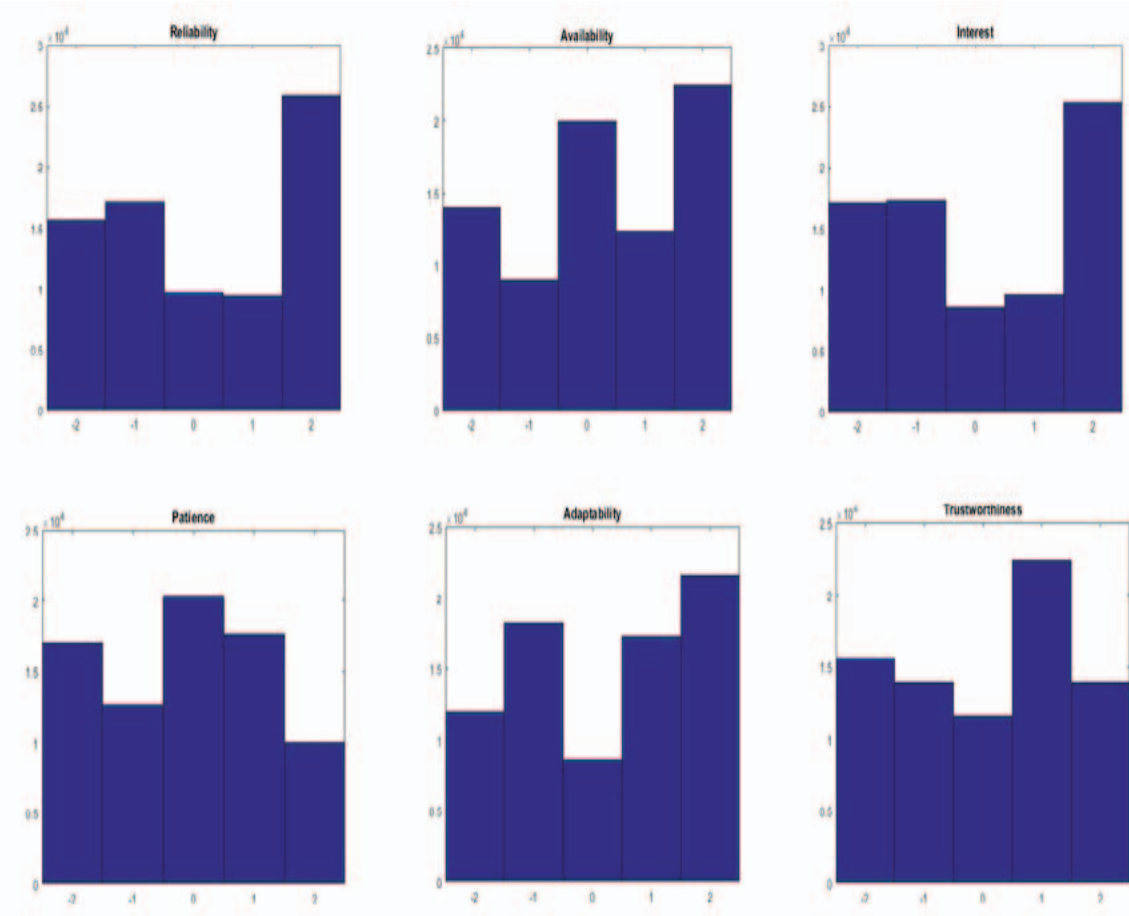
Fig. 5: Histogram diagram of the input and output variables.

Figure 8 contains the Rule Viewer of a fuzzy system that executes related rules for specific entries and displays the defuzzification final output value.

5. EVALUATING THE PROPOSED APPROACH

To evaluate the proposed approach, we have used the Epinions dataset, which is a social network dataset. In this way, we performed our own assessment on a part of the data set, including the first 2000 nodes and 77589 edges. One of the benefits of this dataset is that it is a real dataset and is widely used in research in the field of social networking. To simulate this approach, the MATLAB tool and Mamdani Fuzzy Inference System are used to assess the trustworthiness of the users.

During the simulation of the output of the fuzzy system, according to Table 4, the trustworthiness was classified into 5 categories.
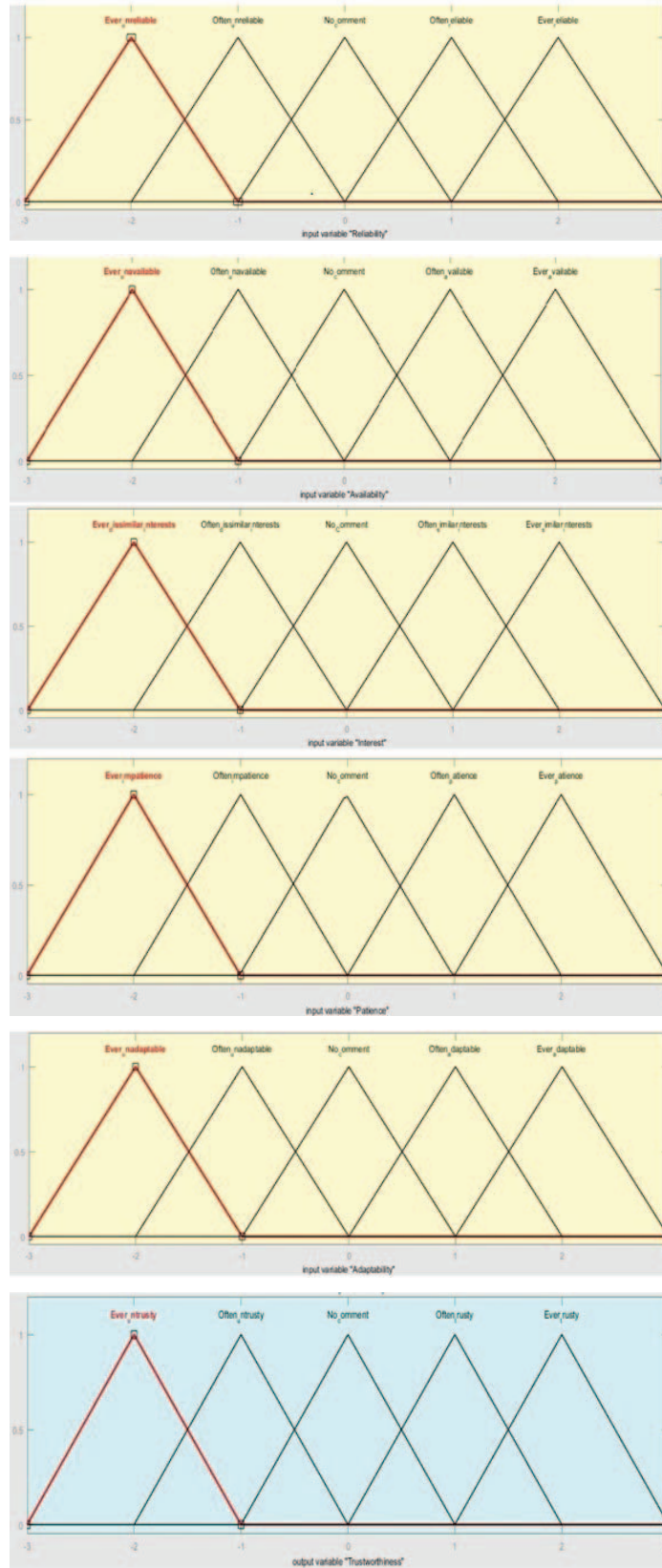
Fig. 6: Fuzzy sets related to our input and output variables.
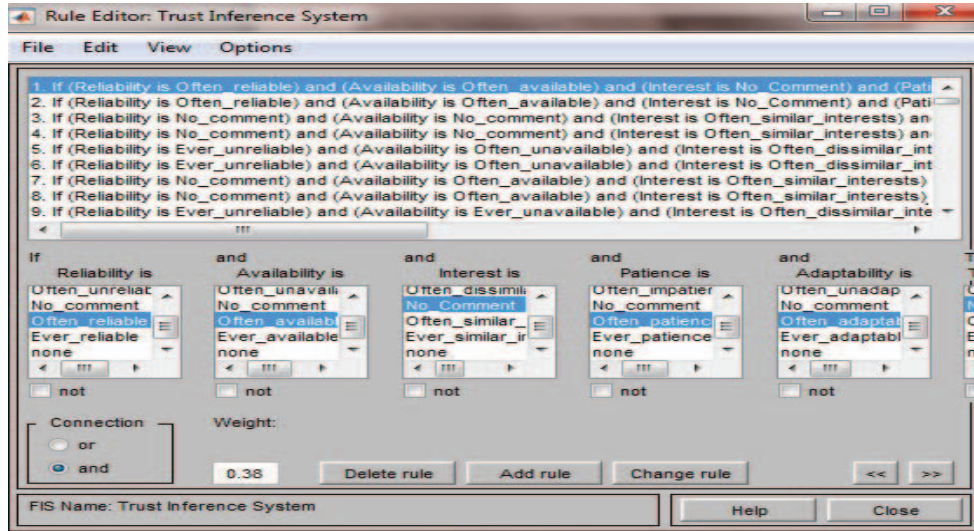
Fig. 7: Illustration of the defined rules.
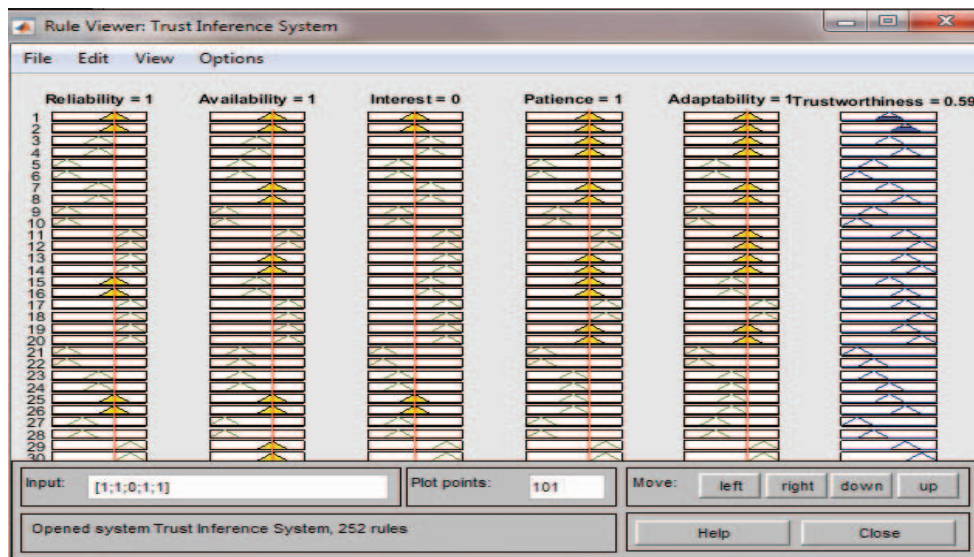
Fig. 8: Rule Viewer of fuzzy system.

Table 4: Trustworthiness categories of users

Rating Category	Trustworthiness
-2	Ever untrusty
-1	Often untrusty
0	No comment
1	Often trusty
2	Ever trusty

For a more accurate evaluation of the fuzzy system, we have examined various types of fuzzy systems, which are presented in Table 5. For the input and output variables, we used the Trimf membership function. The overall structure of this function is given in Eq. (1).

$$f(x;a,b,c) = \begin{cases} 0, x \leq a \\ \dfrac{x-a}{b-a}, a \leq x \leq b \\ \dfrac{c-x}{c-b}, b \leq x \leq c \\ 0, c \leq x \end{cases} \tag{1}$$

As shown in Table 5, the bases of fuzzy logic used min, prod methods in which the overall structure of the fuzzy reasoning methods are based on Eqs. (2) and (3).

$$min(a, b) = \begin{cases} a, a \leq b \\ b, a \succ b \end{cases} \tag{2}$$

$$prod(a,b) = a*b \tag{3}$$

We used gravity centre (centroid), bisector, MOM (Mean of Maximum) and SOM (Smallest of Maximum) methods for defuzzification, which are given in Eqs. (4) to (6).

$$x_{centroid} = \frac{\int x \times \mu_i(x)\, dx}{\int \mu_i(x)\, dx} \tag{4}$$

$$\int_{\alpha}^{x_{bisector}} \mu_i(x)\, dx = \int_{x_{bisector}}^{\beta} \mu_i(x)\, dx \tag{5}$$

$$MOM\ (a,\ b)\ =\ (a+b)\ /\ 2 \tag{6}$$

Table 5: Features of the different fuzzy system

FIS Name	FIS Type	MF Type	And Method	Or Method	Implication Method	Aggregation	Defuzzification Method
FIS 1	mamdani	trimf	min	max	min	max	centroid
FIS 2	mamdani	trimf	prod	max	prod	max	centroid
FIS 3	mamdani	trimf	min	probor	min	probor	centroid
FIS 4	mamdani	trimf	prod	probor	prod	probor	centroid
FIS 5	mamdani	trimf	min	max	min	max	bisector
FIS 6	mamdani	trimf	prod	max	prod	max	bisector
FIS 7	mamdani	trimf	min	probor	min	probor	bisector
FIS 8	mamdani	trimf	Prod	probor	prod	probor	bisector
FIS 9	mamdani	trimf	min	max	min	max	MOM
FIS 10	mamdani	trimf	prod	max	prod	max	MOM
FIS 11	mamdani	trimf	min	probor	min	probor	MOM
FIS 12	mamdani	trimf	prod	probor	prod	probor	MOM
FIS 13	mamdani	trimf	min	max	min	max	SOM
FIS 14	mamdani	trimf	prod	max	prod	max	SOM
FIS 15	mamdani	trimf	min	probor	min	probor	SOM
FIS 16	mamdani	trimf	prod	probor	prod	probor	SOM

5.1 Parameters of Fuzzy System Performance Evaluation

After simulating the fuzzy system described in evaluating the proposed approach, to evaluate the performance of the different fuzzy systems, we considered 10% of the dataset to use as test data and examined the performance of fuzzy systems. For evaluating the fuzzy system performance from various measures including precision, recall, and F-score, we compared them with each other. How to calculate the Precision, recall and F-score is noted in Eqs. (7), (8), and (9), respectively.

$$\text{precision} = \frac{\text{TruePositive}}{(\text{TruePositive})+(\text{FalsePositive})} \times 100 \tag{7}$$

$$\text{recall} = \frac{\text{TruePositive}}{(\text{TruePositive})+(\text{FalseNegative})} \times 100 \tag{8}$$

$$\text{F-score} = \frac{2 \times \text{recall} \times \text{precission}}{\text{recall}+\text{precission}} \tag{9}$$

We also calculated the error obtained from the trustworthiness by different fuzzy systems in comparison with the trustworthiness in test data of the main dataset as MAE's (Mean Absolute Error), which is given in Eq. (10). According to Eq. (10), CTi refers to the calculated value of trust, and RTi is the real trust value, and N is the total number of test data.

$$\text{MAE} = \frac{\sum_{i=1}^{N} |C_{Ti} - R_{Ti}|}{N} \tag{10}$$

The numbers derived from the calculation of these measures and the error rate obtained on the test dataset in various fuzzy systems are given in Table 6.

Table 6: Calculation of these measures and the error rate in fuzzy systems

Fis name	Precision	Recall	F-score	error
FIS1	0.8222	0.9547	0.8835	0.0085
FIS2	0.8222	0.9547	0.8835	0.0071
FIS3	0.8222	0.9547	0.8835	0.0089
FIS4	0.8222	0.9547	0.8835	0.0076
FIS5	0.7991	0.9654	0.8744	0.0062
FIS6	0.7991	0.9654	0.8744	0.0048
FIS7	0.8222	0.9547	0.8835	0.0074
FIS8	0.8222	0.9547	0.8835	0.0060
FIS9	0.7991	0.9654	0.8744	0.0014
FIS10	0.7991	0.9654	0.8744	0.0016
FIS11	0.7991	0.9654	0.8744	0.0077
FIS12	0.7991	0.9654	0.8744	0.0016
FIS13	0.7991	0.9654	0.8744	0.0068
FIS14	0.7991	0.9654	0.8744	0.0016
FIS15	0.7991	0.9654	0.8744	0.0077
FIS16	0.7991	0.9654	0.8744	0.0016

Also, the comparison of precision measures for various fuzzy systems is in Fig. 9. According to Fig. 9 the best result belongs to FIS1-4 and FIS7-8 with 0.822. The comparison of the recall measures for various fuzzy systems is shown in Fig. 10. The results of Fig. 10 show that FIS5-6 and FIS9-16 have achieved the highest recall with 0.9655. The comparison of the F-score measure for various fuzzy systems is presented in Fig. 11. According to Fig. 11, FIS1-4 and FIS7-8 have achieved the highest F-score with 0.8835 and the comparison of the obtained error rate for various fuzzy systems is shown in Fig. 12 which shows the results in Fig. 9 have the lowest error mid with 0.0014.
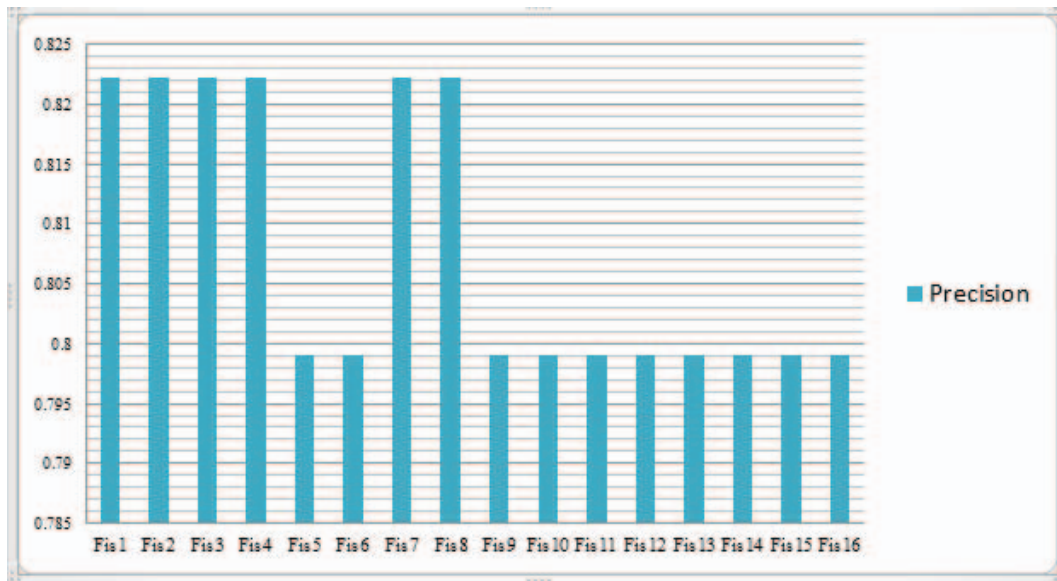

Fig. 9: Comparison of the precision measure for various fuzzy systems.
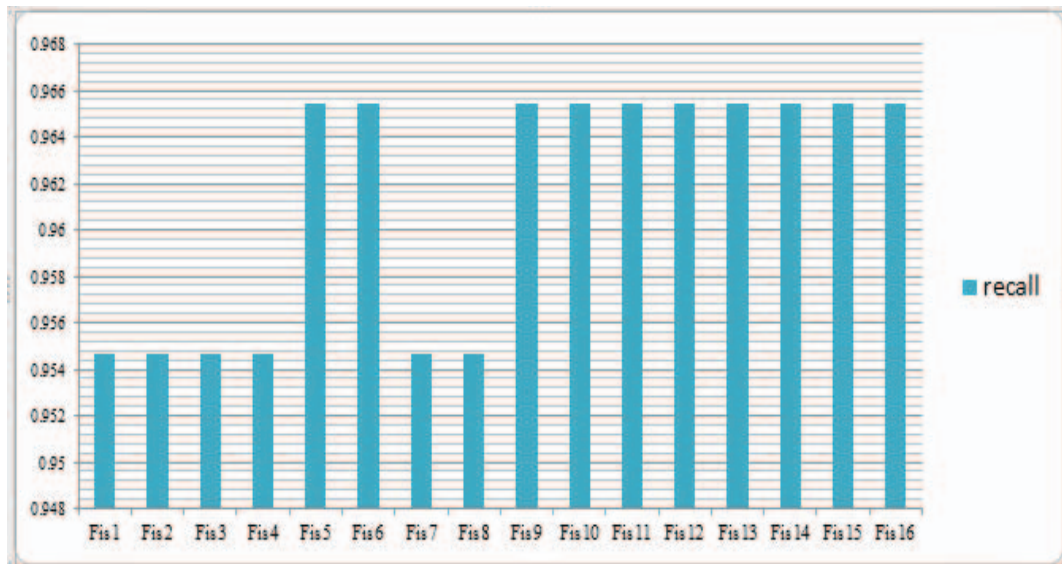

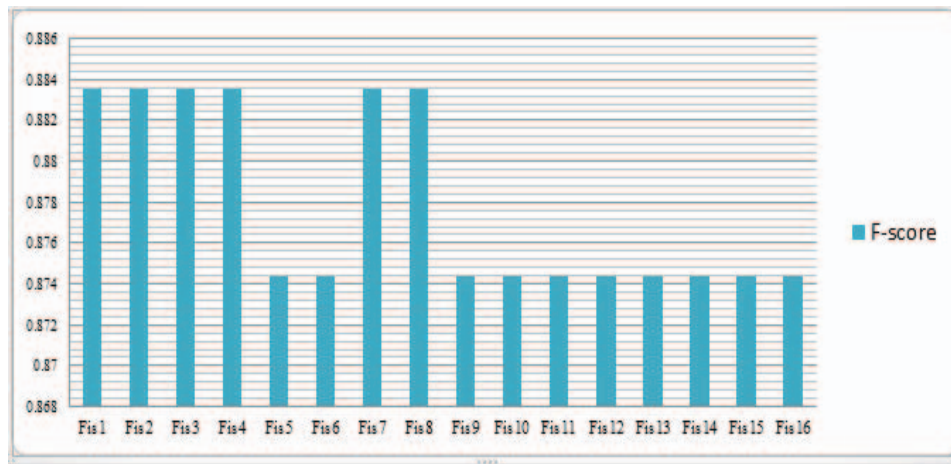Fig. 10: Comparison of the recall measure for various fuzzy systems.

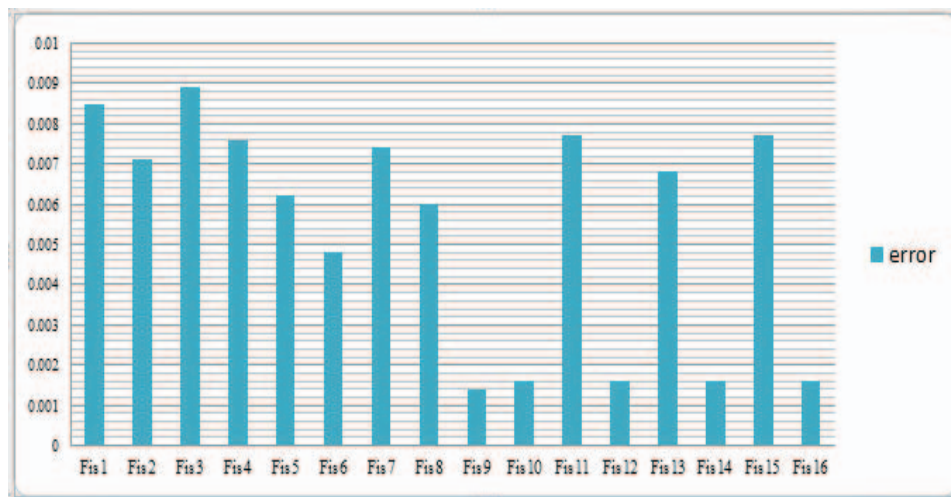Fig. 11: Comparison of the F-score measure for various fuzzy systems.

Fig. 12: Comparison of the obtained error rate for various fuzzy systems.

6. CONCLUSION

In this paper, we proposed and discussed a fuzzy system for evaluating trustworthiness of the users based on personality attributes in a social network. In the proposed system, our method includes a ranking of 5 personality characteristics such as reliability, availability, interest, patience and adaptability when the users interact with each other. These ratings were analysed using the fuzzy system to obtain the trustworthiness of the users. A fuzzy trust inference system has been used because fuzzy systems have the ability to deal with imprecise and uncertain information. Trust can be considered as a set of one or more personality characteristics. The proposed fuzzy system is extendable because in this system, trust can be defined as a set of one or more personality attributes. The attributes can also be expanded. The information extracted through the application of this proposed fuzzy system can be used in many issues related to social networks.

According to the results, all considered fuzzy systems have error mid less than 0.015 and among the FIS systems, FIS9 has the lowest error mid with 0.0014. Also, all considered fuzzy systems have an F-score greater than 0.86 and among FIS systems, FIS1-4 and FIS7-8 have achieved the highest F-score with 0.8835. Based on the results, the proposed fuzzy system shows an acceptable accuracy and it can be useful for evaluating the trustworthiness of users.

In future work, we can focus on developing and improving a set of fuzzy rules to make it more precise and accurate. The proposed approach can also be developed to be able to use more or different personality attributes as inputs of the fuzzy system.

REFERENCES

[1]   Firdhous M, Ghazali O, Hassan S. (2012) Trust management in cloud computing: a critical review. International Journal on Advances in ICT for Emerging Regions, 4(2): 24-36.

[2]   McKnight H, Chervany N. (2001) Conceptualizing trust: A typology and e-commerce customer Relationships model. Proceedings of the 34th Annual Hawaii International Conference on System Sciences.

[3]   Marsh SP. (1994) Formalising trust as a computational concept. PhD Thesis. University of Stirling.

[4]   Moturu ST, Liu H. (2011) Quantifying the trustworthiness of social media content. Distributed and Parallel Data-bases, Springer, 29(3): 239-260.

[5]   Golbeck J, Hendler J. (2006) Inferring binary trust relationships in web-based social networks. ACM Transactions on Internet Technology, 6(4): 497-529.

[6]   Singh S, Sidhu J. (2016) An Approach for Determining Trust-worthiness of Individuals in a Web-Based Social Network. Arabian Journal for Science and Engineering, 41(2): 461-477.

[7]   Zhang Q, Yu T, Irwin K. (2004) A classification scheme for trust functions in reputation-based trust Management, ISWC'04 Proceedings of the 2004 International Conference on Trust Security and Reputation on the Semantic Web, 127, pp 52-61.

[8]   Sherchan W, Nepal S, Paris C. (2013) A survey of trust in social networks. ACM Computing Surveys, 45(4): 1-33.

[9]   Lazarsfeld P, Merton R. (1954) Friendship as a social process: A substantive and Methodological Analysis. In Freedom and Control in Modern Society, pp. 18-66.

[10] Young AL, Quan-Haase A. (2009) Information revelation and internet privacy concerns on social Network sites: A case study of Facebook. Proceedings of the Fourth International Conference on Communities and Technologies, pp. 265-274.

[11] Suryanarayana G, Taylor RN. (2004) A survey of trust management and resource discovery Technologies In peer-to-peer applications. Institute for Software Research University of California, Irvine.

[12] Watts DJ. (1999) Small Worlds: The Dynamics of Networks Between Order and Randomness. Princeton University Press.

[13] Golbeck JA, Hendler J. (2005) Computing and applying trust in web-based social networks, (Phd Thesis). University of Maryland.

[14] Zhou R, Hwang K. (2007) Power trust: A robust and scalable reputation system for trusted peer-to-peer Computing. IEEE Transactions on Parallel and Distributed Systems,18(4): 460-473.

[15] Maheswaran M, Tang HC, Ghunaim A. (2007) Towards a gravity based trust model for social networking Systems. 27th International Conference on Distributed Computing Systems Workshops, 24.

[16] Adali, S., Escriva, R., Goldberg, M.K., Hayvanovych, M., Magdon-Ismail, M., Szymanski, B.K., Wallace, W.A., Williams, G.T. (2010) Measuring behavioral trust in social networks. 2010 IEEE International Conference on Intelligence and Security Informatics, 150-152.

[17] Trifunovic S, Legendre F, Anastasiades C. (2010) Social trust in opportunistic networks. INFOCOM IEEE Conference on Computer Communication Workshops, pp. 1-6.

[18] Nepal S, Paris C, Bista SK, Wanita S. (2013) A trust model based analysis of social networks. International Journal of Trust Management in Computing and Communications, 1(1): 3-22.

[19] Mohanapriya M, Krishnamurthi I. (2014) Trust based DSR routing protocol for mitigating cooperative Black hole at-tacks in ad hoc networks. Arabian Journal for Science and Engineering, 39(3): 1825-1833.

[20] Shirgahi H, Mohsenzadeh M, Seyyed Javadi HH. (2016) Trust estimation of the semantic web using Semantic web clustering. Journal of Experimental &Theoretical Artificial Intelligence, 29(3): 537-556.

[21]   Castelfranchi C, Falcone R, Pezzulo G. (2003) Trust in information sources as a source for trust: a fuzzy approach. Proceedings of the Second International Joint Conference on Autonomous Agents and Multiagent Systems, pp. 89-96.

[22]   Tajeddine A, Kayssi A, Chehab A, Hassan A. (2006) PATROL-F- A comprehensive reputation-based trust model with fuzzy subsystems. International Conference on Autonomic and Trusted Computing, pp. 205-216.

[23]   Akhoondi M, Habibi J, Sayyadi M. (2008) Towards a model for inferring trust in heterogeneous social networks. In: Second Asia International Conference on Modeling and Simulation, pp. 52–58.

[24]   Gan Z, He J, Ding Q, Varadharajan V. (2009) Trust relationship modelling in e-commerce-based social network. In: International Conference on Computational Intelligence and Security, 1: 206-210.

[25]   Jøsang A, Hayward R, Pope S. (2006) Trust network analysis with subjective logic. in Proc. ACSC, Hobart, TAS, Australia. pp. 85-94.

[26]   Danesh AH, Shirgahi H. (2020). Predicting trust in a social network based on structural similarities using a multi-layerd perceptron neural network. IIUM Engineering Journal, 22(1): 103-117.   https://doi.org/10.31436/iiumej.v22i1.1622

SARIMA-LSTM COMBINATION FOR COVID-19 CASE MODELING

Imam Tahyudin[1], Rizki Wahyudi[2]*and Hidetaka Nambo[3]

[1]Department of Information System, Universitas Amikom Purwokerto, Purwokerto, Indonesia
[2]Department of Informatics, Universitas Amikom Purwokerto, Purwokerto, Indonesia
[3]Artificial Intelligence Laboratory, Kanazawa University, Japan

*Corresponding author: rizkiw@amikompurwokerto.ac.id

ABSTRACT: The study of SARIMA method in combination with LSTM is interesting to do. This combination method can be convincing and significant because the data collected is numerical and saved based on time. In addition, the proposed method can anticipate datasets, either linear or non-linear. Based on several previous studies, the SARIMA method has the advantage of completing linear datasets while the LSTM method excels in achieving non-linear datasets. Also, both methods have been shown to have an accuracy value compared to some other methods. This study tried to combine the two through several stages of the first stage of applying the SARIMA method using fit datasets (linear data) then residual Dataset (non-linear data) analysed using the LSTM method. The result of the combination methods will be checked for the accuracy value. This research will be compared by using SARIMA and LSTM methods separately. The Dataset used as a trial is COVID-19 patient data in the United States. The results showed that the combination of SARIMA-LSTM method is better than either SARIMA or LSTM alone with RMSE of 0.33905765 and MAE of 0.29077017.

ABSTRAK: Gabungan kaedah kajian SARIMA dengan LSTM adalah menarik untuk dikaji. Gabungan kaedah ini meyakinkan dan penting kerana data yang dikumpulkan bersifat numerik dan disimpan berdasarkan waktu. Selain itu, kaedah yang diusulkan ini dapat menerima set data, samada berkadar langsung atau tidak langsung. Berdasarkan beberapa penelitian sebelumnya, kaedah SARIMA mempunyai faedah dalam melengkapi set data linear, sedangkan kaedah LSTM berguna dalam mencapai set data tidak-linear. Tambahan, kedua-dua kaedah ini terbukti memiliki nilai ketepatan lebih baik berbanding beberapa kaedah lain. Kajian ini cuba menggabungkan keduanya melalui beberapa tahap. Tahap pertama mengunakan kaedah SARIMA secara set data (data linear) kemudian baki set data (data tidak-linear) dianalisa menggunakan kaedah LSTM. Dapatan dari gabungan kedua-dua kaedah tersebut akan diperiksa nilai ketepatannya. Kajian ini akan dibandingkan melalui kaedah SARIMA dan LSTM secara berasingan. Set data yang digunakan adalah merupakan data pesakit COVID-19 dari Amerika Syarikat. Dapatan kajian menunjukkan gabungan kaedah SARIMA-LSTM memiliki nilai ketepatan yang lebih baik berbanding kaedah SARIMA secara berasingan, dan LSTM dengan RMSE adalah sebanyak 0.33905765 dan MAE sebanyak 0.29077017.

KEYWORDS: *SARIMA; LSTM; SARIMA-LSTM; COVID-19 patients*

1. INTRODUCTION

The term SARIMA designates a seasonal autoregressive integrated moving average. One of the time series method's topics is this model. To handle problems involving time-run results, time series are frequently used. The time-series methodology is used in a

variety of domains, including the economics and financial turnaround results at hospitals [1-3].

A discussion of the time series method was held to complete the modelling of potential bioelectric plant data. Using autoregressive (AR), moving average (MA), and ARIMA models are one example. However, some of these models have not produced the best value. The average error rate for mean square error (MSE) and the mean absolute error (MAE) continues to be strong. Although the average prediction accuracy is still about 75% [4-6]. Therefore, this study aims to increase accuracy by using another time series model, SARIMA. In this study, the SARIMA method was combined with the LSTM method.

The combination of SARIMA with other methods is proven to have better accuracy results. Among them is the combination of the SARIMA method with other methods, including the SVM method, to predict the production value of the machine industry in Taiwan [7]. The results showed that SARIMA hybrid accuracy with SVM is better than with each method. Other studies used hybrid ARIMA with ANN for forecasting pollution index in cities throughout Southeast Asia and further research used the same approach to predict tourists coming at Minangkabau international airport [8]. The results showed the accuracy value of hybrid methods is better. Subsequent research compared SARIMA and ANN methods to predict power absorption in Turkey's electricity users [9]. After 12 weeks, the results showed that the ANN method's MAPE value was 1.8% better than SARIMA because it had a MAPE of 2.6%. However, in certain conditions, such as the time after a holiday, the result is the opposite. Another study combined SARIMA with SVM, and then in analysis using clustering [10], this research was used to predict passengers at northern Iranian stations. The result is a better mix of these approaches than the individual methods. As a result, the integrated approach outperforms the respective processes. Additional research on the combination of SVR-SARIMA models was done for tourist forecasting [11], for the best model's determination using the decision support system PROMETHEE II. The result is the same combination method is better.

Thus, this study combined the SARIMA method with LSTM. The SARIMA model successfully predicts a person's position for linear data set type better than the deep learning method [12], and also the SARIMA model has been tested with high accuracy of about 80% [13]. According to research, the Long-Short Term Memory (LSTM) Recurrent Neural Network on Workload Forecasting Models for Cloud Datacentres has generated empirical results. The proposed method achieves high accuracy in prediction by reducing average squared errors by up to 3.17×10^{-3} [14]. Therefore, we use both methods because both can solve problems for linear and non-linear data sets. In addition, this study will compare the SARIMA-LSTM combination with each method separately.

2. METHOD

2.1 ARIMA Model

ARIMA is a term derived from its parts: autoregressive (AR), integration (I), and moving average (MA) shape. In general, the ARIMA models are classified into two types, namely non-traditional (non-seasonal) ARIMA and Seasonal ARIMA models [15-17]. The ARIMA model is as follows: ARIMA (p,d,q). p represents the sum of AR values, d is the value of integration (I), and q is the MA value. In general, the ARIMA model (p,d,q) can be seen from the model as follows:

$$(1 - \phi_1 B .... \phi_p B^p)(1 - B)^d Y_t = c + (1 + \theta_1 B ..... + \theta_q B^q) e_t \tag{1}$$

There are 3 main components in the model, the first being AR (p),

$$(1-\phi_1 B.... - \phi_p B^p) \tag{2}$$

The second is differentiation through I (d),

$$(1 - B)^d Y_t \tag{3}$$

The third was indeed MA (q),

$$(1 + \theta_1 B..... + \theta_q B^q) e_t \tag{4}$$

c, on the other side, is a constant value.

2.2 Seasonal ARIMA Model

The seasonal ARIMA, or SARIMA model, is a model or shape that repeats itself at regular intervals. For stationary datasets, seasonality can be detected from the ACF plot. If the ACF visualization shows seasonal patterns, it will be done with a different solution [18-20]. In general, the seasonal ARIMA equation is shown in eqn. 5.

$$ARIMA(p,d,q)(P,D,Q)^s \tag{5}$$

where (p,d,q) is the non-seasonal ARIMA model index, while (P, D, Q) is the seasonal ARIMA model, and S is the number of periods on the seasonal model.

For example, if ARIMA (1,0,0), then the model follows the following eqns. 6 and 7:

$$(1 - \phi_1 B)Y_t = c \tag{6}$$

where is $BY_t = Y_{t-1}$. So

$$Y_t = c + \phi_1 Y_{t-1} \tag{7}$$

To detect seasonal datasets, there are several chart techniques including sequential plots, seasonal plot subseries, multiple box plots, and autocorrelated plots. The study will use autocorrelated schemes to detect seasonality. One of the solutions for this autocorrelation plot is to use seasonal differential operators.

2.3 LSTM

Long-short-term Memory (LSTM) is a form of RNN that consists of a collection of cells with features that allow them to memorize data sequences. Data streams are captured and stored in cells. The cell then connects one module from the past to another, allowing data to be transmitted from several previous instances to the present. The data in every cell can be rejected, screened or started adding as a result of the gates in every cell in preparation for the cells that come after [19,21].

The gates focus on a neural network with sigmoidal shape layers, and the active cells either transfer data or discard it. Each sigmoid layer generates a number between 0 and 1, indicating the sum of each data segment that must be permitted in every cell. More precisely, The estimated low value assumes that "nothing should be allowed to pass"; while forecast one shows that "let it all pass". Every LSTM has three types of gates that regulate a state for every cell:

1) **Forget Gate** produces a value between 0 and 1, with 1 denoting success. "fully save this"; whereas 0 says "ignore this."

2) **Memory Gate** The sigmoid layer, following either by the tanh layer, determines which of the cell's most recent data must be kept. The first sigmoid layer, known as

the "doorway layer," selects which values to modify. The tanh layer then generates a new candidate value vector, which can be added to the state.

3) **The Output Gate** determines what to make from each cell. The final value will be determined by the cell state as well as newly added filtered data.

If the distance is vast, the RNN will be unable to predict the next result. Consider the following text: "I go to work every day" and "I work hard at the office." The location's name is the next possible word for current knowledge, but deciding what kind of location to use is difficult. Since there was some related knowledge in the previous period, RNN cannot learn to relate information. As a result, LSTM is a solution for overcoming these flaws.

LSTMs can study long-term dependencies. Remembering information for a long time is the default behavior. Some of the equations show this module as follows [22], [23].

$$r_t = sigm(W_{xr}x_t + W_{hr}h_{t-1} + b_r) \tag{8}$$

$$z_t = sigm(W_{xz}x_t + W_{hz}h_{t-1} + b_z) \tag{9}$$

$$\tilde{h}_t = tanh(W_{xh}x_t + W_{hh}(r_t \odot h_{t-1}) + b_h) \tag{10}$$

$$h_t = z_t \odot h_{t-1} + (1 - z_t) \odot \tilde{h}_t \tag{11}$$

2.4 Combination of SARIMA Method with LSTM

The steps of this combination are described in Fig. 1.
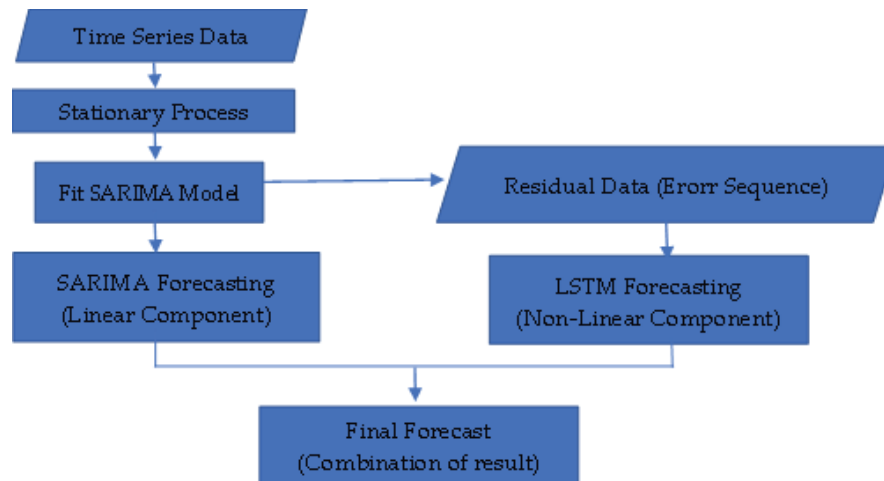
Fig. 1: Combination SARIMA-LSTM Model of COVID-19 patient.

Based on Fig. 1, the combination of the two methods is as follows: (1) Prepare datasets; in this case, the Dataset used is the COVID-19 patient death data in a country affected by COVID-19. (2) Analysis process using the SARIMA model. The method includes the identification process. This process is checked using the Box-Jenkins process. That is the process of determining static data. The seasonal Dataset is then examined by looking at the ACF and PACF values. (3) If the Dataset is seasonal, then the next step determines the best SARIMA model. (4) SARIMA Fit model is forwarded for the forecasting process for linear components. While residual data is used for the forecasting process using the LSTM method for non-linear components. (5) The last

step is the combined result of forecasting the two methods, further measuring MSE values.

3. RESULTS AND DISCUSSION

3.1 SARIMA Model Implementation

In implementing the SARIMA method, COVID-19 patients who died based on gender in the United States were used. The original data used as many as 1008 datasets but because many values were empty (missing value), the empty data was deleted. The net data was 711 datasets. The analysis process used R and Minitab software.

3.1.1 Identification

As a dataset trial, male COVID-19 patients' datasets were used. A plot of male COVID-19 patients who died in the United States is shown in Fig. 2.
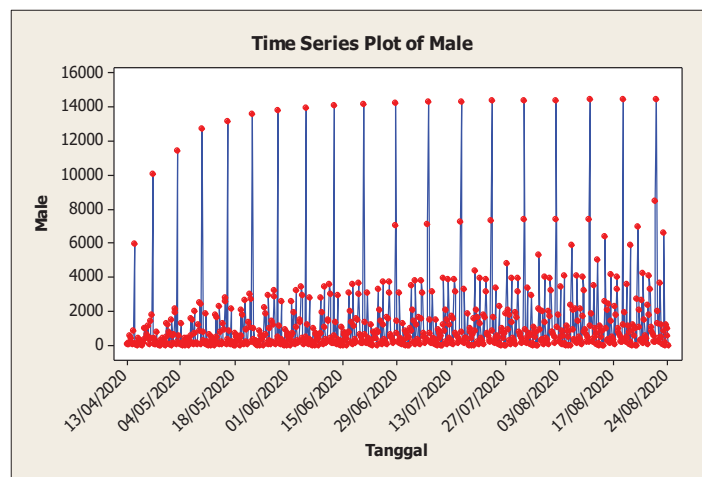
Fig. 2: Visual Dataset of male COVID-19 patients who died in the USA.

Following stationary check dataset of male COVID-19 patients.

a) Stationary check of variety with Cox Box test Results obtained as follows:
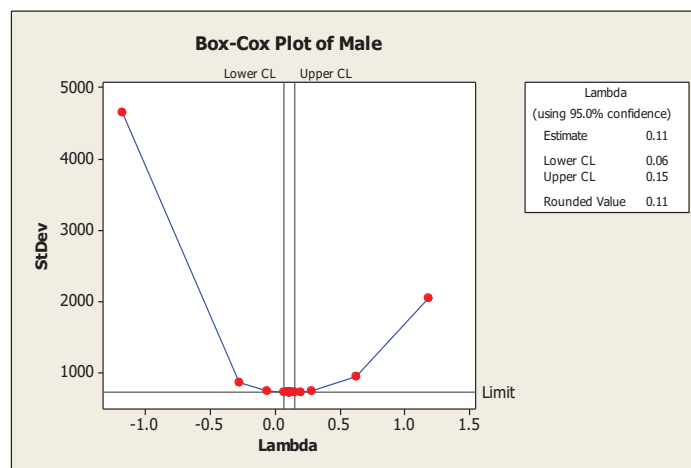
Fig. 3: Visual Dataset of male COVID-19 patients who died in the USA.

Because the value is still 0.11 should be worth 1. So, the transformation process is carried out as follows:
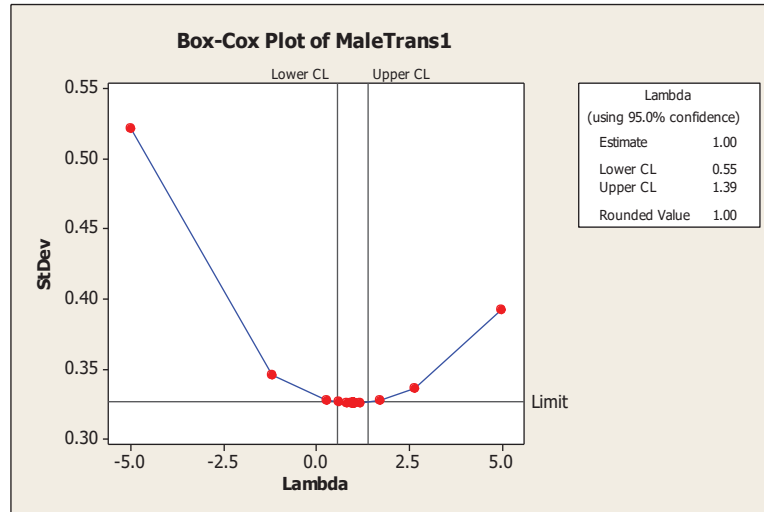
Fig. 4: Cox Box Transformation.

Since the lambda value = 1 is stationary. It then checked stationary against the average by looking at its ACF and PACF scores.

b) Stationary checks against averages by checking ACF and PACF values

Based on ACF and PACF lag, 1-3 images are still inside the significance interval. Then it has been declared stationary against the average.
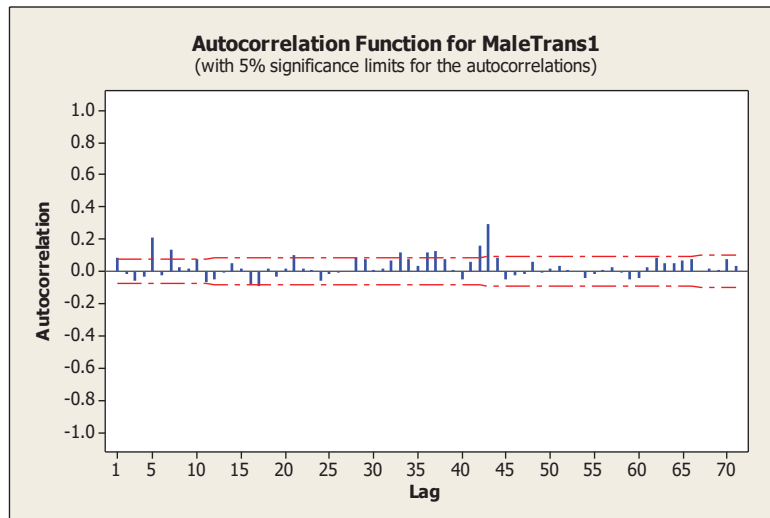
Fig. 5: ACF.
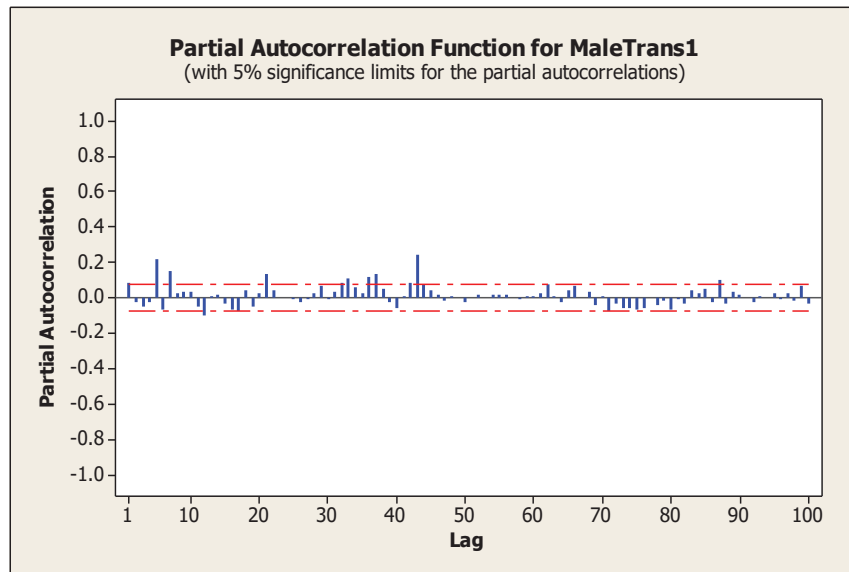
Fig. 6: PACF.

Based on Fig. 12, it appears that there is a trend. That is, there is an increase in the number of COVID-19 patients who die per 10 datasets. Therefore, the identification process is carried out further by differencing

3.1.2 Estimation

In this process, an analysis is carried out based on the sex of the male.
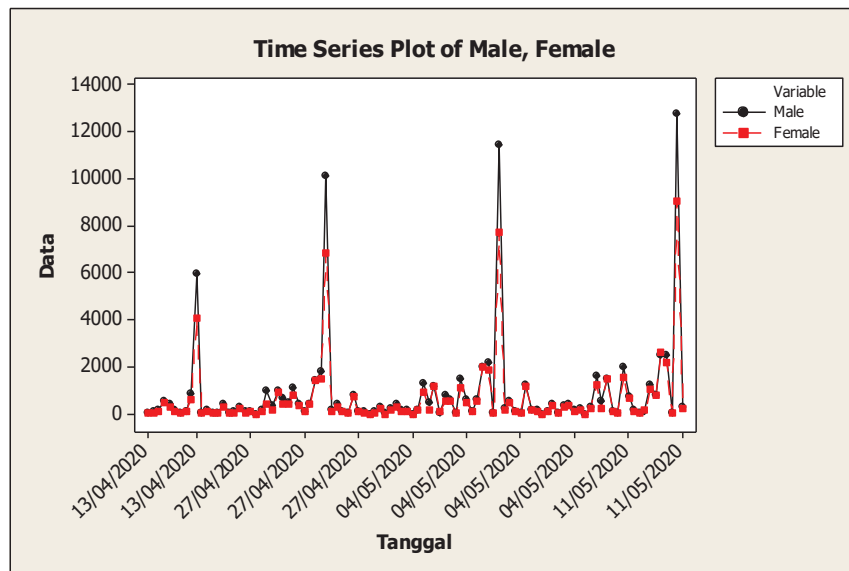
Fig. 7: DATASET of COVID-19 patients in the USA of the male gender.

Once the first differencing process trend is known lag=1, The model is formed with a non-seasonal model first by inspecting the graph autocorrelation function (ACF) and partial autocorrelation function (PACF). The following ACF and PACF charts were obtained:
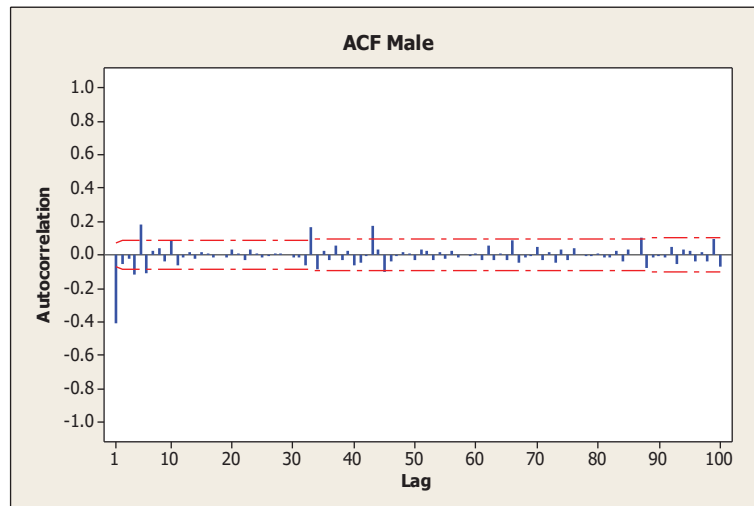
Fig. 8: ACF graph of male COVID-19 patients in America non-seasonal ARIMA models
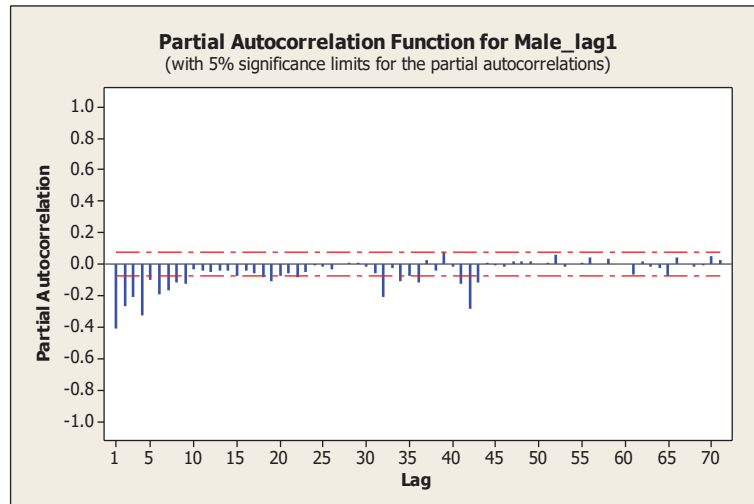
Fig. 9: PACF graph of male COVID-19 patients in America non-seasonal ARIMA model.

The ACF chart shows the dying down as much as five lags. Meanwhile, the PACF chart shows the cut-off pattern. Thus, the non-seasonal ARIMA model formed is ARIMA (5,1,0). They are furthermore checking the non-seasonal ARIMA model.

The step to determine the seasonal ARIMA model is the same as that performed to find the best model in non-seasonal ARIMA by determining its ACF and PACF charts. The seasonal value determines the difference. In this case, it is 10 because for every 10 datasets, there is a significant increase in COVID-19 patient deaths.

3.1.3 Model Evaluation

At this stage, checking the error value and other values. Based on the output of the auto_arima, the evaluation value as follows.

SARIMA $(2,1,2)(0,0,2)^{12}$

Next, check the error value and accuracy. Here are the evaluation values obtained:

AIC   = 340.08

BIC   = 374.8

RMSE   = 0.44236361

MAE   = 0.33180744

These values are the best value when compared to other models.

3.1.4 Forecasting

Based on Fig. 10, the number of COVID-19 patients who died of male gender in the USA, in general, decreased for the following forecasting result. The average difference is about 500 people.
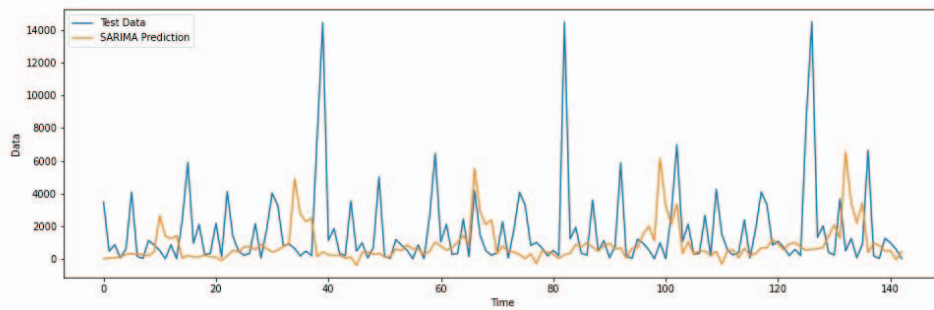
Fig. 10: Male COVID-19 patient forecasting graph using SARIMA.

3.2 Implementation of LSTM and Combination of SARIMA-LSTM method

This analysis used the parameters of batch size of 100, the look_back of seven data to previous, and the epoch for learning of 100. Furthermore, for the forecasting process we split the data set with the composition of 80% training data and 20% testing data from the same data: male COVID-19 patients in the USA. Based on the analysis using LSTM obtained an RMSE value of 0.35847506 and MAE of 0.29837463. Based on RMSE and MAE results, the values are smaller than the SARIMA result, so it can be said that LSTM is better than SARIMA. From Fig 11, it appears that the number of COVID-19 patients who died on average tends to decrease.
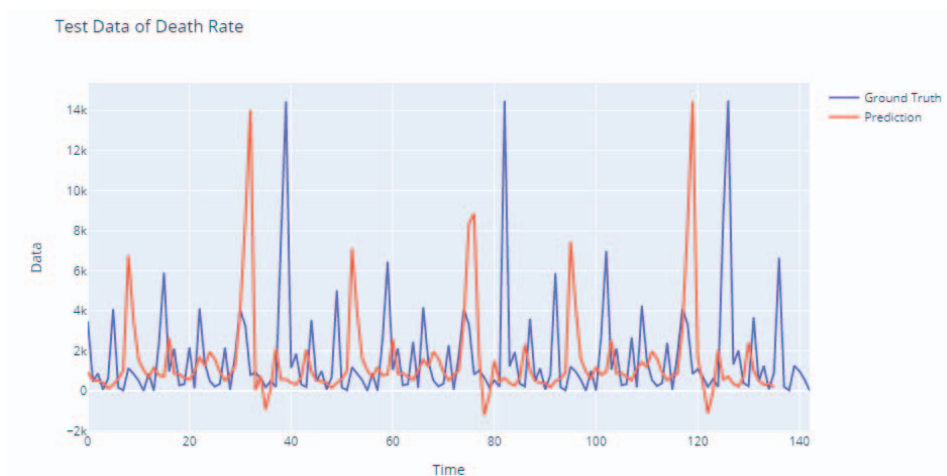
Fig. 11: Graph forecasting male COVID-19 patients using LSTM method.

For the next test, the SARIMA method combined with LSTM was done to determine how much accuracy through RMSE and MAE value obtained and prediction result. Based on the calculation resulted that an RMSE value was 0.33905765 and MAE was 0.29077017.

Those results presented that the RMSE and MAE of combination SARIMA-LSTM was better than the SARIMA and LSTM methods (Table 1). The results of combination SARIMA and LSTM are seen in Fig 12. This figure performed that the result is the best result because the predicted data is almost similar with real data. The number of COVID-19 suspected deaths decreased to near-zero. In addition, the table of comparison of RMSE and MAE are presented in Table 1. This result presented that the combination of SARIMA and LSTM is the best method for predicting the death of COVID-19 patients in the USA.
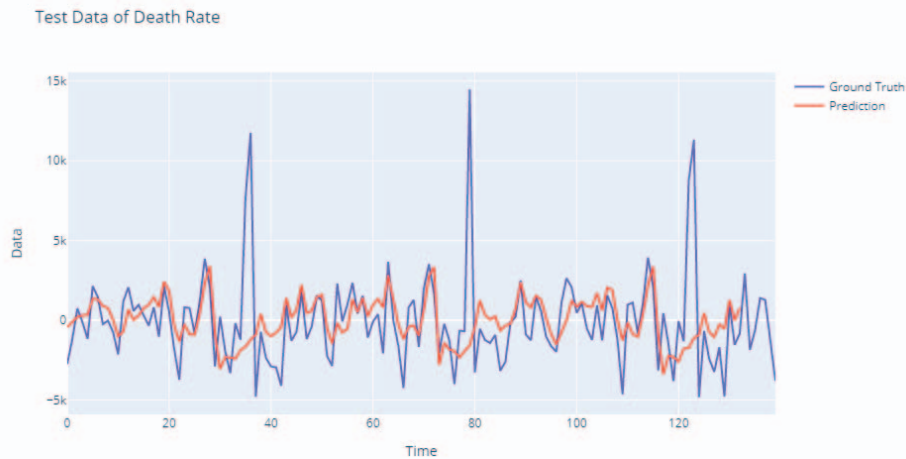
Fig. 12: Male COVID-19 patient forecasting using SARIMA-LSTM combination method

Table 1: The comparison of RMSE and MAE from SARIMA, LSTM,
and combination SARIMA-LSTM

Parameters	SARIMA	LSTM	SARIMA-LSTM
RMSE	0.44236361	0.35847506	0.33905765
MAE	0.33180744	0.29837463	0.29077017

4. CONCLUSION

Based on the results of the study, the combination SARIMA-LSTM method is the best one. It performed better than the SARIMA or LSTM methods separately. Based on the results of general predictions using all three methods, there was a decrease in the number of male COVID-19 patients who died in the USA on average. This research has the limitation of not explaining the mortality number of patients in every state within the USA. For future work, the analysis will be carried out using a combination of SARIMA – PARCD methods.

REFERENCES

[1]   Davis RA. (2014) Introduction to statistical analysis of time series. Department of Statistics Columbia University, pp. 1-24.

[2]   Borkowf CB. (2002) Time-Series Forecasting. Technometrics, 44(2): 194-195. https://doi.org/10.1198/tech.2002.s718.

[3]   Schlüter T. (2012) Knowledge discovery from time series (Doctoral dissertation, Universitäts-und Landesbibliothek der Heinrich-Heine-Universität Düsseldorf).

[4]   Chen KY, Wang CH. (2007) A hybrid SARIMA and support vector machines in forecasting the production values of the machinery industry in Taiwan. Expert Systems with Applications, 32(1): 254-264. https://doi.org/10.1016/j.eswa.2005.11.027

[5]   Chi YN. (2021) Time Series Forecasting of Global Price of Soybeans using a Hybrid SARIMA and NARNN Model: Time Series Forecasting of Global Price of Soybeans. Data Science: Journal of Computing and Applied Informatics, 5(2): 85-101. https://doi.org/10.4108/eai.2-8-2019.2290473

[6]   Ozozen A, Kayakutlu G, Ketterer M, Kayalica O. (2016) A combined seasonal ARIMA and ANN model for improved results in electricity spot price forecasting: Case study in Turkey. In 2016 Portland International Conference on Management of Engineering and Technology (PICMET) (pp. 2681-2690). IEEE. https://doi.org/10.1109/PICMET.2016.7806831.

[7]   Parviz L. (2020) Comparative evaluation of hybrid SARIMA and machine learning techniques based on time varying and decomposition of precipitation time series. Journal of Agricultural Science and Technology, 22(2): 563-578. Retrieved from: http://jast.modares.ac.ir/article-23-26018-en.html

[8]   Abellana DPM, Rivero DMC, Aparente ME, Rivero, A. (2020) Hybrid SVR-SARIMA model for tourism forecasting using PROMETHEE II as a selection methodology: a Philippine scenario. Journal of Tourism Futures. https://doi.org/10.1108/JTF-07-2019-0070

[9]   Tahyudin I, Nambo H. (2018) Comparison Study of Deep Learning and Time Series for Bioelectric Potential Analysis. In 2018 3rd International Conference on Information Technology, Information System and Electrical Engineering (ICITISEE) (pp. 79-83). IEEE. https://doi.org/10.1109/ICITISEE.2018.8720998

[10]   Tahyudin I, Nambo H. (2018) SARIMA Model of Bioelectic Potential Dataset. In International Conference on Big Data, Cloud and Applications (pp. 367-378). Springer, Cham. https://doi.org/10.1007/978-3-319-96292-4_29

[11]   Kumar J, Goomer R, Singh AK. (2018) Long short term memory recurrent neural network (LSTM-RNN) based workload forecasting model for cloud datacenters. Procedia Computer Science, 125: 676-682. https://doi.org/10.1016/j.procs.2017.12.087

[12]   Benvenuto D, Giovanetti M, Vassallo L, Angeletti S, Ciccozzi M. (2020) Application of the ARIMA model on the COVID-2019 epidemic dataset. Data in Brief, 29: 105340. https://doi.org/10.1016/j.dib.2020.105340

[13]   Ceylan Z. (2020) Estimation of COVID-19 prevalence in Italy, Spain, and France. Science of The Total Environment, 729:138817.

[14]   Zeroual A, Harrou F, Dairi A, Sun Y. (2020) Deep learning methods for forecasting COVID-19 time-Series data: A Comparative study. Chaos, Solitons & Fractals, 140: 110121

[15]   NIST/SEMATECH: Seasonality (2012). http://www.itl.nist.gov/div898/handbook/pmc/section4/pmc443.htm. Accessed 23 September 2020

[16]   Qi C, Zhang D, Zhu Y, Liu L, Li C, Wang Z, Li X. (2020) SARFIMA model prediction for infectious diseases: application to hemorrhagic fever with renal syndrome and comparing with SARIMA. BMC medical research methodology, 20(1): 1-7. https://doi.org/10.1186/s12874-020-01130-8

[17]   Hamilton JD. (2020) Time series analysis. Princeton university press.

[18]   Sherstinsky A. (2020) Fundamentals of recurrent neural network (RNN) and long short-term memory (LSTM) network. Physica D: Nonlinear Phenomena, 404: 132306. https://doi.org/10.1016/j.physd.2019.132306

[19]   Reddy BK, Delen D. (2018) Predicting hospital readmission for lupus patients: An RNN-LSTM-based deep-learning methodology. Computers in biology and medicine, 101: 199-209. https://doi.org/10.1016/j.compbiomed.2018.08.029

[20]   Qi J, Liu X, Tejedor J. (2020) Variational inference-based Dropout in recurrent neural networks for slot filling in spoken language understanding. arXiv Preprint arXiv:2009.01003

[21]   Li C, Zhao L, Cai B. (2020) Size prediction of railway switch gap based on RegARIMA model   and   LSTM   network.   IEEE   Access,   8,   198188-198200. https://doi.org/10.1109/ACCESS.2020.3034687

[22]   Z. Liu *et al.*, "Entity recognition from clinical texts via recurrent neural network," *BMC Med. Inform. Decis. Mak.*, vol. 17, no. Suppl 2, 2017, doi: 10.1186/s12911-017-0468-7

[23]   M. A. Jishan, K. R. Mahmud, A. K. Al Azad, M. S. Alam, and A. M. Khan, "Hybrid deep neural network for bangla automated image descriptor," *Int. J. Adv. Intell.   Informatics*,   vol.   6,   no.   2,   pp.   109–122,   2020. https://doi.org/10.26555/ijain.v6i2.499

FORECASTING OF INFECTION PREVALENCE OF *HELICOBACTER PYLORI* USING REGRESSION ANALYSIS

KOMILJON USAROV[1], ANVARJON AHMEDOV[1],
MUSTAFA FATIH ABASIYANIK[2] AND KU MUHAMMAD NA'IM KU KHALIF[1]

[1]*Centre for Mathematical Sciences College of Computing & Applied Sciences of Computer Science Universiti Malaysia Pahang, 26300 Kuantan, Pahang, Malaysia.*
[2]*Pritzker School of Molecular Engineering, The University of Chicago, Edward H. Levi Hall, 5801 South Ellis Avenue Chicago, Illinois 60637, USA.*

[*]*Corresponding author: ukomiljon@gmail.com*

ABSTRACT: Global warming may have a significant impact on human health because of the growth of the population of harmful bacteria such as *Helicobacter pylori* infection. It is crucial to predict the prevalence of a pathogen in a society in a faster and more cost-effective way in order to manage caused disease. In this research, we have done predictive analysis of *H. pylori* infection spread behavior with respect to weather parameters (e.g., humidity, dew point, temperature, pressure, and wind speed) of Istanbul based on a database from Istanbul Samatya Hospital. We developed a forecasting model to predict *H. pylori* infection prevalence. The goal is to develop a machine learning model to predict *H. pylori* (Hp) related infection diseases (e.g., gastric ulcer diseases, gastritis) based on climate variables. The dataset for this study covered years from 1999 to 2003 and contained a total of 7014 rows from the Samatya Hospital in Istanbul. The weather information related to those years and location, including humidity (H), dew point (D), temperature (T), pressure (P) and wind speed (W), were collected from the following website: https://www.wunderground.com. In this paper we analyzed the forecasting model, which was used to predict *H. pylori* infection prevalence, by non-linear multivariate linear regression model (MLRM). We applied the non-linear least square method of minimization for the sum of squares to find optimal parameters of MLRM. Multiple Regression Method was used to determine the correlation between a criterion variable and a combination of predictor variables. It was established that the Hp infection disease is most influenced by humidity. Hp prevalence is modelled using the Multiple Regression Method equation, the average H, D, T, P, and W were the most important parameters to deviation of the datasets (testing dataset was 17% and 18% for training dataset). This showed that the statistical model predicts the Hp prevalence with about 83% accuracy of the testing data set (11 months) and 87% accuracy of the training data set (42 months). Based on the proposed model, monthly infection can be predicted early for medical services to take preventative measures and for government to prepare against the bacteria. In addition, drug producers can adjust their drug production rates based on forecasting results.

ABSTRAK: Pemanasan global mungkin mempunyai kesan langsung terhadap kesihatan manusia kerana pertambahan populasi bakteria merbahaya seperti infeksi *H. pylori*. Adalah penting bagi mengesan kehadiran patogen dalam masyarakat bagi mengawal penularan penyakit dengan cepat, dan melalui kaedah kurang mahal. Kajian ini berkaitan analisis ramalan penularan infeksi *H. pylori* secara langsung terhadap parameter cuaca (cth: kelembapan, titik embun, suhu, tekanan, kelajuan angin) di Istanbul berdasarkan data dari Hospital Samatya Istanbul. Kajian ini membentuk model ramalan bagi menjangka

penyebaran infeksi *H. pylori*. Matlamat adalah bagi mencipta model pembelajaran mesin bagi mengjangka penyakit berkaitan infeksi *H. pylori* (Hp) (cth: penyakit ulser gastrik, gastrik) berdasarkan pembolehubah cuaca. Dari tahun 1999 ke 2003, set data telah digunakan bagi mempelajari di mana sejumlah 7014 baris dari Hospital Samatya di Istanbul. Informasi berkaitan tahun-tahun tersebut dan lokasi mengenai kelembapan (H), titik embun (D), suhu (T), tekanan (P) dan kelajuan angin (W) dikumpul dari laman sesawang https://www.wunderground.com. Kajian ini menggua pakai model ramalan bagi meramal kelaziman infeksi *H. pylori*, melalui model regresi berkadaran multivariat tidak-berkadaran (MLRM). Kaedah Kuasa Dua Terkecil tidak linear digunakan bagi pengurangan jumlah ganda dua bagi mencapai parameter optimum MLRM. Kaedah Regresi Gandaan digunakan bagi mencari persamaan antara kriteria pembolehubah dan gabungan pembolehubah ramalan. Dapatan menunjukkan infeksi penyakit Hp adalah disebabkan oleh faktor kelembapan. Penyebaran Hp dimodel menggunakan persamaan Kaedah Regresi Gandaan, purata H, D, T, P dan W adalah parameter terpenting bagi sisihan data latihan iaitu sebanyak 17% dan 18% bagi set data latihan. Ini menunjukkan model statistik menjangkakan penyebaran Hp adalah sebanyak 83% adalah tepat pada set data yang diuji (selama 11 bulan) dan 87% tepat pada set data latihan (selama 42 bulan). Berdasarkan model yang dicadangkan ini, infeksi bulanan dapat di jangka lebih awal bagi membendung servis kepada perubatan dan kerajaan bersiap-sedia memerangi bakteria ini. Tambahan, prosedur jumlah ubatan dapat dihasilkan lebih atau kurang daripada jumlah ubatan berdasarkan dapatan ramalan.

KEY WORDS: *H. pylori; infectious disease prediction; multivariate linear regression*

1. INTRODUCTION

Helicobacter pylori is highly prevalent in approximately 50% of the world's population [1], causes inflammation in the stomach and leads to chronic gastritis, peptic ulcer diseases (PUD), gastric ulcers (GU), duodenal ulcers (DU), and eventually gastric cancer in the human stomach [1,2,3]. In the United States, about 10% of the population will develop a duodenal ulcer at some point in their lives. Peptic ulcer disease affects about 4 million people annually in the world [4]. The occurrence of peptic ulcer disease is similar in men and women. Approximately 11%-14% of men and 8%-11% of women will develop peptic ulcer disease in their lifetime. The mortality rate for peptic ulcer disease is approximately one death per 10,000 cases. The mortality rate due to ulcer hemorrhage is approximately 5%. According to GLOBOCAN 2018 data, stomach cancer is the 3rd most deadly cancer with an estimated 783,000 deaths in 2018 [5]. It causes high cost to society and even brings on high risk to human lives.

The prediction of *H. pylori* prevalence has essential impact on the minimizing of the transmission of *H. pylori* related infectious diseases, which is a core function of public health law. Laws can be affected that prevent prevalence of the infection, but it is crucial to know early about the infection prevalence using forecasting models. The literature consists of some interesting research work related to forecasting models for infections such as malaria, scarlet fever, chickenpox [5] combining Big Data and Neural Networks. Moreover, there are some articles about predictions based on environmental factors which have a great impact on the prevalence of the infections. For instance, Song et al. built a time series model based on eight climate variables to predict hand, foot, and mouth disease [6]. In addition, Lu et al. showed that average daily sunshine time correlated positively with *H. pylori* infection [1]. Previous studies showed that using climate variables can be more accurate and efficient to predict infection prevalence.

Since there is no prediction model for *H. pylori* disease prevalence, we set a goal to design forecasting model for *H. pylori* prevalence based on the following environmental factors: humidity, dew point, temperature, and wind speed by using outstanding machine learning tools such as multivariate linear regression model (MVLR). This model will enable market players (e.g., doctors, government, pharmaceutical firms, etc.) to take sufficient precautions before outbreaks.

Ultimately, by building the forecasting model, we have proven that it is possible to predict the *H. pylori* infection prevalence and to know early information about the spread of the infection. It gives a chance to act for prevention procedures against the infection, which leads not only to reducing the prevalence of the infection, but it also minimizes social costs for the public and saves many people's lives. Furthermore, it can increase hospital services for patients and drug producers can develop drugs based on the demand of the patients.

2. MATERIALS AND METHODS

2.1 Research Data

From the original dataset from 7014 patients, only non-null values of CLO attribute were selected, leaving 4388 patients between 1999 to 2003 in the Samatya hospital in Istanbul, Turkey, which includes 48 attributes such as visiting date, gastritis cancer, DU, GU, gastritis, abdominal pain, stomachache, and CLO results. The ages were divided into below 20, 20-30, 30-40, 40-50, 50-60, and above 60 years old, representing 2%, 13%, 19%, 24%, 21% and 30% of the total dataset, respectively. More than half of patients were above 50 years old. Cases were 16% of DU, 18% of deformative pylorus, 19% of (peptic ulcer) (PU), 27% of deformative bulbus, 41% of erosive duodenitis, 46% of feel pain, 58% Hp infected, 22% stomachache, 93% of pangastritis and 99% of gastritis of the patients. In addition, there were 51% male and 49% female patients. The bacterial infection of each patient was detected by a special test called CLO and patients with a positive CLO test were assumed to be infected (Table 1).

Table 1: Baseline and outcome clinical characteristics of *H. pylori* patients

Parameters	4388 of patients (%) percentage from total patients
Female	2247 (51%)
Male	2141 (49%)
Pain	2015 (46%)
Hp	2547 (58%)
Pangastritis	4087 (93%)
Erosive duodenitis	1811 (41%)
Gastritis	4347 (99%)

Weather data (WD), (Humidity - the concentration of water vapor present in the air, dew point - the temperature to which air must be cooled to become saturated with water vapor, temperature - a degree of heat or cold the can be measured using a thermometer in degrees on the Fahrenheit, Celsius, and Kelvin scales, pressure or air pressure - the force per unit of area exerted on the Earth's surface by the weight of the air above the surface, wind speed or wind flow speed - a fundamental atmospheric quantity caused by air moving

from high to low pressure, usually due to changes in temperature) including humidity (%), dew point (°F) (https://en.wikipedia.org/wiki/Dew_point), temperature (°F), pressure (Hg), wind speed (mph) was obtained from historical data by average daily information in the https://www.wunderground.com/history website, joined with the visitor date attribute. The joined data was transformed into a monthly dataset using sum of Hp and mean of humidity, dew point, temperature, pressure, wind speed aggregate functions. The final data contains V (number of visitors), Hp (sum of Hp), H (mean of humidity), D (mean of dew point), T (mean of temperature), P (mean of pressure), W (mean of wind speed) attributes and 53 months of observed rows (see Table 2). All of this was performed using Google Colab Notebook (https://colab.research.google.com/) and Python3 (https://www.python.org/) machine learning libraries (https://scipy.org/) on Google's Cloud TPU Server.

The dataset above was divided into a train subset and a test subset with a ratio of 80% and 20%, respectively. It means that all 53 months of rows were split into 42 months of rows of training data subset and 11 months of rows of testing data subset.

2.2 Method

The following multivariate linear regression model was used to forecast Hp based on Table 2 data:

$$y = f(H, D, T, W) =$$
$$\beta_1 sin^2(\rho_1 H + \rho_2) sin^2(\rho_3 T + \rho_4) \ + \ \beta_2 sin^2(\rho_5 H + \rho_6) sin^2(\rho_7 T + \rho_8) \ +$$
$$\beta_3 sin^4(\rho_9 D + \rho_{10}) sin^4(\rho_{11} W + \rho_{12}) + \beta_4 sin^4(\rho_{13} D + \rho_{14}) sin^4(\rho_{15} W + \rho_{16}) +$$
$$\beta_5 sin(\rho_{17} H D + \rho_{18}) + \beta_6 \tag{1}$$

Where:

y - dependent variable (Hp – the number patients who had positive CLO infection test),
H - the average of humidity (%)
D - the average of dew point (°F)
T - the average of temperature (°F)
W - the average of wind speed (MPH)
ρ_{1-18} - non-linear regression coefficients,
β_{1-5} - regression coefficients,
β_6 - constant.

2.3 The Algorithms

In order to determine which ρ_{1-18} and β_{1-6} vector paraments give the best fit to the data, the sum of squares of the residuals is minimized. The residuals are defined for each observed data-point as

$$\varepsilon_i = y_i - f(H_i, D_i, T_i, W_i) \tag{2}$$

Where y_i is the number of the total infected per month by *H. pylori* in the given region. We perform the leastsq command (nonlinear least square solver) in SciPy in python from scipy.org.

2.4 MVLR Assumptions

In order to achieve validity of the tests of hypothesis (like t-test, F-test) and to enhance that OLS estimators are the Best Linear Unbiased Estimator (BLUE), it needs to follow four base assumptions:

1. The relationship between the dependent variable and the independent variables is linear.

2. The residuals are independent.

3. Homoscedasticity.

4. Normality of residuals with mean equals to zero.

The Durbin-Watson statistic (DW) was used to check that residuals are independent. If DW is between 1.65 and 2.35, there is no autocorrelation. If DW is between 1.21 and 1.65 or between 2.35 and 2.79, the test is inconclusive [7]. Homoscedasticity is a word used for the "constant variance" assumption. The regression model assumes that the residuals have the same variance throughout. When this assumption is violated, the problem is called "heteroscedasticity," or changing variance. We used the Breusch – Pegan and White test to check it. Errors need to be a normal probability distribution. This makes no difference to the estimates of the coefficients, or the ability of the model to forecast. But it does affect the F- and t-tests and confidence intervals. We used more testing algorithms such as Jarque–Bera Test (JB), Shapiro-Wilk Test, D'Agostino's K-squared Test, Anderson-Darling Test because it is a very important assumption to rate the model.

3. RESULTS AND DISCUSSION

3.1 Statistical Analysis

In Table 2, the four-year hospital statistics show the average monthly infection rate was 58% among average monthly visitors (78 ± 44) of 45.1 patients among average 78.4 visitors per month in four years. It is shown that more than half of visitors were infected by *H. pylori* infection.

Table 2: Statistics of monthly data

	count	mean	std	min	25%	50%	75%	max
Total Visitors	53	78.4	44	1	49	81	100	190
Total Hp	53	45.1	25	0	26	47	60	113
Humidity (°F)	53	72	8.7	54	68	72	78	92
Wind Speed (mph)	53	9.8	2.2	3.5	8.7	10	11	17
Dew Point (°F)	53	50.6	12	22	44	50	60	73
Temperature (°F)	53	61.2	13	36	52	61	72	82

n=53, which is the total number of months in the study

Correlations of attributes for both data sets can be seen in Table 3. H attribute negative correlates to total Hp. D and T were correlated positive with 0.10 and 0.15 respectively.

Table 3: Correlations between given variables for monthly transformed data

	Total Hp	**H**	**W**	**D**	**T**
Total Hp	1.00	-0.25	-0.02	0.10	0.15
H	-0.25	1.00	0.14	-0.30	-0.53
W	-0.02	0.14	1.00	-0.14	-0.12
D	0.10	-0.30	-0.14	1.00	0.96
T	0.15	-0.53	-0.12	0.96	1.00

The box plot graph shows that for 5 years the number of visitors was close each month of year in January, February and September. However, in June and July there was very high difference between the number of visitors for each year. While the infected number of patients was very close in January, February, and August, there was a wide spread of numbers and the highest number of the infected patients with Hp in April, June, and July (Fig. 1).
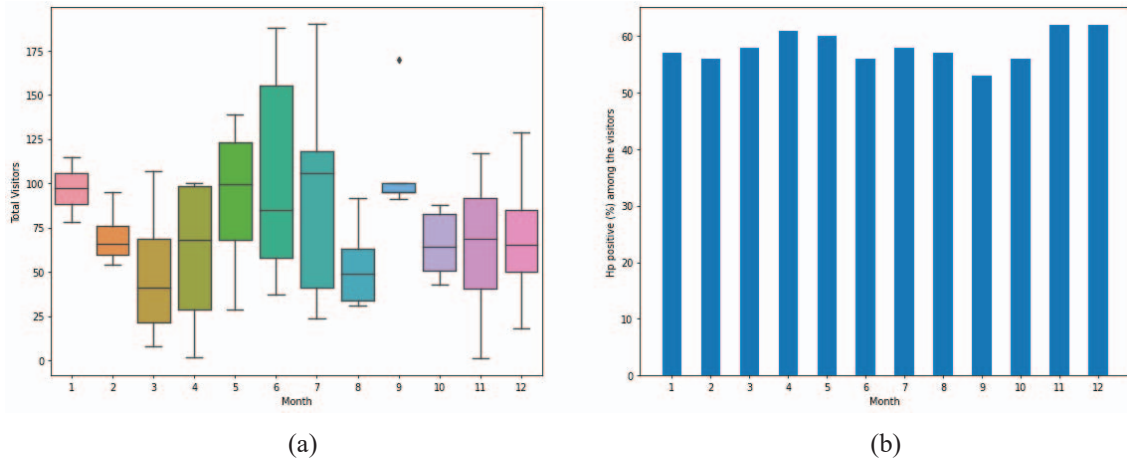
(a)   (b)

Fig. 1: The box plot for total visitors (a) and the Hp infected patients in percentage among visitors (b) are demonstrated by months.

We found various behaviors of the independent variables, such as the number of visitors and the number of Hp infected patients, in different climate conditions. According to the given dataset, the behavior of the independent variables was maximized, when weather temperature was 75-80 ℉, the humidity was 75%-80%, the pressure was between 29.8 mmHg and 30 mmHg, the wind speed was between 9 MPH and 10 MPH, and the dew point was between 45 ℉ and 50 ℉, 60 ℉ and 65 ℉. All of those factors were significant since null hypothesis were rejected ($p<0.05$) (Fig. 2).
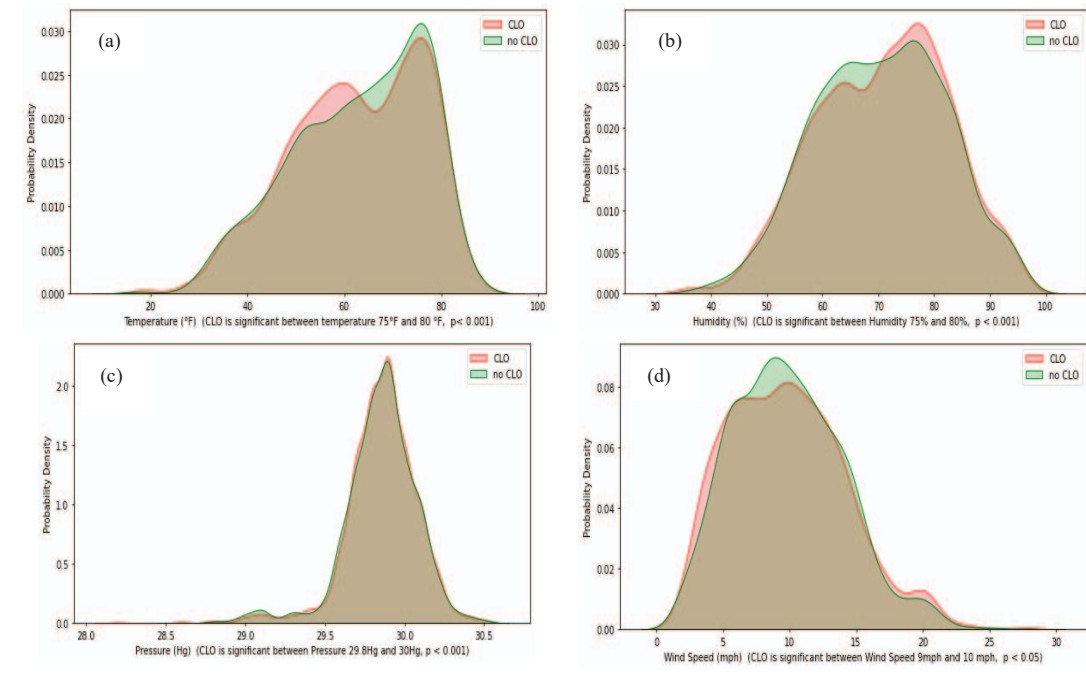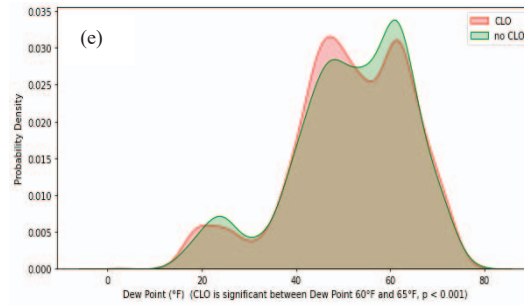
Fig. 2: For monthly average data, Hp positive and negative factors are represented by forecast weather variables: temperature (a), humidity (b), pressure (c), wind speed (d), dew point (e).

In addition, the behavior of the independent variables was highly impacted for the 45-50 years old patients (p-value<0.05) (Fig. 3). Moreover, the number of CLO infected patients grew until 50 years old, and it began to drop after that.
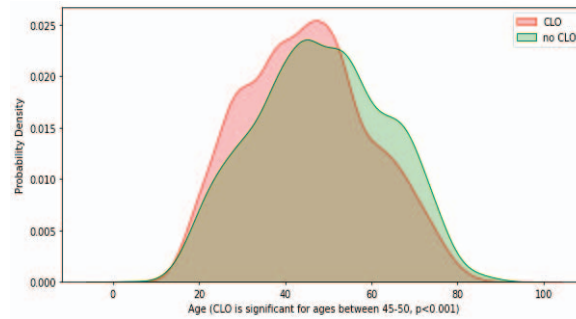
Fig. 3: The positive and negative CLO factors are represented by age of the patients.

Here we studied monthly and yearly statistics for NV and NC. NV and NC were more in June and September (p-value<0.05 each) than other months. Also, it is significant for March and August where there were p-values < 0.05 (Fig. 4a). There was strong growth of the number of visitors and CLO patients between 1999 and 2002 and it reached a peak in 2002 (it is significant for 2002, p-value<0.05) and dropped significantly in 2003. Note that there were no records for last two months in 2003 (November and December of data in 2003 (Fig. 4b).
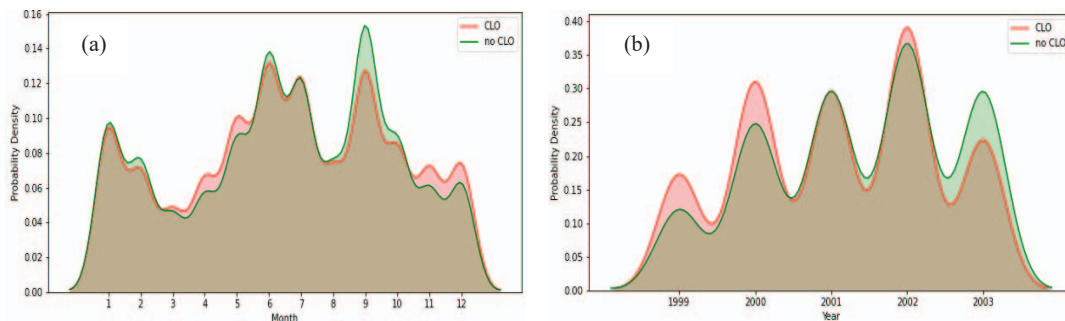
Fig. 4: The positive and negative CLO factors are represented by month (a) and year (b).

3.2 Model

Using Eq. (2) we obtained optimal parameters of Eq. (1) the proposed model described for Hp infection prevalence by the below mathematical formula:

$y = f(H, D, T, W) = 31.1237 sin^2(3.7370H - 121.6778) sin^2(2.9952T+112.3183) +$

$68.2460 sin^2(7.1261\ H + 0.2939) sin^2(8.8473\ T+17.8187) +$

$72.6059 sin^4(12.4216\ D\text{-}15.3039) sin^4(12.4320\ W+27.8774)+$

$70.2747 sin^4(16.9445\ D+20.2464) sin^4(18.7481\ W+21.9338) +$

$19.8196 sin(22.0029\ HD+12.7998) + 1.6339$ (3)

The MVRM was obtained with a training subset of data. This formula predicts the accuracy with coefficient of determination (R^2) equal to 87% and 83% for train data (42 months) and test data (11 months), respectively (Fig. 4). And adjusted R^2 is 85% which is high. It means that the correlation coefficient between the observed value of the dependent variable and the forecast value based on the regression model was high.

ANOVA table showed that the value of F statistic was 48.36 and the significance of F was zero which is less than the critical value ($p<0.001$). The null hypothesis was rejected. It means that the model is significant.

3.3 Regression Assumptions

The proposed model was linear by β_{1-6} coefficients. It gives us the first assumption true. DW test was 1.998 which lies between 1.65 and 2.35. Therefore, there is no autocorrelation between residuals and predicted values (Fig. 5b). Thus, the model held 2 assumptions. The Breusch–Pegan Test showed that the null hypothesis was not rejected ($p>0.05$), meaning that the model holds 3 assumptions. It can be seen in Fig. 5a. by the QQ plot, which easily proves that it is homoscedasticity. The last assumption is also true for the given model and the mean of residuals is zero. In addition, Jarque–Bera(JB), Shapiro-Wilk, D'Agostino's K-squared, Anderson-Darling tests rejected null hypothesis ($p>0.05$) which means the residuals are normally distributed (Fig. 5c).

(a) QQ plot.   (b) Independence of residuals.   (c) Distribution of residuals.
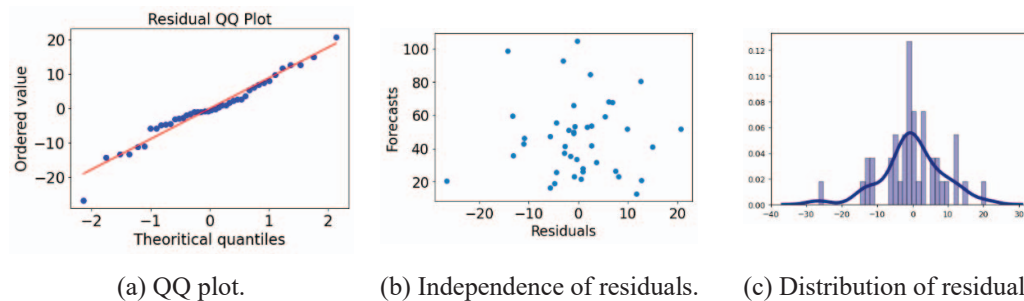
Fig. 5: Residuals analysis.

3.1 Forecast Results

The forecasts result of training and testing data were represented by Fig. 6, where it was separated by a grey vertical line. By date (month, year) and the number of CLO are represented by x-axis and y-axis, respectively. Actual data is in blue color, training data is in green and testing data is in red color. The forecasting data started from November, 2002 until October 2003, which means that almost all 1-year forecasts are highly accurate.

We calculated lower and upper prediction intervals using

Upper Prediction Interval $\mathbf{UPI}_i = \hat{y}_i + z\sqrt{\text{MSE}}$

Lower Prediction Interval $\mathbf{LPI}_i = \hat{y}_i - z\sqrt{\text{MSE}}$ (4)

Where:

Mean Squared Error (MSE) = $\frac{1}{n}\sum(y_i - \hat{y}_i)^2$ (5)

$z = 1.645$, the forecasted data with a 90% prediction interval   (6)

Prediction intervals for train data and test data **UPI**$_i$ and **LPI**$_i$ are represented by green dot line and red dot line, accordingly with 90% probability ($z = 1.645$). (Fig. 7a and Fig. 7b).
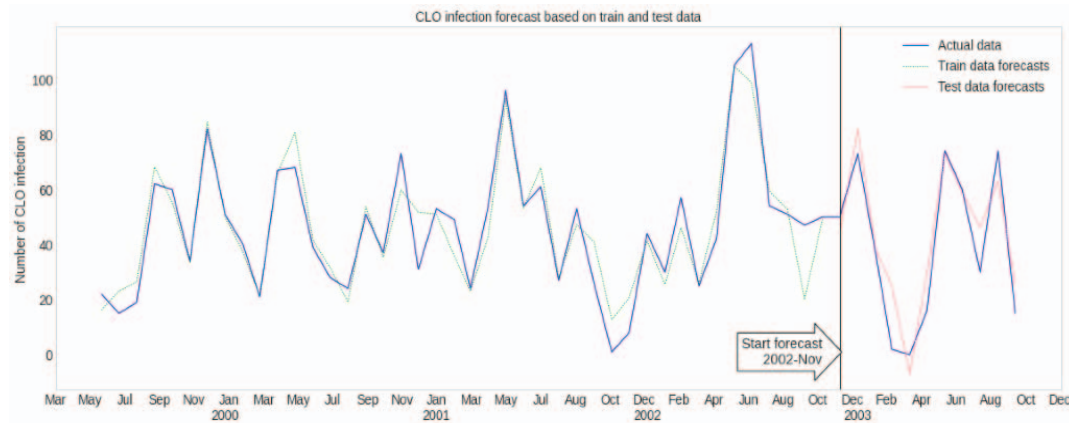
Fig. 6: True train and test data and its forecasts. (The grey line is separator between train and test data).
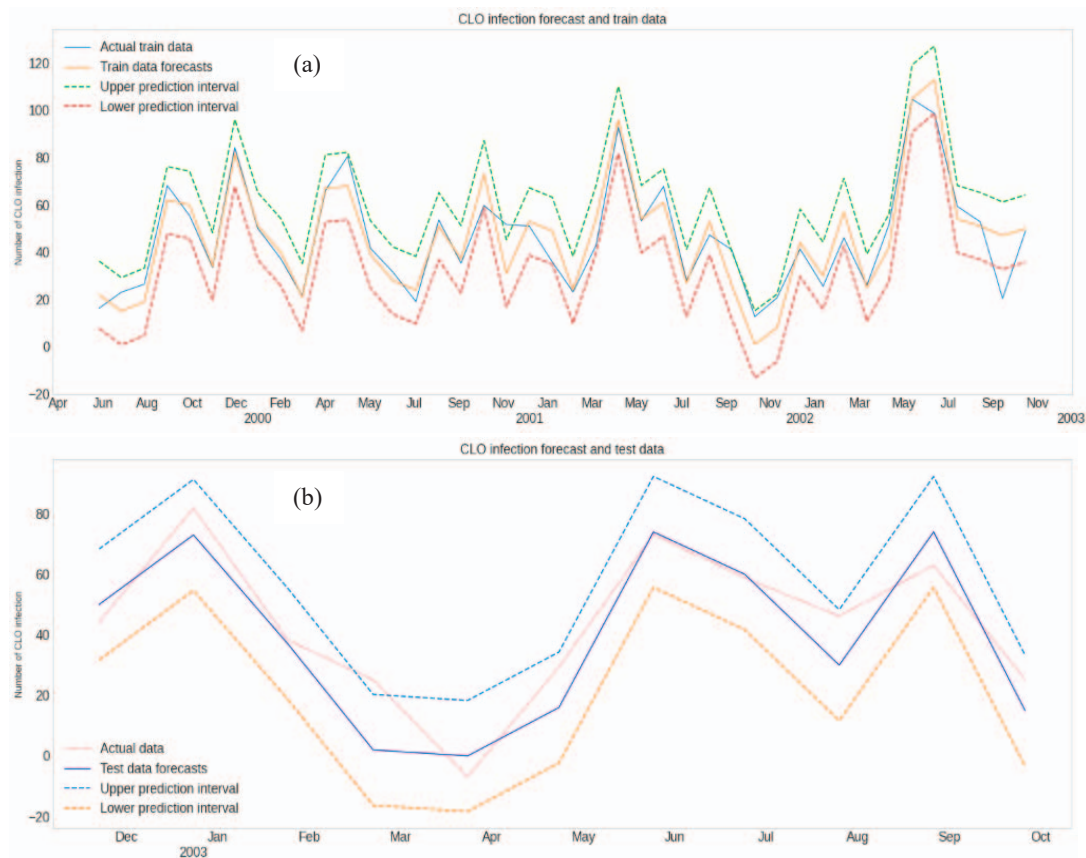
Fig. 7: Train data prediction with a 90% prediction interval ($z = 1.645$, MSE = 79.29) for MVRM in (a), test data prediction with a 90% prediction interval ($z = 1.645$, MSE = 124.13) for MVRM in (b.)

4. CONCLUSIONS

In this paper, we proposed non-linear MVRM to predict the prevalence of H. pylori infection prevalence based on the patients records of the hospital. If average monthly climate variables are introduced, the model predicts the number of *H. pylori* infection related to the given month's average climate variables. The proposed model uses to find patterns of H. pylori infection behavior based on the mean of humidity, dew point, temperature, and wind speed of months. Our researched showed that only the forecasting model achieves more accurate results by using the combinations of the given climate variables.

Since the infectious disease is a social problem, it can impact not only personal health, but can also cause widespread damage. Therefore, this research is being conducted to minimize social cost by predicting the prevalence of the *H. pylori* infection. The aim of this study was to design a forecasting model to predict *H. pylori* infection, which does not exist in the research papers yet, by using various input climate variable techniques based on non-linear MVRM with high accuracy. For this reason, we used non-linear Least Square method to find the regression coefficients of the model. The proposed model is significant since it holds four base assumptions of MVRM and gives 83% and 87% accuracy for training and testing dataset, respectively.

The proposed model helps to conduct precise predictive analysis of H. pylori infection prevalence for 1 year based on the dynamics of climate variables. Keeping in mind importance of climate variables in the forecast modelling of H. pylori infection prevalence we found high correlation between the climate factors and the prevalence. This model gives high accurate early forecast results which can be used by hospitals or governments to do early prevention acts against the infection prevalence, since it is critical to safe life of people and reduce cost in society. The proposed model is not only giving highly accurate results, but also it is easy to use by excel or sample calculators.

The obtained results of prediction analysis of *H. pylori* infection prevalence can be extended to the region with a similar climate condition. In further research, the model can be improved with different regions of databases and climate factors and also to check weather to possibly simplify mathematical formula of the proposed model by reducing the climate variables.

REFERENCES

[1] Lu C, Yu Y, Li L, Yu C, Xu P. (2018) Systematic review of the relationship of Helicobacter pylori infection with geographical latitude, average annual temperature and average daily sunshine. BMC gastroenterology, 18(1): 50.

[2] Tang MY, Chung PH, Chan HY, Tam PK, Wong KK. (2019) Recent trends in the prevalence of *Helicobacter pylori* in symptomatic children: A 12-year retrospective study in a tertiary centre. Journal of pediatric surgery, 54(2): 255-257.

[3] Peek Jr RM, Blasser MJ. (1997) Pathophysiology of *Helicobacter pylori*-induced gastritis and peptic ulcer disease. The American journal of medicine, 102(2): 200-207.

[4] Thorsen K, Søreide JA, Kvaløy JT, Glomsaker T, Søreide K. (2013) Epidemiology of perforated peptic ulcer: age-and gender-adjusted analysis of incidence and mortality. World Journal of Gastroenterology, 19(3): 347.

[5] Rawla P, Barsouk A. (2019) Epidemiology of gastric cancer: global trends, risk factors and prevention. Przeglad gastroenterologiczny, 14(1): 26.

[6] Song Y, Wang F, Wang B, Tao S, Zhang H, Liu S, Ramirez O, Zeng, Q. (2015) Time series analyses of hand, foot and mouth disease integrating weather variables. PloS one, 10(3): e0117296. https://doi.org/10.1371/journal.pone.0117296

MECHANICAL AND THERMAL CONDUCTIVE PROPERTIES OF NATURAL AND SYNTHETIC CELLULOSE REINFORCED EPOXY COMPOSITES

OMRAN A. SHABEEB[1], DAWOOD S. MAHJOOB[2], HAMID M. MAHAN[2] AND MUAMMEL M. HANON[2,3*]

[1]*Middle Technical University, Electrical Engineering Technical College, 10022 Baghdad, Iraq.*
[2]*Middle Technical University, Baqubah Technical Institute, 32001 Diyala, Iraq.*
[3]*Mechanical Engineering Doctoral School, Szent István Campus, MATE University, 2100 Gödöllő, Hungary.*

[*]Corresponding author: Sharba.Muammel.M.Hanon@phd.uni-szie.hu

ABSTRACT: Natural and synthetic cellulose-based composites have been used widely as they have many advantages, the most significant of which are lightweight, durable, strong, flexible, and resistant to corrosion. Although several studies have reviewed the characteristics of these composites, only limited research has investigated combining both natural and synthetic cellulose together. In this study, the thermal and mechanical properties of epoxy resin reinforced with different additives (sawdust and industrial cellulose) will be explored. To do this, four samples of different materials were prepared at room temperature. The first sample consisted of 100% epoxy, whilst the next sample contained 95 wt.% epoxy and 5 wt.% industrial cellulose. The third sample contained 95 wt.% epoxy and 5 wt.% natural cellulose (sawdust), and the final sample contained 95 wt.% epoxy, 2.5 wt.% natural cellulose and 2.5 wt.% industrial cellulose. The findings indicated that mechanical properties and thermal insulation can be enhanced by adding natural cellulose to the mixture. Compared to the pristine epoxy, the improvement ratios for mechanical properties were as follows: tensile strength 25%, impact strength 16.6%, and hardness 6.9%, while the results were negative for bending resistance (3.9% less). In terms of thermal properties, the sawdust/epoxy composite showed better insulation (29% higher) than neat epoxy resin. These promising findings suggest the proposed composite can be a good alternative in numerous applications such as automotive parts and building construction that require superior mechanical characteristics and thermal insulation.

ABSTRAK: Komposit semula jadi dan sintetik berasaskan selulosa telah banyak digunakan secara meluas kerana ia mempunyai banyak faedah, dan yang paling penting ianya ringan, tahan lama, kuat, fleksibel dan tahan hakisan. Walaupun terdapat banyak kajian telah dilakukan pada ciri-ciri yang terdapat pada bahan komposit ini, terdapat kurang kajian dilakukan ke atas gabungan Bersama kedua-dua bahan semua jadi dan sintetik selulosa. Kajian ini adalah tentang suhu dan ciri-ciri mekanikal damar epoksi yang diperkukuhkan dengan pelbagai bahan tambahan seperti serbuk gergaji dan selulosa industri. Bagi menghasilkan bahan kajian ini, empat sampel dari bahan berbeza disediakan pada suhu bilik. Sampel pertama terdiri daripada epoksi 100%, sementara sampel berikutnya mengandungi epoksi 95 wt.% dan selulosa industri sebanyak 5 wt.%. Sampel ketiga mengandungi epoksi 95 wt.% dan 5 wt.% selulosa semula jadi (dari serbuk gergaji), dan sampel terakhir mengandungi epoksi 95 wt.%, dan selulosa semula jadi 2.5 wt.% dan selulosa industri 2.5 wt.%. Dapatan kajian menunjukkan ciri-ciri mekanikal dan penebat suhu boleh dipertingkatkan dengan menambah selulosa semula jadi dalam campuran. Jika dibandingkan dengan epoksi asal, nisbah penambah baikan bagi ciri-ciri mekanikal adalah

seperti berikut: kekuatan tegangan 25%, kekuatan hentaman 16.6% dan kekerasan adalah sebanyak 6.9%, sementara dapatan kajian adalah negatif bagi rintangan ketika membengkok (iaitu berkurang sebanyak 3.9%). Dari segi ciri-ciri haba, komposit serbuk gergaji/epoksi menunjukkan sebagai penebat yang baik (meningkat 29%) berbanding damar epoksi bersih. Penemuan yang bagus ini menunjukkan, komposit yang di cadangkan ini dapat menjadi alternatif terbaik dalam pelbagai kegunaan seperti bahagian-bahagian automotif dan pembinaan bangunan yang memerlukan peningkatan ciri-ciri mekanikal dan penebat haba.

KEYWORDS: *natural composites; sawdust; mechanical properties; thermal conductivity; cellulose*

1. INTRODUCTION

Environmental awareness has led researchers to reconsider the design of engineering products for the construction, packaging, future, and vehicle industries. Polymer elements have become favorable parts for numerous applications due to their excellent characteristics [1]. In recent times, increasing attention has been paid to the use of a modified thermoset polymer [2]. Epoxy resins are polymeric or semi-polymeric materials that are part of the thermosets group and are widely used in composite materials [3]. Moreover, epoxy resin has become more popular than alternative products due to its beneficial properties, such as high chemical, thermal, electrical, and mechanical strength [4]. Multiple materials can be mixed to create a composite substance that has a unique combination of properties [5]. Epoxy resin modification is thus an innovative approach to polymer material production [6]. This material can be used to support other materials, which has enabled many workers to improve their properties in this field and to accomplish desired targets [7–9].

Recently, polymers have been reinforced with small amounts of strong fillers, as this can substantially enhance the mechanical and thermal properties [10–14]. It is thus sensible to seek other economically friendly raw materials (fillers) that could strengthen the properties of such products [15]. Modified epoxy resins are often used nowadays because they have great thermal, mechanical, and electrical properties when used to manufacture natural fiber-reinforced composites [16]. As they are environmentally safe and user-friendly, natural fibers are one of the most important components added to epoxy resin [17]. Unlike normal engineering fibers (such as glass, aramid, or carbon), natural fibers are widely usable, sustainable, recyclable, and cost-effective sources of fibers [18].

Natural materials, when compared to man-made materials, can provide a good combination of favorable properties, such as rigidity, strength, and low weight [19]. Natural fibers are also less harmful to the environment than synthetic fibers. Natural fibers are less erosive, which means that as they wear off, the devices' performance may not be affected, and they have a more hospitable manufacturing environment than synthetic fibers [20–22]. Studies exploring the topic demonstrate that sawdust can be added to polymer matrices from various sources, including trees, cellulosic powders, microcrystalline cellulose, natural fibers, and other waste materials produced during woodworking and food processing [23].

Composite materials are made up of two or more materials that have completely separate characteristics and do not dissolve or mix with one another [24]. By combining precise amounts of materials with inherited properties, new materials with modified and better properties can be created [25]. A chunk of wood is made up of long cellulose fibers that are held together by a chemical called lignin [26]. The overlapping materials are lightweight and provide excellent thermal and electrical insulation. Thus, in recent years, they have become increasingly more popular in various fields [27,28]. Natural fiber

insulation is arguably the most practical way to produce environmentally friendly composites. Numerous studies have investigated natural fiber-reinforced composites. In recent years, polymer composites have been studied in great depth [29,30] and sawdust has been found to serve as an insulator, slowing heat flow and conduction. This ultimately enhances its capacity to isolate [31].

It has recently been discovered that, by adding a small quantity of strong fillers to polymers, the mechanical and thermal performance of the composites can be significantly improved [32]. Given their great insulation capacity, these composites can be applied for a variety of purposes. For instance, they can be used to fill the spaces between the interior and exterior sections of walls, or the floor, roof, ceiling, or insulation boards. Moreover, they can be used to manufacture aircraft and automobile parts and furniture. They are thus beneficial in many industries, including transport and even medicine [33].

Plenty of materials (natural and synthetic) have been investigated as reinforcements for polymer composites, as shown by the literature reviewed above. However, the additives utilized to form composites have not yet been fully covered, and there is still much to explore. Combining both natural and synthetic cellulose together in one composite was rarely inspected. Therefore, the present study aims to determine the effect of various combinations of additives, which are made from natural cellulose (sawdust) and industrial cellulose, on the mechanical properties (through tensile, flexural, impact, and hardness tests) and the thermal conductivity of composites, where epoxy is the matrix material. To the best of our knowledge, the combinations of additives utilized here have never been studied before.

2. EXPERIMENTAL WORK

2.1 Material Properties

Epoxy resin (ER) was used as a matrix material for the composites prepared. Epoxy is created by combining the liquid resin and an appropriate hardener. The ratio for resin to hardener is typically 2 to1, which enables the substance to cure perfectly. The epoxy resin used in this study was obtained from Sky Bahrain and contained the Sikadur-52 hardener. The specifications of the epoxy, as per the manufacturer, are presented in Table 1.

Table 1: Specifications of epoxy resin used in the study

Tensile strength (MPa)	Modulus of elasticity (MPa)	Percent elongation (%)	Density (g/cm^3)	Water absorption (%)	Shear strength (MPa)	Flexural strength (MPa)
37	1800	7	1.1	1.5	29.6	63

Industrial cellulose (IC), which is made up of carbon, oxygen, and hydrogen, is a very intricate carbohydrate. Properties of cellulose – $[(C_6H_{10}O_5)_n]$: Many properties are determined by the extent of polymerization, the chain length, and the number of glucose molecules that make up the polymer molecule. Cellulose is tasteless, odorless, and chiral, as well as being both insoluble and biodegradable, and appears in the form of white powder. The physical, mechanical, and thermal properties of the industrial cellulose are tabulated in Table 2.

Table 2: Specifications of industrial cellulose

Tensile strength (MPa)	Modulus of elasticity (MPa)	Percent elongation (%)	Density (g/cm³)	Water absorption (%)	Flexural strength (MPa)	Thermal conductivity (W/m-k)	Specific heat capacity (j/g.°C)
22.1 – 41.4	1005 – 1850	3.7 – 25	1.17 – 1.21	1.3 –1.8	29 – 55.8	0.17 – 0.33	1.26 – 1.67

The natural cellulose (NC) used is sawdust that is produced during the process of sawing wood (type jam wood). This sawdust was collected from the carpentry workshop of the Baquba Technical Institute, Middle Technical University, Iraq. It was then sifted using a sieve with apertures of 50 μm to obtain very fine particles (see Fig. 1a).
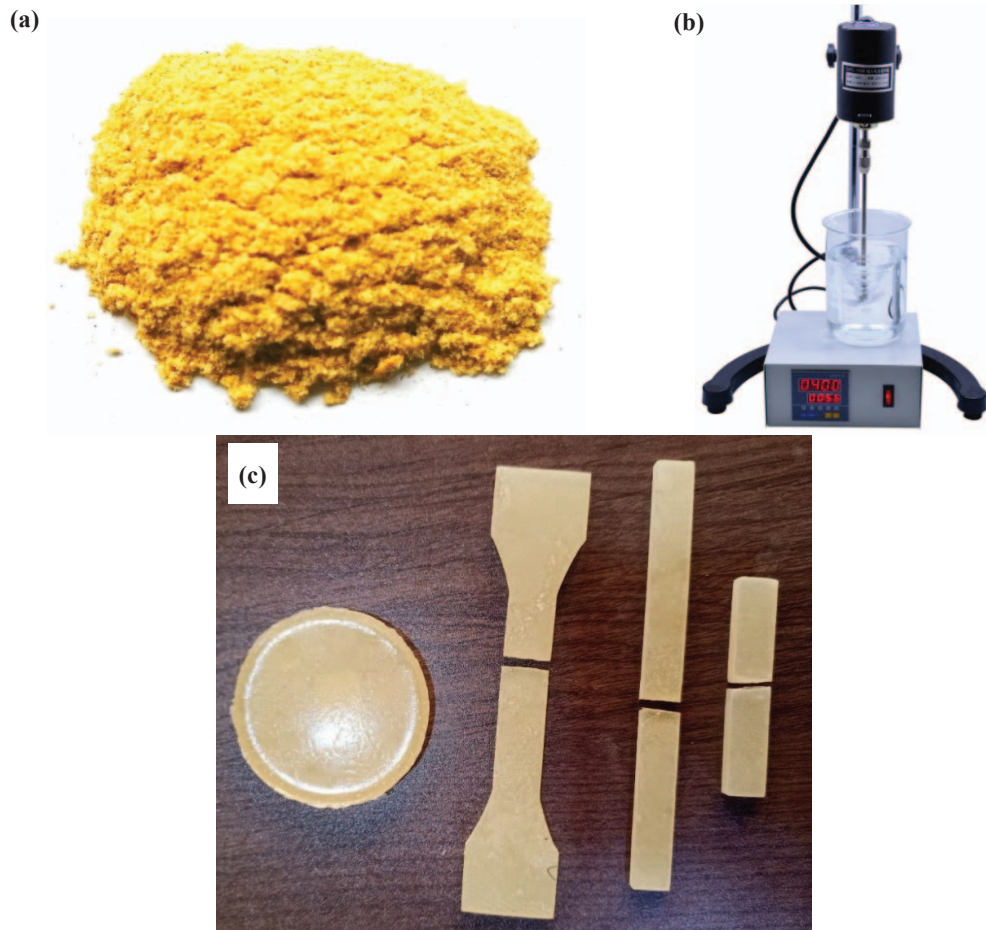
Fig. 1: (a) Physical appearance of natural cellulose (sawdust), (b) digital electric laboratory mixer, and (c) physical appearance of specimens (type ER+NC) after testing.

2.2 Preparing the Polymer Composite

Four square glass molds measuring (130 mm * 130 mm * 5 mm) were used in this experiment. To create casting samples, four polymeric compounds were prepared. These were made up of a base material epoxy resin mixed with a hardener at a mixing ratio (2:1). Once mixed, additives from industrial and natural cellulose were added to the composites for reinforcement (proportions presented in Table 3). The mixing process was carried out utilizing a digital electric laboratory mixer (see Fig. 1b) at room temperature and lasted 15 minutes. Subsequently, samples were left for a day and then placed in an oven for 5 hours

at 60 °C. The primary reason for doing this was to eliminate internal stresses, tangle the chains in the mixture and harden and depressurize the sample [34].

Table 3: Designation and composition of composites

Sample No.	Reinforcement %		
	Cellulose (C)	Epoxy (E)	Sawdust (N)
ER	-	100	-
ER+IC	5	95	-
ER+NC	-	95	5
ER+NC+IC	2.5	95	2.5

2.3 Testing

Physical (thermal conductivity and hardness) and mechanical (tensile, bending, and impact) properties tests were performed on the polymeric compound samples. All experiments were carried out at room temperature, in accordance with American standards (ASTM). A CNC router machine was used to cut three samples of each polymeric compound to the required dimensions. The physical appearance of specimens (of one composite) is shown in Fig. 1c.

Regarding the physical properties' testing, Lee's Disc (type Griffin and George, England) was used to assess the thermal conductivity of the samples as per ASTM-D7340. The sample (disc) was sandwiched between the discs of the test setup. The heater was turned on, and the thermostat was adjusted to the desired temperature. In essence, thermal conductivity refers to a material's resistance to thermal transfer, which reflects the amount of heat that flows through it directly or indirectly. For each polymeric composition, three samples were tested for thermal conductivity. The sample's hardness was determined according to the ASTM D2240 using a durometer hardness tester (also known as the Shore D hardness tester) due to the low hardness of the polymeric compounds. When the indenter is forced into the testing material, the amount of resistance is measured and shown on a digital screen (scale). The key reason for performing the hardness test is to determine whether the material is suitable for use under specific conditions. For each polymeric compound, the hardness test was performed on three samples, during which the average readings for each sample were taken.

In terms of the testing of the mechanical characteristics, the sample tensile tests were carried out at room temperature using the universal testing equipment (see Fig. 2a) in accordance with ASTM D638-Type 1. Thus, a 5 mm/min crosshead speed was used. For each polymeric compound, the tensile test was carried out on three samples, and, during the process, the average results were recorded. During the tensile test, specimens were tightened adequately to avoid sliding. The flexural test of the samples was done in accordance with (ASTM-D790) and was measured using the universal hydraulic press, as the experimental setup seen in Fig. 2b. The two supports grip the specimen firmly, and the span length between them is 65 mm. The samples were tested with a loading rate of 2 mm/min. The flexural strength values are determined by the average of three bending tests. As illustrated in Fig. 2c, a Charpy impact test was performed in accordance with ASTM-E23 to evaluate the impact strength of the developed composites. A pendulum was used to break the unnotched specimen, with the test piece held tightly at each end. It is very important to perform a mechanical shock test to ensure that a material is safe. In this test, the extent to which a material is resistant to sudden shocks is evaluated. All specimens' dimensions used in the tests are shown in Fig. 3.
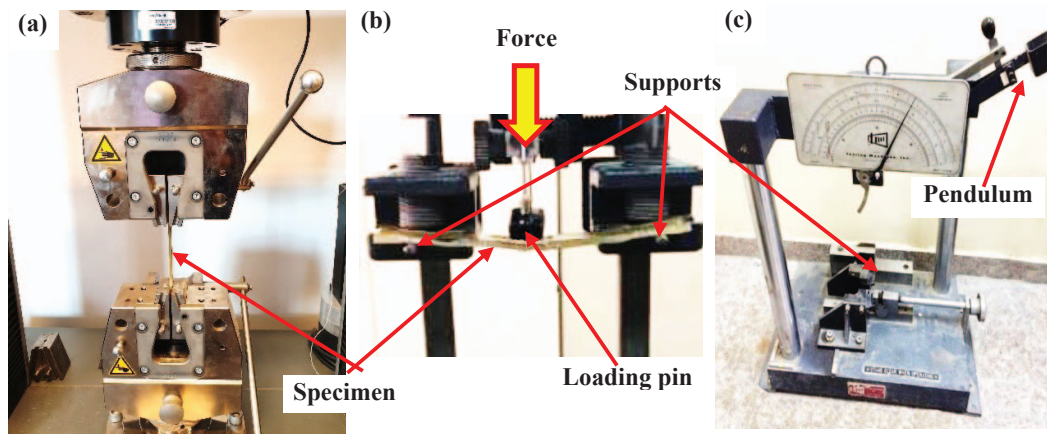
Fig. 2: Experimental setup of mechanical tests (a) tensile, (b) flexural, and (c) impact.

Thermal conductivity test specimen (ASTM-D7340)

Hardness test specimen (ASTM-D2240)

Tensile test specimen (ASTM-D638, tape 1)

Bending test specimen (ASTM-D790)

Impact test specimen (ASTM-E23)

Fig. 3: Sample's dimensions of physical and mechanical properties tests.

3. RESULTS AND DISCUSSION

3.1 Physical Properties: Thermal Conductivity

The conductivity can be influenced by the existence of interfacial layers, free volume, and gaps or cracks within the inner structure. When fillers are loaded as particles during the sample's preparation, they might generate gaps because air voids (created while mixing) are

unable to escape due to the particles. Therefore, all specimens containing particles were found to reduce the thermal conductivity of composites as compared to the pristine epoxy. As wood is a heat-insulating material, the sample with the polymeric compound (ER+NC) had the lowest thermal conduction efficiency (see Fig. 4) and hence provided the best thermal insulation. When compared to the epoxy resin specimen (the reference specimen), the improvement rate was 29%. This indicates that the presence of wood contributed to reducing the thermal conductivity of composites due to owning less thermal conductivity than epoxy as well as being in a form of particles within the matrix. The tendency of the results obtained agrees with the f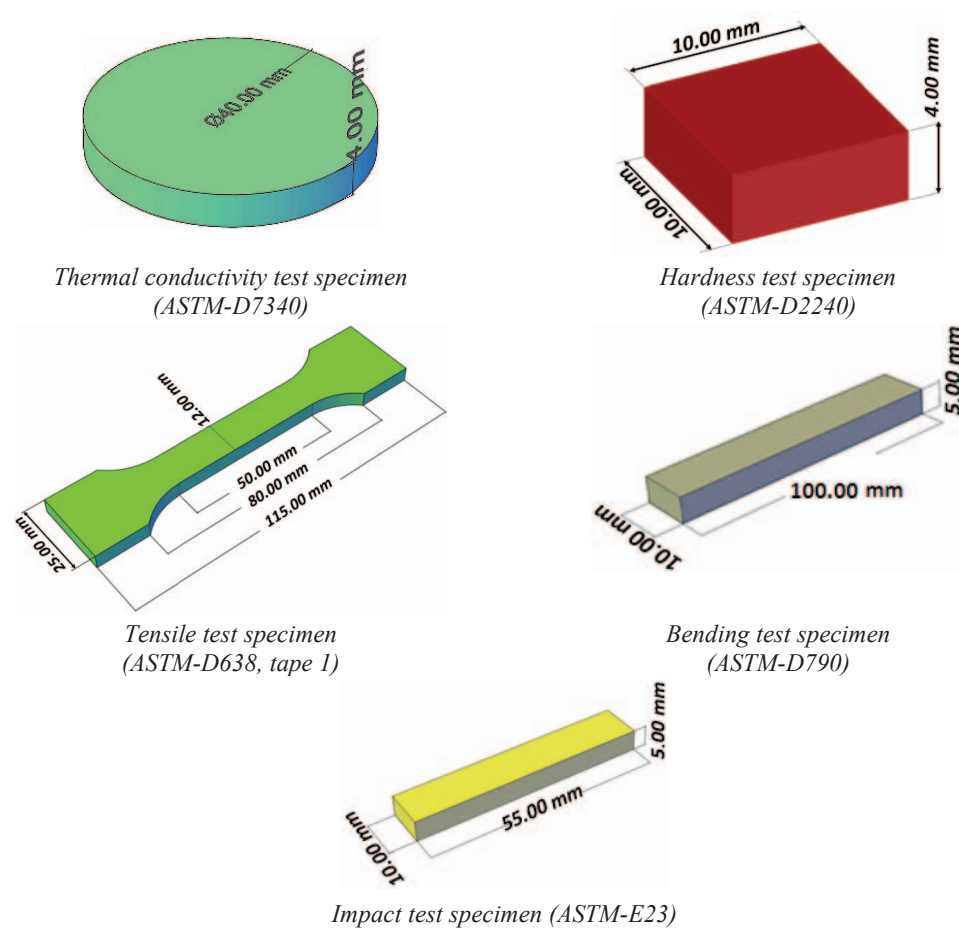indings of a previous study [35]. They reported that adding 10 wt.% of wood dust to a composite reduces the composite's heat conductivity by around 67.1% compared to the neat epoxy resin.
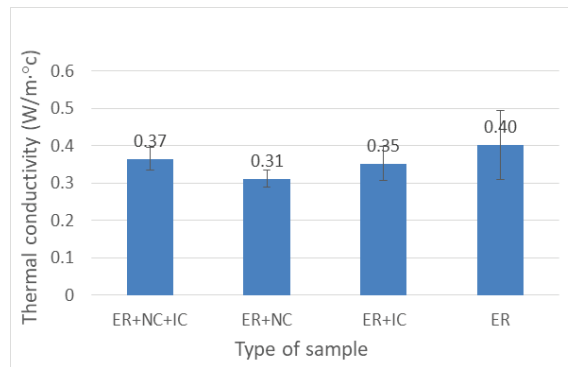
Fig. 4: Relationship between thermal conductivity and the proportions of additives to epoxy.

3.2 Physical Properties: Hardness (Shore D)

Figure 5 shows that the epoxy sample (ER+NC) reinforced with natural cellulose (sawdust) has the best hardness. This is because the natural cellulose particles in the composite are arranged in a uniform pattern. This strengthens the bonds in the polymeric chain. This is because adding natural cellulose to the compound impedes cracks formation during the preparation, which increases the bonding of the atoms, and thus increases the hardness value.
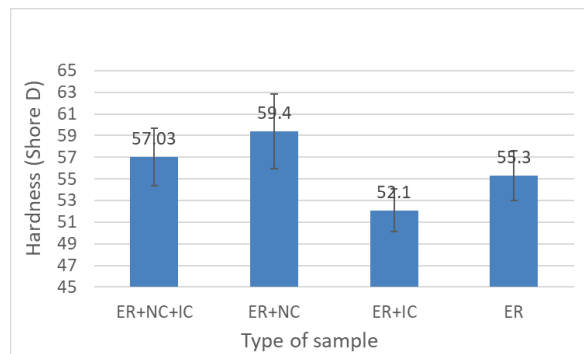
Fig. 5: Relationship between hardness and the proportions of additives to epoxy resin.

These findings suggest that indentation can be avoided through strong bonding. Thus, the improvement rate for this (ER+NC) sample was 6.9% higher than the reference sample. On the other hand, the hardness of the (ER+IC) was reduced by 6.1%. According to Homkhiew et al. [36], the Shore D hardness of composites (rubberwood sawdust reinforced

thermoplastic natural rubber) increases as the amount of wood sawdust increased. They attributed this to the fact that wood sawdust has a far greater hardness than the matrix material (thermoplastic elastomer), and that adding wood particles reduces the elasticity or flexibility of polymer chains, which results in stiffer composites. This is in good agreement with the outcomes of the current study.

3.3 Mechanical Properties: Tensile Strength

The best tensile strength was identified (see Fig. 6) in the polymeric compound sample that was reinforced with natural cellulose (ER+NC) and this is due to the fact that the particles in sawdust join the fibers and strengthen the bonds between atoms. This is because sawdust, when loaded, serves as a barrier to interference movement inside the base material, decreasing the chance of plastic deformation [37]. As a result of this strong adhesive property, an improvement rate of 25% was achieved in comparison to the epoxy resin reference sample. However, the tensile strength of the (ER+IC) sample was found to be nearly 20% worse. According to Kumar et al. [38], wood dust (as filler) has good characteristics because it improves the mechanical properties of the polymeric resin. They stated that 10 wt.% fill provides the best tensile properties.


Fig. 6: Relationship between tensile strength and the proportions of additives to epoxy resin.

3.4 Mechanical Properties: Flexural Strength

The flexural strength of materials was measured in order to determine their capacity to withstand bending forces. The test results for the four samples revealed that the sample (ER+IC) prepared with industrial cellulose was the least resistant (36.4% lower) in comparison to the pure epoxy resin reference sample. However, as Fig. 7 shows, the sample (ER+NC) containing natural cellulose (sawdust) produced essentially identical results to the epoxy resin samples. This means that, even after the additive materials were added, there was no improvement in flexural strength. This can be ascribed to a lack of adhesion at the filler/matrix contact. Furthermore, as the particle-matrix interface is stressed, the number of microcracks increases, causing the crack to widen and fracture to occur. As a result, adding sawdust to the polymer matrix did not result in an improvement in flexural strength. Other researchers have disclosed similar outcomes [35].
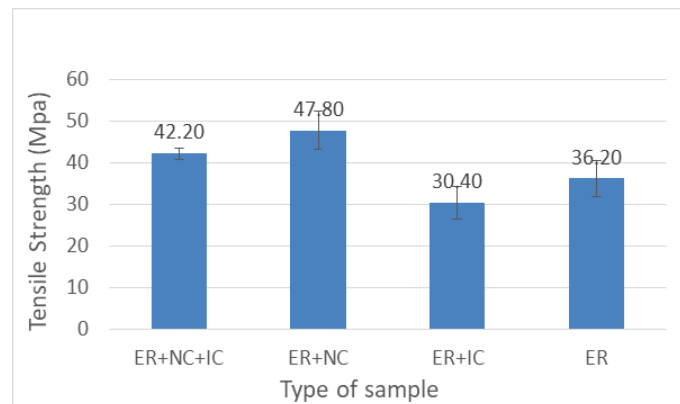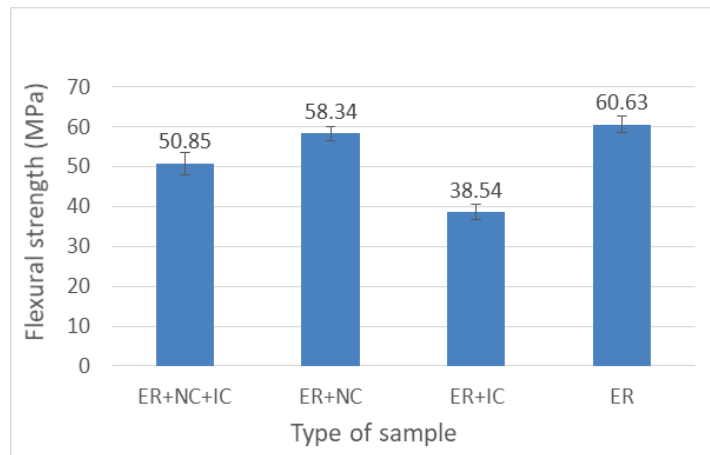
Fig. 7: Relationship between flexural strength and the proportions of additives to epoxy.

3.5 Mechanical Properties: Impact Strength

The findings are presented in Fig. 8. It is evident that the polymeric compound sample (ER+NC) reinforced with natural cellulose (sawdust) demonstrated the best impact strength. This is owing to the robust cohesion that exists between the sawdust and the epoxy. As a consequence, sawdust particles increase the amount of energy needed to break the sample. This energy is defined by the interface bonding's strength between the reinforcing materials' surfaces and the polymeric mix composite material's components [39]. Thus, a 16.6% improvement was achieved in this sample compared to the reference sample. On the other hand, the impact strength of the (ER+IC) sample was found to be reduced by 16.2%, whilst that of the (ER+NC+IC) sample was reduced by 2%.
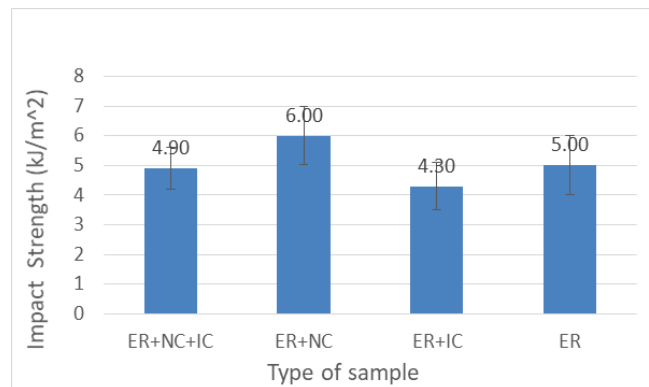
Fig. 8: Relationship between impact strength and the proportions of additives to epoxy.

4. CONCLUSIONS

Based on the experiments carried out in this study, the following conclusions have been made.

1- Physical properties:

- The thermal conductivity tests revealed that the polymeric sample with the best thermal insulation was the (ER+NC) sample containing 95% epoxy and 5% sawdust. This sample was found to be 29% more effective than the pure epoxy reference sample (ER).

- Sawdust was found to be most effective in the hardness tests. This was evident from the polymeric compound (ER+NC) sample which had the best hardness test results with an improvement rate of 69%.

2- Mechanical properties

- The findings of the tensile test also favored the (ER+NC) polymeric sample, as it showed the highest tensile strength with an improvement rate of 25%.

- The (ER+IC) sample was found to have the lowest bending strength in the bending test (which was 36.4% lower than the reference test), whereas the polymeric compound (ER+NC) sample seemed to have a bending resistance similar to that of the pure epoxy resin (ER) sample.

- The findings of the impact test also showed that the sample containing epoxy and sawdust had the highest impact strength and was 16.6% better than the reference sample.

Moreover, the findings of this work indicate that sawdust can be employed as a cost-effective and environmentally friendly reinforcer in polymeric compounds. This could be beneficial to many industries. Moreover, different types of wood and mixing ratios can be employed to achieve optimal mechanical and thermal properties.

ACKNOWLEDGEMENTS

REFERENCES

[1]   Hanon MM, Marczis R, Zsidai L. (2020) Impact of 3D-printing structure on the tribological properties of polymers. Ind Lubr Tribol, 72(6): 811-818.   https://doi.org/10.1108/ILT-05-2019-0189

[2]   Abdellaoui H, Bensalah H, Echaabi J, Bouhfid R, Qaiss A. (2015) Fabrication, characterization and modelling of laminated composites based on woven jute fibres reinforced epoxy resin. Mater Des, 68: 104-113. https://doi.org/10.1016/j.matdes.2014.11.059

[3]   Bello SA, Agunsoye JO, Hassan SB, Kana MGZ, Raheem IA. (2015) Epoxy resin based composites, mechanical and tribological properties: A review. Tribol Ind, 37(4): 500-524.

[4]   Paluvai NR, Mohanty S, Nayak SK. (2014) Synthesis and modifications of epoxy resins and their composites: a review. Polym Plast Technol Eng, 53(16): 1723-1758. https://doi.org/10.1080/03602559.2014.919658

[5]   Verma D, Gope PC, Shandilya A, Gupta A, Maheshwari MK. (2013) Coir fibre reinforcement and application in polymer composites: A review. J Mater Environ Sci, 4(2): 263-276.

[6]   Bismarck A, Baltazar-Y-Jimenez A, Sarikakis K. (2006) Green composites as Panacea? Socio-economic aspects of green materials. Environ Dev Sustain, 8(3): 445-463. https://doi.org/10.1007/s10668-005-8506-5

[7]   Müller K, Bugnicourt E, Latorre M, Jorda M, Sanz YE, Lagaron JM, Miesbauer O, Bianchin A, Hankin S, Bölz U, Pérez G, Jesdinszki M, Lindner M, Scheuerer Z, Castelló S, Schmid M. (2017) Review on the processing and properties of polymer nanocomposites and nanocoatings and their applications in the packaging, automotive and solar energy fields. Nanomaterials, 7(4): 74.   https://doi.org/10.3390/nano7040074

[8]   Akter T. (2006) Manufacturing of biocomposite shell mimetic via the powder compaction method.

[9] Khoee S, Hassani N. (2010) Adhesion strength improvement of epoxy resin reinforced with nanoelastomeric copolymer. Mater Sci Eng A, 527(24-25): 6562-6567. https://doi.org/10.1016/j.msea.2010.07.013

[10] Qi S, Li C, Huang Y. (2006) Preparation of SIC hybrid phenolic resin composites. In: AIAA 57th Int. Astronaut. Congr. IAC 2006. pp 5237-5240

[11] Hanon MM, Alshammas Y, Zsidai L. (2020) Effect of print orientation and bronze existence on tribological and mechanical properties of 3D-printed bronze/PLA composite. Int J Adv Manuf Technol, 108(1-2): 553-570. https://doi.org/10.1007/s00170-020-05391-x

[12] Mahan HM, Mahjoob D, Mahmood KI. (2018) Mechanical properties of alumina nano-particles and glass fiber, Kevlar fiber reinforced composites. J Eng Appl Sci, 13(21): 9096-9100. https://doi.org/10.3923/jeasci.2018.9096.9100

[13] Ismail M, Rejab MRM, Siregar JP, Mohamad Z, Quanjin M, Mohammed AA. (2020) Mechanical properties of hybrid glass fiber/rice husk reinforced polymer composite. Mater Today Proc, 27: 1749-1755. https://doi.org/10.1016/j.matpr.2020.03.660

[14] Ismail M, Rejab MRM, Siregar JP, Muhamad Z, Quanjin M. (2020) Tensile properties of hybrid woven glass fibre/PALF reinforced polymer composite. In: Proc. 4th Int. Manuf. Eng. Conf. 5th Asia Pacific Conf. Manuf. Syst. (iMEC-APCOMS 2019). Springer-Singapore, Putrajaya, Malaysia, pp 448-454

[15] Chen H, Ginzburg VV, Yang J, Yang Y, Liu W, Huang Y, Du L, Chen B. (2016) Thermal conductivity of polymer-based composites: Fundamentals and applications. Prog Polym Sci, 59: 41-85. https://doi.org/10.1016/j.progpolymsci.2016.03.001

[16] Abdul-Hussein AB. (2019) Effect of industrial powder on mechanical properties of glass fiber reinforced epoxy composite. Iraqi J Phys, 12(25): 8-24. https://doi.org/10.30723/ijp.v12i25.300

[17] Kumar SS. (2020) Effect of natural fiber loading on mechanical properties and thermal characteristics of hybrid polyester composites for industrial and construction fields. Fibers Polym, 21(7): 1508-1514. https://doi.org/10.1007/s12221-020-9853-4

[18] Girijappa YGT, Rangappa SM, Parameswaranpillai J, Siengchin S. (2019) Natural fibers as sustainable and renewable resource for development of eco-friendly composites: A comprehensive review. Front Mater, 6: 226. https://doi.org/10.3389/fmats.2019.00226

[19] Xiao M, Feng B, Gong K. (2002) Preparation and performance of shape stabilized phase change thermal storage materials with high thermal conductivity. Energy Convers Manag, 43(1): 103-108. https://doi.org/10.1016/S0196-8904(01)00010-3

[20] Chandramohan D, Marimuthu. (2011) A review on natural fibers. Int J Res Rev Appl Sci, 8(2): 194-206.

[21] Chand N, Fahim M. (2008) Tribology of natural fiber polymer composites. Cambridge, England, Woodhead Publishing Ltd, Elsevier. https://doi: 10.1533/9781845695057

[22] Hameed IS, Mahan HM, Hameed AS. (2020) Microwave power absorption evaluation of river shell particles reinforced polyester composite. Period Polytech Electr Eng Comput Sci, 64(2): 192-199. https://doi.org/10.3311/PPEE.14263

[23] Mohan N, Senthil P, Vinodh S, Jayanth N. (2017) A review on composite materials and process parameters optimisation for the fused deposition modelling process. Virtual Phys Prototyp, 12(1): 47-59. https://doi.org/10.1080/17452759.2016.1274490

[24] Swain PTR. (2013) Physical and mechanical behavior of Al_2O_3 filled jute fiber reinforced epoxy composites. Int J Curr Eng Technol, 2(2): 67-71. https://doi.org/10.14741/ijcet/spl.2.2014.13

[25] Deng S, Zhang J, Ye L, Wu J. (2008) Toughening epoxies with halloysite nanotubes. Polymer (Guildf), 49(23): 5119-5127. https://doi.org/10.1016/j.polymer.2008.09.027

[26] Waliszewska B, Mleczek M, Zborowska M, Goliński P, Rutkowski P, Szentner K. (2019) Changes in the chemical composition and the structure of cellulose and lignin in elm wood exposed to various forms of arsenic. Cellulose, 26(10): 6303-6315. https://doi.org/10.1007/s10570-019-02511-z

[27] Tanaka T, Montanari GC, Mülhaupt R. (2004) Polymer nanocomposites as dielectrics and electrical insulation- perspectives for processing technologies, material characterization and future applications. IEEE Trans Dielectr Electr Insul, 11(5): 763-784.

https://doi.org/10.1109/TDEI.2004.1349782

[28] Shaari N, Jumahat A, Yahya KH, Sulaiman MF. (2014) Impact resistance of woven fiber reinforced polymer composites. Adv Environ Biol, 8(3): 2662-2668.

[29] Cicala G, Cristaldi G, Recca G, Latteri A. (2010) Composites based on natural fibre fabrics. Woven Fabr Eng, 17:317–342. https://doi.org/10.5772/10465

[30] Peças P, Carvalho H, Salman H, Leite M. (2018) Natural fibre composites and their applications: A review. J Compos Sci, 2(4): 66. https://doi.org/10.3390/jcs2040066

[31] Surin VG, Mogilevskii BM, Chudnovskii AF. (1972) Effect of additives on the thermal conductivity of cyclohexane. J Eng Phys, 23(1): 904-905. https://doi.org/10.1007/BF00826269

[32] Abenojar J, Tutor J, Ballesteros Y, del Real JC, Martínez MA. (2017) Erosion-wear, mechanical and thermal properties of silica filled epoxy nanocomposites. Compos Part B Eng, 120: 42-53. https://doi.org/10.1016/j.compositesb.2017.03.047

[33] Yin J, Li G, He W, Huang J, Xu M. (2011) Hydrothermal decomposition of brominated epoxy resin in waste printed circuit boards. J Anal Appl Pyrolysis, 92(1): 131-136. https://doi.org/10.1016/j.jaap.2011.05.005

[34] Mahan HM, Farhan MM, Shaalan TG. (2019) Studying some mechanical properties of river shell particle polymer matrix composite. J Southwest Jiaotong Univ. doi: 10.35741/issn.0258-2724.54.4.17

[35] Al-Shabander BM. (2013) Investigation of flexural properties and thermal conductivity for wood dust filled epoxy. J Al-Nahrain Univ Sci, 16(3): 104-109. https://doi.org/10.22401/JNUS.16.3.14

[36] Homkhiew C, Rawangwong S, Boonchouytan W, Thongruang W, Ratanawilai T. (2018) Composites from thermoplastic natural rubber reinforced rubberwood sawdust: Effects of sawdust size and content on thermal, physical, and mechanical properties. Int J Polym Sci, 2018: 1-11. https://doi.org/10.1155/2018/7179527

[37] Hosseinizand H, Sokhansanj S, Lim CJ. (2018) Co-pelletization of microalgae chlorella vulgaris and pine sawdust to produce solid fuels. Fuel Process Technol, 177: 129-139. https://doi.org/10.1016/j.fuproc.2018.04.015

[38] Kumar R, Kumar K, Sahoo P, Bhowmik S. (2014) Study of mechanical properties of wood dust reinforced epoxy composite. Procedia Mater Sci, 6: 551-556. https://doi.org/10.1016/j.mspro.2014.07.070

[39] Dinesh S, Kumaran P, Mohanamurugan S, Vijay R, Singaravelu DL, Vinod A, Sanjay MR, Siengchin S, Bhat KS. (2020) Influence of wood dust fillers on the mechanical, thermal, water absorption and biodegradation characteristics of jute fiber epoxy composites. J Polym Res, 27(1): 9. https://doi.org/10.1007/s10965-019-1975-2

Purwanto et al.

CHARACTERISTICS OF LEACHATE UPON HYDROTHERMAL TREATMENT PROCESSING: CASE STUDY OF AMPANG DISTRICT MUNICIPAL SOLID WASTE LEACHATE

HADI PURWANTO[1*], SITI SALWA KHAMIS[1], HAMZAH MOHD SALLEH[2], ALYA NAILI ROZHAN[1], MOHAMED ABD RAHMAN[1] AND RASHIDI OTHMAN[3]

[1]Department of Manufacturing and Materials Engineering, Faculty of Engineering,
[2]International Institute for Halal Research and Training,
[3]Herbarium Unit, Department of Landscape Architecture,
Faculty of Architecture and Environmental Design,
International Islamic University Malaysia,
Jalan Gombak, 53100 Kuala Lumpur, Malaysia.

[*]Corresponding author: hadi@iium.edu.my

ABSTRACT: Municipal solid waste (MSW) leachate is a hazardous liquid produced from decomposition of solid waste with high amount of organic matter and ammonia-nitrogen with obnoxious smell. This study aimed to investigate the behavior of MSW leachate when subjected to hydrothermal treatment using an autoclave set up at below water critical points (temperatures of 100 °C, 150 °C, and 200 °C at 0.1 MPa, 0.4 MPa and 1.6 MPa, respectively) with 15 min and 60 min holding time. Physicochemical characterization of the setup at 200 °C and 1.6 MPa at 60 min holding time indicates a feasible parameter when materials that caused the dark color and obnoxious smell were almost completely removed. Over 99% of chemical oxygen demand and ammonia nitrogen was eliminated when treated with hydrothermal treatment and yielded a condensed liquid product that complied with permissible limits set by the National Water Quality Standard Malaysia and the World Health Organization for wastewater discharges for irrigation purposes. Chromatographic analysis indicated that most of the organic compounds present in the raw leachate was removed. This processing is believed to be an environmentally friendly method that can treat MSW leachate rapidly, and it has the potential to be used as an effective alternative to existing leachate treatment technologies.

ABSTRAK Larut lesap daripada sisa pepejal perbandaran merupakan cecair merbahaya yang berlaku semasa penguraian sisa pepejal dengan jumlah bahan organik dan ammonia-nitrogen yang tinggi dengan bau menjengkelkan. Kajian ini bertujuan bagi mengkaji sifat larut lesap ini apabila melalui rawatan hidroterma menggunakan autoklaf yang ditetapkan di bawah titik kritikal air (suhu 100 °C, 150 °C, dan 200 °C pada 0.1 MPa, 0.4 MPa dan 1.6 MPa masing-masing) dengan tempoh masa 15 minit dan 60 minit. Sifat fizikal kimia yang dirawat pada suhu 200 °C, 1.6 MPa selama 60 minit menunjukkan satu parameter yang boleh dilaksanakan apabila warna gelap dan bau yang menjengkelkan hampir dikurangkan sepenuhnya. Lebih 99% ammonia nitrogen disingkirkan apabila dirawat dengan rawatan hidrotherma dan menghasilkan air bersih yang mematuhi had yang dibenarkan oleh Piawaian Kualiti Air Kebangsaan Malaysia (NWQSM) dan Pertubuhan Kesihatan Sedunia (WHO) bagi pelupusan air sisa pepejal bagi tujuan pengairan. Analisis kromatografi menunjukkan bahawa sebahagian besar sebatian organik yang terdapat dalam larut resap telah disingkirkan. Pemprosesan ini diyakini merupakan kaedah mesra

Purwanto et al.

alam yang dapat merawat dengan cepat, dan berpotensi digunakan sebagai alternatif efektif untuk teknologi rawatan larut lesap sedia ada.

KEYWORDS: *municipal solid waste; leachate; hydrothermal; organic compound*

1. INTRODUCTION

The recent economic, demographic, and technological development of society have led to an increase in the production of municipal solid waste (MSW), which consequently causes a waste disposal problem. Landfills are the most widely used method to dispose MSW since it is simple, feasible and cost effective; it minimizes carbon dioxide (CO_2) and controls methane (CH_4) and leachate emissions [1] especially in sanitary landfills. However, the conventional landfilling method has a lot of negative impacts on the environment. Open MSW dumpsites nowadays have become looming hotspots for water, air, and land pollution [2]. As waste generation increased, more waste would be dumped into landfill that would simultaneously lead to an increase in landfill leachate generation. Unfortunately, waste is still being wantonly discarded in open dumps all over the world, while the substantial resources spent in remediation suggest that landfill leachate is a significant source of groundwater pollution [3]. In Malaysia, Act 672, gazetted in 2007, is the law that deals with solid waste and public cleansing management. The plans and strategies formulated in line with Act 672 were projected to bring about huge transformation in MSW management in the country. However, the authorities face a huge challenge in the implementation of the National Policy regarding MSW management [4]. The strategies to reduce waste to be sent to landfill do not seem to produce the expected results. Landfill is still the main MSW disposal approach [5] and solid waste sent to landfill is increasing every year [6].

Landfill leachate generally contains organic matter (biodegradable, but also refractory to be biodegraded), ammonia-nitrogen (NH_3-N), heavy metals, and chlorinated organic compounds and inorganic salts [7]. The main concern about those compounds in environmental matrices is that they are hazardous and of difficult decomposition by soil and aquatic microorganisms [8]. Inhabitants who live near the dumps are particularly at risk of consuming contaminated water. Domestic water use for drinking, bathing, or washing in nearby areas may lead to exposure to volatile organic compounds (VOCs) [9], mercury [10], polychlorinated biphenyl (PCBs) [11], or polyaromatic hydrocarbon (PAHs) [12]. A laboratory analysis by Griffith et al. [13] identified 593 sites in the US where contaminated groundwater was used for drinking purposes. In the state of New Jersey for example, leachate from the site of Lipari Landfill has migrated into nearby streams and lakes adjacent to a residential area and contaminated most of the water pathways causing an increase in the proportion of low-birth-weight babies (2.5 kg) and lowering the birth weight for the population living closest (within 1 km radius) to the landfill. Studies on leachate demonstrate that it contains compounds such as PAHs, alkenes, ketones, esters, alcohols [14], phthalates, phenols and nitrogen compounds [15], carboxylic acids, amines, amides, aldehydes and carbohydrates [16]. These pollutants have accumulative, threatening, and detrimental effects on the survival of aquatic life forms, ecology, and food chains leading to enormous problems in public health including carcinogenic effects, acute toxicity, and genotoxicity [12,17-19].

Solid waste landfills are often reported to have serious and recurring leachate contamination issues, and the pollution is caused by the design of the landfill and existing leachate treatment system that are not able to fully accommodate the increasing volume of solid waste received [20]. Biological processing is usually carried out to remove the contaminants, especially the organic contents and total Kjeldahl nitrogen (TKN) in the form

of ammonium – from leachate, to meet the compliance limits before being discharged into the environment [21]. Conventional biological treatment process usually consists of two stages: denitrification and nitrification. However, the conventional pathway involves higher operational cost due to the requirement of high amounts of oxygen during the nitrification when pure oxygen is used to supplement the air system and carbon during the denitrification process [22]. The most common approach to leachate treatment involves biological and physical or chemical leachate treatment in combinations. Leachate contains recalcitrant to biological process substance that cannot be treated using either one of the processes alone. All the contaminants make the treatment of leachate complex and expensive [23].

Advanced oxidation process (AOP) has gained importance over the past few years due to its potential to biologically destruct resistant organic molecules and micro pollutants, enhancing the quality of discharge waters from secondary treatment units [24]. Of all the AOPs, the hydrothermal oxidation process (sub- and super-critical) has received particular attention for its complete conversion without producing any harmful intermediates [25]. AOP is also referred to as hydrothermal treatment process. Hydrothermal treatment below the critical points of water has been widely employed for the solubilization, extraction, and liquefaction of target materials [26]. Subcritical water has hydrolytic and pyrolytic reaction characteristics, which result from a decrease in the dielectric constant and increase in the ion product of water at temperatures and pressures below and near 374 °C and 22.1 MPa [27- 28] . Most researchers have focused on solubilization and extraction to recover valuable organic compounds such as glucose and organic acids [27,29-31]. Some researchers have dealt with hydrothermal treatment as pretreatment prior to fermentation, gasification, composting, and other processes [26,32-35]. Many have focused on treatment using supercritical water, which is the process that occurs in water above its critical points [36-41]. Only a few researchers focus on treating MSW leachate by employing hydrothermal treatment below the critical points water. Kirmizakis et al. [42] employs hydrothermal treatment below the critical points water to treat landfill leachate at temperatures in the range of 100 ºC to 374 ºC but requires chemicals as a catalyst for the treatment. In this work, hydrothermal treatment below critical points condition was performed to treat MSW leachate samples from the area of Ampang district, Selangor, Malaysia. Physicochemical characteristics of the leachate samples such as color, odor, pH, chemical oxygen demand (COD), ammonia-nitrogen (NH_3-N) and the organic compound composition of the leachate were mainly investigated. The experimental results were then compared with the standard discharge limit by the National Water Quality Standard Malaysia (NWQSM) and the World Health Organization (WHO) at the permissible limits for contaminants present in wastewater discharges for irrigation purposes.

2. MATERIALS AND METHOD

2.1 Material

Fresh MSW leachate was collected from several garbage trucks for municipalities in the area of Ampang district, Selangor owned by *KDEB* Waste Management Sdn Bhd (KDEBWM) for the sampling. Each garbage truck had a temporary leachate storage tank below it, which allowed excess liquids in the MSW to infiltrate and accumulate in the tank. MSW leachate sample went directly from the tank into container. Collected MSW leachate was filtered using a 1.5 mm mesh to remove solid particles and was stored at 4 ºC.

2.2 Hydrothermal Treatment Processing Setup

Fig. **1** shows the laboratory-scale experimental apparatus for the hydrothermal treatment. The reactor was loaded up to ¾ volume of the reactor. Raw MSW leachate (50 mL) and 130 mL distilled water were put in a batch type autoclave reactor and sealed. Saturated steam and pressure were set at 100-200 ºC and 0.1-1.6 MPa depending on working temperature. The reactor was held for 15 min or 60 min after reaching all the setup conditions. The reactor was quenched with cooling water at room temperature in the condenser to terminate further reactions from occurring after the intended holding time. The clean liquid was collected as the product of the hydrothermal treatment and the inorganic particles that had settled at the bottom of the reactor were discharged.
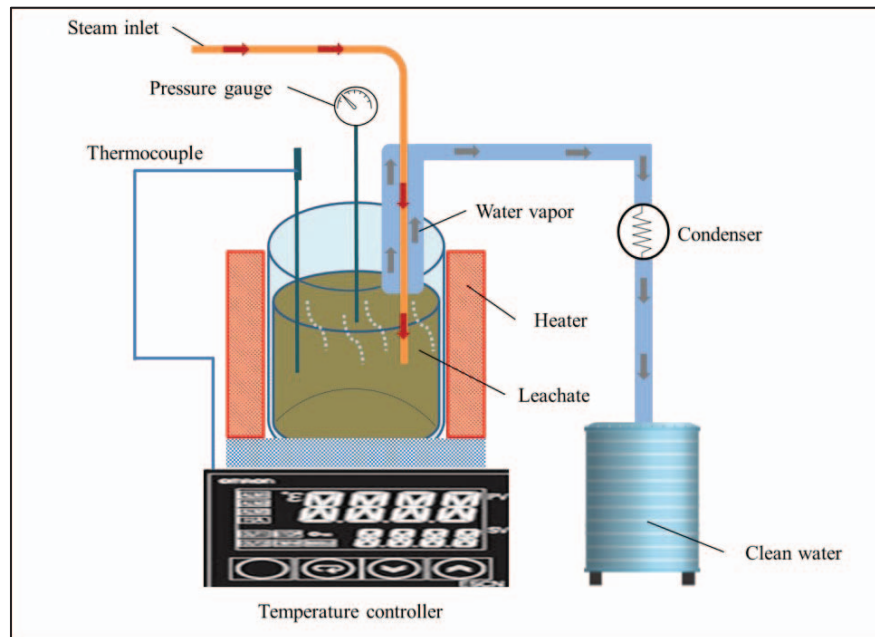
Fig. 1: Laboratory-scale experimental apparatus for the hydrothermal treatment.

2.3 Physicochemical Analysis

The parameters for characterization were chosen according to the leachate pollution index (LPI) that provides an overall pollution potential of a landfill site in identifying whether the MSW leachates are hazardous or not. Physicochemical parameters were analyzed for color, odor, pH, chemical oxygen demand (COD), and ammonia-nitrogen (NH_3-N) composition. Color and odor were observed according to the physical appearance of the sample and indicated using sensorial technique by smelling the samples respectively. pH was analyzed using a pH meter, COD was determined by the colorimetric method, and NH_3-N was measured by the salicylate method (385 HACH DR/3900 Spectrophotometer) using the APHA standard methods [43]. The removal percentage of COD and NH_3-N was computed based on following equation:

$$Percentage\ of\ removal\ (\%) = ((Xi - Xf)/Xi) * 100\%$$

where percentage removal represents percentage of COD and NH_3-N removed from raw MSW leachate, Xi refers to average initial raw reading of COD and NH_3-N before treatment, and Xf is the average final reading of COD and NH_3-N after treatment.

2.3.1 pH Sampling

The pH values were measured immediately after the samples were taken from the garbage truck. Three representative samples from each garbage truck were put into glass closed containers. The fresh sample was stirred, and pH meter electrode was placed in the leachate sample and measurement recorded when the readings stabilized. The electrode was rinsed several times with distilled water and blotted dry before placing into the sample. The same steps were followed for pH measurements of treated leachate.

2.3.2 Chemical Oxygen Demand (COD)

A high range COD digestion reagent vial was used for the sample concentration up to 15000 mg/L range like MSW leachate. The leachate sample was made homogenous by gently swirling and inverting the container several times for 30 sec, before 0.2 mL leachate was pipetted into the COD digestion reagent vial. The vial was capped tightly, rinsed with deionized water, and wiped clean with paper towel. The vial was inverted gently several times to make sure the content was mixed and was placed into the 150 °C preheated DRB 200 reactor for two hours. A blank sample was prepared with 0.2 mL deionized water instead of the leachate. After 20 minutes, the DRB 200 reactor was turned off. Both sample and blank vials were gently inverted before allowing them to cool down to room temperature. Measurements were made with a spectrophotometer set at 620 nm wavelength.

2.3.3 Ammonia Nitrogen (NH$_3$-N)

The blank sample was prepared by filling the sample cell with 10 mL deionized water, followed by the leachate sample preparation by filling the cell with 10 mL leachate sample. Both were filled with ammonia salicylate reagent powder pillow (Hach Malaysia Sdn Bhd), and the cells were inverted to dissolve the reagent well. After three minutes of reaction time, both cells were filled with ammonia cyanurate powder pillow. The cap was closed, and cells were shaken to mix well. After 15 min, the green color formed in the presence of NH$_3$-N was measured at 655 nm.

2.4 Organic Compound Composition

The organic compound composition was determined based on the standard APHA method [43]. Samples were prepared according to Turki et al. [44] with slight modifications. Sample (0.01 g) was brought to 1 mL volume with ethanol and filtered (0.2 μm nylon membrane) prior to gas chromatography – mass spectrometry (GC-MS) analysis using a HP-5MS fused silica capillary column (30 m × 250 μm i.d. and 0.5 μm film thickness; Agilent Technologies). The GC oven temperature was programmed as follows: 80 °C held for 2 min and raised at 10 °C/min to 250 °C (held for 10 min). Helium was the gas carrier, and the flow rate was set at 1.07 mL/min. The sample injection (1.0 μL) was set on a splitless mode at 250 °C with solvent delay of 4 min. Detection was conducted by a mass selective detector with electron impact ionization at 70 eV, in selected ion monitoring mode. MS transfer line temperature was at 250 °C, and the MS was operated in full scan in electron ionization mode with an electron multiplier voltage of 1588 V. The mass scanning was set to be of a range of m/z 40 to 500. The semi-quantification and the removal of persistent compounds in each stage of the process were performed by comparing the corrected areas of specific peaks to the peak area.

3. RESULTS AND DISCUSSION

3.1 Physicochemical Characteristics

MSW raw leachate was a dark-cloudy colored liquid (brown and black), very acidic, offensive, and sometimes had a very pervasive smell. The pH of the samples collected from several garbage trucks owned by KDEBWM during the transportation of the MSW to the landfill were between 3.00–3.54 (average of 3.27). The COD ranges between 47000–55000 mg/L in raw leachate samples (average of 51000 mg/mL) and the NH_3-N varied between 2950–4042 mg/L in the raw leachate samples (average of 3496 mg/L). The pH of the samples when subjected to hydrothermal treatment as a function of temperature is shown in Fig. 2. The pH of hydrothermal treatment from 15 min to 60 min holding time was maintained within acceptable range limit.
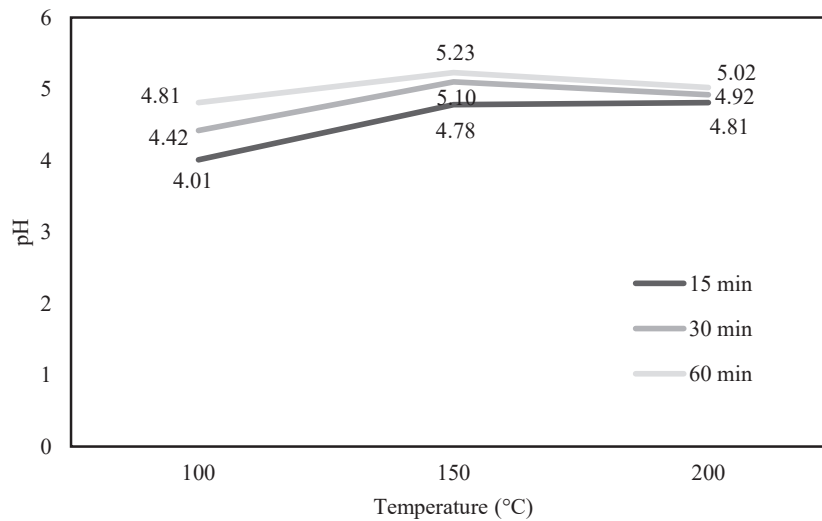
Fig. 2: Effect of temperature on pH change after hydrothermal.

Table 1: The physicochemical characteristics of MSW leachate from Ampang district, Selangor

No.	Parameter	Raw leachate	Hydrothermal treated			NWQSM standard*	NWQM standard*
			100 °C, 0.1 MPa, 15 min	150 °C, 0.4 MPa, 30 min	200 °C, 1.6 MPa, 60 min		
1	Color	Dark brown, cloudy	Very light yellow, clear	Light yellow, clear	Almost transparent, clear	-	-
2	Odor	Obnoxious	Less obnoxious	Less obnoxious	No odor	-	-
3	pH	3.00-3.54	4.00-4.03	5.00-5.20	5.00-5.05	5.0-8.0	6.5-8.5
4	COD (mg/L)	47000-55000	7800-8800	230-248	48-52	100	250
5	NH_3N (mg/L)	2950-4042	2301-2809	12.8-15.9	0.20-0.21	2.7	-

*Discharge standard at Class IV for irrigation.

The result shows that with the increasing pH value, COD and NH_3-N showed decline, and organic compounds in the treated leachate became significantly simpler than raw MSW

leachate, as can be seen in Table 1. Raw leachate is a potentially hazardous material to lifeforms because biochemically it exhibited low pH, high COD, and high NH_3-N. Among the three set up parameters, temperature of 100-200 ºC, pressure of 0.1-1.6 MPa and holding time of 15 min or 60 min, the conditions of 100 °C, 1.6 MPa and 15 min holding time yielded condensed treated leachate that is characterized by very light yellow and clear liquids with some obnoxious smell. Only 30% of NH_3-N and 84% of COD was eliminated when treated with hydrothermal treatment that required further treatment to reach permissible limits. The conditions of 200 °C, 1.6 MPa with 60 min holding time provided the highest hydrothermal treatment performance on the raw MSW. Under these conditions, the final condensed liquid, which is clear and without any obnoxious smell (Table 1), complies with the National Water Quality Standard Malaysia (NWQSM) and the World Health Organization (WHO) standards at the permissible limits for contaminants presents in wastewater discharges for irrigation purposes. Percentage removal of COD and NH_3-N under minimum and maximum condition of hydrothermal treatment is shown in Table 2, calculated based on equation in section 2.3. Treatment at 100° C, 0.1 MPa with 15 min holding time causes 84% of COD and only 30% of NH_3-N to be degraded and removed. Treatment at higher temperature and longer holding time of 200 °C, 1.6 MPa with 60 min results in removal of over 99% of COD and NH_3-N. The results indicate that the hydrothermal treatment has significant impact on the reducing of organic substances in the leachate to meet the standard content in the wastewater discharging for irrigation purposes.

Table 2: Percentage removal of COD and NH_3-N

No.	Parameter	Percentage removal	
		100 °C, 0.1 MPa, 15 min	200 °C, 1.6 MPa, 60 min
1	COD (mg/L)	84%	99%
2	NH_3-N (mg/L)	30%	99%

3.2 Organic Compound Composition

A large number of organic compounds were identified in GC-MS based on a query mass spectrum with reference mass spectrum in the library of PAHs and PCBs. There were no detectable PCBs in MSW raw and treated leachate samples. Table 3 shows the list of PAHs found in the tested raw MSW samples. PAHs distribution data for the raw MSW leachate showed major contribution of low molecular weight PAHs (2-3 rings) molecular structures such as 2-fluorobiphenyl, 4-terphenyl-d4, naphthalene-d8, phenanthrene-d10, etc. Besides, there was also minor presence of higher molecular weight PAHs (4-6 rings) structures such as chrysene-d10, perylene-d12, chrysene, 3-methylchloanthrene, benzo(*b*)fluoranthene, benzo(*k*)fluoranthene, and benzo(*a*)pyrene. Compounds that have more rings are much more stable and may hardly experience losses due to weathering processes such as solubilization, evaporation/ volatilization and natural biodegradation.

The presence of benzo(*a*)pyrene consisting of five fused benzene rings for example, even at the smallest composition, in the distribution data of the leachate is enough to be of concern and requires effective efforts to eliminate it. Immediate steps should be taken to limits its spread to the environment. This is because this compound is highly hazardous and is listed as a Group 1 carcinogen by the International Agency for Research on Cancer, IARC [45]. Benzo(*a*)pyrene is hazardous to human health because it will attack the nervous system, immune system, and reproductive system, react and bind to DNA, and result in mutations and eventually cancer in the body [46-48].

The compounds of concern in MSW leachate are those that are potentially hazardous, belonging to xenobiotic organic compounds including PAHs and halogenated organics like the PCBs. PAH organic pollutants are the most long-lived families of toxic chemicals. PAHs are strongly hydrophobic and lipophilic as well as have the propensity to accumulate in the tissue of any living thing [49] that can undergo long range transport and move into otherwise pristine environments. PCBs are toxic persistent organic pollutants that are harmful to humans and the environment due to their lipophilic characteristic and not easily degraded in the environment. Both PAHs and PCBs are therefore the focus of the MSW leachate analysis. The elimination of PAHs and PCBs in treated leachate is important to avoid undesirable adverse effects on human health.

Table 3: List of PAHs found in raw MSW leachate

No	RT (min)	Compound	% PAHs detected	% PCBs detected
1	7.16	2-Fluorobiphenyl	12.66867	nd
2	10.89	4-Terphenyl-d4	11.98621	nd
3	6.09	Naphthalene-d8	8.62133	nd
4	9.31	Phenanthrene-d10	7.87956	nd
5	8.66	Chrysene-d10	7.49305	nd
6	4.5	Phenol-d5	7.41990	nd
7	6.34	Phenanthrene-d10	6.91754	nd
8	11.94	Chrysene-d12	6.78624	nd
9	5.39	Nitrobenzene-d4	6.53955	nd
10	3.6	2-Fluorophenol	6.37875	nd
11	7.83	Acenaphthene-d10	4.64253	nd
12	4.85	1,2-Dichlorobenzene-d4	3.66190	nd
13	13.28	Perylene-d12	3.65857	nd
14	8.61	2,4,6-Tribromophenol	2.47231	nd
15	4.85	1,4-Dichlorobenzene-d4	2.47227	nd
16	9.89	Benzyl butyl phthalate	0.33581	nd
17	5.24	3&4-Methylphenol	0.03793	nd
18	8.84	Di-n-butyl phthalate	0.00669	nd
19	11.97	Bis(2-ethylhexyl) phthalate	0.00368	nd
20	11.97	Di-n-octyl phthalate	0.00368	nd
21	12.52	7,12-Dimethyl benz(a)anthracene	0.00340	nd
22	7.86	Diethyl phthalate	0.00201	nd
23	11.97	Chrysene	0.00181	nd
24	7.69	Acenaphthylene	0.00175	nd
25	12.4	3-Methylchloanthrene	0.00114	nd
26	6.08	4-Chlorophenol	0.00073	nd
27	6.11	Naphthalene	0.00064	nd
28	11.92	Benz(a)anthracene	0.00059	nd
29	12.93	Benzo(b)fluoranthene	0.00057	nd
30	4.65	2-Chlorophenol	0.00054	nd
31	12.96	Benzo(k) fluoranthene	0.00041	nd
32	13.22	Benzo(a)pyrene	0.00023	nd

RT (retention time); nd (not detected)

The chromatograms of raw MSW leachate and two hydrothermally treated leachates at 200 °C are shown in Fig. 2. The behavior of the chemical changes on the organic loads in the leachate during hydrothermal treatment can be seen clearly in the changes of chromatogram peaks. Most compounds, especially PAHs, existed in raw leachate, went missing when held at 200 °C, 1.6 MPa with 15 min of holding time. But some new compounds that are hazardous to environment like benzene, nitroso-, 2-pyrrolidinone, sec-butyl nitrite, and cetene appeared. This means exposing raw leachate with hydrothermal treatment at 15 min of holding time has removed PAHs and the reaction may cause the derivatives of new compounds from PAHs of smaller molecular weight and change their molecular structure. For example, benzene, nitroso- is a single-ring benzene structure that

derives from the existence of benzene. Improper setup parameters in hydrothermal process may result in some hazardous compounds appearing. However, in this case, the compounds that appeared were selectively less reactive and not stable due to their lower molecular weight.
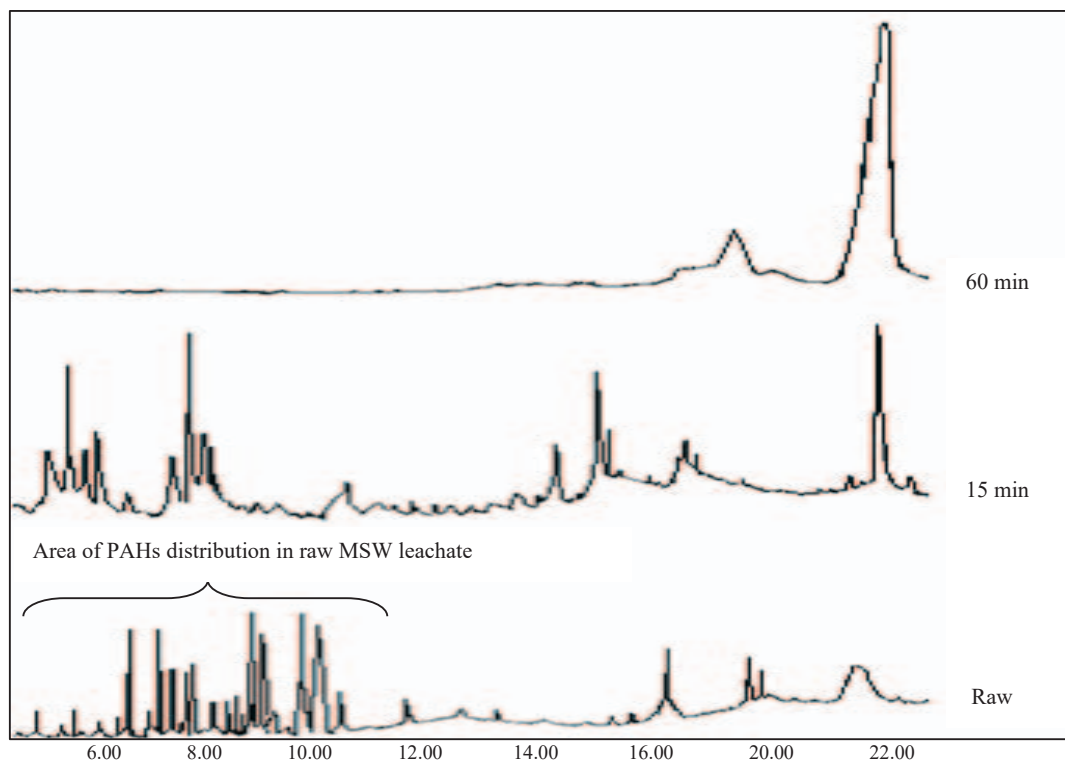

Fig. 2: The chromatograms of raw MSW leachate (bottom) and hydrothermally-treated leachate at 200 °C held for 15 min (middle) and 60 min (top), respectively.

As the treatment holding time increased, the intensity and/or peak abundance became smaller. As indicated earlier, the conditions of 200 °C, 1.6 MPa with 60 min holding time showed the highest performance for the hydrothermal treatment of raw MSW leachate. Under these conditions, there was no detectable presence of PAHs but there were new compounds with significant peak intensity corresponding to alpha-amyrin, lupeol, and eicosane. All these compounds come from the lipid family and do not have any record of being hazardous compounds by the Globally Harmonized System of Classification and Labelling of Chemicals (GHS) report. Lipids formed from the process are believed to be the natural oils that come out from the hydrothermal processing of MSW leachate in a hot and pressurized environment. Hydrothermal liquefaction of organic content in the leachate may happen along the treatment in the thermochemical conversion of the organics into liquid fuels. Temperature and pressure that is set in a closed reactor causes a thermal depolymerization process converting the wet organics, and other macromolecules, into a crude-like oil result.

The hydrothermal conversion of leachate into clean water involves the process of vaporization, condensation, and collection of condensate product (clean water). Leachate is a mixture of liquids containing organic and inorganic components. The hot and pressurized conditions vaporize the leachate and cause compounds in the mixture to break-up into smaller fragments, some of which are dissolved in water. The organic matter that makes

leachate hazardous are converted into simpler dissolved compounds during the process and the gaseous species was collected as clean water following condensation. Inorganic components were collected as residues of the process.

4. CONCLUSION

Characteristics and behavior of raw municipal solid waste leachate sampled from the Ampang district, Selangor, Malaysia were experimentally investigated under hydrothermal treatment at various temperatures. The fresh raw leachate was dark brown and black color cloudy liquid that was potentially hazardous with average pH, COD and NH_3-N of 3.27, 51000 mg/L, and 3496 mg/L. The decrease in the area of intensity in the GC-MS chromatograms reflects the removal of compounds from the raw leachate and their greatly reduced quantity after the hydrothermal treatment. Treatment at 15 min holding time is insufficient to cause the compounds in the leachate to be degraded and removed which is inferred from peak areas comparison in the chromatograms for treated and raw leachate. Treatment at longer holding time of 60 min and higher temperature appear to cause more compounds to be removed. Most compounds were removed from the leachate sample that was hydrothermally treated at 200 °C, 1.6 MPa and 60 min, thus giving favorable parameters: 99% of COD and NH_3-N were removed over raw leachate and complied with the National Water Quality Standard Malaysia and the World Health Organization standards for permissible limits for contaminants present in wastewater discharges for irrigation use. The results indicated that proper parameter setup on hydrothermal treatment cause an effective conversion of poisonous aromatic and complex organic compounds in the leachate into clean water so that burden to the environment can be reduced. It would provide a potential solution to leachate problems and reduce water pollution if the proposed process was implemented to process leachate on an industrial scale.

ACKNOWLEDGEMENT

REFERENCES

[1] Ramírez-Sosa DR, Castillo-Borges ER, Méndez-Novelo RI, Sauri-Riancho MR, Barceló-Quintal M, Marrufo-Gómez JM. (2013) Determination of organic compounds in landfill leachates treated by Fenton–Adsorption. Waste Management, 33(2): 390-395. https://doi.org/10.1016/j.wasman.2012.07.019

[2] Peter AE, Nagendra SS, Nambi IM. (2019) Environmental burden by an open dumpsite in urban India. Waste management, 85, 151-163. https://doi.org/10.1016/j.wasman.2018.12.022

[3] Christensen TH, Kjeldsen P, Bjerg PL, Jensen DL, Christensen JB, Baun A. (2001) Albrechtsen H.-J. r.; Heron G. Biogeochemistry of landfill leachate plumes. Appl. Geochem, 16, 659-718. https://doi.org/10.1016/S0883-2927(00)00082-2

[4] Manaf LA, Samah MAA, Zukki NIM. (2009) Municipal solid waste management in Malaysia: Practices and challenges. Waste Manag 29: 2902-2906. https://doi.org/10.1016/j.wasman.2008.07.015

[5] Abas MA, Wee ST. (2014) The Issues of Policy Implementation on Solid Waste Management in Malaysia. Int J Conceptions Manag Soc Sci 2(3): 12-17.

[6] Mahidin DSDMU. (2020) Department of Statistics Malaysia Press Release: Compendium of Environment Statistics, Malaysia 2020. Dep Stat Malaysia 2015(2)

[7] Li W, Zhou Q, Hua T. (2010) Removal of organic matter from landfill leachate by advanced oxidation processes: A review. International Journal of Chemical Engineering.

https://doi.org/10.1155/2010/270532

[8]   Nascimento Filho ID, von Mühlen C, Caramão EB. (2001) China DDP Despachante de Frete Marítimo taxas transporte da para Saba/em todo o mundo. Química Nova, 24(4): 554-556. https://doi.org/10.1590/S0100-40422001000400017

[9]   Hamar GB, Mcgeehin MA, Phifer BL, Ashley DL. (1996) Volatile organic compound testing of a population living near a hazardous waste site. Journal of Expo Anal Environ Epidemiol 6(2): 247-255.

[10] Reif JS, Tsongas TA, Anger WK, Mitchell J, Metzger L, Keefe TJ, Tessari JD, Amler R. (1993) Two-stage evaluation of exposure to mercury and biomarkers of neurotoxicity at a hazardous waste site. Journal of Toxicol Environmental Health, 40(2-3): 413-422. https://doi.org/10.1080/15287399309531808

[11] Stehr-Green PA, Burse VW, Welty E. (1988) Human exposure to polychlorinated biphenyls at toxic waste sites: Investigations in the United States. Arch Environ Health 43(6): 420-424. https://doi.org/10.1080/00039896.1988.9935861

[12] Moraes PB, Bertazzoli R. (2005) Electrodegradation of landfill leachate in a flow electrochemical reactor. Chemosphere, 58(1): 41-46. https://doi.org/10.1016/j.chemosphere.2004.09.026

[13] Griffith J, Duncan RC, Pellom AC. (1989) Cancer mortality in U.S. Counties with hazardous waste sites and ground water pollution. Arch Environmental Health, 44(2): 69-74. https://doi.org/10.1080/00039896.1989.9934378

[14] Sang YM, Gu QB, Sun TC, Li FS. (2008) Color and organic compounds removal from secondary effluent of landfill leachate with a novel inorganic polymer coagulant. Water Science and Technology, 58(7): 1423-1432. https://doi.org/10.2166/wst.2008.446

[15] Marttinen SK, Kettunen RH, Rintala JA. (2003) Occurrence and removal of organic pollutants in sewages and landfill leachates. Science of the total environment, 301(1-3): 1-12. https://doi.org/10.1016/S0048-9697(02)00302-9

[16] Monje-Ramirez I, De Velasquez MO. (2004) Removal and transformation of recalcitrant organic matter from stabilized saline landfill leachates by coagulation–ozonation coupling processes. Water Research, 38(9): 2359-2367. https://doi.org/10.1016/j.watres.2004.02.011

[17] Park JY, Batchelor B. (2002) A multi-component numerical leach model coupled with a general chemical speciation code. Water research, 36(1): 156-166. https://doi.org/10.1016/S0043-1354(01)00207-X

[18] Gajski G, Oreščanin V, Garaj-Vrhovac V. (2012) Chemical composition and genotoxicity assessment of sanitary landfill leachate from Rovinj, Croatia. Ecotoxicology and Environmental Safety, 78: 253-259. https://doi.org/10.1016/j.ecoenv.2011.11.032

[19] Mukherjee S, Mukhopadhyay S, Hashim MA, Sen Gupta B (2015) Contemporary environmental issues of landfill leachate: assessment and remedies. Critical Reviews in Environmental Science and Technology, 45(5): 472-590. https://doi.org/10.1080/10643389.2013.876524

[20] Hemananthani S. (2017) Minister: Leachate contamination must be addressed. The Star. https://www.thestar.com.my/news/nation/2017/07/10/a-very-dirty-dirty-headache-minister-leachate-contamination-must-be-addressed/

[21] Hoang VY, Jupsin H, Le VC, Vasel JL. (2012) Modeling of partial nitrification and denitrification in an SBR for leachate treatment without carbon addition. Journal of Material Cycles and Waste Management, 14(1): 3-13. https://doi.org/10.1007/s10163-011-0033-x

[22] Show PL, Pal P, Leong HY, Juan JC, Ling TC. (2019) A review on the advanced leachate treatment technologies and their performance comparison: an opportunity to keep the environment safe. Environmental monitoring and assessment, 191(4): 1-28. https://doi.org/10.1007/s10661-019-7380-9

[23] Wang K, Li L, Tan F, Wu D. (2018) Treatment of landfill leachate using activated sludge technology: A review. Archaea, 2018: 1-10. Article ID 1039453. https://doi.org/10.1155/2018/1039453

[24] Du X, Zhang R, Gan Z, Bi J. (2013) Treatment of high strength coking wastewater by supercritical water oxidation. Fuel, 104: 77-82. https://doi.org/10.1016/j.fuel.2010.09.018

[25] Reddy SN, Nanda S, Hegde UG, Hicks MC, Kozinski JA. (2015) Ignition of hydrothermal

flames. RSC Advances, 5(46): 36404-36422. https://doi.org/10.1039/c5ra02705e

[26] Hwang I-H, Aoyama H, Matsuto T, Nakagishi T, Matsuo T. (2012) Recovery of solid fuel from municipal solid waste by hydrothermal treatment using subcritical water. Waste Management, 32(3): 410-416. https://doi.org/10.1016/j.wasman.2011.10.006

[27] Kang K, Quitain AT, Daimon H, Noda R, Goto N, Hu HY, Fujie K. (2001) Optimization of amino acids production from waste fish entrails by hydrolysis in sub and supercritical water. The Canadian Journal of Chemical Engineering, 79(1): 65-70. https://doi.org/10.1002/cjce.5450790110

[28] Brunner G. (2009) Near critical and supercritical water. Part I. Hydrolytic and hydrothermal processes. The Journal of Supercritical Fluids, 47(3): 373-381.

[29] Ren LH, Nie YF, Liu JG, Jin YY, Sun L. (2006) Kinetics study on photochemical oxidation of polyacrylamide by ozone combined with hydrogen peroxide and ultraviolet radiation. Journal of Environmental Sciences, 18(4): 660-664.

[30] Watchararuji K, Goto M, Sasaki M, Shotipruk A. (2008) Value-added subcritical water hydrolysate from rice bran and soybean meal. Bioresource technology, 99(14): 6207-6213. https://doi.org/10.1016/j.biortech.2007.12.021

[31] Lamoolphak W, De-Eknamkul W, Shotipruk A. (2008) H production and characterization of protein and amino acids from silk waste. Bioresource Technology, 99(16): 7678-7685. https://doi.org/10.1016/j.biortech.2008.01.072

[32] Eley MH, Guinn GR, Bagchi J. (1995) Cellulosic materials recovered from steam classified municipal solid wastes as feedstocks for conversion to fuels and chemicals. Applied Biochemistry and Biotechnology, 51(1): 387-397. https://doi.org/10.1007/BF02933442

[33] Sawayama S, Inoue S, Minowa T, Tsukahara K, Ogi T. (1997) Thermochemical liquidization and anaerobic treatment of kitchen garbage. Journal of fermentation and bioengineering, 83(5): 451-455. https://doi.org/10.1016/S0922-338X(97)82999-6

[34] Kato A, Matsumura Y. (2003) Hydrothermal Pulping of Wet Biomass as Pretreatment for Supercritical Water Gasification Studies Using Cabbage as a Model Compound. Journal of the Japan Institute of Energy, 82: 97-102. https://doi.org/10.3775/jie.82.97

[35] Papadimitriou EK, Barton JR, Stentiford EI. (2008) Sources and levels of potentially toxic elements in the biodegradable fraction of autoclaved non-segregated household waste and its compost/digestate. Waste Management & Research, 26(5): 419-430. https://doi.org/10.1177/0734242X08088697

[36] Onwudili JA, Williams PT. (2007) Hydrothermal catalytic gasification of municipal solid waste. Energy and Fuels, 21: 3676-3683. https://doi.org/10.1021/ef700348n

[37] Marrone PA, Hong GT. (2007) Supercritical water oxidation. Environmentally Conscious Materials and Chemicals Processing, 385-453. https://doi.org/10.1002/9780470168219.ch13

[38] Gidner A, Stenmark L. (2001) Supercritical water oxidation of sewage sludge–State of the art. In Proceedings of the IBC's Conference on Sewage Sludge and Disposal Options: 26-27 March 2001; Birmingham, England; 1-16. Elsevier Karlskoga.

[39] Cocero MJ, Martín A, Bermejo MD, Santos M, Rincón D, Alonso E, Fdez-Polanco F. (2003) Supercritical water oxidation of industrial waste from pilot to demonstration scale. In Proceedings of the 6th International Symposium on Supercritical Fluids: 28-30 April 2003; Versailles, France.

[40] Behnia I. (2013) Treatment of aqueous biomass and waste via supercritical water gasification for the production of CH$_4$ and H$_2$. Master thesis. The University of Western Ontario, Chemical and Biochemical Engineering Department.

[41] Veriansyah B, Kim JD. (2007) Supercritical water oxidation for the destruction of toxic organic wastewaters: A review. Journal of Environmental Sciences, 19(5): 513-522. https://doi.org/10.1016/S1001-0742(07)60086-2

[42] Kirmizakis P, Tsamoutsoglou C, Kayan B, Kalderis D. (2014) Subcritical water treatment of landfill leachate: Application of response surface methodology. Journal of Environmental Management, 146: 9-15. https://doi.org/10.1016/j.jenvman.2014.04.037

[43] APHA (2005) Standard Methods for the Examination of Water and Wastewater. Stand Methods. https://doi.org/ISBN 9780875532356

[44] Turki N. (2013) Determination of organic compounds in landfill leachates treated by

coagulation-flocculation and Fenton-adsorption. Journal of Environmental Science Toxicology Food Technology, 7(3): 18-25. https://doi.org/10.9790/2402-0731825

[45] Baan R, Gross Y, Straif K. (2009) A review of human carcinogens-Part F: chemical agents and related occumations. The Lancet Oncology, 10(12): 1143-1144.

[46] McCallister MM, Maguire M, Ramesh A, Aimin Q, Liu S, Khoshbouei H, Aschner M, Ebner FF, Hood DB. (2008) Prenatal exposure to benzo(*a*)pyrene impairs later-life cortical neuronal function. Neurotoxicology, 29(5): 846-854.

[47] Clark RS, Pellom ST, Booler B, Ramesh A, Zhang T, Shanker A, Maguire M, Juarez PD, Patricia MJ, Langston MA, Lichtveld MY, Hood DB. (2006) Validation of research trajectory 1 of an Exposome framework: Exposure to benzo(*a*)pyrene confers enhanced susceptibility to bacterial infection. Environmental Research, 146: 173-184.

[48] Ramesh A, Inyang F, Lunstra DD, Niaz MS, Kopsombut P, Jones KM, Hood DB, Hills ER, Archibong AE. (2008) Alteration of fertility endpoints in adult male F-344 rats by subchronic exposure to inhaled benzo(*a*)pyrene. Experimental and Toxicologic Pathology, 60(4-5): 269-280.

[49] Vane CH, Kim AW, Beriro DJ, Cave MR, Knights K, Moss-Hayes V, Nathanail PC. (2014) Polycyclic aromatic hydrocarbons (PAH) and polychlorinated biphenyls (PCB) in urban soils of Greater London, UK. Applied Geochemistry, 51: 303-314. https://doi.org/10.1016/j.apgeochem.2014.09.013

THE EFFECT OF LAYER THICKNESS ON REPEATABILITY OF 3D PRINTED PLA PARTS PRODUCED USING OPENWARE 3D PRINTER

NORMARIAH CHE MAIDEEN[*]**, MOHD IKMAL HISHAM ABDUL RAHIM, SALINA BUDIN, KOAY MEI HYIE AND HAMID YUSOFF**

Centre for Mechanical Engineering Studies, Universiti Teknologi MARA, Cawangan Pulau Pinang, Permatang Pauh Campus, 13500 Pulau Pinang, Malaysia.

[*]*Corresponding author: normariah@uitm.edu.my*

ABSTRACT: Fused Filament Fabrication (FFF) is categorized as an additive manufacturing process, recognized as the simplest way to accomplish 3D printing. Previous studies have proven that FFF can be trusted to create custom parts with high complexity. However, some performance issues still exist with this method that must be resolved to improve conventional manufacturing techniques. One of them is its repeatability performance that is debatable when it comes to producing repetitive runs of similar parts. Printing parameter is one of the factors that play a significant role on the repeatability performance of parts produced. In this study, the effect of layer thickness on the repeatability of 3D printed PLA, produced using an Openware 3D printer (Espresso F220), was investigated. Two product geometries (Part A and Part B) were produced. Layer thickness was chosen as a variable parameter (0.1 mm, 0.2 mm, and 0.3 mm) for each geometry. Data to measure repeatability of the printed PLA parts were determined based on the measurements of length, width, thickness and surface roughness for each geometry. Then, repeatability performance was analyzed through One-way ANOVA analysis. From the results, the layer thickness parameter did influence dimensional quality and repeatability of samples produced. Part length and thickness offered better repeatability performance, to both product geometries being compared, in width and surface roughness. The study reveals that variations in sample properties depends on not only one, but also every printing parameter involved. Repeatability performance can be improved by identifying the ideal combination of printing parameters to produce good part quality.

ABSTRAK: : Fabrikasi Filamen Fius (FFF) yang dikategori sebagai proses pembuatan tambahan, diakui sebagai kaedah termudah bagi menghasilkan pencetakan 3D. Kajian terdahulu telah membuktikan bahawa FFF dapat menghasilkan komponen khas yang kompleks. Walau bagaimanapun, beberapa isu peningkatan mutu masih berlaku, iaitu kaedah ini masih perlu diperbetulkan bagi membaiki teknik pembuatan konvensional. Salah satu adalah peningkatan keterulangan bagi menghasilkan komponen yang serupa secara berulang. Parameter pencetakan adalah salah satu faktor yang berperanan penting bagi peningkatan keterulangan komponen yang dihasilkan. Kajian ini mengkaji tentang kesan ketebalan lapisan terhadap kebolehulangan PLA bercetak 3D yang dihasilkan melalui pencetak Openware 3D (Espresso F220). Dua geometri produk (bahagian A dan B) dihasilkan. Ketebalan lapisan dipilih sebagai parameter pemboleh ubah (0.1mm, 0.2mm dan 0.3mm) bagi setiap geometri. Data bagi mengukur keterulangan bahagian PLA yang bercetak ditentukan berdasarkan pengukuran panjang, lebar, ketebalan dan kekasaran permukaan bagi setiap

geometri. Kemudian, peningkatan keterulangan dianalisa melalui analisis ANOVA Sehala. Dapatan hasil menunjukkan, parameter ketebalan lapisan mempengaruhi kualiti dimensi dan kebolehulangan sampel yang dihasilkan. Panjang dan ketebalan bahagian mempunyai peningkatan keterulangan yang lebih baik bagi kedua-dua geometri produk berbanding lebar dan kekasaran permukaan. Dapatan menunjukkan bahawa variasi sifat sampel tidak hanya bergantung pada satu, malah pada setiap parameter pencetakan yang terlibat. Peningkatan keterulangan dapat diperbaiki dengan mengenal pasti kombinasi parameter pencetakan yang ideal bagi menghasilkan kualiti bahagian terbaik.

1. INTRODUCTION

Fused Filament Fabrication (FFF) process comes under additive processes, which proves that this process is a filament extrusion-based process integrated with a CAD system, materials science, computer numeric control, and extrusion process to create 3D parts directly from a CAD model [1]. FFF is also known as Fused Deposition Modelling (FDM) which has been invented by Stratasys. Inc in the USA in 1990 and has become one of the world's best-known 3D printing techniques [1,2]. FFF shapes the 3D structure of individual layers of thermoplastic extruded filaments such as polylactic acid (PLA), which have sufficiently low melting temperatures for use in existing non-dedicated facilities in melting extrusion [2,3]. To date, FFF technology is widely present in different sectors, including engineering, biomedical, food and so forth [4,5].

With multiple printing parameters associated with the process, the substantial and ideal parameters for better structural and physical properties, such as accuracy and repeatability, of parts produced need to be identified, due to the applications of 3D printing in the market [6]. Researchers have taken various means to improve both structural and physical properties since FFF/FDM were introduced. Yet, for a long time, FFF work remained restricted to process parameters, such as layer thickness, and to individual materials [7]. Mohan N et al. [8] reviewed the optimization of the FFF process materials and process variables. FFF printers commonly embrace thermoplastic materials such as PLA, ABS, metal matrix composites, ceramic composites and natural fiber composites.

The simple and portable extrusion process is applicable in many different materials making FFF an affordable technology for research institutes, industries and domestic consumers with the capability of revolutionizing many different fields by providing the means to implementing innovative concepts [9,10].

Despite many applications and services offered by 3DP, this particular technology is still not completely utilized by manufacturers in terms of end-use goods due to numerous obstacles, one of them is the restricted variation in repeatability [11]. As the technology world grows, several series of 3D printing machines have been produced with different machines offering different repeatability performance. Other than that, process parameters also play a major role in determining the repeatability of parts produced by FFF. Since dimensional properties for functional components are crucial, the impacts of system parameters on repeatability are essential to examine as stated by Rebecca Kurfess [12]. The researcher stated that in order to characterize the relationships among the various parameters and the repeatability of the parts, further tests should be carried out before these 3D printed parts are used in positions where precision is important. Additional research is therefore needed to determine parameters of the printer such as the build orientation, layer thickness

and feed rate, especially since the literature on the physical characteristics of parts being produced by FFF is rather scarce. FFF has proven to be able to produce good quality products. However, there are numerous procedural issues, with respect to product repeatability in particular. The machine's capability and whether it will be affected by type of FFF machine used or not, is essential in ensuring that the product's performance is highly predictable. Previous studies revealed that research on 3D printing has focused on aspects of accuracy rather than machine repeatability performance. Past studies have proven that some printing parameters influenced the finished product quality. Eventually, one of the printing parameters, layer thickness, should also affect this matter. Therefore, there is a possibility to determine the repeatability performance of FFF machine in producing PLA parts with different layer thickness.

Thus, in this work, repeatability performance of the 3D Espresso F220 is investigated. Two product geometries are proposed in this work to further investigate the repeatability of this machine. The two product geometries (part A and part B) of PLA samples were material printed with variation in layer thickness (0.1 mm, 0.2 mm, and 0.3 mm). Surface roughness, width, height, and depth of 30 fabricated parts were measured. The repeatability performance of the machine in producing PLA material has been concluded from this study through One-way ANOVA analysis.

2. METHODOLOGY

Four steps are conducted in this study to identify the effect of layer thickness on repeatability of 3D printed PLA parts. Details for each step are explained in the subsections below.

2.1 Product Geometry

In this study, to measure the reliability performance, two product geometries were used (Part A and Part B). Part A refers to ASTM D638 Type I standard dimension. The design and dimension of the products is shown in Fig. 1.
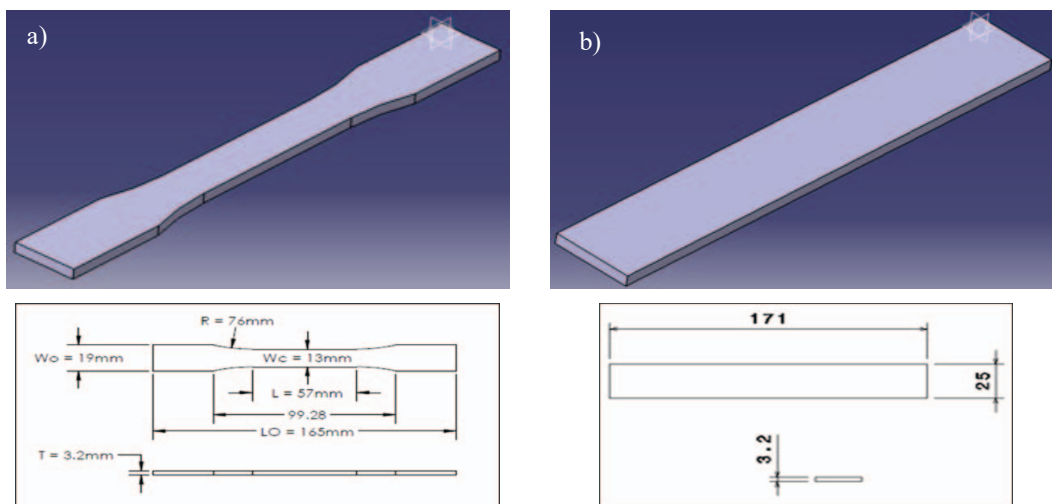

Fig. 1: (a) Part A (above: geometry, below: dimension) and
(b) Part B (above: geometry, below: dimension).

2.2 Sample Fabrication

Part A and Part B were printed using an Openware 3D printer (3D Expresso F220). Printing parameters for 3D printing of product geometries is shown in Table 1. PLA feedstock filament was used for all samples. All printing parameters in Table 1 were fixed except layer thickness. In this study, layer thickness varies in three levels which were 0.1, 0.2, and 0.3 mm. Five replications were produced for each layer for both Part A and Part B product geometries. Therefore, the sampling size was 30. Figure 2 shows a 3D Expresso F220 machine that was used in this study.

Table 1: 3D printing parameter

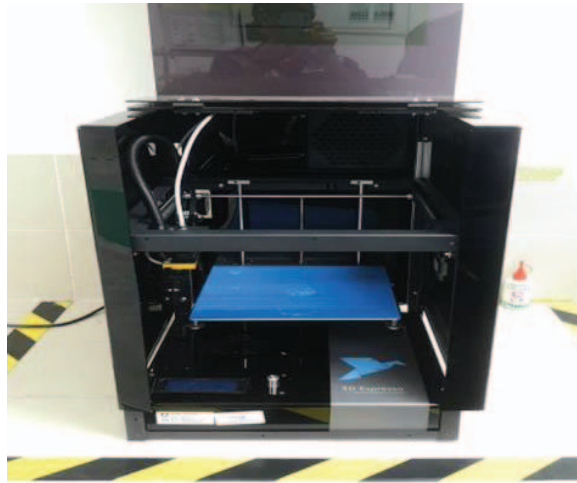| Printing Parameter	Value
Feedstock filament	Polylactic acid (PLA)
Feedstock filament (diameter)	1.75 mm
Liquefier / Extruder temperature	210 °C
Bed temperature	50 °C
Infill percentage	90%
Infill pattern	Line
Printing direction	30°/60°
Layer thickness	0.1 mm, 0.2 mm, 0.3 mm
Printing orientation	X, Y, Z
Printing speed	60 mm/s

Fig. 2: 3D Espresso F220 machine.

2.3 Sample Measurement and Data Collection

The data to measure repeatability of the printed PLA parts are determined based on the measurement of length, width, thickness, and surface roughness for each product geometry (Part A and Part B). A digital vernier caliper was used to measure length, width, and thickness while a Mitutoyo surface roughness tester (SURFTEST SJ-210) was used to measure surface roughness. Table 2 shows the measurement location for each product geometry. For surface roughness, the dial indicator was placed at the midline of the top surface for both geometries.

2.4 Repeatability Performance

In this study, one-way ANOVA is used to get repeatability performance. The null hypothesis, H_o and alternate hypothesis H_1 used described in Table 3.

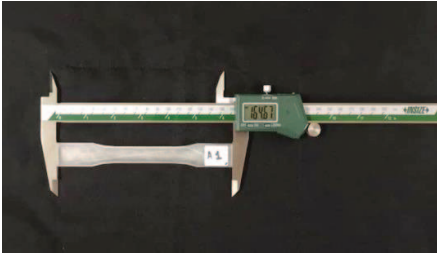Table 2: Location of measurement for length, width, and thickness

Measurement	Location of measurement (Part A)	Location of measurement (Part B)
Length		
Width		
Thickness		
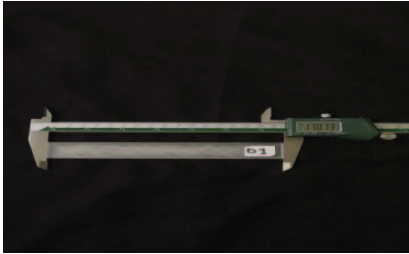
Table 3: Repeatability Hypothesis

Hypothesis	Description
Null Hypothesis	H_o = Different layer thickness does not affect the repeatability of 3D printed PLA produced using 3D Espresso F220.
Alternate Hypothesis	H_1 = Different layer thickness does affect the repeatability of 3D printed PLA produced using 3D Espresso F220.

Data recorded was analyzed using one-way ANOVA where the single factor would be layer thickness. By using this method, data was analyzed and variance was evaluated between and within groups, which were then identified by F-value, critical F-value, and P-

value. Calculations involved in identifying these three significant values were presented in equations (1) through (12).

$$\text{Mean value, } \bar{x} = \frac{\sum x}{n} \tag{1}$$

Where $\sum x$ is the total of samples value of each group, while n is the number of samples. Then, all mean values were added up together. Next, the sum of squares, $\sum(x^2)$ for each group was calculated before being added up. Later, the calculation continued with standard deviation, σ, of each layer thickness group before being summed together as eqn. (2). Then, from the data measurement table, degree of freedom was calculated through eqns. (3), (4), and (5).

$$\text{Standard deviation, } \sigma = \sqrt{\frac{\sum_{i=1}^{n}(x_i - \bar{x})^2}{(n-1)}} \tag{2}$$

$$\text{Between groups (BG)} = k - 1 \tag{3}$$

$$\text{Within groups (WG)} = N - k \tag{4}$$

$$\text{Totals degree of freedom} = N - 1 \tag{5}$$

Where k acts as the number of groups, which are group of layer thickness, while N is the total sample size. From that, calculation moved onto Sum Square (SS) that involve correction factor (CF) (eqn. (6)) and sum of squares for totals (SST) (eqn. (7)), between (SSB) (eqn. (8)) and within groups (SSW) (eqn. (9)).

$$CF = \frac{(\sum \sum x)^2}{N} \tag{6}$$

$$SST = \sum \sum (x^2) - CF \tag{7}$$

$$SSB = \left\{ \sum \left[\frac{(\sum x)^2}{n} \right] \right\} - CF \tag{8}$$

$$SSW = SST - SSB \tag{9}$$

This has led to the calculation of Mean Square (MS) that involves the mean square between (MSB) (eqn. (10)) and within groups (MSW) (eqn. (11)). Subsequently, F-value, F_o calculated using the result of MSB and MSW (eqn. (12)).

$$MSB = \frac{SSB}{BG} \tag{10}$$

$$MSW = \frac{SSW}{WG} \tag{11}$$

$$F_o = \frac{MSB}{MSW} \tag{12}$$

Then, P-value was determined using F_o through F distribution table. Lastly, alpha level, α (controlled by researcher and related to confidence levels), was determined before being used to find critical F-value, F_c through the same F distribution table. After all values were verified, all the data was then tabulated. Next, comparison was made between F-value and critical F-value, as well as between P-value and alpha level, α that will bring to conclusion in two conditions, as stated below.

$$(F_o > F_c), (P - value < \alpha) : Statistically\ significant$$

$$H_o \text{ is false and can be rejected.}$$

Whereas,

$$(F_o < F_c), (P - value > \alpha) : Statistically\ insignificant$$
$$H_o \text{ is true and accepted.}$$

From the comparison, the result obtained proved whether H_o was a false statement for both product geometry samples. Thus, this result reflected the repeatability efficiency of 3D printed PLA produced whether it was being influenced by layer thickness differences or not.

3. RESULTS

Table 4 shows a summary of result from one-way ANOVA that was conducted for data collection for both product geometries. In this study, 0.05 of confidence level was used. Thus, $F_c= 3.89$ is same for all measurements. Based on hypothesis stated in the previous section, an influence of layer thickness to the repeatability performance can be made. Based on Table 5, hypothesis conclusion on each measurement was made. In the process of producing parts for both product geometries, layer thickness did influence the repeatability performance of the printed part. This result showed that, during formation of length dimension and thickness dimension of the parts, the machine was able to produce repetitive length and thickness, regardless of the different product geometry, with a total of 30 samples produced at three different layer settings. The sampling size used was able to give a significant result for this study.

Table 4: One-way ANOVA results for all measurements for both product geometries

Measurement	Part A			Part B		
	F_o	F_c	P	F_o	F_c	P
Length	9.4957	3.89	0.0034	5.2588	3.89	0.0229
Width	2.4852	3.89	0.1250	12.6481	3.89	0.0011
Thickness	10.8723	3.89	0.0020	4.7981	3.89	0.0294
Surface roughness	52.4052	3.89	0.0000012	0.3243	3.89	0.7291

Table 5: Hypothesis conclusion

Measurement	Part A	Part B
Length	Layer thickness does effect	Layer thickness does effect
Width	Layer thickness does not effect	Layer thickness does effect
Thickness	Layer thickness does effect	Layer thickness does effect
Surface roughness	Layer thickness does effect	Layer thickness does not effect

On the other hand, for formation of width dimension, layer thickness did not affect the production of part A, but did affect the production of part B. Fig. 3 shows a trend of width measurement for part A. The trend showed a decrease in width over the number of samples due to repeatability performance of the machine during producing the samples and of the shrinkage factor of the material after the process. The width value seems to be repeatable for 0.1 mm layer thickness and 0.2 mm layer thickness. However, the variation of the samples dropped at 0.3 mm layer thickness as the width measurements showed obvious differences between each other. It showed that the longer the time taken to complete the process, the width became less varied (0.1 mm layer thickness took longer time compared to 0.3 mm). This can be proven by the standard deviation calculation, which has indicated that the standard deviation of the 0.3 mm layer thickness spread over a wide range of values

is higher than the other two-layer thicknesses. For this study, the constant printing parameter fit with 0.1 mm layer thickness leads to an optimal shrinkage percentage of PLA (0.3%-0.5%) and moderate Coefficient Linear of Thermal Expansion (CLTE: $8.5 \times 10^{-5}/{}^{\circ}C$), thus giving a low variation in the sample's width. Therefore, when the layer thickness increased, the shrinkage percentage also increased if the same value for other parameters was used throughout the study. The distance between the sample locations and the nozzle can also be taken into consideration. As the nozzle moved further from its natural position, the solidified rate for each layer in one sample became higher. Thus, this will affect the final dimension of the sample.
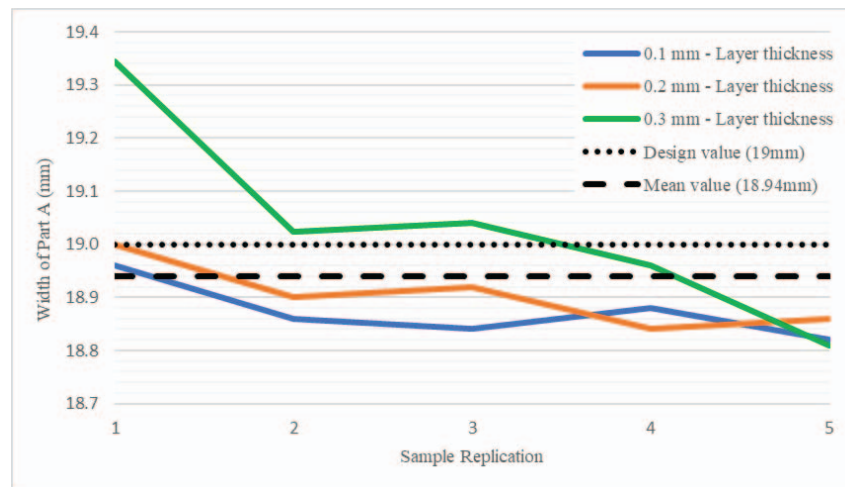

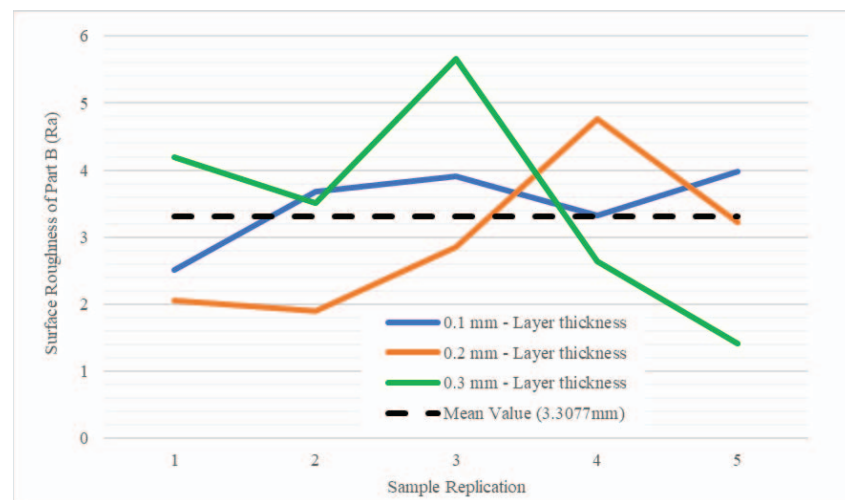Fig. 3: Trend of width measurement for part A.

Fig. 4: Trend of surface roughness measurement for Part B.

Based on the results of surface roughness, layer thickness did not influence in the formation of part B, however it did affect in producing part A. For the surface roughness of 3D printed part B, based on Fig. 4, roughness value seems to be repeatable for 0.1 mm layer thickness. However, the variation of the samples dropped as the layer thickness increased, as the roughness readings had spread out over a large range of values. By standard deviation calculation, the statement can be proven, which showed that the standard deviation of the 0.3 mm layer thickness was higher (1.5979) than the other two-layer thicknesses (0.2 mm =

1.1482, 0.3 mm =1 .5979). Thus, it revealed that the constant printing parameter that was suitable for use with 0.1mm layer thickness that produced a low variation of roughness reading of straight cut samples. However, by changing the constant parameter value, the variation can still be improved.

The temperature of the bed was one variable that can be used to improve repeatability and surface roughness. According to previous studies, among printing temperatures, the lower printing bed temperature offers an increase in quality of surface between printing temperatures. If the temperature decreased for all the samples in the set of data, the surface roughness of all the samples decreased. Therefore, the results became better and had an increase in repeatability performance of the data. However, this will affect the final dimension of the sample, as a drop-in bed temperature will lead to an increase in thermal stress of PLA. This will then cause faster solidification process and in this case, warping deformation tended to occur. Regardless of the case, the optimal printing parameter combination should be defined to produce the highest possible repeatability of a set of samples.

4. CONCLUSION

In this study, two product geometries were proposed and fabricated to study the effect of layer thickness on repeatability of 3D printed PLA parts using an Openware 3D printer (3D Espresso F220). In total, 30 samples were produced that involved repetition of 5 samples for three variations of layer thickness (0.1 mm, 0.2 mm, 0.3 mm). The sampling size was significant to quantitatively measure the repeatability performance of the product geometry produced. Part length, width, thickness, and surface roughness for both product geometries was measured to analyze using the one-way ANOVA method. From the analysis, repeatability performance was achievable when length and thickness dimension were produced for both product geometries. For width dimension, layer thickness did not affect the fabrication of part A. For surface roughness, fabrication of Part B was not affected by layer thickness. However, the best layer thickness in ensuring repeatability of 3D printed parts in this study is 0.3 mm for part A that ensured repeatable performance in length and surface roughness. While layer thickness recorded at 0.1 mm for part B geometry ensured repeatable performance in thickness and surface roughness. Some improvements can be made to enhance the repeatability for measurements that were not achieved such as by using optimal printing parameter combinations, shrinkage factors, and temperature settings.

REFERENCES

[1] Zhao Y, Chen Y, Zhao Y. (2019) Novel mechanical models of tensile strength and elastic property of FFF AM PLA materials: Experimental and theoretical analyses. Mater. Des., 181:108089.
[2] Chacon JM, Caminero MA, Garcia-Plaza E, Nunez PJ. (2017) Additive manufacturing of PLA structures using fused deposition modelling: Effect of process parameters on mechanical properties and their optimal selection. Mater. Des., 124: 143-157.

[3]   Tymrak BM, Kreiger M, Pearce JM. (2014) Mechanical properties of components fabricated with open-source 3-D printers under realistic environmental conditions. Mater. Des., 58: 242-246.

[4]   Yao T, Deng Z, Zhang K, Li S. (2019) A method to predict the ultimate tensile strength of 3D printing polylactic acid (PLA) materials with different printing orientations. Compos. Part B Eng., 163: 393-402.

[5]   Durga Prasada Rao V, Rajiv P, Navya Geethika V. (2019) Effect of fused deposition modelling (FFF) process parameters on tensile strength of carbon fibre PLA. Mater. Today Proc.

[6]   Padyal P, Mulay A, Dhanvijay MR. (2019) Experimental assessment of Repeatability of Openware 3D Printer. 1352-1357.

[7]   Harris M, Potgieter J, Archer R, Arif KM. (2019) Effect of material and process specific factors on the strength of printed parts in fused filament fabrication: A review of recent developments. Materials, 12(10): 1664.

[8]   Mohan N, Senthil P, Vinodh S, Jayanth N. (2017) A review on composite materials and process parameters optimisation for the fused deposition modelling process. Virtual Phys. Prototyp, 12(1): 47-59.

[9]   Wang L, Gramlich W.M, Gardner DJ. (2017) Improving the impact strength of Poly(lactic acid) (PLA) in fused layer modeling (FLM). Polymer (Guildf), 114: 242-248.

[10]   Harris M, Potgieter J, Arif K, Archer R. (2017) Large scale 3D printing: Feasibility of novel extrusion-based process and requisite materials. 24th Int. Conf. Mechatronics Mach. Vis. Pract. M2VIP 2017, pp 1-6.

[11]   Albaiji NFS. (2018) Repeatability case study of the 3D printer in the School of Engineering and Applied Science Lab.

[12]   Rebecca K. (2017) A parametric study of the repeatability of 3D printed LEGO® – like mechanical couplings. Bachelor of Science in Mechanical Engineering Thesis. Massachusetts Institute of Technology (MIT).

CHARACTERIZATION AND SINTERING PROPERTIES OF HYDROXYAPATITE BIOCERAMICS SYNTHESIZED FROM CLAMSHELL BIOWASTE

CHUI KIM NG[1*], KIT YEE SARA LEE[2], CHIN HONG TAN[1], SINGH RAMESH[3,4], CHEN HUNT TING[5], YEA DAT CHUAH[6], CHOU YONG TAN[3], AND UBENTHIRAN SUTHARSINI[7]

[1]*Centre for Advanced Materials, Department of Materials Engineering, Faculty of Engineering & Technology, Tunku Abdul Rahman, University College, 53300 Kuala Lumpur, Malaysia.*
[2]*Center of Systematic Innovation Research, Department of Mechanical Engineering, Faculty of Engineering & Technology, Tunku Abdul Rahman, University College, 53300 Kuala Lumpur, Malaysia.*
[3]*Centre of Advanced Manufacturing & Material Processing (AMMP), Department of Mechanical Engineering, Faculty of Engineering, University of Malaya, 50603 Kuala Lumpur, Malaysia.*
[4]*Department of Mechanical Engineering, Faculty of Engineering, Universiti Teknologi Brunei, Tunku Highway, Gadong BE1410, Brunei Darussalam.*
[5]*Department of Mechanical and Materials & Manufacturing Engineering, Lee Kong Chian Faculty of Engineering and Science, Universiti Tunku Abdul Rahman, Jalan Sungai Long, Bandar Sungai Long, Cheras, 43000 Kajang, Selangor Darul Ehsan, Malaysia.*
[6]*Department of Mechanical, Materials and Manufacturing (M3) Engineering, University of Nottingham Malaysia, Jalan Broga, 43500 Semenyih, Selangor Darul Ehsan, Malaysia.*
[7]*Department of Physics, University of Jaffna, Jaffna JA 40000, Sri Lanka.*

[*]Corresponding author: ngck@tarc.edu.my

ABSTRACT: Hydroxyapatite (HA) is a type of calcium phosphate-based bioactive ceramic that resembles the mineral phase of bone and teeth with great potential for bone substitution and biomedical implants. Biogenic-derived HA emerges as a cheap and eco-sustainable alternative to improve waste utilization. However, hydroxyapatite has limited applications due to its apparent brittleness, thus prompting investigation for enhanced sintering properties. In the present study, the combination of calcination and chemical precipitation technique was used to extract hydroxyapatite (HA) from ark clamshells (*Anadara granosa*). The method successfully produced HA powder with a Ca/P ratio of 1.6 and characteristic bands corresponded to pure HA via Fourier Transform Infrared Spectroscopy (FTIR). The synthesized HA powder was then sintered at temperatures ranging from 1200 °C to 1300 °C, followed by mechanical evaluation of the density, Vickers hardness, fracture toughness and grain size. It was revealed that the samples sintered at 1250 °C achieved a relative density of ∼88%, Vickers hardness of 5.01 ± 0.39 GPa, fracture toughness of 0.88 ± 0.07 MPa.m$^{1/2}$ and average grain size of ∼3.7 μm. Overall, the results suggest that ark clamshell synthesized HA (ACS) had the potential to be used as functional bioceramics for biomedical applications.

ABSTRAK: Hidroksiapatit (HA) adalah sejenis seramik bioaktif berasaskan kalsium fosfat yang menyerupai fasa mineral tulang dan gigi, berpotensi besar mengantikan tulang dalam implan bioperubatan. HA yang berasal dari biogenik muncul sebagai alternatif yang murah dan eko-lestari dalam menambah baik pengurusan sisa. Walau bagaimanapun, hidroksiapatit mempunyai aplikasi yang terhad kerana mempunyai kerapuhan yang ketara, menyebabkan penyelidikan diperlukan bagi meningkatkan sifat sintering. Gabungan teknik kalsinasi dan pemendakan kimia telah digunakan dalam kajian ini, bagi

mengekstrak hidroksiapatit (HA) dari kulit kerang (*Anadara granosa*). Kaedah ini telah berjaya menghasilkan serbuk HA dengan nisbah 1.6 Ca/P dan jalur puncak sepadan dengan HA tulen melalui Spektroskopi Inframerah Transformasi Fourier (FTIR). Serbuk HA ini kemudian disinter pada suhu antara 1200 °C hingga 1300 °C, diikuti penilaian mekanikal pada ketumpatan, kekerasan Vickers, kerapuhan dan ukuran bijirin. Hasil ujian menunjukkan bahawa sampel yang disinter pada suhu 1250 °C mencapai ~88% ketumpatan relatif, kekerasan Vickers 5.01 ± 0.39 GPa, kerapuhan pada 0.88 ± 0.07 MPa.m$^{1/2}$ dan purata ukuran butiran ~ 3.7 µm. Secara keseluruhan, dapatan menunjukkan bahawa kulit kerang HA yang disentisis (ACS) berpotensi sebagai bioseramik bagi aplikasi bioperubatan.

KEYWORDS: *hydroxyapatite; bioceramics; chemical synthesis; calcination; sintering*

1. INTRODUCTION

Hydroxyapatite (HA) with a chemical formula of $Ca_{10}(PO_4)_6(OH)_2$, is a type of calcium phosphate-based ceramic that comprises the main mineral constituent to human bones and teeth, which is widely used in dental and orthopedic applications. The conventional methods to synthesize HA are solid-state, mechanochemical, chemical precipitation, hydrolysis, sol-gel, hydrothermal, emulsion, sonochemical, high-temperature processes or a combination of a few techniques [1]. Among these methods, wet-chemical precipitation is the most promising and low-cost technique [2,3].

In recent years, biowaste-derived HA has attracted attention as numerous food wastes such as bones, eggshells and seafood shells had piled up in landfill globally. Specifically, shell wastes such as oyster, mussel, scallop, clam and cockle are discarded in an abundant amount. Million tons of shell wastes have been discarded and piled up in landfills in China, Taiwan, Spain, South Korea, Peru, Indonesia, Nigeria, and Malaysia [4-7]. Instead, these shell wastes could be utilized to synthesize HA owing to the rich calcium carbonate ($CaCO_3$) content [8-10]. Typically, HA has been successfully synthesized via hydrothermal synthesis method by utilizing various species of clamshell such as *Strombus gigas*, *Tridacna gigas* [11], *Venerupis* [12]*, Corbicula* [13,14]*, Mercenaria* [15], and *Anadara granosa* [16]. However, the majority of studies did not report the mechanical properties of sintered HA. In the current study, *Anadara granosa* clamshell will be used as the calcium precursor to synthesize natural HA powder, followed by characterization of its properties at various sintering temperatures.

2. MATERIALS AND METHODS

2.1 Synthesis of Powder

Biogenic sources such as seashells or eggshells are good natural sources of calcium precursor for the synthesis of HA bioceramics. In this study, the *Anadara granosa* clamshells collected from peninsular Malaysia were used as the starting materials to synthesize HA. The as-received clamshells were washed thoroughly, rinsed with distilled water, and dried in an oven at 80 °C for one hour. The dried clamshells were then crushed, ground and sieved through a 300 µm test sieve. This was followed by calcination at 1000 °C for four hours in an electrical furnace (Carbolite Gero, UK), to transform the calcium carbonate ($CaCO_3$) into calcium oxide (CaO).

Figure 1 depicts the flow chart of the HA synthesis process via wet chemical precipitation technique. First of all, 0.25 M of calcium precursor to 0.15 M of phosphorus precursor was employed to achieve stoichiometric HA with the calcium/phosphorus (Ca/P)

concentration ratio of 1.67. 2.8 g of CaO powder was then added in 200 ml of distilled water to formulate the $Ca(OH)_2$ solution as the calcium precursor. The solution was subsequently magnetic stirred at 400 rpm for an hour and maintained at pH 12. On the other hand, the 2.05 ml concentrated H_3PO_4 (phosphorus precursor) was diluted into 200 ml of distilled water, stirred and kept at about pH 2. Subsequently, the prepared H_3PO_4 solution was then added dropwise into $Ca(OH)_2$ solution to begin the titration process, continued with a vigorous stirring at 700 rpm for 30 minutes. The NH_4OH solution was then added to adjust the pH to 10. This was followed by magnetic stirring at 500 rpm for an hour after the titration process and aging for 21 hours (to form white precipitate). Vacuum filtration was subsequently performed on the precipitates using an electrical aspirator pump (Jerio Tech, Korea). Finally, the precipitate was dried in an oven at 100 °C for 16 hours and then crushed and sieved through a 300 μm test sieve to obtain ark clamshell synthesized HA (ACS) powder.
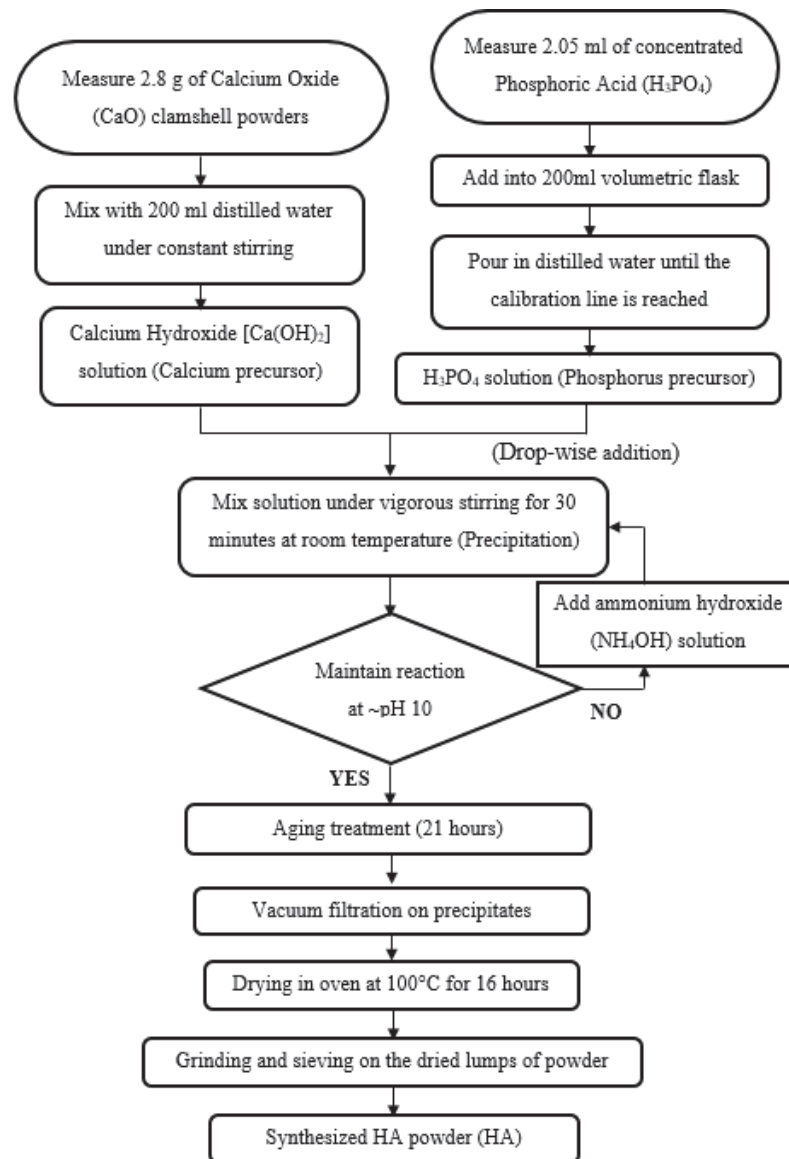

Fig. 1: Flow chart of the HA synthesis process via wet chemical precipitation technique.

2.2 Sample Preparation

The ACS synthesized HA powders were compacted into 20 mm disc samples (Fig. 2) by a hydraulic press machine (Enerpac, USA) at 1000 psi, which was set at a pressure lower than 3000 psi, as recommended by Mel et al. [17]. The green samples were then conventionally sintered (Carbolite Gero, UK) at 1200 °C, 1250 °C and 1300 °C for two hours with a ramp rate of 10 °C/min. The dimension of the green and as-sintered samples was recorded with a digital Vernier caliper (Mitutoyo, Japan) for the shrinkage measurements. Prior to characterization, the sintered disc samples were ground with silicon carbide (SiC) sandpapers and polished to achieve a 1 μm optical reflective surface.

Fig. 2: HA green samples.

2.3 Characterization and Mechanical Property Evaluation

A Fourier transform infrared (FTIR) Spectrum 65 Spectrometer (Perkin Elmer Inc., USA) was used to identify the functional groups and composition present in the synthesized powder, at the scan range of 650 to 4000 cm^{-1}. Differential scanning calorimetric (DSC)/ Thermogravimetric analysis (TGA) (TA Instruments, USA) was employed to determine the weight loss and phase change of synthesized HA powder, from room temperature to 1400 °C, with a heating rate of 10 °C/min under nitrogen gas environment. Bulk density measurement was also performed on the sintered samples using the Archimedes' principle, by taking the theoretical density of HA as 3.156 g/cm^3. The microstructure of synthesized and sintered samples was examined via scanning electron microscopy (SEM) (SEC Co. Ltd., Korea). Energy dispersive X-ray (EDX) spectroscopy was used to determine the Ca/P ratio of the synthesized and sintered samples. The grain size of the sintered samples was measured using the linear intercept method according to ASTM E112-96. Vickers hardness of the sintered samples was evaluated via micro-hardness tester (Bowers ESEWAY, UK), with an applied load of 200 gf at a loading time of 10 seconds based on ASTM E384-99. For each sample, at least five indentations were used to obtain the average hardness and to calculate the standard deviation value. Fracture toughness was also obtained via the relationship derived by Niihara et al. [18].

3. RESULTS AND DISCUSSION

3.1 FTIR Analysis of ACS Synthesized HA Powder

The functional groups in the ACS synthesized HA powder were identified using FTIR and the spectrum is shown in Fig. 3. The result confirms that the synthesized powder exhibited the typical spectrum of pure HA powder, with the chemical groups of phosphate group (PO_4^{3-}), hydroxyl groups (OH^-) and carbonate groups (CO_3^{2-}). The distinctive peaks at 1025 cm^{-1} and 1087 cm^{-1} are corresponding to the PO_4^{3-} (v_3), while the peak at 962 cm^{-1} corresponds to the PO_4^{3-} (v_1). On the other hand, weak characteristic peaks observed at 3350 cm^{-1} and 3570 cm^{-1} could be related to the OH^- group. The FTIR peaks exhibited key characteristics of HA phase. The peaks at 1456, 1420 cm^{-1} and 874 cm^{-1} show the presence of CO_3^{2-} in the samples. Similar carbonate bands were also reported in previous studies [19-20].
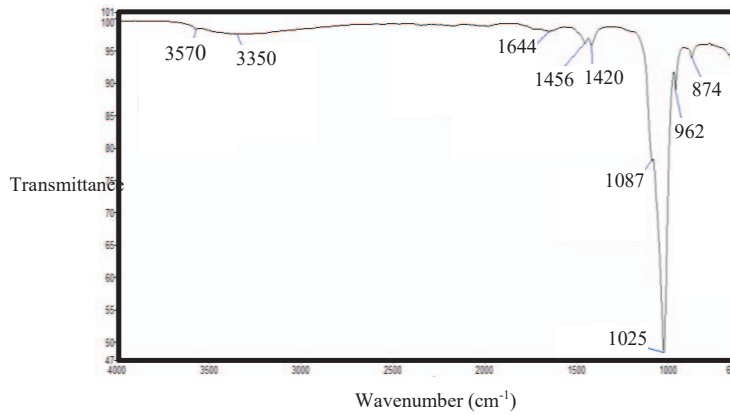
Fig. 3: FTIR spectrum of ACS synthesized HA powder.

3.2 EDX Analysis

Figure 4 shows that the EDX spectrums of ACS synthesized and sintered HA samples consist of three main elemental constituents of HA bioceramics, which are calcium (Ca), phosphorus (P) and oxygen (O). From the atomic percentage (At %), the calculated Ca/P ratio of synthesized biogenic HA powder is 1.60, while the sintered HA bioceramics increased to ~1.88 when sintered at 1200 °C and 1250 °C, and reached at 1.97 when sintered at 1300 °C. The obtained Ca/P ratio from this work deviated from the theoretical value for pure stoichiometric HA of 1.67. Similar observation was reported by Ramesh et al. [21]
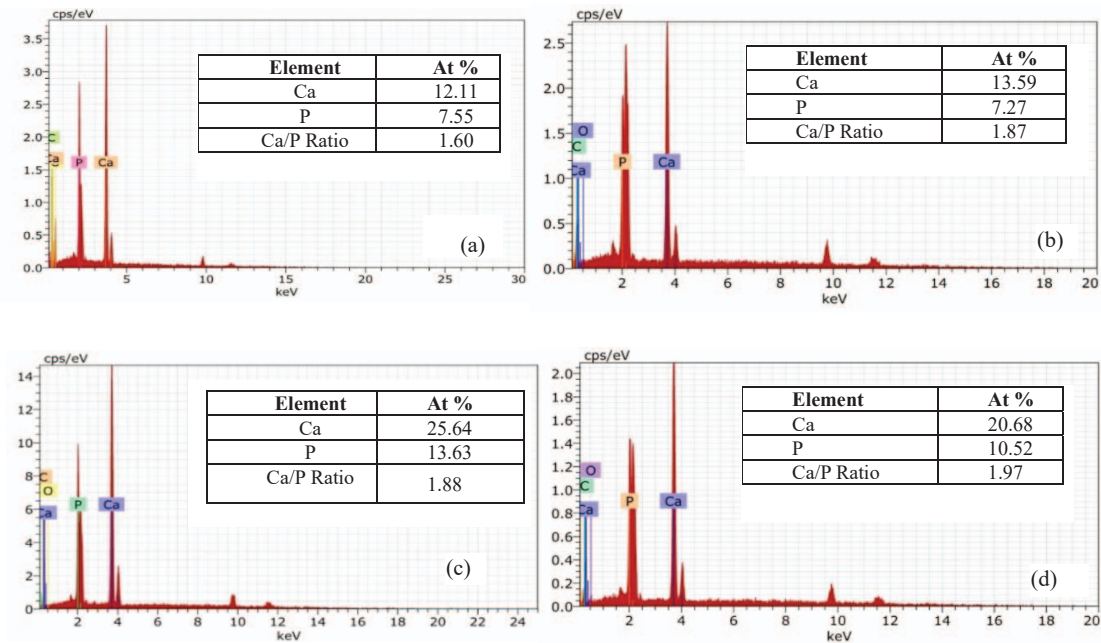

Fig. 4: EDX spectrum ACS (a) synthesized HA powder, sintered HA at (b) 1200 °C, (c) 1250 °C, and (d) 1300 °C.

3.3 Microstructural and Grain Size Analysis

Figure 5 (a) shows the SEM micrograph of the ACS synthesized HA powder, which consists of large agglomerates. The microstructural evolution of the ACS sintered HA ceramics is presented in Fig. 5 (b)-(d). The SEM investigation revealed that the average grain size for the sintered HA samples increases with the increase of sintering temperatures. The results show a gradual increase in grain size from 2.14 µm at 1200 °C to 3.70 µm at 1250 °C. As the sintering temperature increased to 1300 °C, the grain size dramatically increased to 6.44 µm. Accelerated grain growth in HA samples sintered beyond 1250 °C implied a change in phase stability of HA.

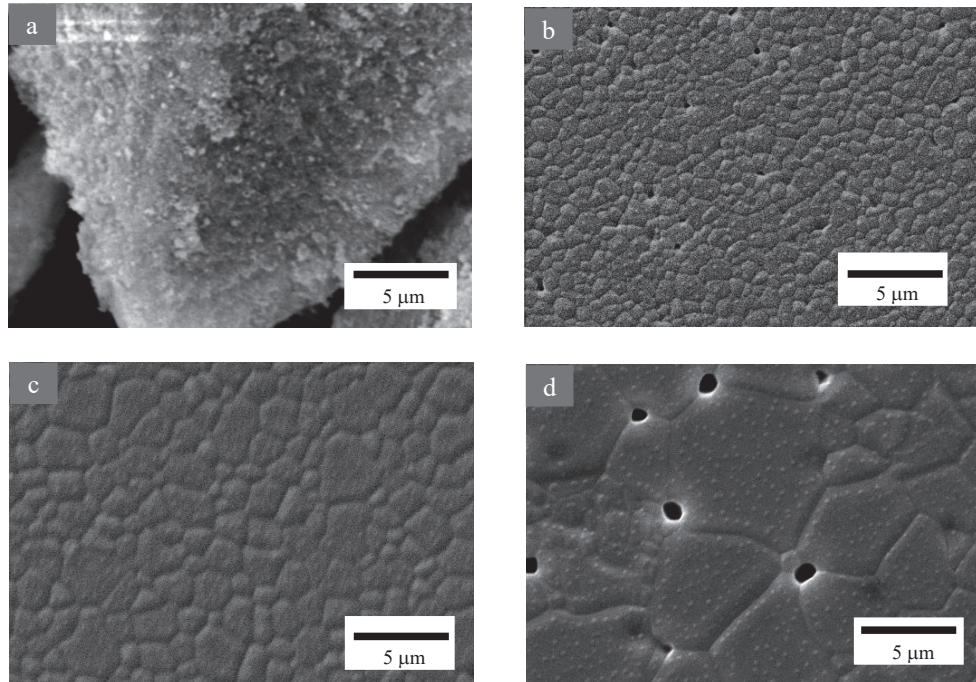Fig. 5: SEM images of (a) ACS synthesized HA powder and sintered HA at (b) 1200 °C,
(c) 1250 °C, and (d) 1300 °C.

3.4 Thermal Stability Analysis

Figure 6 shows the differential scanning calorimetric (DSC)/ thermogravimetric analysis (TGA) measurement of the ACS synthesized HA powder. At 300 °C, a pronounced weight loss of ~5.3% was observed from total weight loss of 7.6% of the HA sample. The weight loss could be ascribed to the evaporation of physically adsorbed water molecules. With additional heating upon 500°C, the insignificant weight loss (~0.75%) is attributed to the release of interstitial water molecule in the crystal lattice of HA. An endothermic peak at ~1000 °C can be postulated as dehydroxylation and decarboxylation of the HA powder. Weight loss at higher temperatures may be due to the dissociation of HA to tricalcium phosphate (TCP) and tetracalcium phosphate (TTCP). The decomposition of HA phase is believed to cause the increased in the average grain size and reduced the mechanical properties of the HA.
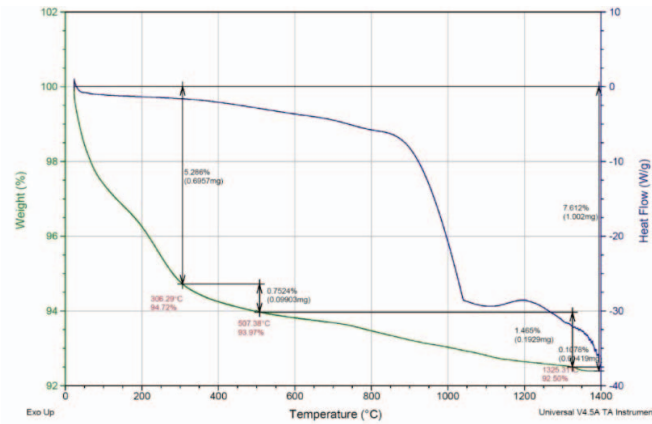
Fig. 6: DSC/ TGA plot of the ACS synthesized HA powder.

3.5 Mechanical Properties

The effect of sintering temperature on the relative density, Vickers hardness, and fracture toughness of HA ceramics are presented in Table 1. The density of ACS sintered HA increased from 83.8% at 1200 °C to 88% at 1250 °C. A slight decrease in density (86.7%) was observed when the sintering temperature increased to 1300 °C. The result is in agreement with the grain growth of the sintered HA as shown in the SEM images. On the other hand, the Vickers hardness of the sintered HA increased from 4.35 ± 0.43 GPa at 1200 °C to a maximum of 5.01 ± 0.39 GPa at 1250 °C. When the sintering temperature reached 1300 °C, the Vickers hardness was reduced to 4.03 ± 0.35 GPa, which is corresponding with the reduction in relative density and the grain growth of the sintered HA. This is in agreement with Aminzare and co-authors, where the Vickers hardness of the sintered biomimetic-synthesized HA decreased from 2.52 GPa to 2.23 GPa when sintered at 1250 °C and 1300 °C, respectively [22].

In the current study, the fracture toughness exhibited similar trends as the hardness, i.e. the fracture toughness increased from 0.67 ± 0.20 MPa.m$^{1/2}$ to a maximum of 0.88 ± 0.07 MPa.m$^{1/2}$, when sintered at 1200 °C and 1250 °C, respectively. This was followed by a decrease to 0.71 ± 0.10 MPa.m$^{1/2}$ when the sintering temperature reached 1300 °C. Similarly, the decreased fracture toughness at 1300 °C is related to the decrease of relative density. It is postulated that the reduced density and mechanical properties at 1300 °C was due to the decomposition of HA phase at a high sintering temperature regime (>1250 °C) [22-23]. The results also show that calcium-rich HA with the Ca/P ratio of 1.88 possessed an overall higher density and mechanical properties as compared to HA with Ca/P ratio of 1.97.

Table 1: The properties of ACS sintered HA

Sintering temp/ holding time	Grain size (μm)	Relative density (%)	Vickers Hardness (GPa)	Fracture toughness (MPam$^{1/2}$)
1200 °C/ 2 hrs	2.14	83.8	4.35 ± 0.43	0.67 ± 0.20
1250 °C/ 2 hrs	3.70	88.0	5.01 ± 0.39	0.88 ± 0.07
1300 °C/ 2 hrs	6.44	86.7	4.03 ± 0.35	0.71 ± 0.10

4. CONCLUSION

The present study revealed that ACS synthesized HA samples were successfully synthesized via the calcination and wet chemical precipitation using ark clamshells (*Anadara granosa*) as the calcium precursor. The results also show that ACS sintered HA with the Ca/P ratio of 1.88 possessed a higher density (~88%) and mechanical properties (Vickers hardness of ~5 GPa and fracture toughness of ~0.88 MPa.m$^{1/2}$) when sintered at 1250 ºC, which shows that the phase stability of HA was retained up to 1250 ºC and the decomposition of HA to TCP and TTCP occurred above 1250 ºC. The finding of this study would promote the recycling and reuse of the animal shells or bones to convert biowaste into value added biomedical products which would help in attaining Sustainable Development Goal targets. Future research would encompass further works on two-step or hybrid sintering routes to produce finer microstructure with enhanced mechanical properties.

REFERENCES

[1] Sadat-Shojai M, Khorasani MT, Dinpanah-Khoshdargi E, Jamshidi A. (2013) Synthesis methods for nanosized hydroxyapatite with diverse structures. Acta Biomaterialia, 9(8): 7591-7621. https://doi.org/10.1016/j.actbio.2013.04.012

[2] Hongquan Z, Yuhua Y, Youfa W, Shipu L. (2003) Morphology and formation mechanism of hydroxyapatite whiskers from moderately acid solution. Materials Research, 6: 111-115. Retrieved from https://www.scielo.br/pdf/mr/v6n1/v6n1a20.pdf

[3] Hablee, S, Sopyan I, Mel, M, Salleh, H.M. and Rahman, MM. (2018) Effect of poly (ethylene glycol) on the injectability, setting behavior and mechanical properties of calcium phosphate bone cement. IIUM Engineering Journal, 19(2): 192-202.
https://journals.iium.edu.my/ejournal/index.php/iiumej/article/view/913

[4] Mo KH, Alengaram UJ, Jumaat MZ, Lee SC, Goh WI, Yuen CW. (2018) Recycling of seashell waste in concrete: A review. Construction and Building Materials, 162: 751-764. https://doi.org/10.1016/j.conbuildmat.2017.12.009

[5] Hembrick-Holloman V, Samuel T, Mohammed Z, Jeelani S, Rangari VK. (2020) Ecofriendly production of bioactive tissue engineering scaffolds derived from egg- and sea-shells. Journal of Materials Research and Technology, 9(6): 13729-13739. https://doi.org/10.1016/j.jmrt.2020.09.093

[6] Saharudin SH, Shariffuddin JH, Nordin NI. (2017) Biocomposites from *Anadara granosa* shells waste for bone material applications. IOP Conference Series: Materials Science and Engineering, 257: 012061. Retrieved from https://iopscience.iop.org/article/10.1088/1757-899X/257/1/012061/pdf

[7] Musa B, Raya I, Natsir H. (2016) Synthesis and Characterizations of Hydroxyapatite Derived Blood Clam Shells (*Anadara granosa*) and Its Potency to Dental Remineralizations. 12(4): 527-38. Retrieved from https://www.ripublication.com/ijac16/ijacv12n4_04.pdf

[8] Bee SL, Hamid ZA. (2020) Hydroxyapatite derived from food industry bio-wastes: Syntheses, properties and its potential multifunctional applications. Ceramics International, 46(11, Part A): 17149-17175. https://doi.org/10.1016/j.ceramint.2020.04.103

[9] Pu'ad NM, Koshy P, Abdullah HZ, Idris MI, Lee TC. (2019) Syntheses of hydroxyapatite from natural sources. Heliyon, 5(5): e01588. https://doi.org/10.1016/j.heliyon.2019.e01588

[10] Núñez D, Elgueta E, Varaprasad K, Oyarzún P. (2018) Hydroxyapatite nanocrystals synthesized from calcium rich bio-wastes. Materials Letters, 230: 64-68. https://doi.org/10.1016/j.matlet.2018.07.077

[11] Vecchio KS, Zhang X, Massie JB, Wang M, Kim CW. (2007) Conversion of bulk seashells to biocompatible hydroxyapatite for bone implants. Acta Biomaterialia, 3(6): 910-918. https://doi.org/10.1016/j.actbio.2007.06.003

[12] Bramhe S, Kim TN, Balakrishnan A, Chu MC. (2014) Conversion from biowaste Venerupis clam shells to hydroxyapatite nanowires. Materials Letters, 135: 195-198. https://doi.org/10.1016/j.matlet.2014.07.137

[13] Onoda H, Yamazaki S. (2016) Homogenous hydrothermal synthesis of calcium phosphate with calcium carbonate and corbicula shells. Journal of Asian Ceramic Societies, 4(4): 403-406. https://doi.org/10.1016/j.jascer.2016.10.001

[14] Alif MF, Aprillia W, Arief S. (2018) A hydrothermal synthesis of natural hydroxyapatite obtained from Corbicula moltkiana freshwater clams shell biowaste. Materials Letters, 230: 40-43. https://doi.org/10.1016/j.matlet.2018.07.034

[15] Pal A, Nasker P, Paul S, Chowdhury AR, Sinha A, Das M. (2019) Strontium doped hydroxyapatite from Mercenaria clam shells: Synthesis, mechanical and bioactivity study. Journal of the Mechanical Behavior of Biomedical Materials, 90: 328-336. https://doi.org/10.1016/j.jmbbm.2018.10.027

[16] Azis Y, Jamarun N, Arief S, Nur H. (2015) Facile synthesis of hydroxyapatite particles from cockle shells (*Anadara granosa*) by hydrothermal method. Oriental journal of chemistry, 31:1099-1105.

[17] Mel M, Abdeen FR, and Sopyan I. (2011). Fabrication of Ceramic Membrane Chromatography for Biologics Purification. IIUM Engineering Journal, 12(4): 115-124.

[18] Niihara K, Morena R, Hasselman DP. (1982) Evaluation of KIc of brittle solids by the indentation method with low crack-to-indent ratios. Journal of Materials Science Letters, 1(1): 13-16.

[19] Ramesh S, Natasha AN, Tan CY, Bang LT, Ching C.Y Chandran H. (2016) Direct conversion of eggshell to hydroxyapatite ceramic by a sintering method. Ceramics international, 42(6): 7824-7829. https://doi.org/10.1016/j.ceramint.2016.02.015

[20] Kamalanathan P, Ramesh S, Bang LT, Niakan A, Tan CY, Purbolaksono J, Chandran H, Teng WD. (2014) Synthesis and sintering of hydroxyapatite derived from eggshells as a calcium precursor. Ceramics International, 40(10): 16349-16359. https://doi.org/10.1016/j.ceramint.2014.07.074

[21] Ramesh S, Loo ZZ, Tan CY, Chew WK, Ching YC, Tarlochan F, Chandran H, Krishnasamy S, Bang LT, Sarhan AA (2018) Characterization of biogenic hydroxyapatite derived from animal bones for biomedical applications. Ceramics International, 44(9): 10525-10530. https://doi.org/10.1016/j.ceramint.2018.03.072

[22] Aminzare M, Eskandari A, Baroonian MH, Berenov A, Hesabi ZR, Taheri M, Sadrnezhaad SK. (2013) Hydroxyapatite nanocomposites: Synthesis, sintering and mechanical properties. Ceramics International. 39(3): 2197-2206. https://doi.org/10.1016/j.ceramint.2012.09.023

[23] Ramesh S, Tan CY, Hamdi M, Sopyan I, Teng WD. (2007) The influence of Ca/P ratio on the properties of hydroxyapatite bioceramics. In International conference on smart materials and nanotechnology in engineering. International Society for Optics and Photonics. 6423: 64233A.

EARLIER DENATURATION OF DNA BY USING NOVEL TERNARY HYBRID NANOPARTICLES

JALAL MOHAMMED ZAYAN[1], AKBAR JOHN[2*],
ABDUL KHALIQ RASHEED[3], BATOUL ALALLAM[4], MOHAMMED KHALID[5],
AHMAD FARIS ISMAIL[1], BRYAN RAVEEN NELSON[6]
AND HAMZAH MOHD SALLEH[7]

[1]Department of Mechanical Engineering, International Islamic University Malaysia,
Kuala Lumpur, Malaysia.
[2]Institute of Oceanography and Maritime Studies (INOCEM), Kulliyyah of Science,
International Islamic University Malaysia, Kuantan, Malaysia.
[3]Department of New Energy Science and Engineering, School of Energy and Chemical
Engineering, Xiamen University Malaysia. Jalan Sunsuria, Bandar Sunsuria, 43900 Sepang,
Malaysia.
[4]Integrated Medical Center, Advanced Medical and Dental Institute,13200, Malaysia.
[5]Graphene and Advanced 2D Materials Research Group, Level 4, East Wing - NUB, School of
Science and Technology, Sunway University, Sunway City, Petaling Jaya, 47500, Malaysia.
[6]Institute of Topical Biodiversity and Sustainable Development, Universiti Malaysia Terengganu,
21030, Kuala Nerus, Terengganu, Malaysia.
[7]International Institute for Halal Research and Training (INHART),
International Islamic University Malaysia, Kuala Lumpur, Malaysia

*Corresponding author: akbarhohn50@gmail.com

ABSTRACT: Two novel ternary hybrid nanoparticles (THNp) consisting of graphene oxide (GO) and reduced graphene oxides (rGO) were added to samples of DNA. The effect of the addition of nanoparticles on the thermal denaturation of DNA samples was studied by measuring the absorbance using a temperature-controlled Perkin Elmer UV spectrophotometer. Adding $GO-TiO_2-Ag$ and $rGO-TiO_2-Ag$ nanoparticles lowered the denaturation temperature of template DNA significantly. The nanoparticles affect the denaturation rate. The optimal $GO-TiO_2-Ag$ and $rGO-TiO_2-Ag$ concentrations were found to be 5×10^{-2}, which resulted in 86- and 180-folds augmentation of DNA denaturation (6.5 µg/mL), respectively, while it resulted in 2- and 7-folds augmentation of DNA denaturation (11.5 µg/mL), respectively, at temperature as low as 80 °C. The results indicated that $rGO-TiO_2-Ag$ nanoparticles exhibited significantly higher DNA denaturation enhancement than $rGO-TiO_2-Ag$ nanoparticles, owing to their enhanced thermal conductivity effect. Therefore, these nanoparticles could help to get improved PCR yield, hence enable amplification to be performed for longer cycles by lowering the denaturation temperatures.

ABSTRAK: Dua ternar baru nanopartikel hibrid (THNp) mengandungi oksida grapen (GO) dan oksida grapen yang dikurangkan (rGO) dan dimasukkan ke dalam sampel DNA. Kesan penambahan nanopartikel pada denaturasi termal pada sampel DNA telah dikaji dengan mengukur penyerapan menggunakan kawalan-suhu Perkin Elmer UV spektrofotometer. Penambahan $GO-TiO_2-Ag$ dan $rGO-TiO_2-Ag$ nanopartikel telah mengurangkan suhu denaturasi pada templat DNA dengan nyata. Nanopartikel memberi kesan pada kadar denaturasi. Kepekatan optimal $GO-TiO_2-Ag$ dan $rGO-TiO_2-Ag$ didapati sebanyak 5×10^{-2} menyebabkan penambahan sebanyak 86- dan 180-lipat pada DNA denaturasi (6.5 µg/mL), masing-masing, sementara ia menyebabkan sebanyak 2- dan 7-

lipat penambahan pada DNA denaturasi (11.5 µg/mL), masing-masing, pada suhu serendah 80 °C. Dapatan menunjukkan nanopartikel rGO-TiO₂-Ag mempunyai kenaikan penambahan DNA denaturasi nyata berbanding nanopartikel rGO-TiO₂-Ag, disebabkan kesan kekonduksian penambahan suhu. Oleh itu, nanopartikel ini dapat membantu bagi penambah baikan pengeluaran PCR, membolehkan penguatan dapat dilakukan dalam kitaran lebih lama dengan merendahkan suhu denaturasi.

1. INTRODUCTION

PCR is a widely used tool in molecular biotechnology to generate billions of copies of target DNA from a single templet DNA strand. This mechanism is the basis for detecting genetic mutation and disease diagnosis in various medical and OMICS applications. The PCR process involves three major stages: denaturation, annealing, and extension. These steps are performed by rapid heating and cooling of the samples to a specific temperature at the defined time. The denaturation is the first step of PCR which involves the unwinding of double-stranded DNA into two single-stranded DNA by applying heat [1,2]. From a thermodynamic perspective, the intricate arrangement and bonding of two adjacent base pairs in the DNA (A, T, G, and C) is the most critical aspect for the stability of the DNA double helix. Therefore, the energy required to denature the DNA should be equal to or greater than those bonding energies holding the base pairs. In genetics, pyrimidine/purine (YR) and A: T rich regions are less exposed to the stacking energies due to double hydrogen bonding than the G: C rich region with triple hydrogen bonds. Therefore, the TATATA sequence will melt readily once the reaction is heated to the denaturation temperature. Denaturation or melting is modifying the molecular structure of the DNA by breaking the weakening linkages of the DNA. The application of heat to the DNA sample increases the system's kinetic energy and entropy, leading to transitional and rotational movements between the DNA helix causing a collision of the atoms and molecules with one another in the DNA. These collisions reduce the strength of the hydrogen bonds, which eventually break, allowing a double-stranded DNA helix to unwind into two single strands [3].

The initial denaturation step usually occurs at 94 °C to 98 °C for each amplification cycle depending on the optimal temperature for *Taq* DNA polymerase activity and the G-C content of the template DNA used in the reaction. The denaturation temperature in a PCR assay is usually set at 95 °C, regardless of the characteristics of the DNA template. Therefore, the denaturation temperature may only vary the duration of the denaturation step instead of the temperature. Hence, *Taq* DNA polymerase gradually inactivates under these conditions, and its half-life will be reduced from 130 min at 92.5 °C to 40 min 95 °C [4]. As the amplified product serves as a template in subsequent cycles, the Taq DNA polymerase activity might be limited later. Moreover, some templates of double-stranded DNA wind during a typical denaturation stage, while others will not unwind easily (e.g., DNA templates of mammalian promoter GC-rich sequences are complicated to denature initially). Increasing the temperature of the denaturation step by more than 95 °C can assist in enhancing denaturation, which may lead to better yield. However, biomolecules in PCR reactions are stressed when the denaturation temperature is excessively high. Polymerases' half-times will decrease by a factor of 3–9 between 95 °C and 100 °C, depending on enzyme type [5]. Hence, DNA polymerase activity could be improved by the judicious use of lower denaturation temperatures.

Nanomaterial-assisted PCR technology has emerged to solve this problem by incorporating nanomaterials with excellent thermal conductivity into a PCR reaction [6]. This leads to enhanced DNA denaturation and ultimately improves the PCR yield, as many researchers have studied in the past two decades [7]. In addition, some studies have proven the theory that by using nanoparticles as an additive, the DNA denaturation process starts eventually at temperatures due to the excellent heat transfer property of the nanoparticles used in the PCR reaction [8]. For instance, graphene nanoflakes helped better heat dissipation, leading to enhanced DNA denaturation during the first PCR step [9]. Moreover, hexagonal boron nitride nanoparticles enhanced Acanthamoeba DNA yield at a lower denaturation temperature of 91.5 °C [10].

Two novel ternary hybrid nanoparticles (THNp) consisting of graphene oxide (GO) and reduced graphene oxides (rGO) were synthesized and characterized in a recent study [11]. They were coated with two other nanoparticles, silver (Ag) and titanium dioxide (TiO_2). The potential use of $GO-TiO_2-Ag$ and $rGO-TiO_2-Ag$ THNps as PCR enhancer additives is primarily discussed in this study. The primary target is the first step in the PCR reaction (DNA denaturation step). The use of $GO-TiO_2-Ag$ and $rGO-TiO_2-Ag$ nanoparticles is expected to lower the denaturation temperature template DNA; this could help to get improved PCR yield of product, hence enables amplification to be performed for longer cycles. THNp of five different concentrations to two different concentrations of DNA were used. The samples are investigated in a temperature-controlled spectrophotometer to check the absorbance of DNA with THNp at different concentrations.

2. MATERIALS AND METHODOLOGY

2.1 Synthesis of THNp

The hydrothermal method was used to synthesize THNps as described in our previous study [11]. Graphene oxide (GO) was dispersed in deionized water at 1 mg/mL concentration using an ultrasonic stirring treatment for about two hours. A 10 mL by volume of Titanium isopropoxide was mixed with 10 mL of isopropyl alcohol, and then the solution was added dropwise to 50 mL of GO suspension. Next, 10 mL of 0.2 M $AgNO_3$ was added dropwise to the solution. The solution was stirred for two hours to ensure complete mixing and homogeneity. The pH of the solution was adjusted to 1.1, and then it was heated at 160 °C for 24 hours using a stainless steel autoclave lined with Teflon. The product was washed with ethanol and then with water to remove all the remnants and unreacted ions and finally filtered. The resultant residue ($GO-TiO_2-Ag$ nanocomposites) was dried at 80 °C. $rGO-TiO_2-Ag$ THNps was synthesized with the same procedure; however, ammonia and hydrazine were added to GO suspension to remove oxygen molecules from GO sheets and their functional groups. The characterization of THNp is described in our previous study [11].

2.2 Preparation of THNp-based Nanofluids

$GO-TiO_2-Ag$ THNp were weighted using Sartorius Entris® balance and then dispersed in molecular biology-grade sterile/DI water to make the final stock solution concentration of 5×10^{-2} wt % (Sample A). Next, the THNps were dispersed in DDH_2O and then sonicated using ultrasound probe sonication for 2 min, followed by water bath sonication for about 4 hours to obtain a homogenous solution of nanofluids without sedimentation. The stock solution was then serially diluted for about four more concentrations, named Concentration B(5×10^{-3})wt%, C(5×0^{-4})wt%, D(5×10^{-5})wt%, and E(5×10^{-6})wt%. $rGO-TiO_2-Ag$ nanofluid was prepared in the same way.

2.3 DNA Isolation

A salmon fish tissue sample was used as a template in this study. Genomic DNA was extracted and purified using DNeasy Blood & Tissue Kit (Qiagen, Hilden, Germany) following the manufacturer's protocol. Template concentration was ascertained using Thermo Qubit 3.0 Fluorometer, and it was found to be 11.5 ng/μL and 6.5 ng/μL (A and B resp.) and stored at 4 °C for further use.

2.4 Evaluation of DNA Denaturation by UV Spectroscopy

Perkin Elmer UV spectrophotometer was used to measure the absorbance of samples at 200-400 nm. The thermal denaturation experiments were carried out using two DNA concentrations, named A (6.5 ng/μL) and B (11.5 ng/μL) in the presence and absence of the synthesized graphene-based ternary hybrid nanofluids (GO-TiO$_2$-Ag and rGO-TiO$_2$-Ag) to determine the effect of nanoparticles on the early DNA denaturation. Five levels of concentrations, A(5×10^{-2})wt%, B(5×10^{-3})wt%, C(5×10^{-4})wt%, D(5×10^{-5})wt% and E(5×10^{-6})wt% were tested. The measurements were performed by mixing DNA samples with the nanofluid at the ratio of 5:2 and then filled in a clean 5 mm spectrometer quartz Cuvette cell. The absorbance was measured at various temperature ranges starting at 80 °C, with 2 °C increments, till 96 °C using the Peltier system.

3. RESULTS AND DISCUSSION

3.1 Effects of THNps on DNA Denaturation

The novel GO-TiO$_2$-Ag and rGO-TiO$_2$-Ag ternary hybrid nanoparticles exhibited a superior enhancement of PCR and led to a 28.5% reduction of total cycles and enhanced the PCR yield 16.89-folds for GO-TiO$_2$-Ag and 15.75-folds for rGO-TiO$_2$-Ag, compared to control in our earlier study [refer PCR manuscript]. In this study, the same ternary hybrid nanoparticles were added to two DNA samples (samples A and B), and the absorbance is measured using a spectrophotometer. The absorbance (at 260 nm) of two DNA samples (A:6.5 and B:11.5 ng/μL) with and without the synthesized graphene-based ternary hybrid nanofluids) at five concentration levels at various temperatures were measured as shown in Fig 1. The absorbance of the DNA in the presence of THNp can give us a deeper insight into the behavior of DNA during the denaturation step. GO-TiO$_2$-Ag and rGO-TiO$_2$-Ag THNp exhibited higher absorbance values than the control (without nanoparticles) over the measured temperature range (from 80 °C to 96 °C) in two different DNA samples A and B with concentration, indicating early denaturation of DNA even at temperatures as low as 80 °C.

Interestingly, the concentration of nanoparticles has an impact on the extent of DNA denaturation. A more significant denaturation was exerted with the higher concentration of these nanoparticles than the lower one at all studied temperatures (Fig. 1). When comparing the DNA samples containing the nanoparticles, rGO-TiO$_2$-Ag nanoparticles were significantly more effective than GO-TiO$_2$-Ag THNp at higher concentrations (5×10^{-2}) wt%. The absorbance of the DNA samples containing 5×10^{-2} wt% GO-TiO$_2$-Ag nanoparticles was ~86- and ~2-folds higher than the control DNA samples at 80°C, for DNA samples A and B, respectively, while the absorption in the presence of rGO-TiO$_2$-Ag nanoparticles was ~180- and ~7-folds higher than the control in DNA samples A and B, respectively. Moreover, DNA was denatured earlier in the presence of rGO-TiO$_2$-Ag nanoparticles at a concentration higher than C (5×10^{-4})wt%. At the same time, it was still earlier denatured in the presence of GO-TiO$_2$-Ag even at a concentration as low as E (5×10^{-6}) wt%. These results

indicate the importance of an optimal nanoparticle concentration for the maximal heat transfer effect.

The earlier denaturation of the DNA in the presence of the THNps could be due to the enhanced thermal conductivity of nanoparticles. The denaturation of double-stranded DNA typically happens if the temperature exceeds 90 °C. As the kinetic energy and entropy of the reaction system increase, the transitional and rotational motions, which causes a collision of the atoms and molecules of the reagents, increase. These collisions reduce the strength of the hydrogen bonds, which eventually breaks, allowing a double-stranded DNA helix to unwind into two single strands [12]. Thus, the presence of nanoparticles enhances the DNA's denaturation due to the more excellent heat dissipation in the reaction mixture, which causes a collision of the atoms and molecules between nanoparticles, and PCR reagents [13]. Thus, these results are proof that DNA could be denatured earlier in the presence of THNps. Furthermore, the percentage of enhancement that we achieved is significantly higher than previously published reports.
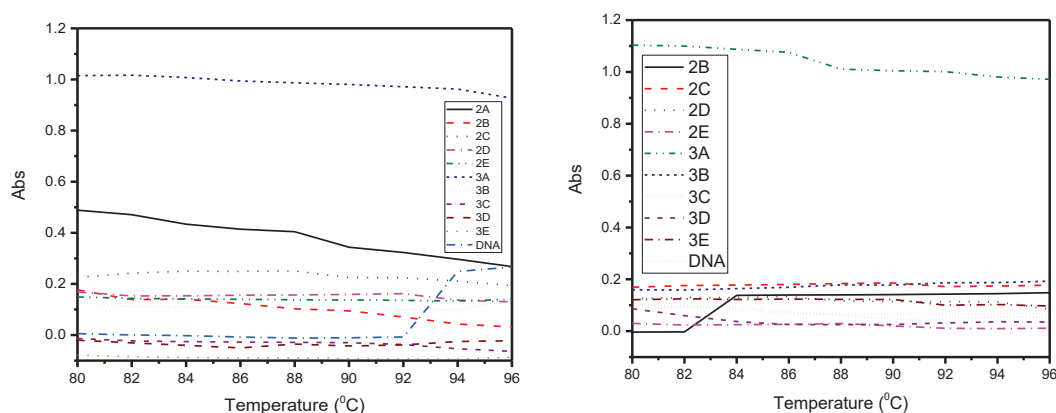

Fig. 1: Near UV absorption spectra (260 nm) of DNA in presence and absence of increasing concentration of GO-TiO$_2$-Ag and rGO-TiO$_2$-Ag (5×10^{-2} - 5×10^{-6} wt%) to determine the effect of nanoparticles on DNA denaturation. To the left, A (6.5 ng/µL), and to the right, B (11.5 ng/µL) DNA samples.

The absorption spectra for GO-TiO$_2$-Ag and rGO-TiO$_2$-Ag over 200 to 400 nm are presented side by side based on the concentration in Figs. 2 and 3. It can be seen from Fig 2, the strong absorption below 210 nm in the DNA spectrum, at all temperatures, resulted from absorptions of phosphate groups and sugar parts. The second maximum DNA absorption position was located at 260 nm due to DNA base absorption. DNA spectra had confirmed that the DNA was denatured at temperature 92-94 °C as all spectra absorption at temperature ≤92 °C were significantly lower than that observed for spectra at temperature ≥ 94 °C. Once the absorbance of UV light in the spectrophotometer has increased until it has completely melted or un-wound to two single strands, the denaturation can be determined. The absorbance will remain constant even if the temperature or heating is further increased. The hypochromic effect refers to the fact that single-strand DNA absorbs 50 percent more UV light than double-strand DNA before reaching the melting point. Renaturation is the reversible process of denaturation, which occurs when the temperature is lowered below the melting point. The renaturation time can be used to calculate the repetitive fractions as well as the base composition [14]. The melting point, or T$_m$, of different DNA will vary depending on various factors such as the length of the DNA strand, base composition, topological condition of DNA, buffer composition, etc. Compared to a longer strand of DNA, a shorter DNA strand will melt faster and more efficiently [15].

Because many variables influence the melting point of DNA, it is difficult to predict the exact melting temperature of a given DNA sequence.
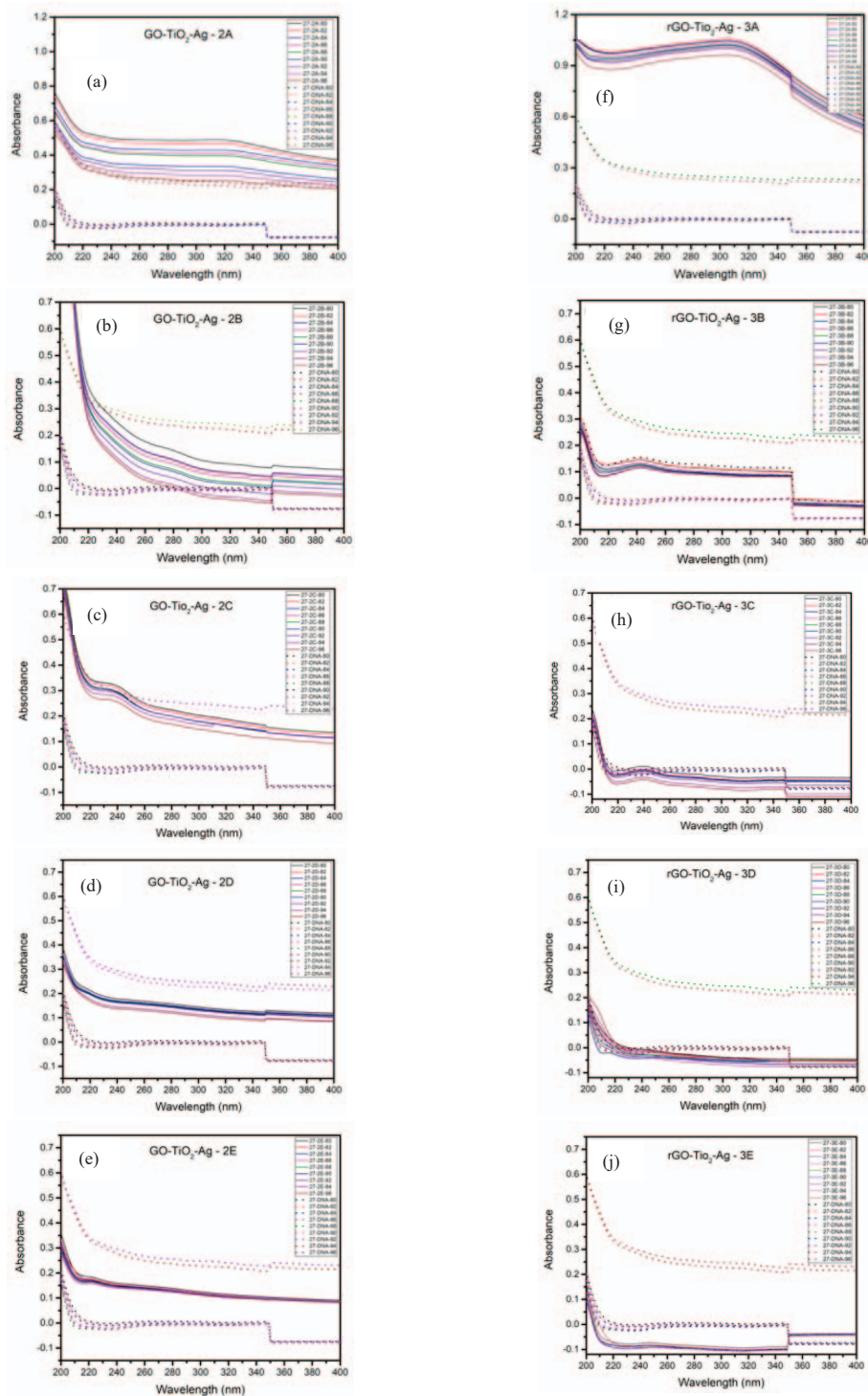

Fig. 2: (a), (b), (c), (d), and (e) are near UV absorption spectra of 6.5 ng/µL DNA in presence and absence of GO-TiO$_2$-Ag samples of concentrations A(5x10^{-2}) wt%, B(5x10^{-3}) wt%, C(5x10^{-4}) wt%, D(5x10^{-5}) wt% and E(5x10^{-6}) wt%, respectively; (f), (g), (h), (i) and (j) are near UV absorption spectra of 6.5 ng/µL DNA in presence and absence of rGO-TiO$_2$-Ag - samples of concentrations A(5x10^{-2}) wt%, B(5x10^{-3}) wt%, C(5x10^{-4}) wt%, D(5x10^{-5}) wt% and E(5x10^{-6}) wt%, respectively.
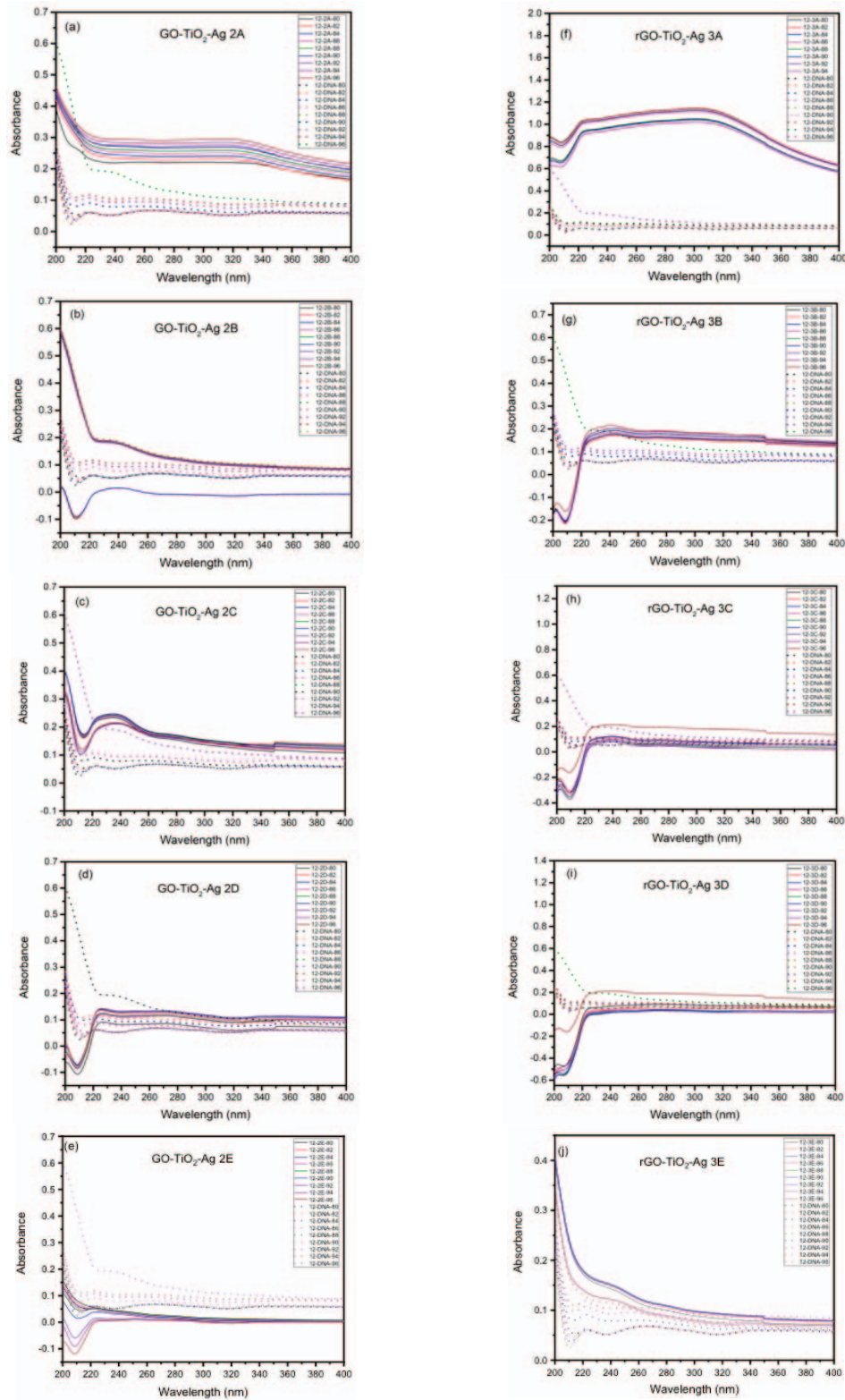
Fig. 3: (a), (b), (c), (d), and (e) are near UV absorption spectra of 11.5 ng/µL DNA in presence and absence of GO-TiO$_2$-Ag samples of concentrations A(5×10^{-2}) wt%, B(5×10^{-3}) wt%, C(5×10^{-4}) wt%, D(5×10^{-5}) wt% and E(5×10^{-6}) wt%, respectively; (f), (g), (h), (i), and (j) are near UV absorption spectra of 11.5 ng/µL DNA in presence and absence of rGO-TiO$_2$-Ag samples of concentrations A(5×10^{-2}) wt%, B(5×10^{-3}) wt%, C(5×10^{-4}) wt%, D(5×10^{-5}) wt% and E(5×10^{-6}) wt%, respectively.

The shift in the DNA absorption peak upon addition of GO-TiO$_2$-Ag reveals the interaction of the DNA–THNps. The significant absorbance increase observed upon the addition of various concentrations of GO-TiO$_2$-Ag at temperature $\leq$ 92 °C indicates that the GO-TiO$_2$-Ag THNps augmented the denaturation of the double-stranded DNA. However, and at a temperature $\geq$ 94° C, a higher DNA denaturation was exhibited with the presence of at least 5×10^{-2} wt% of GO-TiO$_2$-Ag THNps. Similar absorbance patterns can be seen for rGO-TiO$_2$-Ag THNps spectra at all study concentrations except at a concentration of 5×10^{-2} wt%; their absorbance was significantly higher than that of GO counterparts.

Additionally, rGO-TiO$_2$-Ag nanoparticles did not enhance the denaturation at concentration 5×10^{-3} wt% to 5×10^{-6} wt%, indicating the importance of an optimal nanoparticle concentration for the maximal heat transfer effect. A similar absorption pattern was observed for DNA samples A in the presence and absence of THNps; however, DNA absorption peak shift upon THNps addition was more prominent. The DNA denaturation was augmented at all concentrations of THNps except at 5×10^{-6} wt% and 5×10^{-5} wt% for GO-TiO$_2$-Ag and GO-TiO$_2$-Ag, respectively (Fig. 3). Moreover, there was a positive impact of GO-TiO$_2$-Ag THNps concentration on the denaturation. For instance, the absorption of the DNA samples containing 5×10^{-2} wt% and 5×10^{-5} wt% GO-TiO$_2$-Ag nanoparticles was 4.0-, 1.99-folds, respectively, higher than the control A DNA samples, and 54.64-, 20.57-folds, respectively, higher than the control B DNA samples, at 86 °C. Thus, decreasing the concentration of GO-TiO$_2$-Ag THNps in DNA samples, from 5×10^{-2} wt% to 5×10^{-5} wt%, decreased the absorption significantly by 50% and 38% for DNA samples A and B, respectively. On the other hand, reducing the concentration of rGO-TiO$_2$-Ag THNps in the DNA sample, from 5×10^{-2} wt% to 5×10^{-5} wt%, decreased the absorption by 3.4% for DNA samples A and B, respectively. Interestingly, at the lowest concentration of the THNp, their absorbance is negative, which indicates that the UV light passing through the DNA samples in the presence of THNp gives out a greater intensity of light. Therefore, it may have important significance.

4. CONCLUSION

The experiment has demonstrated the impact of adding the two novel ternary hybrid nanoparticles on DNA denaturation. The rationale behind the use of graphene based THNps is its unique heat transfer properties. DNA denaturation data showed that the enhancement of the DNA denaturation was nanoparticle concentration-dependent. The higher concentrations exhibit the maximum enhancement of the DNA denaturation owing to the enhanced thermal conductivity effect. rGO based THNp showed better results at higher concentrations compared to GO-based THNp. We propose THNp can be effectively used to achieve early denaturation of DNA samples.

ACKNOWLEDGEMENTS

REFERENCES

[1]   Fu-Ming SANG, Xin LI, Jia LIU. (2017) Development of nano-polymerase chain reaction and its application. Chinese Journal of Analytical Chemistry, 45(11): 1745-1753.

[2]   Lorenz TC. (2012) Polymerase chain reaction: Basic protocol plus troubleshooting and optimization strategies. JoVE (Journal of Visualized Experiments), 63: e3998.

[3]   Ussery DW. (2013) DNA Denaturation, Brenner's Encycl. Genet. Second Ed., pp. 353-355.

[4]   Shen C, Yang W, Ji Q, Maki H, Dong A, Zhang Z. (2009) NanoPCR observation: Different levels of DNA replication fidelity in nanoparticle-enhanced polymerase chain reactions. Nanotechnology, 20(45): 455103.

[5]   Cazzaniga G, Songia S, Biondi A. (2021) PCR Technology to Identify Minimal Residual Disease. In Leukemia Stem Cells (pp. 77-94). Humana, New York, NY.

[6]   Gabriel S, Rasheed AK, Siddiqui R, Appaturi JN, Fen LB, Khan NA. (2018) Development of nanoparticle-assisted PCR assay in the rapid detection of brain-eating amoebae. Parasitology research, 117(6): 1801-1811.

[7]   Lin YC, Wu HL. (2007) Nano-PCR: Breaking the bottom limit of the PCR denaturation temperature using nanogold. In TRANSDUCERS 2007. IEEE International Solid-State Sensors, Actuators and Microsystems Conference, pp. 391-394.

[8]   Khaliq A, Sonawane PJ, Sasi BK, Sahu BS, Pradeep T, Das SK, Mahapatra NR. (2010) Enhancement in the efficiency of polymerase chain reaction by TiO_2 nanoparticles: crucial role of enhanced thermal conductivity. Nanotechnology, 21(25): 255704.

[9]   Khaliq A, Kafafy R, Salleh HM, Faris WF. (2012) Enhancing the efficiency of polymerase chain reaction using graphene nanoflakes. Nanotechnology, 23(45) 455106.

[10] Rasheed AK, Siddiqui R, Ahmed SMK, Gabriel S, Jalal MZ, John A, Khan NA. (2020) hBN nanoparticle-assisted rapid thermal cycling for the detection of Acanthamoeba. Pathogens, 9(10): 824.

[11] Zayan M, Rasheed AK, John A, Muniandi S, Faris A. (2021) Synthesis and Characterization of Novel Ternary Hybrid Nanoparticles as Thermal Additives in H_2O. ChemRxiv. doi:10.26434/chemrxiv.13710130.v1

[12] Abbotts R, Wilson DM. (2017) 3rd. Coordination of DNA single strand break repair. Free Radic Biol Med., 107: 228-244. doi: 10.1016/j.freeradbiomed.2016.11.039.

[13] Li A, Zhou B, Alves CS, Xu B, Guo R, Shi X, Cao X. (2016) Mechanistic studies of enhanced PCR using PEGylated PEI-entrapped gold nanoparticles. ACS Applied Materials & Interfaces, 8(39): 25808-25817.

[14] Lee JY, Lim HW, Yoo SI, Zhang BT, Park TH. (2006) Simulation and real-time monitoring of polymerase chain reaction for its higher efficiency. Biochemical Engineering Journal, 29(1-2): 109-118.

[15] Bai Y, Cui Y, Paoli GC, Shi C, Wang D, Shi X. (2015) Nanoparticles affect PCR primarily via surface interactions with PCR components: using amino-modified silica-coated magnetic nanoparticles as a main model. ACS Applied Materials & Interfaces, 7(24): 13142-13153.

VIRTUAL PROTOTYPE-BASED KINEMATIC MODELING AND SIMULATION OF A MULTI-MODE AMPHIBIOUS ROBOT

**Mohammed Rafeeq[1], Siti Fauziah Toha[1]*,
Salmiah Ahmad[2] and Mohd Asyraf Mohd Razib[1]**

[1]Department of Mechatronics Engineering,
[2]Department of Mechanical Engineering,
Faculty of Engineering, International Islamic University Malaysia,
Jalan Gombak, 53100 Kuala Lumpur, Malaysia.

*Corresponding author: tsfauziah@iium.edu.my

ABSTRACT: The amphibious robot, which has the capability of multi-mode motion, can maneuver diverse environments with high mobility and adaptability. These are employed in the area of reconnaissance, search and rescue operations, and monitoring. The existing amphibious robots have lower maneuverability over the crawling period on uneven and slope surfaces on the land. In this paper, a kinematic model of the amphibious robot based on virtual prototyping is designed for multi-mode locomotion. ADAMS (Automated dynamic analysis of mechanical systems) is a multi-body dynamic solver adopted to build the simulation model for the robot. The novel amphibious robot employs a Rockerbogie mechanism equipped with wheel paddles. The locomotion analysis on land involves straight-going and obstacle negotiation, which is simulated using ADAMS. The simulation analysis result demonstrates increased maneuverability, achieving a robot's velocity of 1.6 m/s. Normal forces on the front and rear wheels show equal load distribution, contributing more to the robot's equilibrium over uneven terrain. The simulation result reflects the accurate kinematic characteristics of the amphibious robot and provides a theoretical basis for developing an algorithm for robot motion control and optimization. Further, this research will concentrate on the kinematic simulation maneuvering in water mode with the wheel paddle.

ABSTRAK: Robot amfibia yang memiliki berbilang mod pergerakan, dapat bergerak dalam persekitaran berbeza dengan ketinggian mobiliti dan adaptasi. Kebolehan ini dapat digunakan dalam kawasan pengintipan, operasi pencarian dan menyelamat, dan peninjauan. Robot amfibia sedia ada mempunyai kurang kebolehgerakan sepanjang tempoh merangkak pada permukaan cerun dan permukaan tidak rata pada tanah. Dalam kajian ini, model kinematik robot amfibia berdasarkan prototaip maya dibentuk berdasarkan gerak alih pelbagai mod. Sistem Mekanikal Analisis Dinamik Automatik (ADAMS) adalah penyelesai dinamik berbilang badan telah diadaptasi bagi membina model simulasi robot. Robot amfibia baru dicipta berdasarkan mekanisme Rockerbogie beserta padel tayar. Analisis gerak alih atas tanah ini termasuk gerakan-lurus dan rundingan halangan, disimulasi menggunakan ADAMS. Dapatan simulasi kajian menunjukkan peningkatan kebolehgerakan, mencapai halaju robot sehingga 1.6 m/s. Daya tujahan normal pada depan dan belakang tayar menunjukkan keseimbangan agihan beban, menyumbang lebih kepada keseimbangan robot ke atas permukaan yang tidak rata. Dapatan kajian dari simulasi menunjukkan ciri-ciri kinematik yang tepat pada robot amfibia dan menyediakan teori asas bagi membangunkan algoritma kawalan pergerakan

dan pengoptimuman. Seterusnya, kajian ini mengfokuskan simulasi gerakan kinematik dalam mod air beserta padel tayar.

KEYWORDS: *amphibious robot; kinematic modeling; virtual prototype; ADAMS*

1. INTRODUCTION

Nature inspires to develop locomotion systems that exhibit functionality and performance close to the locomotion of animals [1]. Amphibians encourage developing locomotion strategies since they have excellent locomotion features in the terrestrial and aquatic environments. They smoothly transit between these mediums by simply alternating body mechanisms to adapt to the environment. The terrestrial and aquatic locomotion environment like near-shore, shallow waters demand high mobility and adaptability because of diverse terrain profiles such as sand, wetlands, rocks, uneven surfaces, and varying obstacles to overcome for complete maneuvering. Locomotion metrics like mobility and adaptability in these environments are excellent characteristics of amphibious animals [2].

Amphibious robotics has shown advancement in the past two decades; however, the research focuses on developing the propulsive mechanisms of robots to improve mobility performance in the aquatic medium. The research work in the past focused on bio-mimic swimming characteristics to enhance performance in water. However, these amphibious robots' practical applications demand more capabilities on the land environment, including high terrain adaptability and speed on land, thrust performances, and heading control in the aquatic environment. Consequently, maneuvering ability in these robots needs to focus on driving mechanisms and control performance on both land and water.

Amphibious locomotion of snakes utilizes the undulation of their bodies for propulsion and motion on water and land [3]. The locomotion strategies developed to achieve amphibious locomotion are inspired by legged amphibians like water runners and basilisk lizards [4]. The hybrid mechanism combining leg and wheel is adopted in the whegs robot for terrestrial and underwater locomotion. Whegs series use propellers for underwater locomotion and wheel-leg for locomotion on irregular terrain. The amphibious spherical robot by Guo. et al. mimics turtles' legged locomotion on ground and uses waterjet thrusters for generating thrust in underwater environments [5]. The locomotion performance of amphibious robots reported in the literature is suitable for a smooth land environment with lower speed performance in the water. The hybrid mechanisms achieve improved mobility but at the cost of complex control design. An amphibious robot with a single design is proposed with compact control design. The present amphibious robot is suitable for smooth land surfaces, and legged amphibious robots have lower propulsive speed. There is a need for an amphibious robot with higher mobility capable of traversing uneven land.

Traditionally, researchers utilize experimental methods to validate the mechanical design structure. The experimental work is close to the real environment; however, it involves cost and time. The virtual prototyping validates the kinematic characterization of the model to achieve optimal performance before developing the actual prototype [6]. Lin et al. [7] utilizes a virtual prototyping robot to obtain kinematic parameters and validate the model using ADAMS for dynamic analysis of an amphibious spherical robot. Zong et al. [8] study the locomotion performance of amphibious robots using a virtual prototype created in ADAMS. The kinematic simulations validate transformable flipper leg performance on complex terrain and underwater environment. Zhuang et al. [9] propose a hydraulic-driven quadruped amphibious robot leg movement analysis using ADAMS that facilitates gait

selection of quadruped amphibious robots to crawl on uneven terrain. Virtual prototyping of the model aims to achieve optimal performance before developing the actual prototype and facilitates the iterative process to verify the complete model at early stages, reducing the time and cost of development.

Dynamic and kinematic analysis of the rocker-bogie based mechanism in ADAMS is performed to study the working principle of an amphibious robot. Cao et al. [10] illustrate the modeling process of simple linkage mechanisms like gear and a cam performed in an ADAMS environment. Virtual prototyping has become a common tool to analyze the performance of models before they are physically developed. The virtual prototype provides a vital steppingstone for the design optimization of the model. The virtual prototype tool gives the kinematical analysis capability of an amphibious robot, dynamic characteristics, structural parametric study, and static analysis. The robot's complete motion performance analysis is possible by virtual prototyping simulations before physical prototype development. The simulation analysis is also the basis for motor selection and other electronics [11].

To achieve amphibious locomotion in complex environmental conditions, mobility (velocity of robot vehicle on ground and thrust in water) and adaptability in these environments (obstacle negotiating and climbing capability on uneven terrain) are two important performance metrics analyzed in the literature. Mobility of some amphibious robots is discussed. For example, ACM is a snake-inspired amphibious robot that uses a modular design that can propel itself at 0.4m/s. Salamander amphibious robot achieves 0.42 m/s on land 0.28 m/s on water using body undulation and limb design. Turtle robot design uses a spherical body and four legs for motion, achieving a crawling velocity of 22.5 cm/s and surge velocity of 16.5 cm/s. Amphirobot -III uses a modular body design with a wheel propeller fin mechanism giving the speed of 0.59 m/s. Amphihex-I robot uses a flipper leg design that has higher adaptability with a speed performance of 0.2 m/s. The mobility of present amphibious robots is lower and suitable for smooth land surfaces.

Kinematic modeling enables development and verification of the model. The implemented kinematic modeling is divided into two methods- one related to the geometric approach [12,13] and the other concerning the transformation approach. A general approach to kinematic modelling of articulated robots traversing uneven terrain was developed by Tarokh et al. [14]. In this paper, the kinematics modelling of a six-wheel rocker-bogie mobile robot based on the above literature is deduced. The kinematics model will be helpful and fundamental to subsequent studies on the mobile robot's trajectory tracking and motion control [15].

A novel wheel leg hybrid-based amphibious robot with an integrated rocker-bogie wheel paddle mechanism is introduced in this paper to negotiate obstacles on uneven terrain exploiting the legs of the robot and high-speed mobility using wheels attached to legs. The amphibious robot with a rocker-bogie mechanism can maneuver over uneven terrain on land and achieve efficient propulsive maneuvering on the water with a wheel paddle mechanism. The amphibious robot can locomote a single design of multimodal locomotion on multiple terrains of land and water. The unified mechanical design gives the capability of compact control design.

2. KINEMATIC ANALYSIS OF MODEL

Amphibious robots require good propulsive performance on both land and water. In the past literature, amphibious robots were proposed keeping in mind a low demand of terrain

complexity on the land environment. However, a real environment is uneven, demanding maneuvering on complex terrain profiles. The amphibious robot employs either legged, tracked, wheeled, spherical or hybrid mechanisms for propulsion. A legged robot is suitable and adaptable on complex terrains but at the cost of control and lower speed [16]. Wheeled robots are best suited to flat ground surfaces, maneuvering at high speed [17]. However, they are less flexible as compared to legged over uneven terrain. Wheeled robots with passive suspension mechanisms increase adaptability on complex terrain and achieve higher obstacle negotiation capability. Rocker-bogie mechanisms with a passive suspension mechanism with a wheel paddle fin represent a hybrid mechanism for amphibious operation. The hybrid mechanism on land is a wheel-driven mobile robot with passive suspension. The wheel-driven mechanism increases the motion speed and passive suspension increases the adaptability on uneven terrain, thus increasing overall propulsive performance on land.

The general view of the virtual prototype of the amphibious robot is shown in Fig. 1. The amphibious robot virtual prototype consists of two major parts, the rocker-bogie mechanism, and the wheel paddle mechanism. The rocker-bogie mechanism has passive suspension [15].

The mechanism has a single rocker attached to the body by a pivot joint. A differential joint appends the rocker and the bogie. The two rockers and bogies are attached on each side of the chassis (main base). The wheel paddle mechanism is a combination wheel design with paddles on the outer surface of the wheel. The wheel's rotation is utilized for locomotion on land, and the same wheel with paddles is used as propulsion in water.

2.1 Kinematic Modeling

The amphibious robot's main body consists of a rocker-bogie mechanism with six wheels driven by individual actuators. The rocker-bogie is a passive suspension mechanism utilized to adapt to uneven terrain and obstacle negotiation. The rocker-bogie mechanism comprises a rocker attached at the front and two bogies attached to a rocker at the rear end.
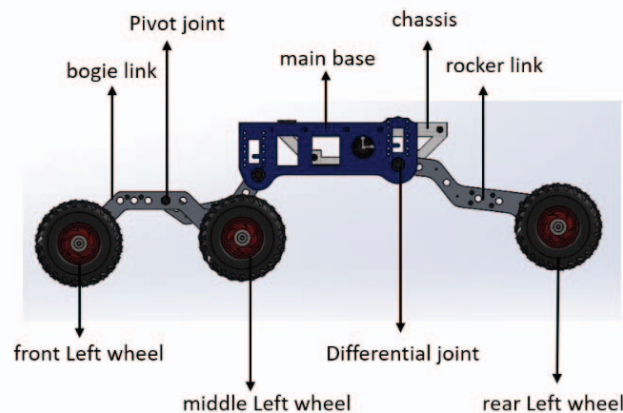

Fig. 1: General view of amphibious robot.

The wheels are attached to the rocker and bogie with joints. The joints are attached with bearings. Solidworks software is utilized to accomplish design indices and carry out the assembly process of the robot body, including the rocker-bogie mechanism and wheels. The ADAMS software accepts geometric position relationships in Parasolid format. Solidworks exports the model in the required format. However, this process loses model features like material, mass information, and mechanisms due to the constrained relationship.
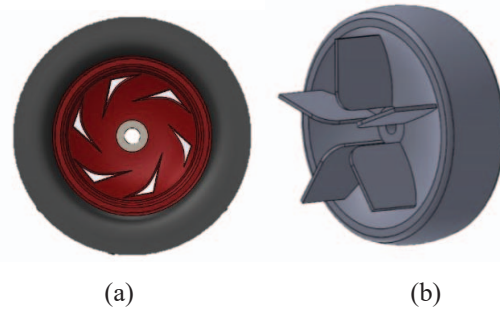
(a)   (b)

Fig. 2: (a) Tire, (b) Wheel paddle.

Additionally, the robot assembly has a large set of parts; the model is highly complex. The model in ADAMS adopts Boolean operation that minimizes the independent parts quantity and retains only the main parts (geometry, mass information) and joints appended to main parts [16]. Figure 2 shows the tire used in the kinematic simulation of the amphibious robot. The amphibious locomotion on the water is achieved using a wheel paddle design. Table 1 and Table 2 detail amphibious robot model specifications.

Kinematic analysis of an amphibious robot on land is considered for simplicity. According to the kinematic theorem, the velocity relationship of wheel locomotion may be described as follows. Eq. (1) and Eq. (2) represent the linear velocity of the left and right wheel, respectively. The velocity relationship is related to the radius of the wheel r and angular velocity of the wheel w_L. The angular velocity of each wheel is related by revolutions of each wheel n_L or n_R. Eq. (3)- Eq. (5) represents the wheel velocities while turning the wheel, where w is the identical turning angular velocity of the wheel.

$$V_L = r.w_L = r.\frac{2\pi n_L}{360} \tag{1}$$

$$V_R = r.w_R = r.\frac{2\pi n_R}{360} \tag{2}$$

$$V_L = w.\left(R \pm \frac{d}{2}\right) \tag{3}$$

$$V_R = w.\left(R \mp \frac{d}{2}\right) \tag{4}$$

$$n = \frac{n_L}{n_R} = \frac{R - \frac{d}{2}}{R + \frac{d}{2}} \tag{5}$$

Table 1: Amphibious robot mechanical structure specification

Structural part	Weight (kg)	Dimensions (mm)
Main base	1.135	240 x 156 x 60
Rocker link	1.410	267 x 96 x 36
Bogie	2.634	256 x 87 x 36
Rocker top	1.022	255 x 105 x 56
Tire/Wheel paddle		120 x 60

The study of kinematics modeling and simulation of amphibious robots is the basis of robot development and optimization. The kinematic analysis verifies the motion model of the moving robot by overcoming the obstacles without tipping or flipping over the terrain profile for the simulation period with the given constraints of the mechanism. The rationality of the kinematics model of the moving robot is verified by analysis of displacement and velocity curves. Designers adopted the ADAMS software to build the simulation model of the robot [21]. The robot's kinematics curve was obtained through the kinematics simulation of linear driving and pivot steering performance. This robots' mechanism design verifies the correctness of the kinematic model.

2.2 Modeling Environment

The modeling environment adopted for virtual prototyping is a widely used dynamic modeling and simulation software ADAMS; the environment facilitates the analysis of dynamic systems. The amphibious robot locomotion speed and drive forces on the wheel-driven mechanism can be obtained using the simulation approach based on ADAMS. However, ADAMS has limitations in modeling complex design structures in the spatial domain. Therefore, a 3D designing environment like Solidworks is employed with Parasolid as a base to design solid parts and assemblies. The Parasolid design is exported in ADAMS for motion analysis.

Table 2: Robot model specifications

Vehicle load	8 kg (78.4 N)
Wheel specification	
- Width	0.06 m
- Radius	0.06 m
- circumference	0.377 m
Motor Torque, M_T	0.7848 Nm

Therefore, by combining the powerful three-dimensional solid modeling functionality of Solidworks with the accurate movement simulation performance in ADAMS through a common data exchange interface [19], the kinematic simulation environment can be established. Then the relationship between structural parameters and propulsive speed can be analyzed, aiming to offer some reference for the optimization design of the propulsive mechanism and motion control.

This work acts as a reference for the optimal design of motion control and the propulsive mechanism by analyzing the structural parameters of the rocker and bogie link lengths, pivot and differential joint angles, rocker and bogie height to wheel center, angle of inclination with respect to ground, and maneuvering speed of the amphibious robot. The analysis is possible by exploiting the excellent three-dimensional modeling capability in CAD software like Solidworks and motion simulation and a common data exchange interface [20-22].

3. RESULTS AND DISCUSSION OF KINEMATIC SIMULATION BASED ON ADAMS

3.1 Straight Going Path

To verify the robot model, it is required to validate the motion stability of the robot. The simulation of the model on land aimed at robot locomotion over the surface along the planned trajectory and tested for stability and heading to reach the target. The rocker-bogie integrated wheel paddle mechanism is designed considering the uneven terrain profile and obstacle negotiation capability. The robot's stability is studied by observing the variation of the center of mass of the robot structure along the horizontal X-axis direction. Figure 4 shows the oscillations are smooth on flat terrain profile and encounter sharp changes when the model encounters the obstacle and steady state after the robot passes over the obstacle stabilizing the overall model. Figure 4 shows center-of-mass variation is lower than the robot head height, confirming the stability of the model. The robot vehicle is stable when it is in a quasi-static state in which it does not tilt over, as the asymmetric suspension system of the passively articulated vehicle has a significant influence on the vehicle's effective stability [23]. The computation of the longitudinal stability of the rover makes use of a statical model as it is not symmetric in the longitudinal direction. In a statical model, the mechanical properties of the suspension system are considered. According to [24], the longitudinal stability of the vehicle is given when all wheels have ground contact, and the condition $N_i > 0$ is satisfied, where N_i is the normal force at the wheel i. It should be noted that even though this condition is compulsory for the statical model to work, a physical robot vehicle does not necessarily tip if a wheel loses contact with the ground.

The velocity of the robot vehicle, as in Fig. 4 in the longitudinal direction, achieves 1.6 m/s, which is higher than similar amphibious robots reported in literature like wheg series [5], RHex and ASGAURD [25,26], wheel leg propeller [27] and aqua robot [16]. However, it is less than the max speed of the seadog amphibious robot [28] of 2.23 m/s, but mobility on the water of the seadog decreases due to the use of the simple non-holonomic wheels as paddle wheels. The peripheral of the wheel is further encased with adhesive material to reduce the fluctuations affecting other parts and system components. The simulation analysis result demonstrates increased maneuverability, achieving a robot's velocity of 1.6 m/s, verifying the theoretical value obtained from Eq. (1) and Eq. (6).

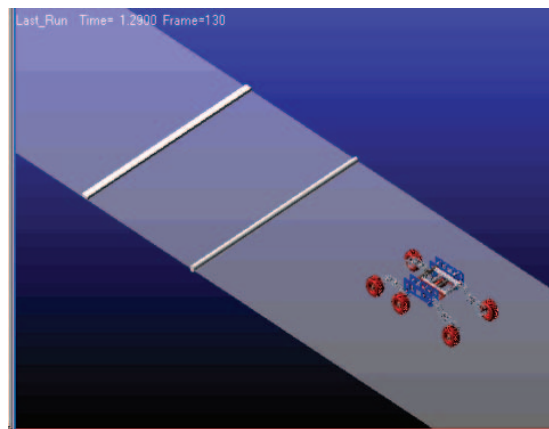$$V_L = r.w_L = r.\frac{2\pi n_L}{360} = 0.06 \cdot \frac{2\pi}{60} 255rpm \ = 1.6 \, m/s \tag{6}$$
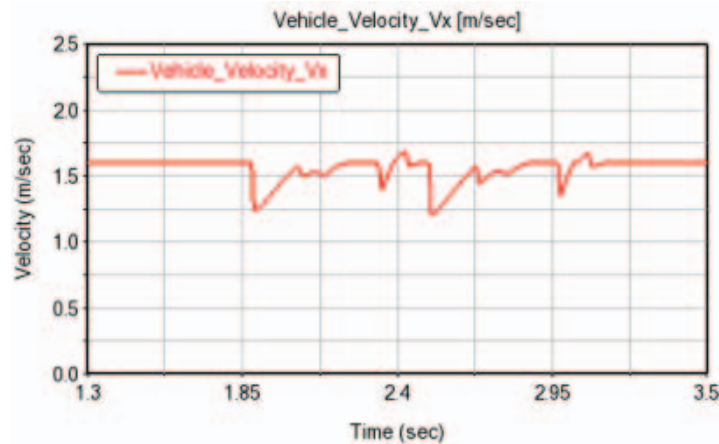

Fig. 3: Terrain profile.

Fig. 4: Velocity of robot in the X direction.

3.2 Obstacle Negotiation of the Amphibious Robot

The terrain profile to test the obstacle negotiation capability of the robot is chosen with different shapes and heights. The obstacle's height should be less than the diameter of the wheel for stability or it will flip over the robot. The obstacle negotiation determines the climbing capacity of the robot. The obstacle shape chosen for simulation is a rigid rectangular block with a height of 20 mm and a width of 50 mm, as shown in Figure 5. The load on each wheel for equilibrium studies using wheel terrain contact forces is discussed in section 3.2.1. The other obstacle chosen is hemispherical with a radial height of 20 mm; these obstacle negotiations exhibit the slip conditions of the robot. Figures 4 and 6 show the velocity and normal forces of all the wheels successfully negotiating at the obstacles of the chosen terrain profile.
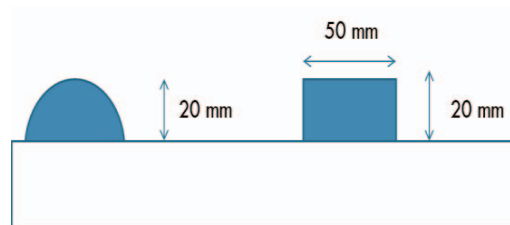

Fig. 5: Obstacle profile.

3.2.1 Wheel Terrain Contact Forces

The mobile robot locomotion on uneven terrain profiles requires a closer look to critically understand the capability of the robot overcoming obstacles completing the trajectory. The wheel ground contact forces analysis facilitates the study of locomotion on uneven terrain profiles. Figure 6 demonstrates the normal forces of the front left tire 1(front wheel), front left tire 2 (middle wheel), and the rear left tire (rear wheel) have equal loading on all wheels up to 1.9 sec because of smooth flat surface. At 1.9 sec, as soon as the left front tire 1(front wheel) touches the hemispherical obstacle, the load is distributed to the middle and rear wheel. The rear wheel is loaded max with a normal force of 29 N at 2.3 sec when both the wheels(bogie) are passed over the hemispherical obstacle. Figure 6 shows the middle wheel peak of normal force at 2.75 sec, indicating the middle wheel is entirely at the top of the 50mm rectangular block. At 2.25 sec, the rear wheel crosses the rectangular block followed by equal forces on all the wheels over the flat smooth surface locomotion at the trajectory completion stage.
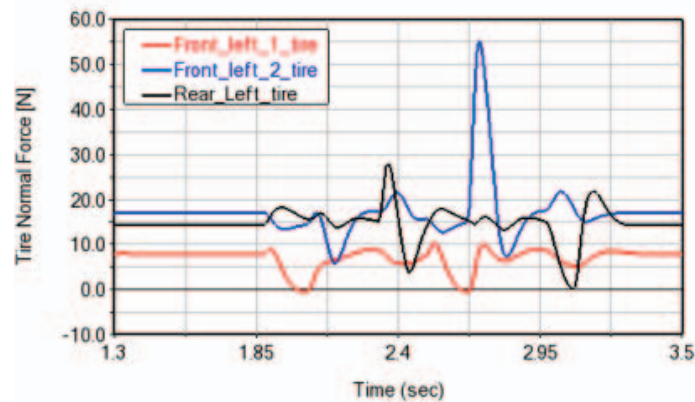
Fig. 6: Normal forces on wheels.

4. CONCLUSION

A novel wheel leg hybrid-based amphibious robot with an integrated rocker-bogie wheel paddle mechanism is introduced in this paper to negotiate obstacles on uneven terrain exploiting the legs of the robot and high-speed mobility using wheels. The existing amphibious robots in the literature [2] have minimal suspension suitable only for flat terrain profiles. However, the suspension is achieved through a legged robot with lower speed and mobility performance on both land and water. The analysis proves that the propulsive principle and feature of the wheel paddle mechanism enable efficient locomotion on land and water. The robot is capable of multimodal locomotion on uneven terrain on terrestrial and aquatic mediums. The simulation in the ADAMS environment provides a basis for the kinematic validation of the model. The kinematic simulation in ADAMS of the virtual prototype amphibious robot measures the speed, angular torque, and velocities of the integrated mechanism.

In this kinematic simulation, the capabilities on a smooth and uneven surface on land are achieved. The capabilities include straight going on a flat surface, and obstacle negotiations over the obstacles of various heights and shapes that are selected for performance evaluation of the model.

In the future, the experiment will be carried out on benchmark terrain profiles considering different height obstacle negotiations for the robot to locomote on land. Furthermore, kinematic simulation using the wheel paddle on the water will be tested. The control capability for the amphibious robot can be carried out using the co-simulation capability of ADAMS and Matlab/Simulink Environment.

ACKNOWLEDMENT

REFERENCES

[1] Karakasiliotis K, Thandiackal R, Melo K, Horvat T, Mahabadi NK, Tsitkov S, Ijspeert AJ. (2016) From cineradiography to biorobots: an approach for designing robots to emulate and study animal locomotion. Journal of The Royal Society Interface, 13(119): 20151089.

[2] Rafeeq M, Toha SF, Ahmad S, Razib MA. (2021) Locomotion strategies for amphibious robots-A review. IEEE Access, 9: 26323-26342.

[3] Hopkins JK, Spranklin BW, Gupta SK. (2009) A survey of snake-inspired robot designs. Bioinspiration & biomimetics, 4(2): 021001.

[4] Park HS, Sitti M. (2009) Compliant footpad design analysis for a bio-inspired quadruped amphibious robot. In Proceedings of IEEE/RSJ International Conference on Intelligent Robots and Systems: October 2009, pp. 645-651.

[5] Boxerbaum AS, Werk P, Quinn RD, Vaidyanathan R. (2005) Design of an autonomous amphibious robot for surf zone operation: part I mechanical design for multi-mode mobility. In Proceedings of IEEE/ASME International Conference on Advanced Intelligent Mechatronics: July 2005, pp. 1459-1464.

[6] Ding R, Yu J, Yang Q, Tan M. (2009) Kinematics modeling and simulation for an amphibious robot: Design and implementation. In proceedings of IEEE International Conference on Automation and Logistics: July 2009, pp. 35-40.

[7] Bi L, Guo J, Guo S. (2015) Virtual prototyping technology-based dynamics analysis for an amphibious spherical robot. In proceeding of IEEE International Conference on Information and Automation: August 2015, pp. 2563-2568.

[8] Zhong B, Zhou Y, Li X, Xu M, Zhang S. (2016) Locomotion performance of the amphibious robot on various terrains and underwater with flexible flipper legs. Journal of Bionic Engineering, 13(4): 525-536.

[9] Zhuang M, Yu ZW, Gong DP, Xu ML, Dai ZD. (2012) Gait planning and simulation of quadruped robot with hydraulic drive based on ADAMS. Machinery Design & Manufacture, 7: 100-102.

[10] Cao X, Cleghorn WL. (2010) Examples and application of ADAMS software in the mechanics of machines teaching. In 5th International Conference on Computer Science & Education: 2010; pp. 1637-1641. doi: 10.1109/ICCSE.2010.5593596.

[11] Ding R, Yu J, Yang Q, Hu X, Tan M. (2009) Platform-level design for a biomimetic amphibious robot.In proceedding of IEEE International Conference on Robotics and Biomimetics: February 2009, pp. 977-982.

[12] Cox J, Wilfong GT. (1990) Autonomous Robot Vehicles. Springer-Verlag, N.Y.

[13] Iagnemma K, Genot F, Dubowski S. (1999) Rapid physics-based rough terrain rover planning with sensor and control uncertainty. In proceedings of IEEE International Conference on Robotics and Automation, Detroit, MI; pp. 2286-2291.

[14] Tarokh M, McDermott G, Hayati S, Hung J. (1999) Kinematic modelling of a high mobility Mars rover. IEEE Conf. on Robotics and Automation, Detroit, MI.

[15] Kumar P. (2010) Modelling and dynamic analysis of Rocker-Bogie Rover for space exploration. PhD thesis, Indian Institute of Technology Roorkee, India.

[16] Dudek G, Giguere P, Prahacs C, Saunderson S, Sattar J, Torres MLA, Georgiades C. (2007) Aqua: an amphibious autonomous robot. Computer, 40(1): 46-53.

[17] Baines R, Fish F, Kramer BR. (2021) Amphibious robotic propulsive mechanisms: current technologies and open challenges. Bioinspired Sensing, Actuation, and Control in Underwater Soft Robotic Systems, 41-69.

[18] Tan J, Wang Z, Liu Z. (2006) Stable programmed manifold solver for virtual prototyping motion simulation, Chinese Journal of Mechanical Engineering (English Edition), 19(1): 76-80.

[19] Liu XP, Zheng JR, Zhu ZG, Gu XL. (2003) Study on graphical data exchange between Adams/View and solidworks. Mechanical Engineer, 12.

[20] Yu JC, Liao JW, Li MY, Li SH. (2003) Design and motion simulation of the autonomous exploration vehicle. In Proc. of the 7th International Conference on Automation Technology: September 2003; pp.1-6.

[21] Malik SM, Lin J, Goldenberg AA. (2006) Virtual prototyping for conceptual design of a tracked mobile robot. In proceedings of Canadian Conference on Electrical and Computer Engineering: May 2006; pp. 2349-2352. IEEE.

[22] Xing H, Guo S, Shi L, Hou X, Liu Y, Liu H. (2020) Design, modeling and experimental evaluation of a legged, multi-vectored water-jet composite driving mechanism for an amphibious spherical robot. Microsystem Technologies, 26(2): 475-487.

[23] Ullrich F, Goktogan AH, Sukkarieh S. (2011) Design optimization of a mars rover's rocker-bogie mechanism using genetic algorithms. In Proceedings from 10th Australian space science conference; pp. 199-210.

[24] Thuer T. (2009) Mobility Evaluation of Wheeled all-terrain Robots - metrics and application, PhD Thesis, Swiss Federal Institute of Technology Zurich (ETH Zurich).

[25] Saranli U, Buehler M, Koditschek DE. (2001) RHex: A simple and highly mobile hexapod robot, Int. J. Robot. Res., 20(7): 616-631.

[26] Eich M, Grimminger F, Bosse S, Spenneberg D, Kirchner F. (2008) Asguard: A hybrid-wheel security and SAR-robot using bio-inspired locomotion for rough terrain. In Proceedings of . ROBIO; pp.774–779.

[27] Yu J, Ding R, Yang Q, Tan M, Zhang J. (2013) Amphibious pattern design of a robotic fish with wheel-propeller-fin mechanisms: amphibious pattern design of a Robotic Fish, J. Field Robotics, 30: 702-716.

[28] Klein MA, Boxerbaum AS, Quinn RD, Harkins R, Vaidyanathan R. (2012) SeaDog: A rugged mobile robot for surf-zone applications. In Proceedings of 4th IEEE RAS EMBS Int. Conf. Biomed. Robot. Biomechatronics (BioRob): June 2012; pp. 1335–1340.